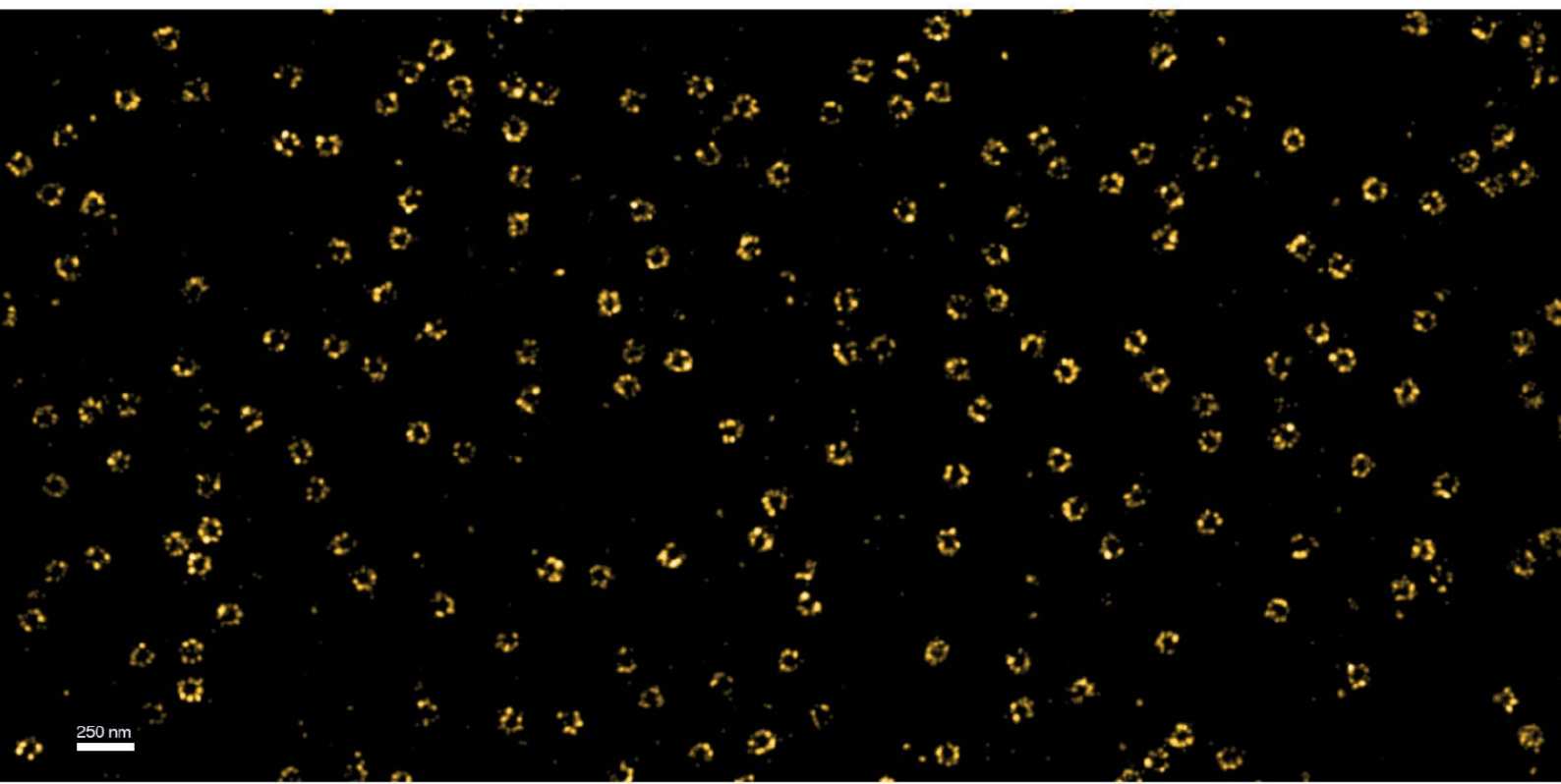


Tino Pleiner

**Rapid nanobody discovery and novel  
nanobody engineering strategies for the  
study of the nuclear pore complex**



**Cuvillier Verlag Göttingen**  
Internationaler wissenschaftlicher Fachverlag



Rapid nanobody discovery and novel nanobody engineering  
strategies for the study of the nuclear pore complex





# **Rapid nanobody discovery and novel nanobody engineering strategies for the study of the nuclear pore complex**

## **Dissertation**

for the award of the degree

'Doctor rerum naturalium'

within the Molecular Biology program

of the Georg-August-Universität Göttingen

Faculty of Biology

Submitted by

**Tino Pleiner**

Born in

Zeitz, Germany

Göttingen, March 2016



## **Bibliografische Information der Deutschen Nationalbibliothek**

Die Deutsche Nationalbibliothek verzeichnet diese Publikation in der Deutschen Nationalbibliografie; detaillierte bibliografische Daten sind im Internet über <http://dnb.d-nb.de> abrufbar.

1. Aufl. - Göttingen: Cuvillier, 2017

Zugl.: Göttingen, Univ., Diss., 2016

© CUVILLIER VERLAG, Göttingen 2017

Nonnenstieg 8, 37075 Göttingen

Telefon: 0551-54724-0

Telefax: 0551-54724-21

[www.cuvillier.de](http://www.cuvillier.de)

Alle Rechte vorbehalten. Ohne ausdrückliche Genehmigung des Verlages ist es nicht gestattet, das Buch oder Teile daraus auf fotomechanischem Weg (Fotokopie, Mikrokopie) zu vervielfältigen.

1. Auflage, 2017

Gedruckt auf umweltfreundlichem, säurefreiem Papier aus nachhaltiger Forstwirtschaft.

ISBN 978-3-7369-9515-4

eISBN 978-3-7369-8515-5



### **Members of the Thesis Committee**

Prof. Dr. Dirk Görlich  
(Supervisor and referee)                      Max Planck Institute for Biophysical Chemistry  
Department of Cellular Logistics  
Göttingen, Germany

Prof. Dr. Peter Rehling  
(Co-referee)                                      University Medical Center Göttingen  
Department of Cellular Biochemistry  
Göttingen, Germany

Prof. Dr. Reinhard Lührmann                      Max Planck Institute for Biophysical Chemistry  
Department of Cellular Biochemistry  
Göttingen, Germany

### **Additional members of the Examination Board**

Prof. Dr. Holger Stark                              Max Planck Institute for Biophysical Chemistry  
Department of Structural Dynamics  
Göttingen, Germany

Prof. Dr. Henning Urlaub                              Max Planck Institute for Biophysical Chemistry  
Bioanalytical Mass Spectrometry  
Göttingen, Germany

Prof. Dr. Detlef Doenecke                              University Medical Center Göttingen  
Department of Molecular Biology  
Göttingen, Germany

Date of oral examination: 13.05.2016





I hereby declare that I completed my thesis entitled 'Rapid nanobody discovery and novel nanobody engineering strategies for the study of the nuclear pore complex' independently and with no other aids or sources than quoted.

This dissertation has not been submitted elsewhere for any academic award or qualification.

Tino Pleiner

Göttingen, March 2016





*'Progress in science depends on new techniques, new discoveries and new ideas,  
probably in that order.'*

- Sydney Brenner -





# Table of Contents

<b>1</b>	<b>SUMMARY</b> .....	<b>1</b>
<b>2</b>	<b>INTRODUCTION</b> .....	<b>2</b>
2.1	THE VERTEBRATE NUCLEAR PORE COMPLEX (NPC).....	2
2.1.1	<i>Nucleocytoplasmic transport</i> .....	3
2.1.2	<i>Structure of the nuclear pore complex</i> .....	6
2.1.3	<i>Composition of the NPC</i> .....	7
2.2	ANTIBODY ENGINEERING .....	14
2.2.1	<i>Structure of antibodies</i> .....	15
2.2.2	<i>Monoclonal antibodies</i> .....	17
2.2.3	<i>Recombinant antibody fragments</i> .....	18
2.2.4	<i>Natural single domain antibodies</i> .....	20
2.3	PHAGE DISPLAY.....	23
2.3.1	<i>Filamentous phage life cycle</i> .....	23
2.3.2	<i>Selection of recombinant antibodies via phage display</i> .....	25
2.4	AIMS OF THIS STUDY .....	28
<b>3</b>	<b>RESULTS</b> .....	<b>29</b>
3.1	A RAPID WORKFLOW FOR NANOBODY DISCOVERY .....	29
3.1.1	<i>Total RNA isolation and RNA quality control</i> .....	31
3.1.2	<i>Library construction via Gibson assembly</i> .....	32
3.1.3	<i>Design of the minimal phagemid</i> .....	34
3.1.4	<i>Selective elution of antigen-bound phages</i> .....	37
3.1.5	<i>Rapid quantification of panning by qPCR</i> .....	37
3.1.6	<i>Cloning of enriched sub-libraries and sequence analysis</i> .....	40
3.2	NOVEL NANOBODY ENGINEERING STRATEGIES .....	42
3.2.1	<i>Functional cytoplasmic expression of nanobodies</i> .....	42
3.2.2	<i>Native purification of endogenous protein complexes using nanobodies</i> .....	45
3.2.3	<i>Site-specific fluorescent labeling of nanobodies</i> .....	49
3.2.4	<i>Imaging with site-specifically labeled nanobodies</i> .....	54
3.2.5	<i>Super-resolution imaging with site-specifically labeled nanobodies</i> .....	58
3.2.6	<i>Rapid epitope mapping via crosslinking mass spectrometry</i> .....	60
3.3	ANTI-NUP NANOBODY TOOLBOX APPLIED TO THE STUDY OF THE NPC.....	62
3.3.1	<i>Generation &amp; characterization of the anti-Nup nanobody toolbox</i> .....	62
3.3.2	<i>Selection of nanobodies against natively isolated xlNup107 complex</i> .....	65
3.3.3	<i>NPC assembly investigation with the anti-Nup nanobody toolbox</i> .....	66



3.3.4	<i>Analysis of interphase and mitotic nucleoporins</i> .....	70
<b>4</b>	<b>DISCUSSION</b> .....	<b>72</b>
4.1	A RAPID PHAGE DISPLAY-BASED NANOBODY DISCOVERY WORKFLOW .....	72
4.1.1	<i>Rapid and accurate library construction via Gibson assembly</i> .....	72
4.1.2	<i>A 'minimal phagemid' facilitates construction of large libraries</i> .....	73
4.1.3	<i>qPCR quantification of phage display</i> .....	75
4.1.4	<i>The importance of a characterization strategy</i> .....	76
4.1.5	<i>Comparison to mass spectrometry-based nanobody production workflow</i> .....	77
4.2	CYTOPLASMIC EXPRESSION OF ENGINEERED NANOBODIES.....	78
4.2.1	<i>Native protein complex isolation</i> .....	80
4.2.2	<i>Reliable fluorescent labeling of nanobodies</i> .....	81
4.2.3	<i>Mapping conformational epitopes via crosslinking mass spectrometry</i> .....	84
4.3	EXPLORATION OF THE ANTI-NUP NANOBODY TOOLBOX .....	85
<b>5</b>	<b>MATERIALS</b> .....	<b>87</b>
5.1	REAGENTS.....	87
5.2	BUFFERS AND SOLUTIONS.....	89
5.3	E. COLI STRAINS AND MEDIA .....	90
5.4	LAB EQUIPMENT .....	91
5.5	SOFTWARE & ONLINE TOOLS.....	92
<b>6</b>	<b>METHODS</b> .....	<b>93</b>
6.1	STANDARD METHODS IN MOLECULAR BIOLOGY .....	93
6.2	PROTEIN BIOCHEMISTRY METHODS.....	97
6.3	NANOBODY LIBRARY CONSTRUCTION .....	103
6.4	PHAGE DISPLAY.....	106
6.5	<i>XENOPUS</i> EGG EXTRACT METHODS .....	113
6.6	FLUORESCENCE MICROSCOPY METHODS.....	116
6.7	STRUCTURAL BIOLOGY METHODS.....	119
<b>7</b>	<b>LIST OF ABBREVIATIONS</b> .....	<b>122</b>
<b>8</b>	<b>CONTRIBUTION BY OTHERS</b> .....	<b>124</b>
<b>9</b>	<b>ACKNOWLEDGMENTS</b> .....	<b>125</b>
<b>10</b>	<b>REFERENCES</b> .....	<b>127</b>
<b>11</b>	<b>CURRICULUM VITAE</b> .....	<b>139</b>
<b>12</b>	<b>LIST OF PUBLICATIONS</b> .....	<b>139</b>



# 1 Summary

Nanobodies are recombinant single-domain antibodies of camelid origin. We set out to generate nanobodies as tools to study vertebrate nuclear pore complexes (NPCs) that constitute the major passageways for nucleocytoplasmic exchange. However, we realized that the standard protocols for nanobody production and application suffered from substantial limitations.

Therefore, we developed an optimized phage display-based workflow for the generation of nanobodies from an immunized animal. It relies on standard techniques and can be completed by a single person within only 14 working days. Using Gibson assembly and a miniaturized phagemid, large nanobody libraries were easily constructed and reliably propagated during phage display. The specificity of elution during panning was enhanced by the selective proteolytic release of antigen-bound phages. This yielded higher enrichment of positive binders. Furthermore, phage titering was replaced by quantitative PCR to quickly analyze phage display selections. The time required to characterize nanobodies was greatly reduced by cloning entire sublibraries after panning directly into a vector that contains all necessary fusion tags for characterization.

The identified nanobodies were functionally expressed in the *E. coli* cytoplasm in a disulfide bond-free form, thus overcoming the engineering limitations imposed by conventional periplasmic secretion. Using protease-cleavable affinity tags, we developed a generic strategy for native protein complex isolation from eukaryotic sources. As a proof of principle we purified the major NPC subcomplexes in high yields and in excellent quality for a direct structural analysis by electron microscopy. We further established a reliable fluorescent labeling strategy of nanobodies that is based on engineered surface cysteines and maleimide chemistry. In contrast to NHS labeling of lysines, maleimide labeling is site-specific, does not interfere with antigen recognition and yields superior imaging reagents. The ectopic cysteines also proved useful as ‘position sensors’ for epitope mapping via crosslinking mass spectrometry.

Based on the optimized workflow, we generated a large toolbox of nanobodies against constituents of *Xenopus* NPCs. In combination with our novel engineering strategies, here we outline how these nanobodies can be used to study various unresolved aspects of NPC structure, assembly and function.



## 2 Introduction

### 2.1 The vertebrate nuclear pore complex (NPC)

A double membrane-bound nucleus is the defining feature of all eukaryotic cells. The nuclear envelope encloses the cell's genetic information and strictly regulates access to it from the surrounding cytoplasm. The advantages of this compartmentalization are manifold. The spatial separation of transcription (nucleus) and translation (cytoplasm) is the basis for the very high fidelity of gene expression and effectively prevents the production of potentially toxic protein fragments from incompletely or incorrectly processed mRNAs. It also enabled alternative mRNA processing mechanisms to evolve that yield different protein products from a single gene thereby increasing the complexity of eukaryotic cells. Furthermore, the regulatory control over access to the genome allowed a temporal-spatial fine-tuning of gene expression e.g. under different environmental conditions or differentiation states.

This physical division of eukaryotic cells necessitates an exchange of macromolecules between the two compartments. Nucleocytoplasmic transport proceeds through circular openings that fenestrate the nuclear envelope (Callan and Tomlin, 1950; Feldherr, 1962). These nuclear pores result from the fusion of the outer and inner nuclear membrane. While the outer nuclear membrane is continuous with the endoplasmic reticulum, access to the inner nuclear membrane is restricted and it thus has a distinct protein composition.

Giant multi-protein assemblies reside in nuclear pores (Gall, 1954; Watson, 1959) and constitute a physical permeability barrier that prevents an intermixing of nuclear and cytoplasmic contents. Under the electron microscope these so-called nuclear pore complexes (NPCs) (Watson, 1959), show an octagonal symmetry along the transport axis (Gall, 1967) (Figure 2.1). The cytosolic side of NPCs shows eight filamentous protrusions, whereas the nuclear side carries a filamentous basket-like structure.

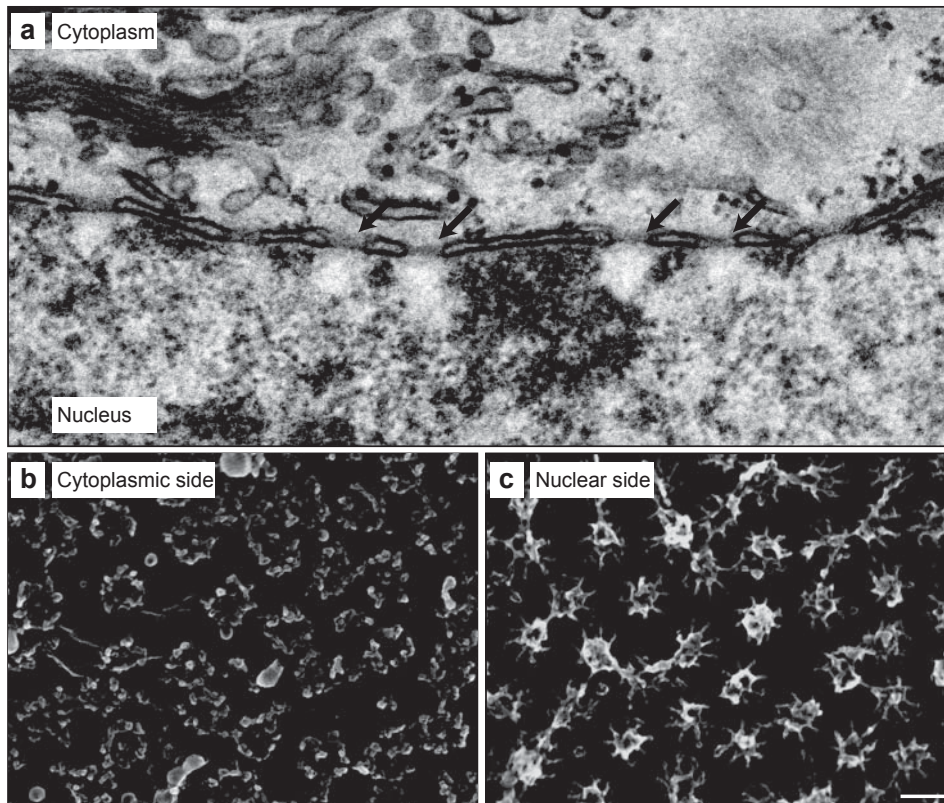


**Figure 2.1. Nuclear pore complexes are embedded in the envelope of cell nuclei.**

(a) Transmission electron micrograph of a HeLa cell nuclear envelope cross-section. Black arrows indicate regions of the nuclear envelope that contain nuclear pores at sites where the outer and inner nuclear membrane are fused. The nuclear side of the pores shows distinct exclusion zones that correspond to the nuclear basket region. (b) Scanning electron microscopy (SEM) image of a *Xenopus* oocyte nuclear envelope from the cytosolic side. The octagonal nuclear pore complexes display unconnected filamentous protrusions. (c) SEM image of a *Xenopus* oocyte nuclear envelope from the nuclear side. Filamentous basket-like structures emanate from the nuclear pore complexes. All images were kindly provided by Dr. Volker Cordes (MPI for Biophysical Chemistry, Göttingen).

### 2.1.1 Nucleocytoplasmic transport

Nucleocytoplasmic exchange across the nuclear envelope can occur in two modes – passive and facilitated (reviewed in Görlich and Kutay, 1999). Simple passive diffusion is efficient only for proteins less than 20-30 kDa in size and 4-5 nm in diameter (Mohr et al., 2009). Above this size limit passive diffusion is very slow. Facilitated nuclear transport is a carrier-mediated process and very efficient even for very large proteins and protein complexes. This mode of transport allows directional import and export of proteins and requires the cargo molecule to possess a specific signature or transport signal that can recruit so-called nuclear transport receptors (NTRs). The first nuclear transport signal to be identified is the classical nuclear localization signal (cNLS) that



confers nuclear import and consists of a stretch of basic amino acids (Dingwall et al., 1982; Kalderon et al., 1984; Lanford and Butel, 1984).

The cNLS is recognized by the import adaptor protein Importin- $\alpha$  (Adam and Adam, 1994; Görlich et al., 1994), which mediates binding to the major NTR of the Importin (Imp) family, Imp $\beta$  (Adam and Adam, 1994; Chi et al., 1995; Görlich et al., 1995; Imamoto et al., 1995). The Imp $\beta$ •Imp $\alpha$ •cargo complex then traverses the NPC. Nuclear pore passage is per se bidirectional, energy-independent and requires interaction of Imp $\beta$  with Phe-Gly (FG) repeat-containing proteins of the NPC. Binding of the small GTPase Ran (Melchior et al., 1993; Moore and Blobel, 1993) in its GTP-bound form (RanGTP) to Imp $\beta$  on the nuclear side of the NPC releases the cargo and Imp $\alpha$  (Görlich et al., 1995; Rexach and Blobel, 1995). The Imp $\beta$ •RanGTP complex then traverses back to the cytoplasmic side of the NPC where disassembly is catalyzed by RanBP1 and rendered irreversible by Ran GTPase activating protein (RanGAP)-stimulated GTP hydrolysis of Ran (Bischoff and Görlich, 1997). This frees Imp $\beta$  to participate in another round of import and leaves RanGDP in the cytoplasm. Imp $\alpha$  also needs to be recycled back to the cytoplasm. A specific export-mediating NTR Exportin (Xpo)-2 (or CAS) performs this task (Kutay et al., 1997).

Exportins bind their cargo together with RanGTP in the nucleus (Stade et al., 1997; Fornerod et al., 1997; Kutay et al., 1997). Assembly of the trimeric Exportin•RanGTP•cargo complex is cooperative and leads to its translocation through the NPC. On the cytoplasmic side, export complex disassembly is triggered by RanBP1 and RanGAP, leading to cargo and RanGDP dissociation. The Exportin can then cycle back to the nuclear side to transport another cargo. The major Exportin of the cell, CRM1, has a very broad cargo range and recognizes classical nuclear export signals composed of multiple spaced hydrophobic residues (Fornerod et al., 1997; Güttler et al., 2010; Kirli et al., 2015).

Both import and export processes constantly shuttle Ran to the cytoplasm where it is converted to its GDP-bound form (RanGDP). RanGDP is shuttled back to the nucleus by a dedicated transport receptor, called Ntf2 (Ribbeck et al., 1998). Importantly, Ntf2 does not require RanGTP for cargo unloading and thus achieves a net transport of Ran. In the nucleus the chromatin-bound guanine nucleotide exchange factor Rcc1 (Bischoff and Ponstingl, 1991) converts RanGDP to RanGTP. The asymmetric localization of



proteins regulating Ran's nucleotide-bound state ensures the establishment of a steep RanGTP gradient across the nuclear envelope that confers directionality to all transport events and renders them irreversible (Görlich et al., 1996b; Görlich et al., 1996a; Izaurralde et al., 1997).

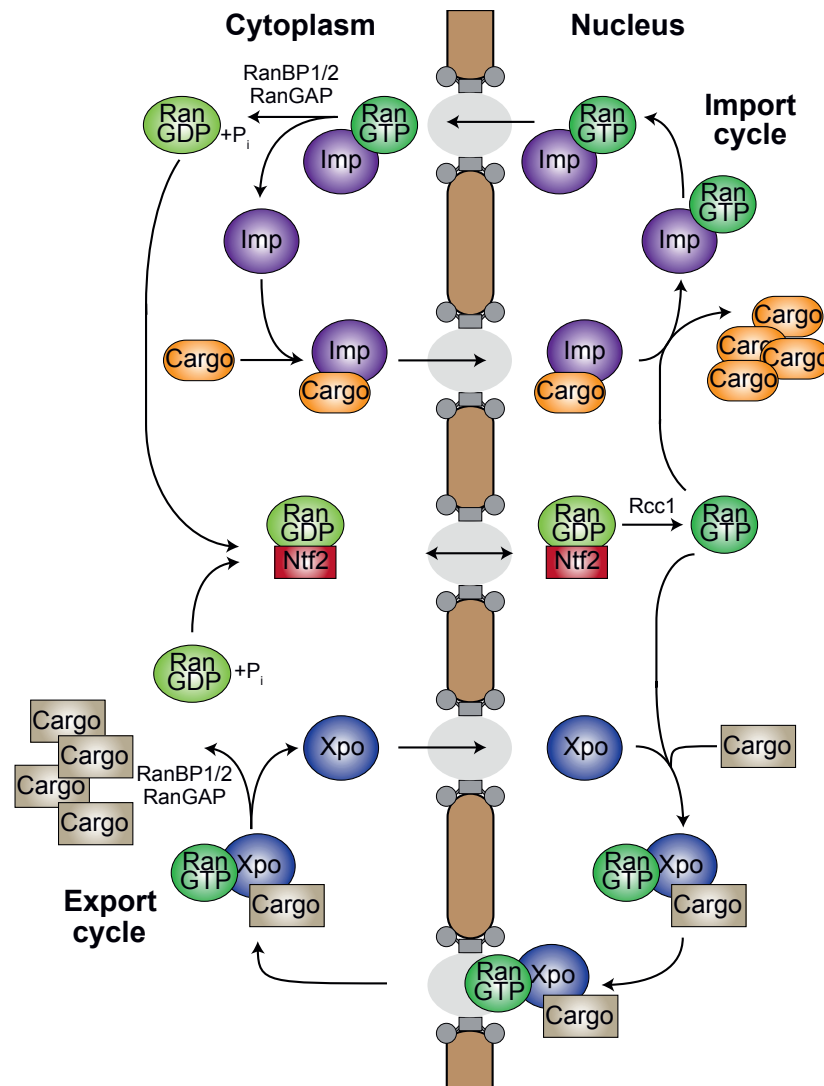


**Figure 2.2. Schematic overview of facilitated nucleocytoplasmic transport.**

Facilitated nuclear transport is divided into import and export processes. Importins (Imp) bind their substrates in the cytoplasm, where RanGTP levels are low. Imp•cargo complexes then traverse the NPC and are dissociated at the nuclear side by RanGTP binding to the Imp. This triggers a conformational change and results in cargo release. The Imp•RanGTP complex cycles back to the cytoplasm where GTP hydrolysis by Ran is triggered by the NPC-bound proteins RanGAP, RanBP1 and RanBP2. This frees the Imp to participate in another round of import. An Export complex assembles in the nucleus upon RanGTP and cargo binding to an Exportin (Xpo). The trimeric complex then traverses the NPC to the cytoplasmic side where GTP hydrolysis leads to its disassembly. The Xpo cycles back to the nucleus where it mediates another round of export. In order to prevent the dissipation of the RanGTP gradient (high concentration in nucleus, low concentration in cytoplasm) RanGDP is transported back to the nucleus by a specific NTR called Ntf2. Transport is per se bidirectional and energy-independent. The RanGTP gradient confers directionality and GTP hydrolysis renders the transport processes irreversible. This figure is adapted from Görlich and Kutay, 1999.



### 2.1.2 Structure of the nuclear pore complex

The structural organization and composition of the NPC is important for understanding its essential function in nucleocytoplasmic transport as a highly selective permeability barrier. Therefore, it has been the subject of intensive investigation. Due its enormous size of around 120 MDa in higher eukaryotes (Reichelt et al., 1990; Ori et al., 2013), structural analysis of the NPC is challenging. Cryo-electron tomography emerged as a suitable technique to study the overall architecture of NPCs (Hinshaw et al., 1992; Bui et al., 2013; Eibauer et al., 2015; von Appen et al., 2015). The NPC scaffold spans around 114 nm in width and 80 nm in height (Figure 2.3). It consists of three ring-like structures that are interconnected and individually anchored to the membrane. Due to a pseudo-twofold symmetry relative to the nuclear envelope plane, the cytoplasmic and nuclear rings appear very similar in architecture. The inner ring shows a distinct structure and encloses the narrowest constriction (~40 nm) of the central transport channel.

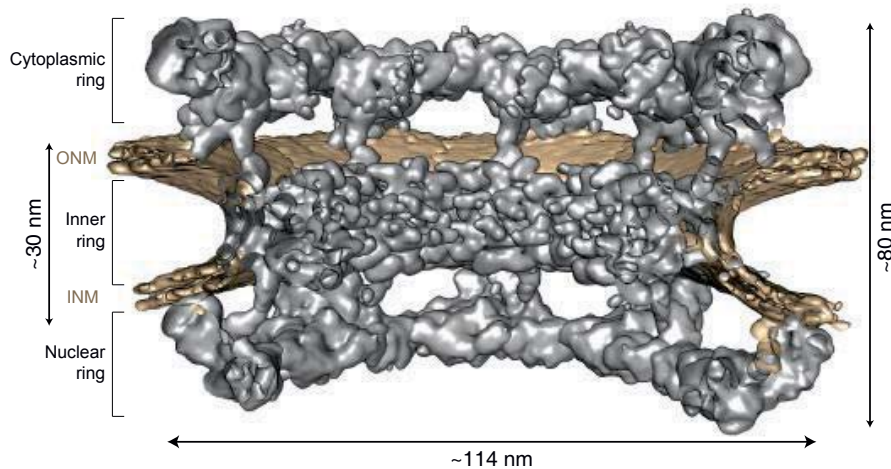


**Figure 2.3. Structure of the human nuclear pore complex scaffold.**

The nuclear pore complex (NPC) is a large multiprotein complex that resides in pore-like openings of the nuclear envelope where outer (ONM) and inner nuclear membrane (INM) are fused. Due to its large size of around 120 MDa cryo-electron tomography (ET) has proven to be the method of choice for structural analysis of the NPC. This image shows a recent cryo-ET reconstruction of the human NPC at 23 Å resolution (prepared from EMD-3103 with UCSF Chimera; von Appen et al., 2015). A cutaway view of the electron density is shown. The major scaffold of the NPC (dark grey) (excluding cytoplasmic filaments and nuclear basket) spans around 114 x 80 nm and has an eight-fold rotational symmetry axis (8 asymmetric units). The NPC is divided into three interconnected ring-like structures (cytoplasmic, inner and nuclear ring). All rings show distinct contact regions with the membrane (brown).

The eightfold-rotational symmetry of the NPC suggested it to be quite a modular assembly. Indeed, only around 30 different proteins (Cronshaw et al., 2002), called



nucleoporins (Nups), form a NPC (Figure 2.4; Figure 2.5). Nups assemble into subcomplexes that can be found as stable building blocks throughout the cell cycle. The subcomplexes in turn form the entire NPC and likely exist in a copy number that is a multiple of 8 (e.g. 16 or 32-fold) (Figure 2.5) (Ori et al., 2013). Nups can be broadly classified into transmembrane Nups, scaffold Nups and Phe-Gly (FG) repeat containing Nups, although this distinction is not absolute and some Nups seem to have dual roles (Fischer et al., 2015). The NPC scaffold is anchored to the pore membrane via transmembrane Nups, whereas the scaffold itself positions FG Nups in the central transport channel. The non-globular FG repeat domains of FG Nups are thought to interact with each other to form a three-dimensional meshwork that constitutes the permeability barrier (Ribbeck and Görlich, 2001; Frey et al., 2006; Frey and Görlich, 2007; Hülsmann et al., 2012).

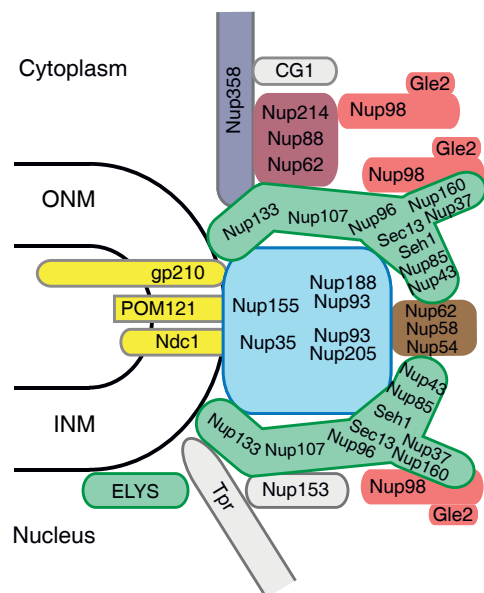


**Figure 2.4. Composition of the NPC.**

Schematic representation of the subcomplex organization and relative localization of Nups within an asymmetric unit of the eightfold rotational symmetric vertebrate NPC. The nuclear and cytoplasmic rings of the structural NPC scaffold are mainly composed of the Nup107 or Y-shaped complex (green). The central inner ring is composed of the Nup93-containing subcomplex (blue). The scaffold is bound to the nuclear envelope via transmembrane Nups (yellow) and further anchors FG-repeat nucleoporins (e.g. Nup98 (red) and the Nup62•Nup58•Nup54 complex (brown)) within the central channel, where they form the permeability barrier. Distinct Nups are present at the cytosolic and nuclear side. The Nup214•Nup88•Nup62 complex is anchored at the cytoplasmic Nup107 complex ring. Nup358/RanBP2 forms the cytoplasmic filaments. Nup153 is a specific binding partner of the Nup107 complex at the nuclear ring. The large Nup TPR forms the nuclear basket. ONM/INM = outer and inner nuclear membrane.

### 2.1.3 Composition of the NPC

The relative arrangement of nucleoporins within the NPC was primarily studied with classical immunogold labeling electron microscopy (Rout et al., 2000; Krull et al., 2004) or with indirect immunofluorescence. Conflicting localization data for many Nups, as a result of these low-resolution approaches, however, make it still quite hard to get a coherent understanding of the molecular architecture of the NPC.

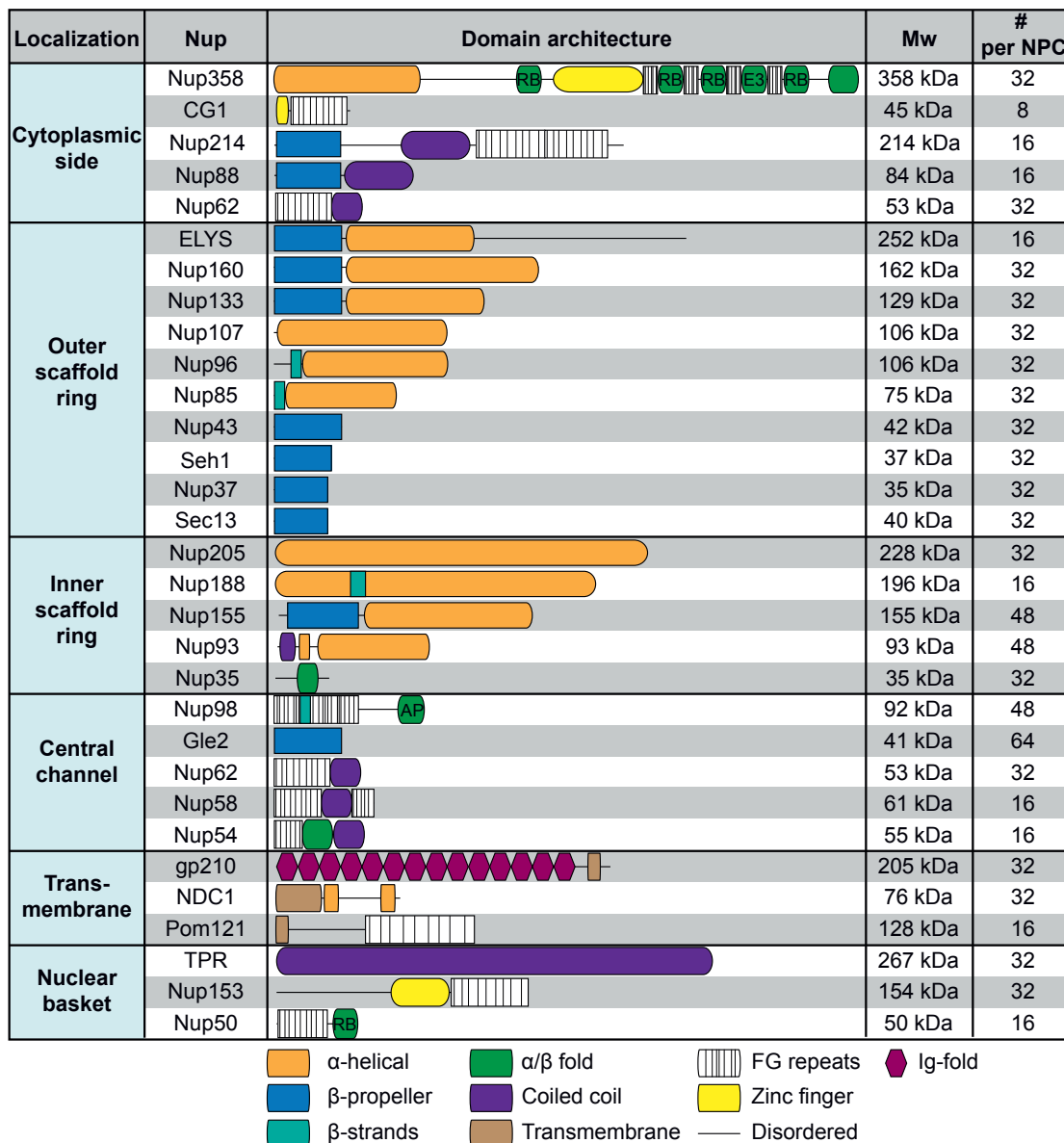


**Figure 2.5. Nucleoporin inventory of human NPCs and their domain architecture.**

Around 30 different proteins are present in vertebrate NPCs in multiple copies. The approximate copy numbers of all Nups (# per NPC) were recently estimated based on mass spectrometry data (Ori et al., 2013). Two fold types are predominantly found in Nups:  $\alpha$ -helical repeats and  $\beta$ -propellers. Many Nups contain incomplete  $\beta$ -propellers that are complemented in trans by other Nups that insert a single  $\beta$ -blade (e.g. Nup98•Gle2, Nup96•Sec13, Nup85•Seh1). Ten Nups possess non-globular Phe-Gly (FG)-repeat domains that bind nuclear transport receptors and participate in the formation of the permeability barrier. The trimeric Nup62•Nup58•Nup54 complex is formed by extensive coiled coil interactions that also contribute to NPC anchorage via Nup93. The Nup214•Nup88•Nup62 complex also involves a coiled-coil interface. RB = Ran-binding domain; E3 = E3 SUMO Ligase domain; AP = autoproteolytic domain. This figure is adapted from Brohawn et al., 2009; as well as from Knockenhauer and Schwartz, 2016.

### Cytoplasmic side

The cytoplasmic filaments of the NPC were shown to be dispensable for nuclear transport in an *in vitro* system (Walther et al., 2002). They are likely formed by the very large nucleoporin RanBP2/Nup358 (Wu et al., 1995; Yokoyama et al., 1995) that lacks



a homologue in lower eukaryotes. RanBP2 has four Ran-binding domains, possesses FG repeats and forms a complex with sumoylated RanGAP (Mahajan et al., 1997). In fact, RanBP2 is itself an E3-SUMO Ligase (Pichler et al., 2002). *In vivo* studies suggested that RanBP2 functions as a platform for efficient nuclear import complex formation (Hutten et al., 2008; Hutten et al., 2009). Recently, an unanticipated role of RanBP2 in organizing the structural arrangement of the cytoplasmic ring was suggested (von Appen et al., 2015).

The Nup214•Nup88•Nup62 complex is a trimeric FG repeat-containing coiled-coil complex (Macaulay et al., 1995; Bastos et al., 1997; Belgareh et al., 1998) that functions as a docking site for CRM1 export complexes (Fornerod et al., 1997; Bernad et al., 2006) and forms a protrusion from the cytoplasmic ring towards the central channel (Bui et al., 2013; Gaik et al., 2015).

It is still unclear how exactly RanBP2 and the Nup214•Nup88•Nup62 complex are anchored to the NPC scaffold.

### **Outer scaffold rings**

A large conserved nucleoporin subcomplex called Nup107-160 or Y-complex (Siniosoglou et al., 1996; Siniosoglou et al., 2000; Vasu et al., 2001) is essential for NPC assembly (Harel et al., 2003; Walther et al., 2003) and forms the cytoplasmic and nuclear rings of the NPC scaffold (Bui et al., 2013). It is the best-characterized NPC subcomplex and consists of ten proteins in higher eukaryotes. Its structural arrangement within the NPC has been intensely studied and multiple different models were proposed (Alber et al., 2007; Hsia et al., 2007; Brohawn et al., 2008). Data derived from various techniques suggested a head-to-tail arrangement of the Y-complex (Alber et al., 2007; Kampmann et al., 2011; Szymborska et al., 2013). Recently, a cryo-EM reconstruction of the human Y-complex could be fitted into a cryo-electron tomogram of the human NPC revealing a surprising double head-to-tail ring arrangement in both cytoplasmic and nuclear ring (16 copies per ring, 32 in total) (Bui et al., 2013; von Appen et al., 2015). Many Nups or Nup fragments of the Y-complex were crystallized individually before and recently also in complex allowing the construction of atomic 3D models of the entire complex (Stuwe et al., 2015b; Kelley et al., 2015).



There is still a debate on whether there is a single or a double head-to-tail ring (Kelley et al., 2015) and whether this arrangement is identical in the cytoplasmic and nuclear rings (Eibauer et al., 2015). Furthermore, species and cell-type-specific differences in NPC structure and composition might exist and are still poorly understood.

### **Inner scaffold ring**

The nucleoporins Nup93, Nup188, Nup205, Nup155 and Nup35 constitute the inner ring of the NPC scaffold, whose architecture is less well understood (Vollmer and Antonin, 2014). Nup93 is essential for NPC assembly and occurs in two distinct subcomplexes with the two large paralogous proteins Nup188 and Nup205 (Grandi et al., 1997; Miller et al., 2000; Theerthagiri et al., 2010; Sachdev et al., 2012). The binding of Nup188 and Nup205 to Nup93 is mutually exclusive and both are dispensable for NPC assembly (Theerthagiri et al., 2010; Sachdev et al., 2012). The yeast Nup93 homologue Nic96 was crystallized and shows a J-like  $\alpha$ -helical fold (Jeudy and Schwartz, 2007; Schrader et al., 2008). Fungal Nup188 and Nup205 assume characteristic S-shaped structures in cryo-EM and bear some resemblance to nuclear transport receptors (Amlacher et al., 2011; Flemming et al., 2012; Andersen et al., 2013). All three proteins were shown to bind FG repeats and this could contribute to a tight sealing of the permeability barrier on the NPC scaffold (Schrader et al., 2008; Andersen et al., 2013).

Nup35 and Nup155 are both essential for NPC assembly (Franz et al., 2005; Hawryluk-Gara et al., 2008), interact with each other and undergo a complicated interaction network with Nup93 and Nup205 of the inner ring (Hawryluk-Gara et al., 2005), as well as with NDC1 and Pom121 at the nuclear pore membrane (Mansfeld et al., 2006; Mitchell et al., 2010; Eisenhardt et al., 2014). Additionally, both proteins were suggested to directly contact membranes (Vollmer et al., 2012; von Appen et al., 2015). They therefore have a major role in membrane anchorage of the NPC scaffold.

Recently, various inner ring scaffold complexes were reconstituted *in vitro* with well-behaved proteins from the thermophilic fungus *Chaetomium thermophilum* (Amlacher et al., 2011; Fischer et al., 2015). The three-dimensional organization of these very flexible complexes within the NPC remains a challenging puzzle for future research.



## Central Channel

The central channel is delineated by FG repeat nucleoporins that form the permeability barrier (Labokha et al., 2013; Schmidt and Görlich, 2016). The structural organization of the permeability barrier is debated, although biochemical data suggest a gel-like FG meshwork (Hülsmann et al., 2012). Therefore, future research needs to obtain information about the exact copy number, 3D localization and configuration of FG Nups to arrive at a mechanistic understanding of nucleocytoplasmic transport.

A prominent FG-repeat Nup complex is the trimeric coiled-coil Nup62•Nup58•Nup54 complex. It is anchored to the inner ring scaffold via coiled-coil interactions with the N-terminus of Nup93. Its stoichiometry and structural organization was the subject of a series of speculative models that were not supported by data (Melcák et al., 2007; Solmaz et al., 2011; Solmaz et al., 2013; Sharma et al., 2015; Koh and Blobel, 2015). Only recently, its 1:1:1 stoichiometry was confirmed by biochemical and structural data (Ulrich et al., 2014; Chug et al., 2015; Stuwe et al., 2015). Interestingly, the kinked and elongated complex could only be crystallized with bound antibodies (camelid nanobody by Chug et al., 2015; synthetic antibody by Stuwe et al., 2015). Recent functional analyses illustrated that NPCs with a functional, although slightly compromised, permeability barrier can form in the absence of the Nup62•Nup58•Nup54 complex (Hülsmann et al., 2012).

Nup98 is the only GLFG-repeat Nup of higher eukaryotes (Radu et al., 1995) and has three orthologues in yeast (Wente et al., 1992; Wente and Blobel, 1994). Nup98 is produced from a larger Nup98-Nup96 precursor protein via autoproteolytic cleavage or via alternative splicing from the precursor mRNA (Fontoura et al., 1999). The absolute C-terminus of Nup98 anchors it at the NPC via interaction with Nup96 and Nup88 in a mutually exclusive manner (Hodel et al., 2002; Griffis et al., 2003; Yoshida et al., 2011; Stuwe et al., 2012). Likely the ‘unstructured region’ and the FG-repeat domain of Nup98 contribute to its NPC anchorage (Griffis et al., 2003; Yoshida et al., 2011; Hülsmann et al., 2012; Fischer et al., 2015). A short  $\beta$ -strand segment, called GLEBS domain, is located within the FG domain of Nup98 and mediates interaction with the essential mRNA export factor Gle2 (Bailer et al., 1998; Pritchard et al., 1999). Importantly, the cohesive FG-repeat domain of Nup98 was found to be essential for formation of the permeability barrier (Hülsmann et al., 2012). Moreover, the



cohesiveness of Nup98 seems to be evolutionary conserved (Schmidt and Görlich, 2015). Its fundamental role is further strengthened by the observation that its phosphorylation-induced dissociation from NPCs at the onset of mitosis is rate-limiting for NPC disassembly and the concomitant breakdown of the permeability barrier (Laurell et al., 2011).

### **Transmembrane Nups**

The role of the three NPC transmembrane proteins of higher eukaryotes (Pom121, NDC1 and gp210) in NPC assembly is debated. None of the three proteins seems to be universally essential and redundancy of their function was suggested (Stavru et al., 2006a; Stavru et al., 2006b). Nevertheless, Pom121 was suggested to play an essential role either for postmitotic NPC assembly (Antonin et al., 2005) or only for interphase NPC assembly (Doucet et al., 2010). Gp210 is a single-pass transmembrane protein with a large luminal domain (Greber et al., 1990). Due to its only very short NPC-exposed domain and the fact that it is not expressed in all cell types (Eriksson et al., 2004; Olsson et al., 2004; Ori et al., 2013), gp210 likely does not play a role in NPC assembly. Pom121 is a single-span transmembrane protein with a long disordered NPC-exposed domain that also contains FG-repeats. Pom121 was shown to bind to Nup155 and Nup160 and could thus link outer and inner ring scaffold (Mitchell et al., 2010). NDC1 is a multi-span membrane-integral protein with a large C-terminal cytoplasmic domain (Stavru et al., 2006a). NDC1 interacts with Nup35 and Nup155 and these interactions seem to be essential for NPC assembly *in vitro* (Hawryluk-Gara et al., 2008; Mitchell et al., 2010; Eisenhardt et al., 2014).

### **Nuclear basket**

The FG-repeat containing Nup153 is localized to the nuclear side of NPCs (Sukegawa and Blobel, 1993; Krull et al., 2004) and likely anchored via its N-terminus to the Nup107 complex of the nucleoplasmic ring (Bastos et al., 1996; Vasu et al., 2001). It contains Zinc-finger domains that are involved in Ran-binding. Nup153 is dispensable for the assembly of a functional permeability barrier (Walther et al., 2001; Hase and Cordes, 2003).



The nuclear basket consists mainly of the large homodimerizing coiled-coil protein TPR (Cordes et al., 1997; Hase et al., 2001; Krull et al., 2004). TPR seems to be anchored via Nup153 to the NPC scaffold (Hase and Cordes, 2003).



## 2.2 Antibody engineering

Since the postulation of the famous 'magic bullet' concept by the Nobel laureate and founding father of modern immunology Paul Ehrlich, scientists were striving to develop specific targeting reagents for disease therapy and basic research. Antibodies constitute the natural defense agents produced by the vertebrate immune system to neutralize and mark pathogenic non-self antigens for destruction by means of tight and specific binding. Hence, antibodies were at the forefront of intense scientific research and were successfully applied in diagnosis, therapeutics and basic research.

Many of the most fundamental molecular biology techniques rely on antibodies and their use has permitted unprecedented insights into the function of their antigens within the context of the cell. Antibodies enable protein detection and quantification (e.g. via Western blotting and Enzyme-linked immunosorbent assays (ELISA)), protein isolation and interaction analysis via immunoprecipitation, protein localization and tracking via immunohistochemistry or immunofluorescence microscopy. Antibodies against cell surface antigens were extremely useful to classify cell types and cell differentiation states and even allowed their physical separation (e.g. via Fluorescence-activated cell sorting).

The sequencing of the human genome revealed the basic inventory of cellular proteins but in order to study the dynamic interplay of all cellular proteins (the proteome) a multitude of well-characterized high quality antibodies and more sophisticated techniques for their application are required. Likewise, many of the most severe human diseases cannot be treated to date due to the difficulty of obtaining truly effective therapeutic antibodies.

These shortcomings of antibody-based binding reagents are the ongoing driving force for intensive research to find the most optimal 'format' of a small, high affine, thermostable, highly soluble and non-immunogenic 'magic bullet'.



### 2.2.1 Structure of antibodies

Antibodies are immunoglobulin (Ig)-type proteins produced by B lymphocytes of the vertebrate immune system to identify and neutralize non-self structures e.g. pathogens like bacteria and viruses. The immunoglobulins of the class IgG are the main effector molecules of the humoral immune response and are therefore the focus of all following descriptions. IgGs are Y-shaped tetrameric proteins composed of two identical copies each of a heavy and a light chain linked by disulfide bonds (Figure 2.6). Initial structural analyses were facilitated by the protease papain that cleaves IgGs into three separate fragments, yielding two antigen-binding fragments (Fab) and one readily crystallizable fragment (Fc) (Porter, 1959). The two Fab fragments are linked via flexible hinge regions to the Fc part. The major building block of all antibodies is the immunoglobulin domain with a characteristic 'Ig fold'. Anti-parallel  $\beta$ -strands are arranged in two  $\beta$ -sheets that pack against each other forming a  $\beta$ -sandwich stabilized by a conserved internal disulfide bond. A heavy chain consists of four Ig-fold domains: one variable (VH) and three constant domains (CH1-3) making it around 50 kDa in

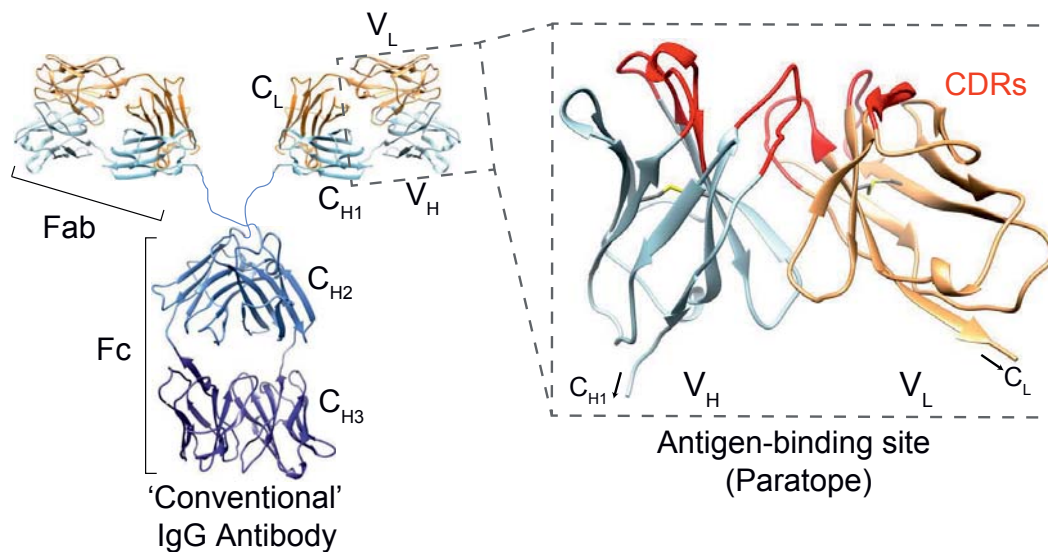


**Figure 2.6. Structure of a conventional IgG antibody.**

The tetrameric IgG molecule is composed of two heavy and two light chains. Each heavy chain (~50 kDa) consists of one variable (V<sub>H</sub>) and three constant domains (CH1-3) (color gradient from N-to C-terminus: light to dark blue). Each light chain (orange) is made up of one variable (V<sub>L</sub>) and one constant domain (C<sub>L</sub>). Light and heavy chains are covalently linked by disulfide bonds between C<sub>L</sub> and C<sub>H1</sub>. The enzyme papain cleaves IgG molecules into three distinct fragments (two antigen-binding (Fab) and one easily crystallizable (Fc) fragment). The antigen-binding site (paratope) is jointly formed by the V<sub>H</sub> and V<sub>L</sub> domains. Each variable domain contributes three hypervariable loops (CDRs; red) giving the paratope an overall cleft-like convex shape that preferentially recognizes linear epitopes. Each IgG molecule has two identical antigen-binding sites and is therefore bivalent. This structure is based on PDB entry 1IGT (Harris et al., 1997).



molecular weight. The constant heavy chain region comes in different isotypes ( $\mu$ ,  $\delta$ ,  $\gamma$ ,  $\alpha$  and  $\epsilon$ ) that critically determine the so-called effector functions of the antibody. A light chain is composed of one variable (VL) and one constant domain (CL) and therefore has only a molecular weight of around 25 kDa. There are two types of light chains: kappa and lambda. The antigen-binding site (paratope) is jointly formed by the variable heavy and variable light chain domains. Due to its tetrameric structure an IgG molecule possesses two paratopes and is thus bivalent. Each variable domain contains three hyper-variable loops that mediate antigen recognition and therefore determine the shape complementarity of the paratope to the antigen. Hence, they were named complementarity-determining regions (CDRs).

The immune system creates a vast diversity of B lymphocytes with distinct membrane-bound immunoglobulins (B cell receptors) that differ foremost in the sequences of their CDR regions and are thus able to adapt to the recognition of an enormous variety of antigens. Upon contact with a complementary antigen and in the presence of co-stimulatory signals these B lymphocytes can differentiate into plasma cells that secrete large amounts of soluble antigen-specific IgG molecules.

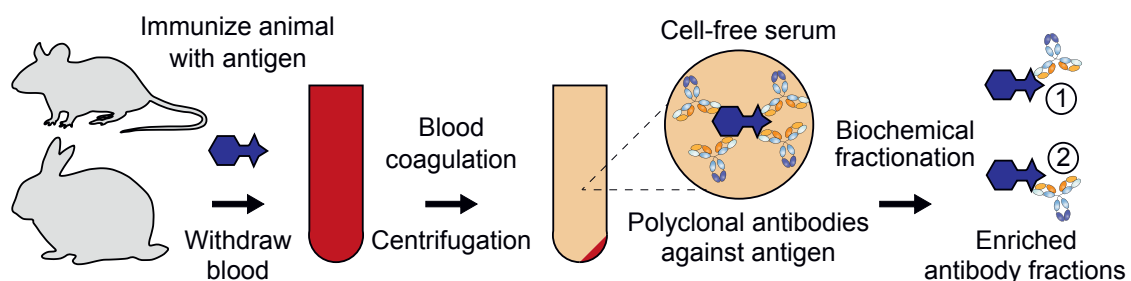


**Figure 2.7. Generation of polyclonal antibodies.**

Animals like mice, rabbits, goats or guinea pigs are repeatedly immunized with an antigen of interest (blue). After the final immunization a blood sample is taken (often all blood of the animal). Following blood coagulation, the clotted blood cells can be separated from the serum by centrifugation. The serum contains polyclonal antibodies. Some of these antibodies are antigen-specific and recognize different regions (epitopes) on the antigen. Using biochemical fractionation approaches like affinity purification antibodies against certain epitopes might be enriched.

This natural immune defense mechanism has been employed for the production of antibodies against antigens of interest for therapeutic or research purposes (Figure 2.7). In particular animals like rabbits, goats, mice and guinea pigs were immunized with antigens of interest and serum from their blood obtained. These immune sera contain a portion of antigen-specific IgG molecules that recognize different epitopes of the antigens and are derived from different B cell clones. Therefore, they are said to be



polyclonal. Polyclonal antibodies can also be affinity-purified from serum and enriched for a target-recognizing population. Due to the dependence on the strength of the immune response and the immunological history of the immunized animal, polyclonal antibodies frequently suffer from large batch-to-batch variability and very often show cross-reactivity to unrelated proteins. Although purification over an antigen column can eliminate non-target binding cross-reacting antibodies, even target-binding antibodies can show genuine cross-reactions to other proteins. Therefore, it is crucial to validate the specificity of each antibody in each of its intended application.

### 2.2.2 Monoclonal antibodies

A breakthrough in antibody production was the development of the hybridoma technology by Georges Köhler and Cesar Milstein (Köhler and Milstein, 1975). The basis of this technique is the fusion of plasma cells of an immunized mouse with myeloma cancer cells leading to chimeric hybridoma cells that can be cultured continuously (Figure 2.8). After selection of hybridoma clones producing antigen-specific antibodies they are clonally expanded. Such a cell line then secretes large amounts of defined ‘monoclonal’ antibodies (mABs) to the culture medium that ideally target a single epitope of their antigen.

The hybridoma technology allowed overcoming problems with antibody yield, specificity and batch-to-batch variability. Hybridomas could easily be cultured or frozen and conserved and shared across laboratories. Highly specific mABs have undoubtedly had enormous impact on human health-care and basic research.

Noteworthy applications of mABs in diagnostic assays are pregnancy tests or blood typing. Many mABs are also successfully applied e.g. in the treatment of inflammatory diseases (anti-TNF $\alpha$  - Adalimumab), breast cancer (anti-HER2 - Trastuzumab) or transplant rejection (anti-CD3 - Muromonab-CD3).

However, their production is still very costly, since it relies on expression in eukaryotic cell culture. Often hybridoma cells also produce more than one type of antibody. Murine mABs can also not directly be used in human therapy due to their immunogenicity, requiring their humanization. Full-length mABs can also not be expressed in the reductive cytoplasm of eukaryotic cells limiting their use as intracellular inhibitors (intrabodies).



The generation of mABs also still relies on the extent of the immune response of a given animal. Therefore, it is difficult to raise mABs against highly conserved or toxic proteins.

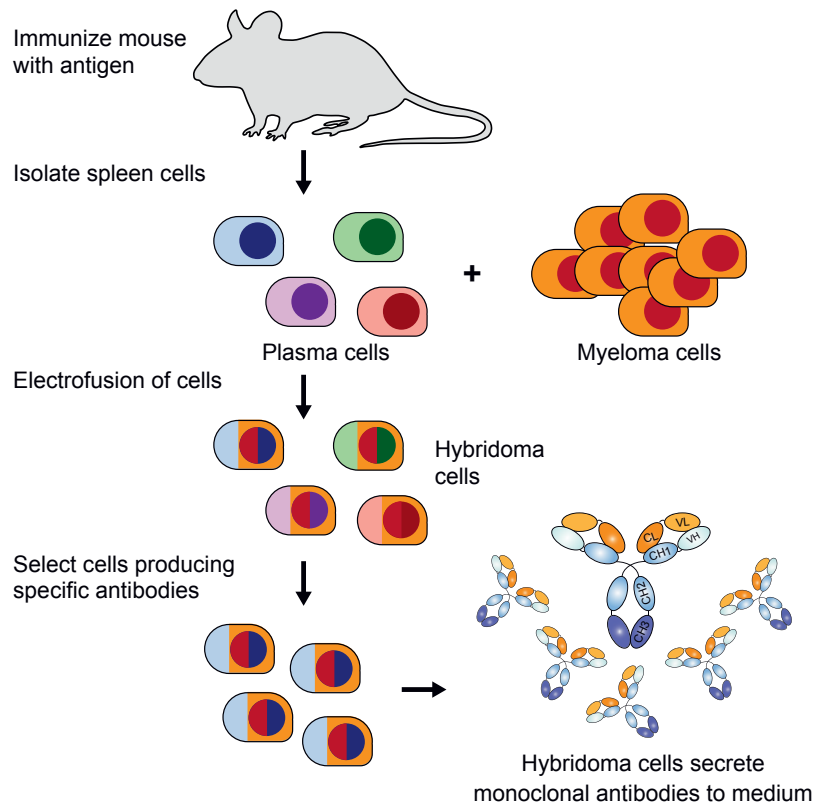


**Figure 2.8. Generation of monoclonal antibodies via the hybridoma technology.**

A mouse is immunized with an antigen of interest. After repeated injections a strong immune response will have formed and antibody-producing plasma cells are isolated from the spleen of the immunized animal. These plasma cells are immortalized by fusing them with myeloma cancer cells. The resulting chimeric cells are termed 'hybridoma' cells and can be passaged unlimitedly. Unfused plasma cells and myeloma cells are actively selected against. Each hybridoma cell ideally produces a monoclonal antibody of unique specificity. Antigen-specific cells are then identified and expanded. Such cells secrete large amounts of specific monoclonal antibodies to the medium.

### 2.2.3 Recombinant antibody fragments

The advance of recombinant DNA technologies revolutionized molecular biology and also enabled the genetic engineering of antibodies. Using universal primers, antibody heavy and light chain coding sequences could be cloned from hybridoma cells and inserted into vectors for expression in *E. coli*, however, only with limited success as they frequently aggregated or were non-functional altogether (Boss et al., 1984; Cabilly et al., 1984). The next step was to generate smaller antibody fragments that would retain antigen-binding (Figure 2.9). In 1988, Better and colleagues reported the first successful expression of a fully active Fab fragment in *E. coli* by periplasmic secretion (Better et



al., 1988). In fact, the bacterially-expressed Fab was as active as the papain-derived Fab fragment from the parental antibody. In the same year, Skerra and Plückthun (1988) reported on the successful *E. coli* expression of an even smaller antibody fragment consisting of only the variable heavy and variable light chain domains. This so-called Fv fragment retained the complete antigen-binding capacity of the original antibody. Huston and colleagues (1988) reported a further improvement of the method by fusing both variable domains into a single polypeptide via a short Gly-Ser linker. The single-chain (sc) Fv fragment format was eventually established for many known mABs and opened up the possibility of facile genetic engineering of antibody binding sites. Especially the use of site-directed mutagenesis to generate more stable and higher affine variants quickly led to a panel of powerful recombinant antibody fragments.

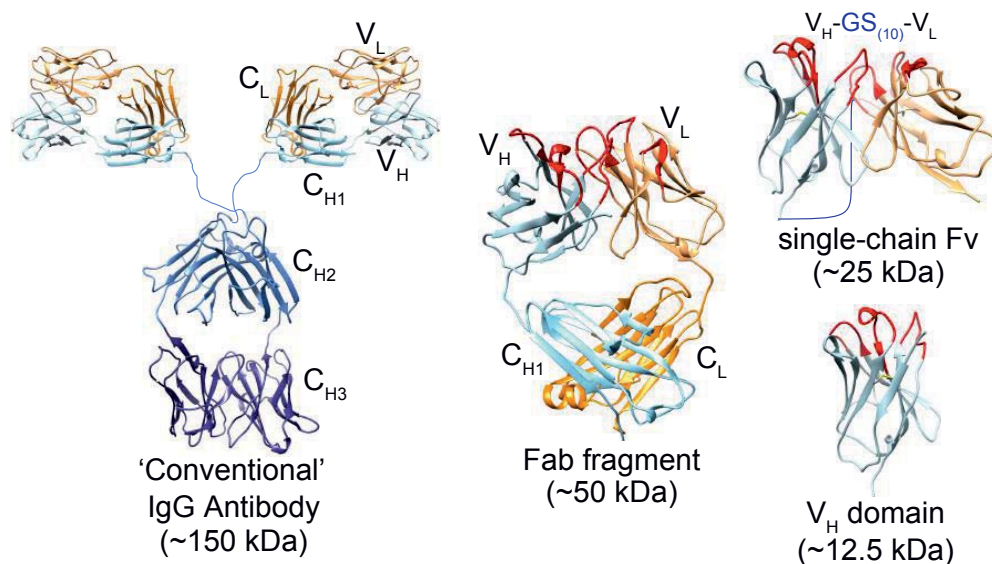


**Figure 2.9. Structures of IgG-derived antibody fragments.**

Smaller fragments can be derived from conventional antibodies by genetic engineering and retain antigen-binding specificity. Fab fragments (~50 kDa) comprise the intact paratope and an additionally stabilizing CH1•CL domain interface. The single-chain Fv fragment (~25 kDa) is constructed by combining variable heavy and variable light domain with a flexible 20aa Gly-Ser linker. Also individual VH domains were shown to be functional in the absence of VL in some cases. The derived fragments can be produced more economically in *E. coli* by secretion to the periplasm. Authentic full-length antibody production relies on eukaryotic glycosylation and thus requires either a high quality hybridoma cell line or human cell culture expression. The derived antibody fragments can also be diversified synthetically and large libraries be constructed from which binders against any given antigen can be retrieved via display technologies.

These advances in antibody engineering opened up the possibility to generate large synthetic antibody (scFv or Fab) DNA libraries with randomized CDR regions (Winter and Milstein, 1991). Using display technologies like phage display (see chapter 2.3.2) such libraries could be searched for binders to any antigen of interest, thereby bypassing



the need for animal immunization and all of its inherent restrictions (Winter et al., 1994).

Although scFv fragments with very high affinity (Boder et al., 2000; Zahnd et al., 2004) could be generated, they often proved to be aggregation-prone or tended to form interchain dimers. Furthermore, it was necessary to construct very large scFv immune libraries to statistically restore as many original VH-VL pairs as possible. This combinatorial problem would be obsolete if single variable domain fragments could be engineered to bind antigens in isolation. Indeed, the successful selection of such 'single-domain antibodies' from murine immune libraries was reported (Ward et al., 1989). These cases, however, remained exceptions and VH domains were often poorly soluble and aggregation prone in the absence of their respective VL domain (Holliger and Hudson, 2005).

The search for the still elusive perfect 'single-domain antibody' gained new momentum when a serendipitous discovery in a Belgian laboratory was made.

#### **2.2.4 Natural single domain antibodies**

In 1993, the discovery of functional heavy-chain antibodies without light chains in the blood of camelids (camels, dromedaries, llamas and alpacas) was reported (Hamers-Casterman et al., 1993). Before that, deviations from the conventional tetrameric structure of antibody molecules were only known to occur in rare types of B lymphocyte disorders called 'heavy chain diseases' (Wahner-Roedler and Kyle, 2005). Only a few years later, homodimeric heavy-chain antibodies were also discovered in the blood of nurse sharks and spotted ratfish (Greenberg et al., 1995; Rast et al., 1998). Phylogenetic analyses suggested that they evolved similar structural features independently and were thus a result of convergent evolution (Nguyen et al., 2002; Flajnik et al., 2011).

The camelid heavy-chain antibodies were found to lack the CH1 domain that is normally responsible for pairing with the light chain in conventional antibodies (Figure 2.10). A single point mutation at the 3' end of the CH1 exon abolishes a donor splice site, leading to its removal during mRNA splicing (Nguyen et al., 1999; Woolven et al., 1999).

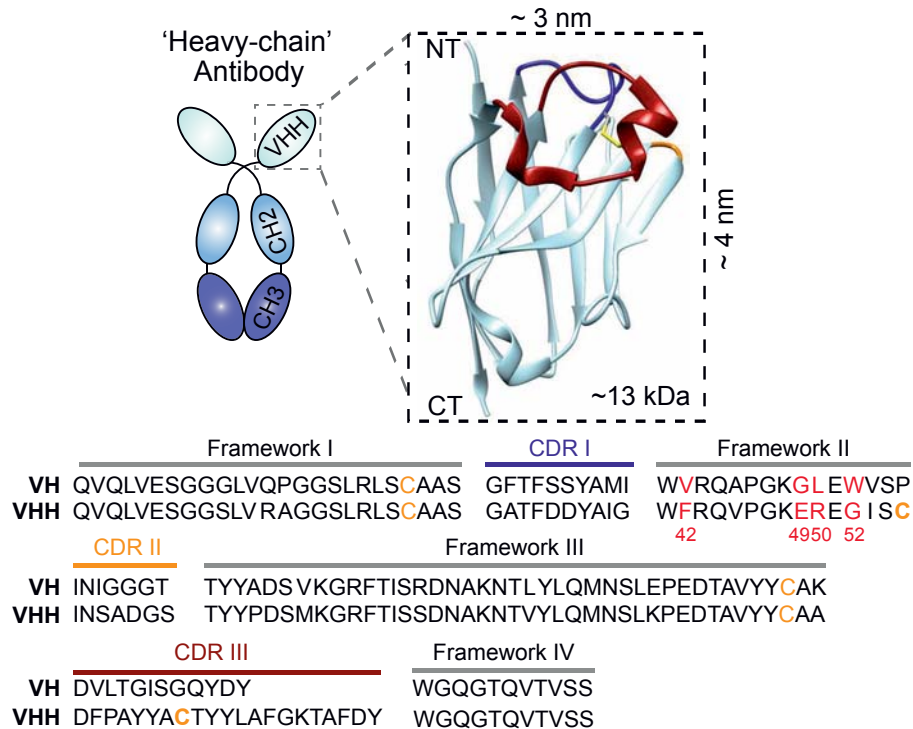


**Figure 2.10. Heavy-chain antibodies and derived VHH domains (nanobodies).**

In contrast to conventional tetrameric antibodies, homodimeric heavy chain antibodies are composed of only two heavy chains and lack light chains. These heavy chains do not possess the constant domain 1 (CH1) that is usually involved in light chain pairing. The variable domain of heavy-chain antibodies (VHH) represents the smallest antigen-binding domain known to occur in nature. It retains its function when isolated and expressed in bacteria. Due to their small size of only 3-4 nm (13 kDa) VHH fragments are also referred to as nanobodies. The typical  $\beta$ -strand architecture of a VHH domain with its three hypervariable loops (CDR I in blue; CDR II in orange; CDR III in dark red) is shown (PDB 1G6V; Desmyter et al., 2001). The alignment of an alpaca VH and VHH domain further illustrates characteristic sequence differences between the domains (highlighted in red) and disulfide-bond forming cysteines are shaded orange. The interloop disulfide bond cysteines of the VHH domain (between framework II and CDR III) are additionally bold. NT = N-terminus; CT = C-terminus.

Importantly, heavy-chain antibodies and conventional antibodies co-exist in the serum of camelids and both are derived from a common IgH locus in the genome (Hamers-Casterman et al., 1993; Achour et al., 2008). However, a dedicated set of variable heavy domain (VHH) genes is employed to generate heavy-chain antibodies (Nguyen et al., 1998). Due to the lack of the light chain, the variable heavy domain (VHH) is solely responsible for antigen-binding. VHH domains further acquired point mutations in the former VH-VL interface (framework II) that render them soluble and functional in the absence of the variable light domain (Muyldermans et al., 1994). These unique sequence characteristics of VHH domains were even transplanted to human VH domains that are rather sticky in isolation due to the absence of the VL binding partner (Davies and Riechmann, 1994). This 'camelization' yielded well-behaved human VH domains.



From initial sequence analysis (Muyldermans et al., 1994) and the first crystal structure of a VHH domain in complex with lysozyme (Desmyter et al., 1996) a further unique feature of VHH domains became obvious. The presence of very long CDR III loops that often fold back onto the framework give VHH domains a prolate shape that is ideal to deeply penetrate into clefts or active sites of enzymes (Desmyter et al., 1996; Lauwereys et al., 1998; De Genst et al., 2006). Such long CDR III loops are frequently the sole mediator of antigen recognition (Desmyter et al., 2001). The unique binding mode and domain shape of VHH domains confers them a predominant preference for conformational epitopes and make them less likely to recognize linear peptides.

Another distinct characteristic of VHH domains is the presence of interloop disulfide bonds (Muyldermans et al., 1994). These additional solvent-exposed disulfide bonds can be found in some VHHs between CDR I and CDR III or framework II and CDR III and are thought to contribute to the overall binding affinity by optimally positioning the long and flexible loops for antigen recognition, thereby reducing the entropic penalty upon binding (Govaert et al., 2012).

Importantly, VHH domains can easily be cloned from lymphocytes of immunized animals and selected against antigens by phage display (see chapter 2.3.2) (Desmyter et al., 1996; Arbabi Ghahroudi et al., 1997). The resulting antigen-binding VHH fragments can be solubly expressed in bacteria and fully retain their high affinity in isolation. Due to their small size, isolated VHH domains were often referred to as nanobodies. In contrast to scFv and VH fragments, nanobodies showed much more favorable biophysical properties including high solubility, low aggregation potential, high thermostability and the ability to reversibly unfold (van der Linden et al., 1999; Pérez et al., 2001; Dumoulin et al., 2002).

All these features put nanobodies as natural single domain antibodies in the spotlight of biomedical and basic research.



## 2.3 Phage Display

### 2.3.1 Filamentous phage life cycle

The filamentous bacteriophages (f1, M13, fd) used in phage display selectively infect 'male' *E. coli* cells carrying F-pili at their surface (Loeb, 1960; Hofschneider, 1963; Hoffman-Berling et al., 1963). Their episomal replication and assembly is not lethal to the host cell, but rather slows down its growth causing a characteristic plaque formation on bacterial lawns. These phages are around 6.5 nm in diameter and their length depends on the size of their genome. Wild type bacteriophages have a 6400 nucleotide circular single-stranded DNA genome and are ~900 nm in length. The genome encodes for 11 proteins that are required for phage replication, virion coat formation and assembly. Only five proteins constitute the actual virion. Around 2700 copies of the  $\alpha$ -helical major coat protein pVIII wrap around the ssDNA genome in a 'fish-scale'-like arrangement to form a tubular structure. The ends of the virion differ in composition and appearance under the electron microscope. The 'pointed' end contains five copies each of the minor coat proteins pIII and pVI, whereas the 'blunt' end contains several copies of pVII and pIX.

The life cycle of a filamentous bacteriophage (Figure 2.11) starts with its infection of a bacterial host cell via its attachment to the F-pilus tip. This interaction is mediated by the N-terminal domain 2 (NT2) (Deng et al., 1999) of the minor coat protein pIII. The F-pilus then retracts and brings the phage close to the bacterial surface. Here, another critical interaction takes place, which assures successful infection. The N-terminal domain 1 (NT1) of pIII interacts with the periplasmic C-terminal domain of the inner membrane receptor tolA (Riechmann and Holliger, 1997; Click and Webster, 1997; Lubkowski et al., 1999), which is part of the conserved tolQRA complex required for infection (Click and Webster, 1998). Via a poorly understood mechanism these interactions enable the lateral release of the phage coat proteins into the inner membrane and the translocation of the ssDNA genome into the cytoplasm. Here, the ssDNA genome is converted into a dsDNA 'replicative form' via synthesis of the complementary '- strand' by host enzymes (Meyer and Geider, 1982). During the initial phase of infection, the replicative form is used to transcribe and translate all phage proteins. The coat proteins as well as the phage assembly & export proteins are integrated into the bacterial membranes (Endemann and Model, 1995).

The proteins pII and pV control the amount of ssDNA genome that is then synthesized via rolling-circle amplification using the replicative form as a template.

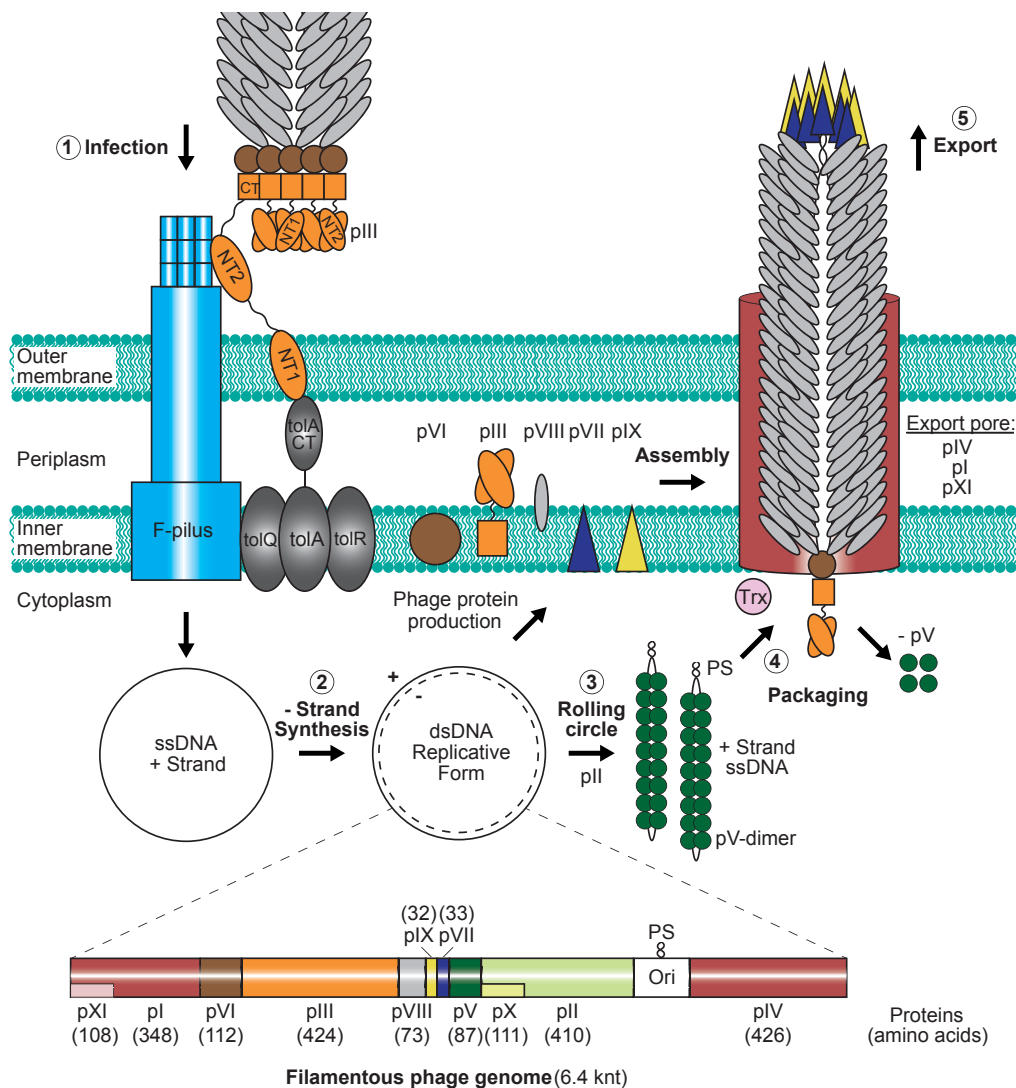


**Figure 2.11. Life cycle of filamentous phages in *E. coli*.**

This scheme illustrates the life cycle of an episomally replicating filamentous phage in *E. coli*. Infection (1) of *E. coli* is initiated by attachment of the phage to a F-pilus via the N-terminal domain 2 (NT2) of protein III. This brings the phage in close contact with the membrane and the N-terminal domain 1 (NT1) of protein III then interacts with the C-terminal (CT) domain of toIA. Via a largely unknown process the phage injects its ssDNA genome into the bacterium. In the cytoplasm a matching ‘- strand’ is synthesized by host enzymes to generate dsDNA called the ‘replicative form’. The replicative form serves as a template for transcription and translation of all phage proteins relevant for phage replication and assembly. In later infection stages pII initiates the rolling circle amplification of circular ‘+ strand’ ssDNA by nicking the replicative form in the f1 origin of replication. The ‘+ strands’ are wrapped by the ssDNA-binding protein pV. The packaging signal (PS) forms a dsDNA hairpin that is recognized by pVII and pIX. Both proteins thus target the genome to the phage export pore (formed by pIV, pI, pXI) for concerted phage assembly and extrusion. The organization of the phage genome is depicted at the bottom and all encoded proteins are listed. Note that the dimensions of the infecting and assembling virions are not drawn to scale. Knt = kilonucleotides; ori = phage origin of replication; Trx = thioredoxin.



The protein pII attaches to a specific site in the phage origin of replication of the dsDNA form, introduces a nick in the '+ strand' and forms a covalent intermediate with its 5'-end (Meyer and Geider, 1979; Asano et al., 1999). The 3'-end of the nick is then elongated by the host DNA polymerase III and the original '+ strand' is displaced. Once a full strand is synthesized, pII catalyzes the formation of a closed ssDNA molecule. Initially these newly synthesized '+ strands' are converted to the replicative form but at later infection stages the ssDNA-binding protein pV cooperatively assembles on '+ strands' to block their conversion. pV further regulates pII translation and thus coordinates ssDNA production and packaging (Fulford and Model, 1988; Michel and Zinder, 1989).

A short region of the '+ strand' forms a hairpin-like dsDNA structure that is not recognized by pV and is essential for virion assembly (Dotto et al., 1981; Bauer and Smith, 1988; Russel and Model, 1989). This so-called packaging signal (PS) targets the ssDNA genome to the phage export pore that spans the two bacterial membranes and is formed by the proteins pIV, pI and pXI (Kazmierczak et al., 1994; Opalka et al., 2003). The pore contains an extended channel of ~8 nm in diameter through which assembling virions are extruded. Phage assembly further requires host thioredoxin (Russel and Model, 1985) and is initiated at the pVII-pIX end of the virion. pVII, pIX and pI were also shown to interact with the PS (Russel and Model, 1989). During assembly pV is replaced with pVIII until the ssDNA genome is completely coated. Then pVI and pIII join and release the complete virion from the bacterial surface. The C-terminal domain of pIII is essential for phage release (Rakonjac et al., 1999). The newly formed virions are now able to infect a new host cell on their own.

### **2.3.2 Selection of recombinant antibodies via phage display**

George P. Smith pioneered the phage display technology. He found that small peptides could be presented on the surface of filamentous phages, when genetically fused to the minor coat protein pIII (Smith, 1985; Parmley and Smith, 1988). These peptides were accessible to antibodies that could thus be used to selectively enrich peptide-fused phages from a larger background of unfused phages via affinity purification. This 'fusion-phage' technology was rapidly extended to the screening of randomized peptide libraries to identify such variants that bind e.g. antibodies with known specificity (Cwirla et al., 1990; Devlin et al., 1990; Scott and Smith, 1990). Importantly, each



virion packages the genetic information of the displayed peptide and thus establishes a genotype-to-phenotype linkage, allowing the DNA sequence of a selected fusion peptide to be retrieved.

In the meantime, antibody engineering advanced significantly and resulted in the generation of functional scFv fragments (see chapter 2.2.3) (Huston et al., 1988; Skerra and Plückthun, 1988). McCafferty et al. then demonstrated that such a scFv fragment can be displayed on phages as a fusion protein with pIII and enriched with immobilized antigen (McCafferty et al., 1990). The field of antibody phage display was born and rapidly extended to screen large libraries of antibody fragments, isolated from immunized animals or produced synthetically, against antigens to identify those with the most favorable properties (Barbas et al., 1991; Breitling et al., 1991; Clackson et al., 1991). However, direct cloning into the relatively large phage genome often led to genetic instabilities and thus deletions within the inserts. Furthermore, the resulting large phage vectors did not allow for a high transformation efficiency of *E. coli*.

As a solution to this problem, the phagemid technology emerged (Barbas et al., 1991; Breitling et al., 1991; Hoogenboom et al., 1991) (Figure 2.12), based on the observation that plasmids harboring a phage origin of replication can be converted into single-stranded DNA and packaged into assembling phages when a so-called helper phage is present that supplies all phage proteins (Dotto et al., 1981). The helper phage genome contains an insertion in its origin of replication and is produced in a low copy number in *E. coli*, thus leading to the preferential packaging of the phagemid (Vieira and Messing, 1987). The phagemid furthermore contains a selective marker and bacterial origin of replication so that it can replicate in the absence of phage proteins. Antibody-pIII fusion proteins are genetically fused to a periplasmic secretion signal and encoded on the phagemid. The fusion protein then competes with the wildtype pIII protein (encoded on the helper phage genome) for assembly into nascent virions. As a result only around 10 % of the produced phages will present one pIII-fusion protein on their surface. This monovalent display is useful during the subsequent affinity enrichment since it avoids the selection of binders with low affinity due to avidity effects.

A typical phage display selection round (Figure 2.12), also called panning, starts with the preparation of a phage library. Such a library ideally contains phages that display all library members as fusions to their coat protein III and contain the respective DNA



sequences in their genome. The phage library is then incubated with the antigen that is e.g. immobilized on a plastic surface or magnetic beads. Phages that display library members with a certain affinity for the antigen are retained on the beads while those that do not display or whose library members don't bind can be washed away.

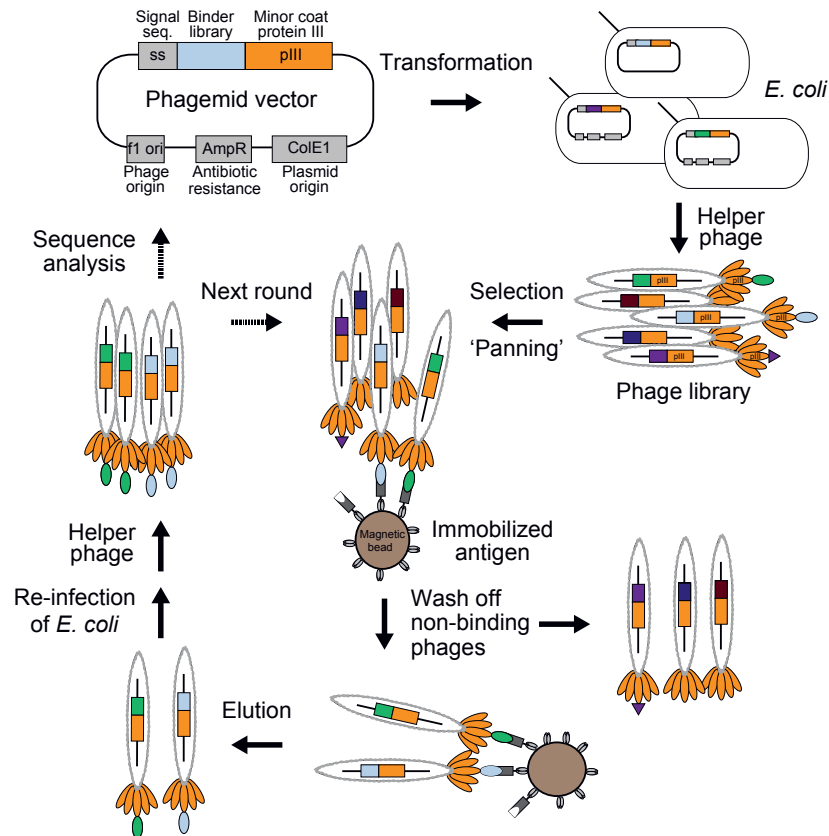


**Figure 2.12. Illustration of a phage display selection cycle.**

Phage display allows for the selective enrichment and amplification of proteins that bind to a certain antigen from a large background of non-binding variants. A library from which such binders are to be identified is cloned as in-frame fusion between a periplasmic secretion signal and the phage coat protein pIII in a phagemid vector. *E. coli* is transformed with the phagemid library and infected with helper phages. The helper phage provides all necessary proteins for the replication and assembly of the phagemid into nascent virions. These virions will incorporate the pIII-fusion protein encoded on the phagemid along with wildtype pIII expressed from the helper phage genome. The resulting phage library can be incubated with antigen immobilized on magnetic beads to selectively enrich phages displaying library members that bind to it. Non-binding phages are washed away and bound phages are eluted and allowed to re-infect *E. coli*. The phagemid DNA can be isolated from these bacteria for sequence analysis or they can be super-infected with helper phages. This produces another phage library in which antigen-specific library members are enriched. Such a more focused library can now be searched e.g. for clones with the highest affinity to the antigen.

Therefore, the binding library members are selectively enriched. After elution, phages are allowed to re-infect *E. coli* and then helper phages are added. This leads to an amplification of the enriched library members. These can now be directly analyzed by DNA sequencing or the resulting phage library can be subjected to another round of



selection. In order to enrich the library members with the highest affinity, the antigen concentration is lowered and the washing stringency is increased in these successive rounds. Alternatively, after initial formation of phage•antigen complexes, non-immobilizable antigen can be added in high molar excess as competitor. This strategy can be used to favor binders with a low off-rate (Hawkins et al., 1992).

Phage display has successfully been used over the last decades to produce recombinant antibodies against disease-relevant target molecules. These antibodies are widely used as therapeutics and diagnostics in biomedicine and as tools in basic research (Holliger and Hudson, 2005; Hoogenboom, 2005; Bradbury et al., 2011).

## 2.4 Aims of this study

We wanted to generate a set of high affinity recombinant antibodies against the major constituents of *Xenopus* NPCs. These binders could be used for the purification of endogenous Nups for structural analyses and functional assays. Furthermore, they would enable precise super-resolution imaging of NPCs, which requires the positioning of fluorescent dyes very close to the antigen in order to obtain maximum resolution.

Camelid-derived nanobodies appeared as the most promising candidates due to their small size, high solubility and thermostability. Nevertheless protocols for their generation were still cumbersome and thus prevented a broader implementation of the nanobody technology in basic research. Due to their conserved internal disulfide bond, nanobodies were routinely expressed in the oxidative periplasm of *E. coli*, thus limiting the final yield and tagging options.

We thus aimed at optimizing the speed and efficiency of the process of nanobody production (chapter 3.1). Further, we intended to explore cytoplasmic expression of (reduced) nanobodies in *E. coli* for the engineering of new fusion constructs for affinity isolations and fluorescence imaging (chapter 3.2).

The resulting toolbox of anti-NPC nanobodies (chapter 3.3) should prove useful for the study of various aspects of NPC biology e.g. as epitope-specific inhibitors of NPC assembly or as tools for the purification of endogenous Nups to study their structure, interactions and their modification pattern.



## 3 Results

### 3.1 A rapid workflow for nanobody discovery

Nanobodies are emerging as superior tools for molecular biology and show great potential to replace conventional antibodies in most of their applications. Due to the often low quality, batch-to-batch variability and even non-specificity of commercial antibodies used in biomedical research (Bradbury and Plückthun, 2015a; Bradbury and Plückthun, 2015b), there is a growing interest of the scientific community in generating recombinant high affinity reagents with known sequence such as nanobodies. At the heart of this effort should be the establishment of a rapid workflow for nanobody discovery. Ideally, such a workflow should rely on established techniques and instrumentation available in standard laboratories.

We set out to meet these criteria and optimized the efficiency and hands-on time of the individual steps of a phage display-based nanobody selection workflow. Our improved protocols enable a single person to identify large panels of nanobodies against multiple antigens in parallel within less than 14 days (Figure 3.1). The following paragraphs deal step-by-step with the details of the novel workflow.

A nanobody discovery project starts with the immunization of a camelid. Although synthetic nanobody libraries have been constructed, they often yield only binders with modest affinity, necessitating cumbersome *in vitro* affinity maturation. Such binders are often also non-specific. We therefore decided to rely on the natural affinity maturation and specificity selection mechanisms that are taking place in the animal. The optimized workflow is, however, equally suited to nanobody selection from a synthetic library.

After repeated immunization of an animal with an antigen of interest, an immune response is generated and B lymphocytes producing antigen-specific matured antibodies are circulating in the blood stream. In order to fully explore the whole immune repertoire of the animal, care has to be taken to maintain diversity during all steps of immune library construction, initial production and panning of the resulting phage library.

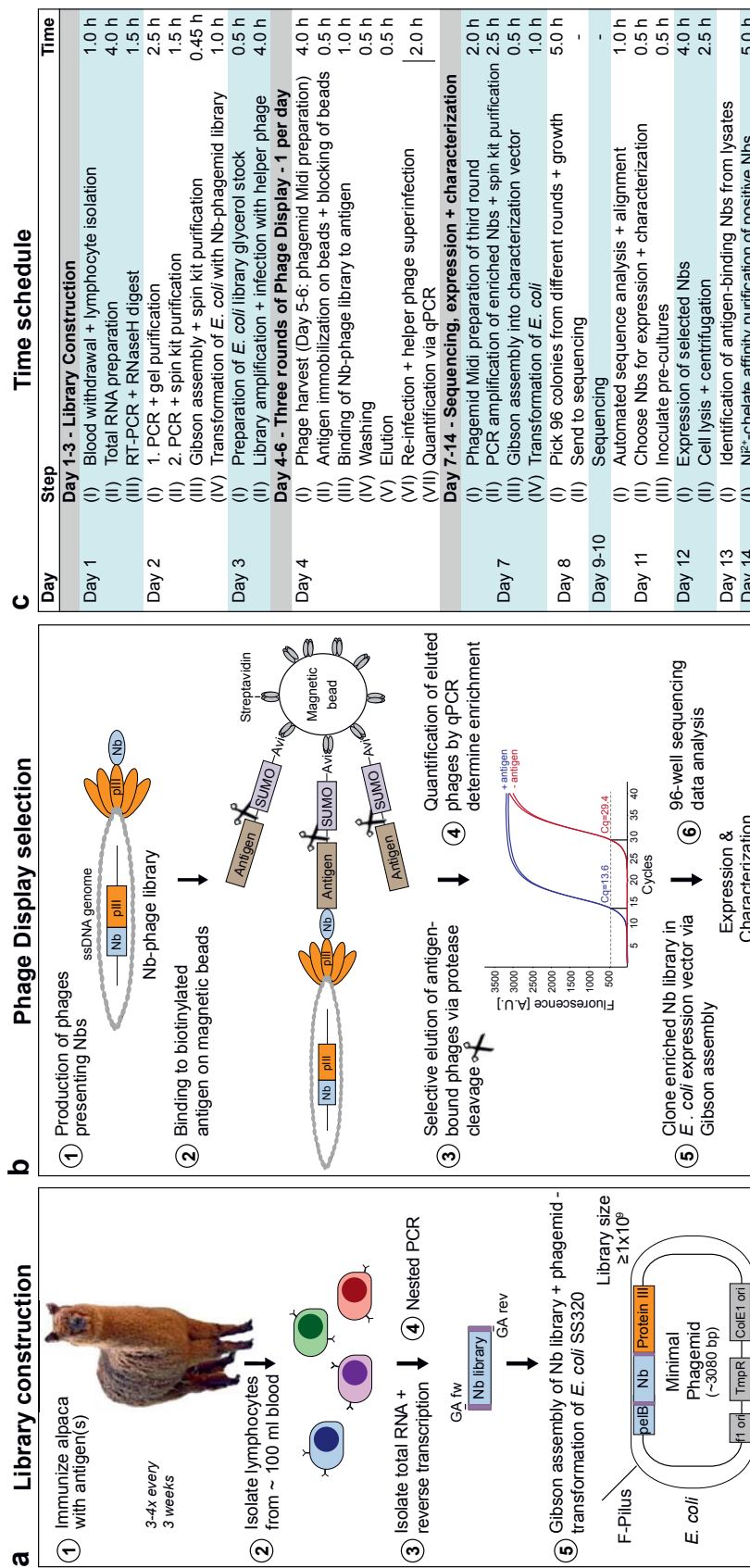


**Figure 3.1. Schematic illustration of the optimized rapid workflow for nanobody discovery.**

(a) After successive immunizations, peripheral blood lymphocytes are isolated from a blood sample. Total RNA is extracted, reverse transcribed and nanobody (Nb) encoding genes are amplified via a nested PCR that introduces Gibson assembly overhangs (GA). The Nb library is then assembled into a newly designed 'minimal phagemid' and transformed into the highly electro-competent *E. coli* strain SS320. (b) Each library member is presented on filamentous bacteriophages, which carry the respective genetic information of the displayed binder. Phages displaying antigen-binding Nbs can be enriched using biotinylated antigen immobilized on magnetic Streptavidin beads. After washing, antigen-bound phages are eluted by specific proteolytic cleavage of the antigen tag. Eluted phages are directly quantified via qPCR to evaluate the success of panning. After three rounds of panning, the enriched binders are then cloned as 'sub-library' into a characterization vector for cytoplasmic expression in *E. coli* and sequenced. Chosen candidates are then expressed, purified and characterized for binding to antigen. (c) Time schedule summarizing the workload needed from the day of blood withdrawal to the day of initial nanobody characterization. A single person can easily complete a nanobody discovery project in 14 working days. Alpaca 'Erna' photo: © MPBpc / Böttcher-Gajewski.



### 3.1.1 Total RNA isolation and RNA quality control

The first critical step of library construction is the preparation of high quality total RNA from peripheral blood lymphocytes (PBLs) of a blood sample. Around 100 ml of blood were usually obtained, containing  $\sim 10^8$  PBLs that were separated from the bulk of erythrocytes based on their different density. Total RNA was then prepared by guanidinium thiocyanate and detergent lysis, followed by acidic phenol-chloroform extraction (Chomczynski and Sacchi, 2006). Special care was taken to freshly prepare all needed solutions one day before use and to avoid RNase contamination during preparation. Importantly, we reproducibly obtained better RNA quality with the self-made extraction solutions than with TRIzol (Thermo Scientific, USA). It is critical to validate the quality of isolated RNA, since any RNA degradation could lead to an irreversible loss of rare clones. We routinely controlled the quality of total RNA preparations by agarose gel electrophoresis and by capillary gel electrophoresis on an Agilent 2100 Bioanalyzer RNA Nano Chip (Figure 3.2). The obtained total RNA usually showed very high quality and a RNA integrity number (RIN) of 9-10 (RINmax = 10). However, in case of strong immune responses, even partially degraded RNA yielded libraries from which positive nanobodies were retrieved.

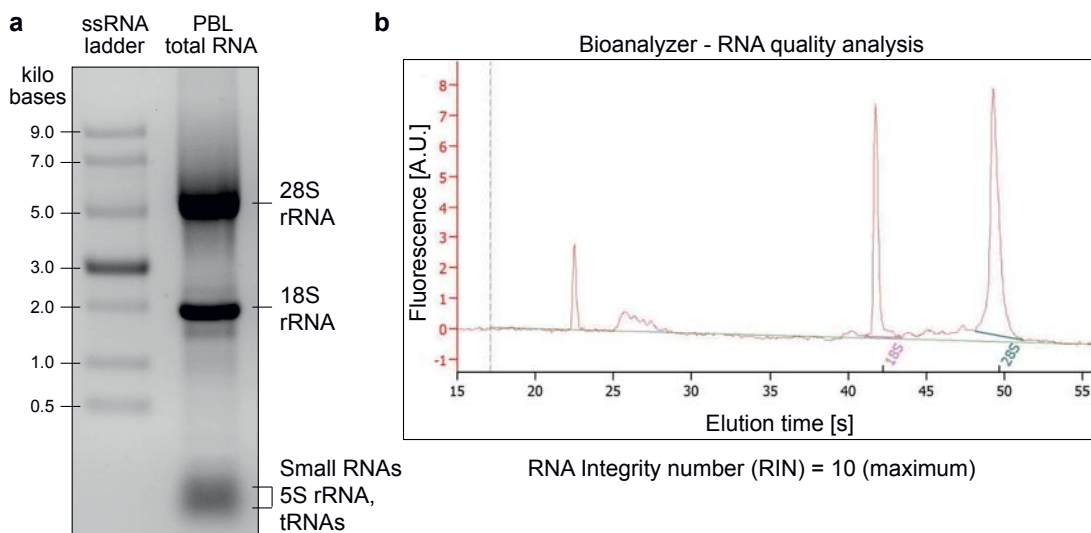


**Figure 3.2. Total RNA extraction from peripheral blood lymphocytes (PBL).**

(a) 2  $\mu$ g total RNA were run on a standard 1 % agarose gel with a ssRNA ladder. The major 28S and 18S rRNA bands are visible. (b) Capillary gel electrophoresis of alpaca PBL total RNA on an Agilent 2100 Bioanalyzer RNA Nano Chip. The electropherogram shows distinct rRNA peaks. Based on the peak shape and the overall purity of the sample a RNA integrity number (RIN) is calculated and serves as a quality measure. The sample analyzed here had the highest possible RIN of 10.



### 3.1.2 Library construction via Gibson assembly

In the next steps of library construction, the variable domains of IgG heavy-chain antibodies (VHHs) have to be selectively amplified by PCR. A concomitant co-amplification of variable domains of conventional IgG antibodies (VHs) has to be avoided. Finally, the obtained library of VHH domains has to be cloned into a phagemid for phage display without losing diversity. All protocols published to date used classical restriction enzyme-mediated cloning (Arbabi Ghahroudi et al., 1997; Rothbauer et al., 2006; Vincke et al., 2012; Pardon et al., 2014). Based on our own sequencing data many of the used enzymes often cleave within the VHH coding sequence e.g. NcoI cleaves 34/100 sequences within CDR I (used by Rothbauer et al., 2006) or PstI cleaves 9/100 sequences (used by Pardon et al., 2014) and therefore lead to the loss of potentially valuable binders. Furthermore, the resulting truncated nanobodies might actually be displayed and cause non-specific background binding in the most critical first round of panning likely suppressing the enrichment of actually positive binders.

We set out to establish a cloning workflow that avoids restriction enzymes and instead is based on a technique called Gibson assembly (Gibson et al., 2009; Gibson, 2011) (Figure 3.3). For this, complementary overhangs are introduced to the VHH library and the phagemid by PCR and both are then joined in an isothermal reaction. First, IgG heavy chain (VH + VHH) mRNA is selectively reverse transcribed with a primer that anneals in the coding region of the second constant heavy chain domain (CH2), common to both types of antibodies. All cDNA is then used as a template for exclusive PCR amplification of VHH genes. This is achieved with primers that anneal within the constant secretion signal and the VHH-specific hinge regions (Maass et al., 2007). We analyzed the DNA sequences of 100 of such PCR I products. Based on this analysis, we designed primers that anneal in the most constant regions of the VHH 5' and 3' ends. These primers further introduce constant Gibson assembly overhangs that were optimized to form no secondary structure and to have a melting temperature of around 48°C for isothermal joining. The phagemid is also amplified with primers that carry the same 5' and 3' overhangs. A critical step is to avoid background due to the carry-over of a transformable vector PCR template. Therefore, the template is specifically linearized and dephosphorylated before PCR (Figure 3.3).

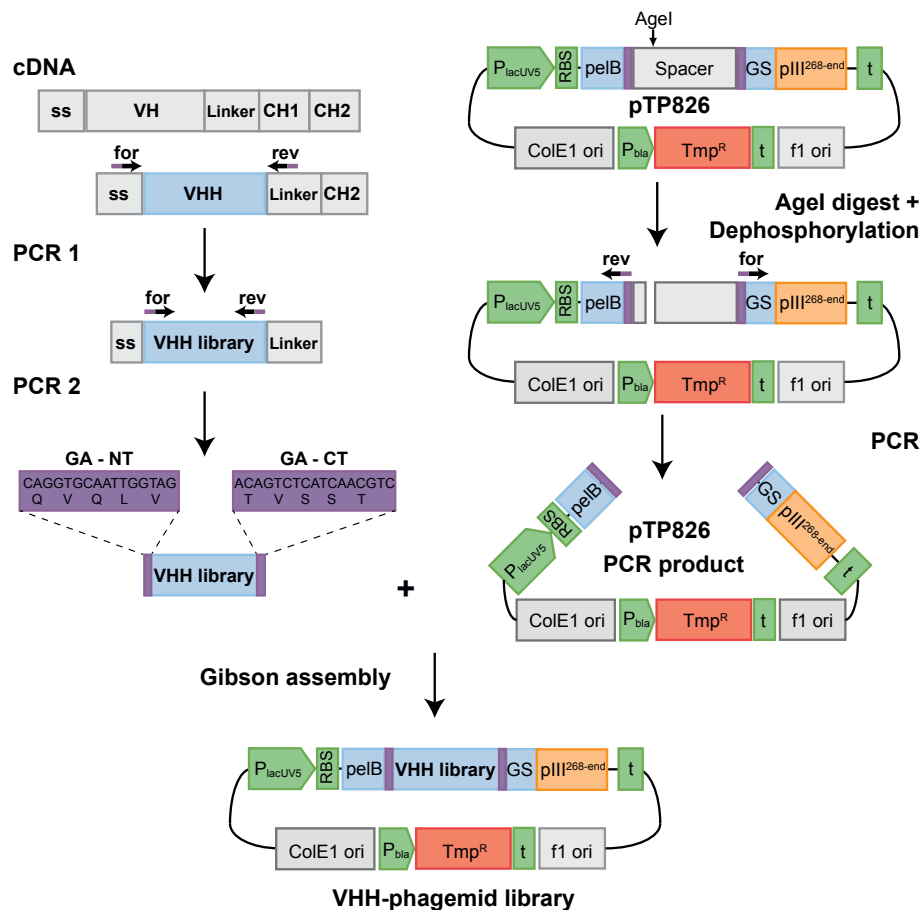


**Figure 3.3. Schematic illustration of nanobody-phagemid library construction.**

(Left panel) cDNA is prepared from total RNA with a constant heavy chain domain 2 (CH2)-specific primer for reverse transcription (Conrath et al., 2001). Then, the variable domains of heavy-chain antibodies (VHs) are selectively amplified by PCR with primers that anneal in their secretion signal (ss) and unique linker regions (Maass et al., 2007). In a second PCR, primers that anneal directly to the nanobody framework regions and further add Gibson assembly overhangs are used. (Right panel) The minimal phagemid pTP826 is linearized with the restriction enzyme AgeI, dephosphorylated and used as template for PCR. The PCR product contains matching Gibson assembly overhangs for final Gibson assembly of the Nb-phagemid library. The elements of the minimal phagemid are discussed in chapter 3.1.3 and Figure 3.4. for = forward primer; rev = reverse primer; NT = N-terminus; CT = C-terminus.

We validated this cloning strategy by sequencing 104 randomly picked colonies after Gibson assembly of a VHH library. 102 clones (98%) contained a unique and correctly inserted nanobody sequence.

The Gibson assembly reaction is desalted and used for transformation of *E. coli* by electroporation. The size of the final library critically depends on the transformation efficiency of the *E. coli* strain. The VHH genes of the initial  $10^7$ - $10^8$  lymphocytes should ideally be represented multiple times to assure that no rare binder is lost. Therefore, we aimed at constructing libraries with at least  $10^9$  individual transformants. Besides using a highly electro-competent *E. coli* strain SS320 for transformation, the reduction of the phagemid size was an important step to routinely construct such large libraries with minimal efforts and costs (see Methods 6.3.4).



### 3.1.3 Design of the minimal phagemid

The transformation efficiency of *E. coli* declines with increasing size of the transformed plasmid (Hanahan, 1983) and effectively determines how many transformations are needed to construct a library of a certain size. We found that routinely used phagemids like pHEN4 (Arbabi Ghahroudi et al., 1997), pMECS (Vincke et al., 2012) or pMES4 (Pardon et al., 2014) contain many unnecessary elements and so we started to systematically delete them individually (Figure 3.4). This work was carried out by my Master student Marc Böhning and was based on pHEN4 as a starting phagemid. First, we removed an old cloning scar originating from the pUC19 source plasmid (Arbabi Ghahroudi et al., 1997; Hoogenboom et al., 1991), resulting in an upstream lacZ $\alpha$  mini open reading frame (Soltes et al., 2007; also deleted in pMES4) and an additional lacZ $\alpha$  fragment downstream of pIII.

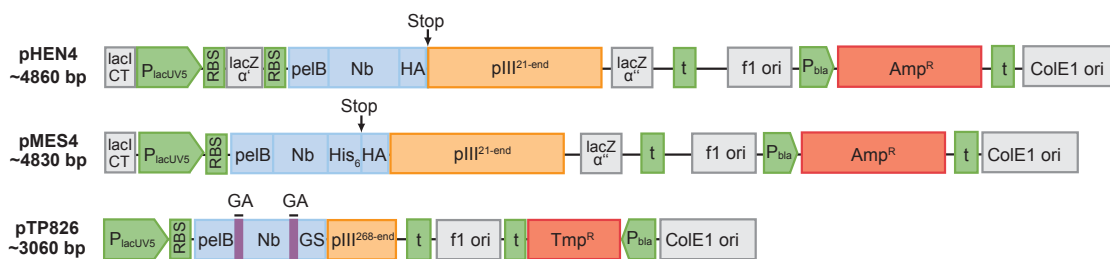


**Figure 3.4. Design of the minimal phagemid pTP826 and comparison with standard phagemids.**

Schematic organization of the phagemids pHEN4 (Arbabi Ghahroudi et al., 1997), pMES4 (Pardon et al., 2014) and the novel minimal phagemid pTP826. Systematic deletions yielded a ~1800 bp reduction in size. Furthermore, the ampicillin resistance cassette (Amp<sup>R</sup>) was replaced with a shorter trimethoprim resistance (Tmp<sup>R</sup>) gene. CT = C-terminus; P = promoter; RBS = ribosomal binding site; pelB = peptate lyase signal sequence; Nb = nanobody; HA = hemagglutinin epitope tag; pIII = bacteriophage minor coat protein III; t = transcription terminator; ori = origin of replication; GA = Gibson assembly overhang; GS = GlySer linker 23 aa.

The amber stop codon between binder and pIII (present in pHEN4 and pMES4) had previously been inserted to allow periplasmic expression of the unfused binder, when switching from an amber-suppressor to a non-suppressor *E. coli* strain (Hoogenboom et al., 1991; Lowman et al., 1991). The secretion of unfused binder, however, also occurs in suppressor strains due to a low suppression frequency of around 10 % (Miller and Albertini, 1983) and competes with binder-pIII fusion secretion. Therefore, we also decided to remove the stop codon. Furthermore, the gene encoding the bacteriophage protein pIII (without signal sequence 1212 bp) was truncated to encode only the essential C-terminus of pIII (471 bp) as described before (Krebber et al., 1997; Lowman et al., 1991). We also removed a lacI fragment that was left in the vector. The ampicillin resistance cassette (993 bp) was replaced with a much shorter gene that encodes



*Bacillus cereus* dihydrofolate reductase (DFHR) (622 bp) and confers resistance to the antibiotic trimethoprim. After each deletion, the resulting phagemid was tested for functionality by assessing the production of phages displaying nanobody-pIII fusion protein. All functional deletions were then combined in the ‘minimal phagemid’ pTP826. In sum, these deletions yielded a remarkable ~1800 bp reduction in size.

We next validated the minimal phagemid in comparison to pHEN4 (Figure 3.5). Virions displaying the anti-Nup98 nanobody TP377 were efficiently produced from both phagemids and could be quantitatively enriched on beads containing the immobilized target Nup98 (Figure 3.5 a). The reconstruction of the promotor region and the deletion of the stop codon did not affect the overall incorporation of nanobody-pIII fusion protein into virions, relative to wildtype pIII, which originates from the helper phage genome. This is defined as the display level.

We further analyzed how the reduction of the phagemid size impacted the transformation efficiency (Figure 3.5 b). For this, we transformed highly electro-competent *E. coli* TG1 cells with the same number of plasmid molecules of pHEN4 and pTP826, both encoding an affibody-pIII fusion protein. As a control pUC19 was also transformed. Due to its reduced size, we obtained a fourfold higher transformation efficiency with the minimal phagemid in comparison to pHEN4. This means that fourfold less transformations are needed to reach a similar library size when working with the minimal phagemid.

Another striking feature of the minimal phagemid was its stable propagation even at high cell densities due to the introduced trimethoprim resistance cassette. Ampicillin, required to propagate pHEN4 or pMES4, is metabolically consumed by the encoded beta lactamase enzyme. At high cell densities, this leads to a loss of selection pressure and consequently to a loss of the phagemid. Trimethoprim cannot be consumed and therefore should assure stable phagemid propagation. We quantified the absolute number of virions that packaged helper phage and phagemid DNA after over night virion production from either pHEN4 or pTP826 (Figure 3.5 c) by qPCR (see Methods 6.4.3.3; discussed in chapter 3.1.5).

Almost 50 % of virions produced from the pHEN4 phagemid packaged a helper phage genome. In contrast, we quantified only 4,4 % helper phage virions produced from the



minimal phagemid. The loss of the pHEN4 phagemid therefore led to an excessive production of helper phage virions. The stable propagation of the minimal phagemid, however, ensures also a stable coupling of the presented binder to its genetic information - a central prerequisite of phage display.

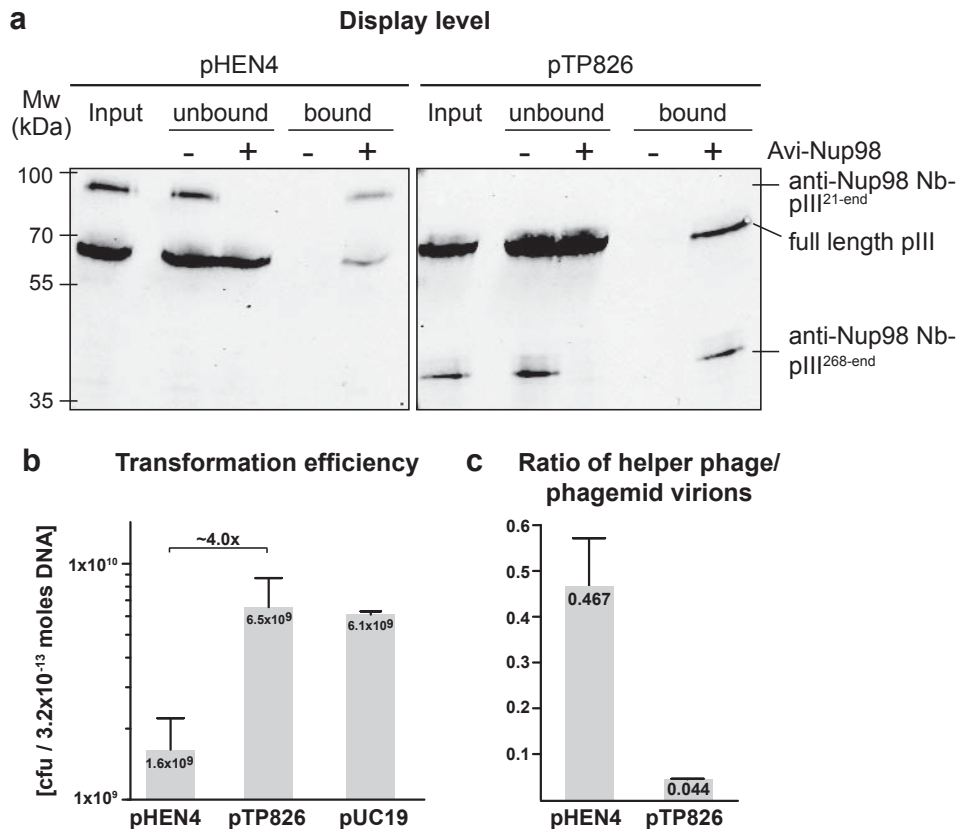


**Figure 3.5. Characterization of the minimal phagemid pTP826.**

(a) Virions produced from pHEN4 and pTP826 display an anti-Nup98 nanobody and can be quantitatively enriched with magnetic Streptavidin beads after in-solution binding to biotinylated Nup98. Phages were eluted with bdSENP1 cleavage. Empty beads served as a negative control. Input, unbound and elution fractions were analyzed by SDS-PAGE and Western Blotting using an anti-pIII monoclonal antibody.

(b) Transformation efficiency of pHEN4 (4679 bp) and pTP826 (2877 bp) encoding an affibody-pIII fusion in comparison to pUC19 (2686 bp). *E. coli* TG1 cells were transformed with 3.2x10<sup>-18</sup> moles of each supercoiled plasmid (corresponds to 10 µg pHEN4), spread on selective agar plates and the number of colony forming units (cfu) counted. The results were then extrapolated to 3.2x10<sup>-13</sup> moles (corresponds to 1 µg pHEN4). Bars represent mean and standard deviation of two transformations.

(c) Quantification of the ratio of helper phage genome to phagemid DNA in virions produced from pHEN4 or pTP826. After over night phage production, 1 µl of culture supernatant was directly used for qPCR quantification of the absolute number of helper phage genomes and phagemids. Each bar represents mean and standard deviation from two independent phage productions. Note that virions produced from the minimal phagemid contained around 10-fold less packaged helper phage genomes. This figure was prepared from data of my Master student Marc Böhning.



### 3.1.4 Selective elution of antigen-bound phages

Phages that present antigen-specific nanobodies are retrieved with antigen immobilized on magnetic beads, the beads are washed and then phages are eluted. An enrichment of specific binders requires an efficient removal of non-specific background-binding phages. Stringent washing is an effective way to reduce background, but also poses the risk to lose binders. Another critical point is the method of phage elution. The standard procedure is denaturing elution with triethylamine (pH ~11.5) (Vincke et al., 2012) or glycine/HCl (pH 2.0) (Steiner et al., 2008) or non-specific trypsin cleavage of the binder-pIII linker sequence (Steiner et al., 2006; Pardon et al., 2014). All these methods do not discriminate between background and antigen-binding phages. Consequently, background binders are co-eluted and co-propagated. Therefore, we reasoned that specific proteolytic cleavage of the tag of the immobilized antigen should help to reduce background. In this way, only antigen-bound phages are gently released under physiological conditions. All antigens used for panning were thus equipped with a biotinylated His<sub>14</sub>-Avi-(GlySer)<sub>9</sub>-bdSUMO/bdNEDD8/scSUMOStar-(GlySer)<sub>9</sub>-tag for immobilization on magnetic Streptavidin beads and subsequent cleavage with the respective specific protease (Frey and Görlich, 2014; Liu et al., 2008). Selective protease elution consistently yielded a low number of background-binding phages and efficiently released antigen-bound phages – resulting in very high enrichment factors (Figure 3.5 a; Figure 3.6, Figure 3.7 c).

### 3.1.5 Rapid quantification of panning by qPCR

The success of a panning is evaluated based on the number of phages in the elution fractions. Since often very little phages are retrieved (e.g. 10<sup>6</sup> virions, ~1.7 attomol), spectrophotometric methods lack the required sensitivity. The classic method of phage enumeration is called titering. Here, exponentially growing *E. coli* cells are infected with a dilution series of the phage stock solution and then plated on selective agar plates. Infective phages will give rise to resistant colonies that can be counted at an appropriate dilution. The major disadvantage of this method is that it is very laborious and that the plates need to be incubated over night for colony growth. A typical titering result of a panning is illustrated for the selection of nanobodies against xINup85 (Figure 3.6).



A quicker method for phage enumeration would allow an evaluation of the panning outcome on the same day, so that the protocols for the selection round on the next day can already be adjusted. For example, if there was little enrichment (<10-fold) in the first round, the antigen concentration in the second round was not as usually decreased. Reducing hands-on time on phage counting would also enable a more rapid screening of multiple different panning conditions or allow the handling of even more selections against different antigens in parallel.

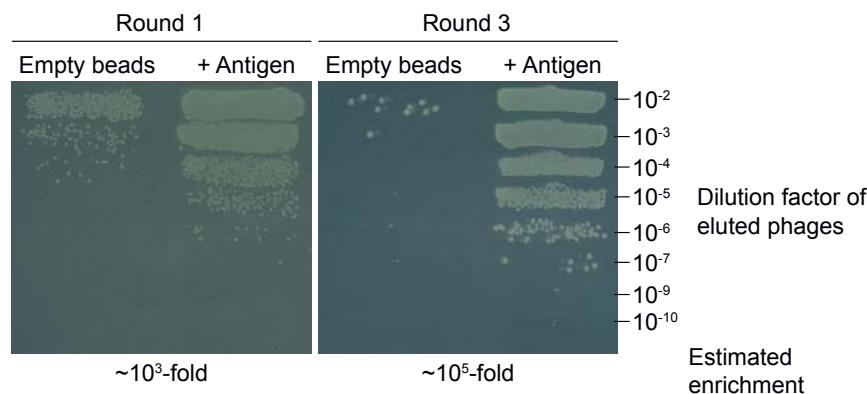


**Figure 3.6. Evaluation of panning rounds by titring of the eluted phages.**

Phages eluted from empty beads or beads with immobilized antigen by bdNEDP1 cleavage in the first and the third round of a panning against xINup85 were diluted in 2YT medium in a 10-fold dilution series. One-tenth of each dilution was mixed with exponentially growing *E. coli* TG1 cells. After 30 min infection at 37°C, an aliquot of infected cells was spread on selective square agar plates. Following over night growth, the number of resistant colonies in +/- antigen elution lanes was compared to evaluate the panning success. A relative enrichment over background (empty beads) can be estimated by comparing dilutions with similar colony count.

We found that virions can be enumerated with qPCR/real-time PCR and that this is frequently used in medical diagnostics (Mackay et al., 2002). Surprisingly, only a few publications described its use for filamentous phage quantification (Jaye et al., 2003; Guo et al., 2006; Dias-Neto et al., 2009). Absolute quantification requires a standard curve. Therefore, we isolated ssDNA of virions produced from the minimal phagemid and generated a serial dilution series. The number of qPCR cycles needed to reach a threshold fluorescence signal was then plotted against the number of template molecules. This yielded a standard curve with very good fit (Figure 3.7 a). Importantly, the used primers were very specific for phagemid DNA and did not give a PCR product on helper phage genome, which is always present in phagemid virion samples.

The final workflow is very simple and requires only around 5-10 min preparation time. Eluted phages are typically diluted 1:100 and 1  $\mu$ l of the dilution is directly pipetted into



the qPCR mix. The initial denaturation step of the qPCR protocol denatures the virion proteins and frees the ssDNA template for amplification.

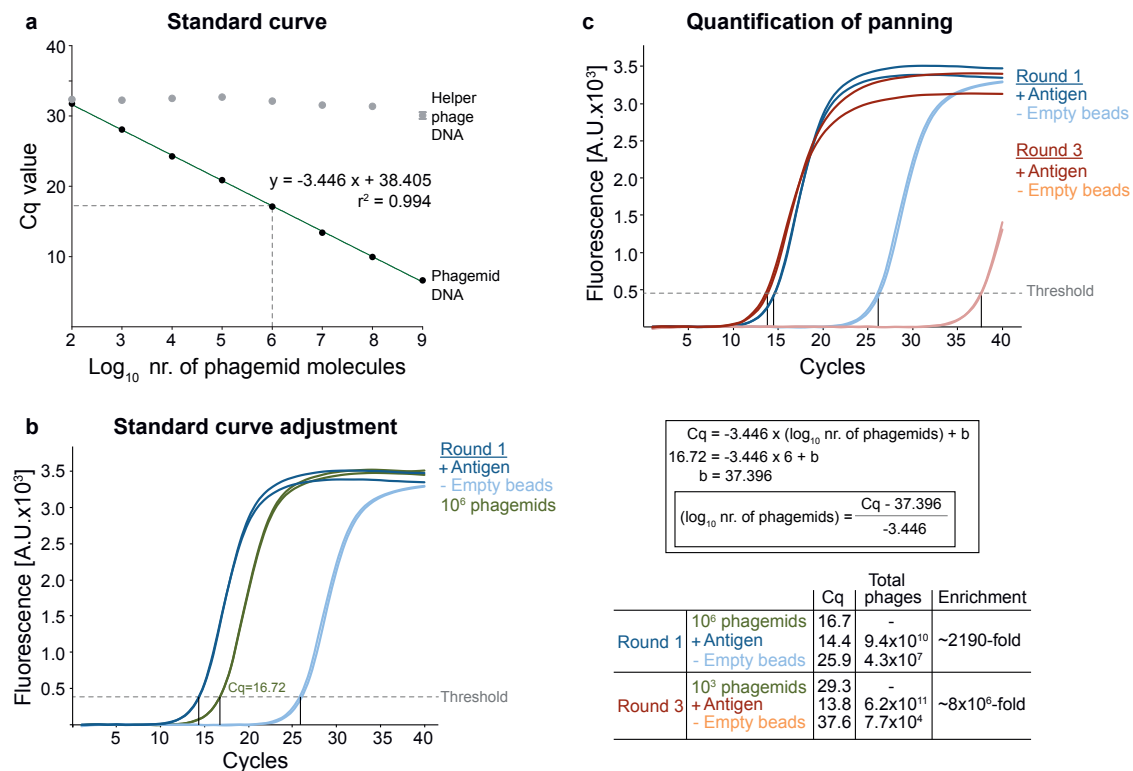


**Figure 3.7. Direct quantification of panning by qPCR.**

(a) Standard curve for phagemid quantification. ssDNA extracted from phagemid virions was gel-purified and the concentration determined. A 10-fold dilution series was prepared and used for qPCR with primers amplifying a 182 bp fragment in the C-terminus of pIII. The threshold cycle number (Cq-value) is plotted against the absolute number of phagemids. No PCR product was obtained when the same primers were used with the M13KO7 helper phage genome, indicating perfect specificity.

(b) Directly after elution, phages are diluted 1:100 and used as input for qPCR quantification. One point of the standard curve (here:  $10^6$  phagemids, Cq-value 16.72) was always measured in the same run and used to adjust the standard curve's intersection with the y-axis (see box for calculation). The absolute number of phages eluted from the +/- antigen beads can thus be determined within ~1 h and used to immediately evaluate panning success.

(c) Overlay of the qPCR quantification of a panning against the native xINup107 complex. Note that the number of phages binding to empty beads is dramatically reduced from round 1 to round 3 leading to an increase of enrichment. Panel (a) was adapted from data of my Master student Marc Böhning.

In Figure 3.7 b-c, qPCR was used to quantify a panning against the endogenous xINup107 complex (see chapter 3.3.2 for details). For every quantification, one point of the standard curve was included and used to adjust the y-axis intersection. In the first round of panning already a 2190-fold enrichment over background was achieved, that could be increased to  $8 \times 10^6$ -fold in the third round.



### 3.1.6 Cloning of enriched sub-libraries and sequence analysis

After completion of a panning, an enriched pool of nanobodies has to be screened for positive antigen-binders that are then further characterized. The standard screening method for the identification of antigen-binding nanobodies is based on an ELISA assay (Vincke et al., 2012; Pardon et al., 2014). The biotinylated antigen is immobilized on plastic-coated neutravidin in a 96-well plate. *E. coli* cells are infected with the eluted phages after panning, individual colonies are grown in a 96-well plate and then nanobody-His<sub>6</sub> fusion protein expression is induced. Periplasmic extracts from all cells in the plate are prepared and subsequently incubated with immobilized antigen. Finally, bound nanobodies are detected with an HRP-coupled anti-His<sub>6</sub> secondary antibody. Positive clones are sequenced, expressed in large scale in the *E. coli* periplasm and purified via Ni<sup>2+</sup> chelate affinity chromatography.

This strategy is not only time-consuming (12 days according to Pardon et al., 2014), but causes additional problems in the downstream characterization of the identified antigen-binding nanobodies. As they are still encoded in the phagemid vector, they can only be produced in the periplasm with a small His<sub>6</sub>-tag. For proper characterization e.g. for specificity or a cytoplasmic expression (outlined in chapter 3.2), a fusion of these nanobodies to other tags is necessary. This, however, requires a cumbersome subcloning of every single nanobody and the subsequent expression and purification of the new constructs. The total characterization effort could thus increase dramatically.

We therefore decided to clone entire enriched sub-libraries into a 'characterization vector' (see chapter 3.3.1, Figure 3.27), which contains tags and modules that enable all relevant characterization steps to be carried out from a single construct. Specifically, *E. coli* cells are infected with eluted phages and a DNA Midi preparation obtained. The enriched nanobody sequences are then amplified by PCR with primers that anneal in the constant Gibson assembly overhangs used for initial library construction. This prevents amplification bias due to differences in priming efficiency. These primers further introduce Gibson assembly overhangs for cloning into the characterization vector. The Gibson assembly reactions are then used to transform an *E. coli* strain that is suitable for protein expression (e.g. BLR or NEB express; see Methods 6.2.1). After over night growth on selective agar plates, 96 colonies are picked and grown in a 96-deep-well plate. Aliquots of all cells are sent to sequencing and the master plate is stored for later



retrieval of individual clones. Nanobody sequences are automatically extracted with an algorithm programmed in Python (by Dr. Koray Kirli). As an example, an alignment of nanobody protein sequences obtained after panning against the xINup107 complex is shown (Figure 3.8 a). Nanobodies are classified based on their CDR III, the dominant antigen-contacting loop (Desmyter et al., 2001; Muyldermans, 2013). This particular panning yielded six different classes and multiple unique sequences. In general, there often is considerable sequence heterogeneity within one class. We employ a consensus-guided strategy (Figure 3.8 b-c) to pick single nanobodies of each class that along with unique nanobodies are then expressed for initial characterization.

We routinely characterize around ~10 nanobodies per panning and had a very high success rate of 85% in average. For some antigens it was 100% (see Figure 3.26). This approach only requires five days hands-on time and including sequencing seven days in total (Figure 3.1). In the next chapter novel strategies to engineer successfully obtained nanobodies for use in affinity purification and imaging are presented.

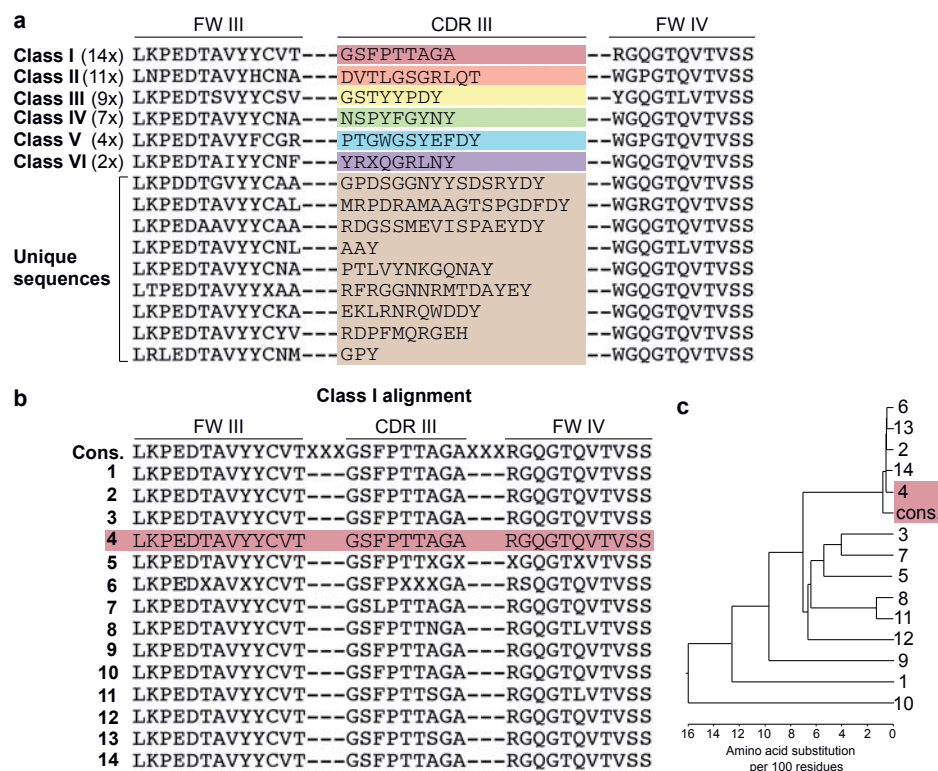


**Figure 3.8. Sequence analysis and consensus-guided choice of nanobodies for characterization.**

(a) Nanobody sequences obtained after panning are automatically extracted and aligned manually according to CDR III similarity. A class has at least two members. (b and c) All 14 members of class I are aligned and a phylogenetic tree including the consensus sequence of the group is shown. Nb4, amongst others, shows the highest similarity to the consensus and is consequently chosen for further characterization. FW = framework.



## 3.2 Novel nanobody engineering strategies

Previously, nanobodies were routinely expressed in the oxidative periplasm of *E. coli* (Vincke et al., 2012; Pardon et al., 2014; Fridy et al., 2014), where the formation of their conserved internal disulfide bond is catalyzed by a network of disulfide oxido-reductases and isomerases (de Marco, 2009). Periplasmic expression comes, however, with several drawbacks. For example, it suffers from low final yields (Baneyx and Mujacic, 2004), probably due to saturation of the secretion machinery and aggregation of precursor proteins in the cytoplasm. Since the secretion of endogenous essential proteins can be outcompeted, high-level periplasmic expression is also toxic for *E. coli*. The limited set of chaperones and high proteolytic activity in the periplasm also restrict the choices of fusion tags that can be used (Feilmeier et al., 2000; de Marco, 2009). For all relevant downstream applications, like affinity chromatography and imaging, protocols developed for conventional antibodies had also been applied to nanobodies. Thereby, no use was made of their recombinant nature and the wealth of genetic engineering strategies. I will outline the resulting limitations of the nanobody technology and present novel strategies to overcome the current problems.

### 3.2.1 Functional cytoplasmic expression of nanobodies

We expressed our anti-Nup nanobodies in the cytoplasm of various *E. coli* strains and found them to be completely functional and well-behaved. Fusing them to expression- and solubility-enhancing tags, like the *E. coli* IF2 N-terminus (Sørensen et al., 2003), a bdSUMO or bdNEDD8 module (Frey and Görlich, 2014) allowed a high-level production of these nanobodies. The yields often exceeded 100 mg per liter of culture and were up to 30 times higher as compared to periplasmic expression (Figure 3.9 a). Successful cytoplasmic expression had been described before for other nanobodies (Olichon and Surrey, 2007; Zarschler et al., 2013; Djender et al., 2014). The authors, however, always assumed disulfide bond formation to be a necessary criterion. For example, Djender et al. used an *E. coli* strain that could accumulate a sulfhydryl oxidase in the cytoplasm before nanobody expression was separately induced. Olichon and Surrey fused nanobodies to the disulfide isomerase DsbC lacking a signal sequence. None of the authors, however, analyzed if their strategies actually led to disulfide bond formation.

We wanted to test whether disulfide bond formation is really necessary for nanobody function. We expressed an anti-Nup93 and an anti-Nup98 nanobody either in the periplasm, in the reductive cytoplasm of *E. coli* BLR or in the cytoplasm of *E. coli* SHuffle. The SHuffle strain was engineered to express DsbC in the cytoplasm and harbors mutations that render its cytoplasm oxidative (Lobstein et al., 2012). The obtained nanobody variants were then treated with a maleimide under denaturing conditions. Reduced nanobodies are thereby modified at their free cysteines, and the resulting size shift distinguishes them from disulfide-containing nanobodies (Figure 3.9 b). While periplasmic secretion resulted in fully oxidized nanobodies, only a fraction of the SHuffle-expressed nanobodies contained a disulfide bond.

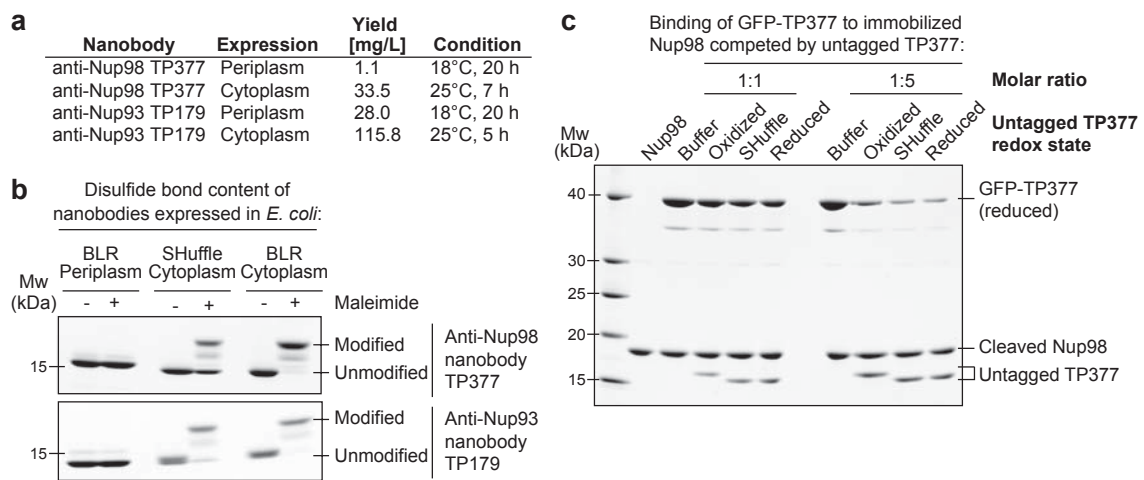


**Figure 3.9. Characterization of nanobodies expressed in the *E. coli* periplasm or cytoplasm.**

(a) Comparison of typical yields for the indicated nanobodies expressed either in the *E. coli* BLR periplasm with a C-terminal His<sub>6</sub>-tag or in the oxidative cytoplasm of *E. coli* SHuffle with an N-terminal His<sub>14</sub>-bdNEDD8-tag.

(b) Analysis of disulfide bond content with a maleimide shift assay. Anti-Nup93 nanobody TP179 and anti-Nup98 nanobody TP377, expressed either in the oxidative periplasm of *E. coli* BLR, in the oxidative cytosol of *E. coli* SHuffle or in the reductive cytoplasm of *E. coli* BLR, were subjected to modification with biotin-PEG<sub>23</sub>-maleimide (1.45 kDa) in SDS PAGE sample buffer (-DTT) and analyzed by non-reducing SDS-PAGE followed by Coomassie-staining.

(c) The redox state of TP377 does not affect its affinity. Biotinylated His<sub>14</sub>-Avi-bdSUMO-tagged Nup98<sup>716-866</sup> was immobilized on Streptavidin agarose and used to bind reduced GFP-tagged TP377. Binding was in the absence or presence of an equimolar amount or fivefold excess of nanobody competitor, namely untagged TP377 produced either in the oxidative periplasm, in the mildly oxidative cytoplasm of *E. coli* SHuffle or in the reductive cytoplasm of BLR. Bound nanobodies were then eluted by proteolytic cleavage of the bdSUMO tag of Nup98 and analyzed by SDS-PAGE followed by Coomassie-staining. Note that the oxidized, disulfide bond-stabilized nanobody (produced in periplasm) behaved like the reduced variant (produced in cytoplasm). Disulfide bond formation therefore does not significantly contribute to the overall affinity.

Cytoplasmic expression in *E. coli* BLR yielded completely reduced nanobodies. One could assume that the antigen affinity of nanobodies is negatively affected by a loss of their scaffold disulfide bond. A competition for antigen-binding revealed, however, no

affinity difference between reduced and disulfide bond-containing anti-Nup98 nanobodies (Figure 3.9 c). As expected, we observed a decreased thermostability of fully reduced anti-Nup98 and anti-Nup93 nanobodies by differential scanning fluorimetry (Niesen et al., 2007) (Figure 3.10). Their melting temperatures of 47°C and 57.5°C are, however, still well above any reasonable incubation temperature for downstream applications.

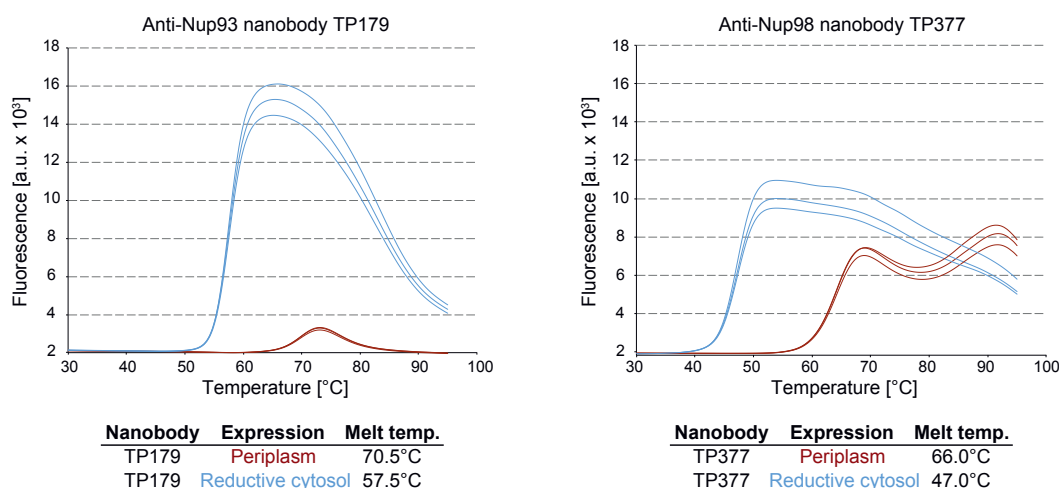


**Figure 3.10. Thermostability of reduced and oxidized nanobodies.**

Differential scanning fluorimetry (Thermofluor assay, Niesen et al., 2007) analysis of nanobodies expressed in the oxidative periplasm (red) or the reductive cytosol (blue) of *E. coli* BLR. The anti-Nup93 and anti-Nup98 nanobodies were heated in the presence of Sypro Orange dye from 30-100°C and thermal unfolding curves were obtained. The melting temperature is derived from the inflection point of the curve.

All nanobodies that we obtained against a variety of antigens could be functionally produced in the *E. coli* BLR cytoplasm with very good yields. Only very few of those nanobodies contained a second pair of cysteines that can form an additional, solvent-exposed disulfide bond between the framework II and CDR III regions, which likely contributes to the overall affinity (Govaert et al., 2012). However, most biochemical applications as well as imaging techniques like STORM require reducing conditions that disrupt accessible disulfide bonds, making such nanobodies a poor option anyway. In fact, nanobodies with a second disulfide bond are quite rare in alpacas. According to our sequence data, only 13.3 % (43/324 sequences from three animals) of unselected and 8.6 % (61/711 sequences of four animals) of selected nanobodies have a second disulfide bond. In 8/13 selections no or only one such nanobody was found. Interestingly, we never observed a second disulfide bond between CDR I and CDR III in our alpaca nanobodies, the common type in dromedaries, camels and llamas (Vu et al., 1997; Nguyen et al., 2000; Harmsen et al., 2000).



### 3.2.2 Native purification of endogenous protein complexes using nanobodies

For affinity chromatography, nanobodies had previously been covalently immobilized on NHS- or epoxy-activated resins via random lysine residues. Therefore, bound target proteins needed to be eluted under harsh denaturing conditions (Rothbauer et al., 2008; Fridy et al., 2014). This is appropriate for identification, but hardly for any further downstream structural or functional analyses of the purified target proteins. A convenient alternative for peptide-binding conventional antibodies had been to elute with a high excess of competing peptide in physiological buffer. Only recently, peptide elution was demonstrated for a nanobody (Braun et al., 2016). Another nanobody that binds the peptide EPEA (De Genst et al., 2010) requires very high salt concentration (2.0 M  $\text{MgCl}_2$ ) for elution at neutral pH (C-tag affinity matrix, Thermo Scientific, USA). Such elution conditions are likely to disrupt protein-protein interactions and thus cannot be considered physiological. Importantly, peptide-binding nanobodies are rare due to the overall preference of nanobodies for conformational epitopes. Therefore, we set out to establish a general strategy to use nanobodies for native protein complex isolation.

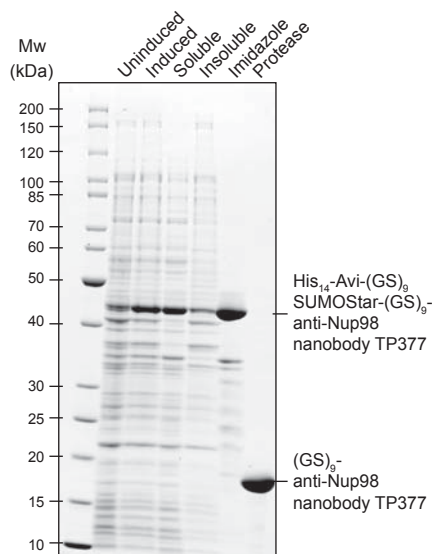


**Figure 3.11. Expression and purification of a nanobody with a protease-cleavable affinity tag.**

SDS-PAGE and Coomassie-staining showing the expression of the anti-Nup98 nanobody TP377 carrying a protease-cleavable affinity tag ( $\text{His}_{14}$ -Avi-(GlySer) $_9$ -SUMOStar-(GlySer) $_9$ ) in the *E. coli* cytoplasm and its one-step purification using  $\text{Ni}^{2+}$ -chelate affinity chromatography and imidazole elution. The Avi-tag mediates binding to Streptavidin after biotinylation by the biotin ligase BirA (Beckett et al., 1999; Schatz, 1993). The tag can be cleaved with nanomolar concentration of SUMOStar protease.

We exploited cytoplasmic expression to engineer nanobodies for affinity purification of endogenous target protein complexes with native elution. For this strategy, we produced  $\text{His}_{14}$ -Avi-(GlySer) $_9$ -SUMOStar-(GlySer) $_9$ -nanobody fusions and purified them by  $\text{Ni}^{2+}$ -chelate affinity chromatography and imidazole elution (Figure 3.11). The Avi peptide can be biotinylated by cytoplasmic co-expression of the biotin ligase BirA in *E. coli* (Schatz, 1993; Beckett et al., 1999). It then mediates binding of the purified



nanobody to Streptavidin magnetic beads. The interspersed long unfolded Gly/Ser-rich linkers minimize steric hindrance effects. The SUMOStar module is an engineered SUMO variant that cannot be cleaved by endogenous eukaryotic desumoylases but by an engineered SUMOStar protease (LifeSensors; Liu et al., 2008). In combination, these modules allow native elution of nanobody-bound target proteins or protein complexes by cleaving the tag with nanomolar concentrations of SUMOStar protease. This strategy also provides a purer and more specific end product, because any protein species that sticks non-specifically to the beads will not be released. Thus, such highly specific protease elution makes the otherwise crucial control for matrix background-binding (Mellacheruvu et al., 2013; Marcon et al., 2015) essentially dispensable.

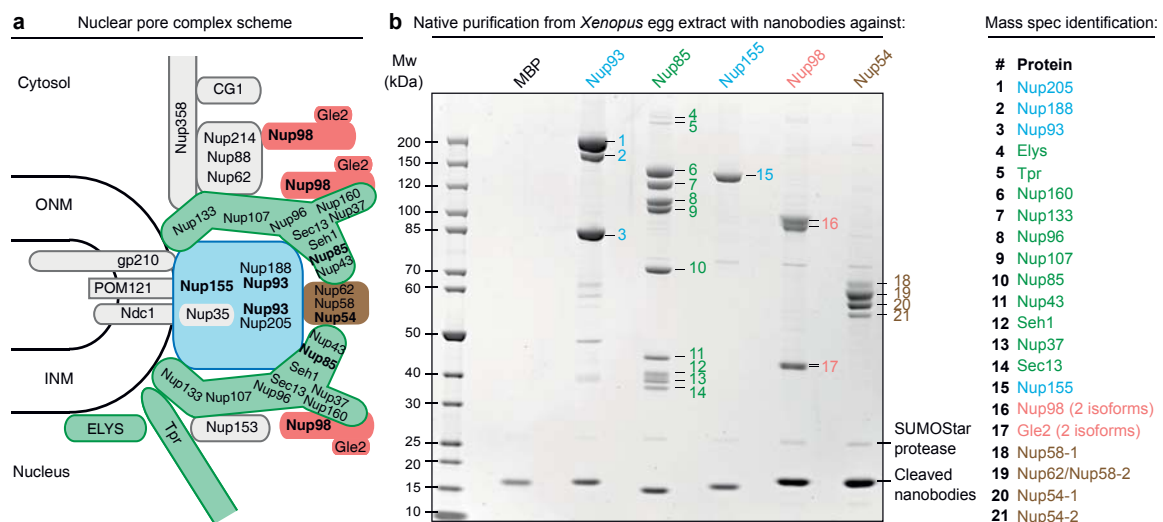


**Figure 3.12. Purification and native elution of NPC subcomplexes with specific nanobodies.**

(a) Schematic representation of the subcomplex organization and relative localization of Nups within an asymmetric unit of the eightfold rotational symmetric vertebrate NPC. The major subcomplexes are color-coded. The Y-shaped complex is represented in green, the Nup93 subcomplex in blue, the Nup62•Nup58•Nup54 complex in brown and the Nup98•Gle2 complex in red. Nups against which nanobodies were raised for native isolation (b) are highlighted in bold. ONM/INM = outer and inner nuclear membrane.

(b) Native purification of major NPC subcomplexes from *Xenopus* egg extract. Biotinylated His<sub>14</sub>-Avi-(GlySer)<sub>9</sub>-SUMOStar-(GlySer)<sub>9</sub>-tagged nanobodies were immobilized on magnetic Streptavidin beads and then incubated with *Xenopus* egg extract. After washing, nanobodies were gently eluted along with their bound target complexes by SUMOStar protease cleavage. One tenth of the eluates were analyzed by SDS-PAGE and Coomassie-staining. All labeled bands were identified via mass spectrometry. The color code represents the subcomplex organization of the NPC as illustrated in (a). A nanobody raised against *E. coli* Maltose-binding protein (MBP) served as a negative control.

As a proof of principle, we purified five nucleoporin complexes from a *Xenopus* egg extract to near homogeneity (Figure 3.12 a-b). For each complex we achieved a ~10 000-fold enrichment within a single native purification step and yields of around 50 %. The anti-Nup85 nanobody TP512 retrieved the ~750 kDa nine-membered Y-complex as well as Tpr and Elys as specific but sub-stoichiometric binding partners.



We obtained substantial amounts of the complex, namely 50-100  $\mu\text{g}$  from as little as 2 ml egg extract, which initially contained  $\sim 150 \mu\text{g}$  or  $\sim 100 \text{ nM}$  of the complex (Wühr et al., 2014). Post-elution with SDS sample buffer indicated a quantitative proteolytic release of the complex from the beads (Figure 3.13 a).

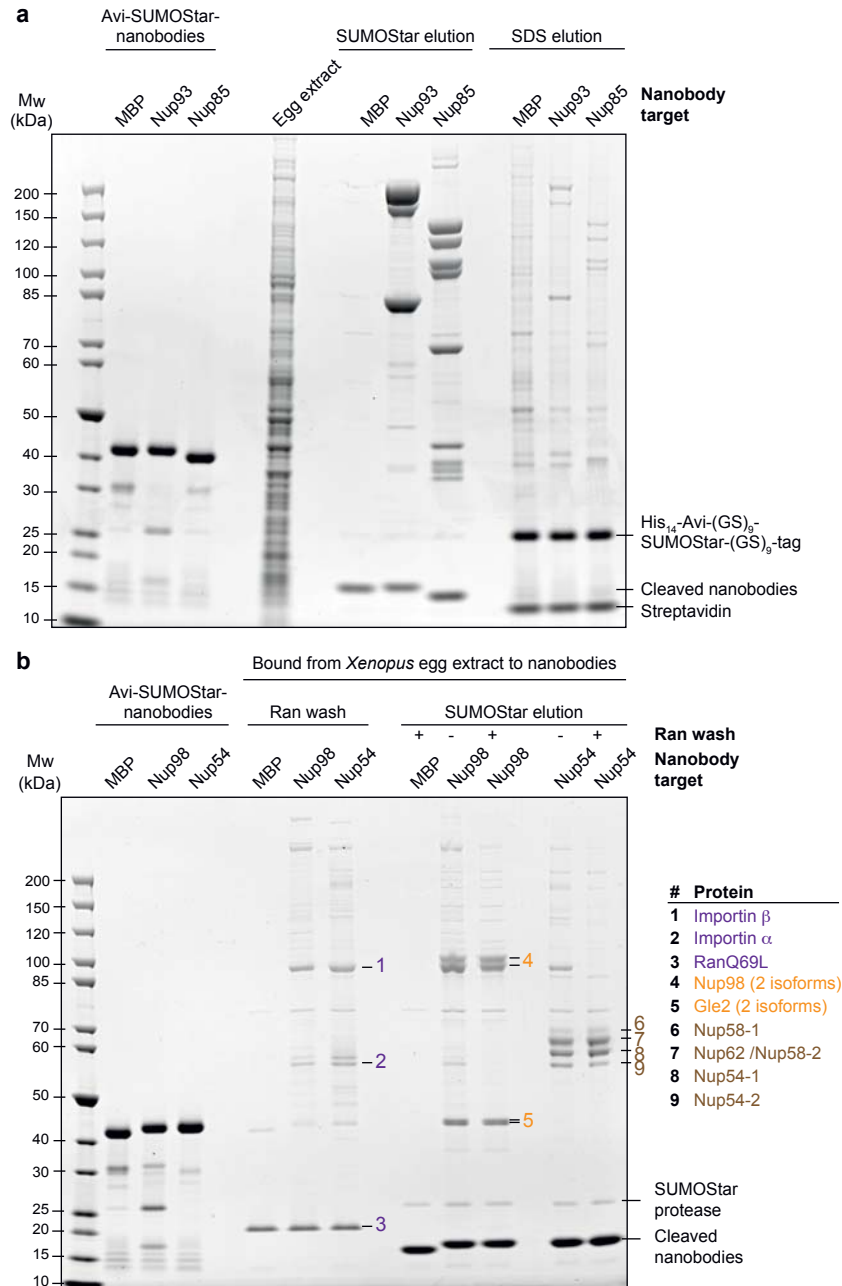


**Figure 3.13. Optimization of native protein complex isolation.**

(a) Analysis of natively purified and remaining bead-bound material. Anti-Nup93 nanobody TP179 and anti-Nup85 nanobody TP512 were used to purify their respective target complexes from crude *Xenopus* egg extract. After native elution with SUMOSStar protease, the beads were heated in SDS-PAGE sample buffer containing 400 mM urea for 10 min at 97°C. One-tenth of all elution fractions is loaded. Note that protease cleavage released the cognate complexes very efficiently and that the remaining bead-bound material essentially represents just the non-specific background, cleaved tags and leaked streptavidin.

(b) Effect of a RanQ69L•GTP wash on FG-repeat Nup purification. FG repeat-bound nuclear transport receptor•cargo complexes were efficiently removed by washing the beads for 10 min at 4°C with 100  $\mu\text{l}$  1  $\mu\text{M}$  RanQ69L<sup>S-180</sup>•GTP before elution with SUMOSStar protease.



The anti-Nup155 nanobody TP557 retrieved Nup155 as a single species. This might appear surprising as Nup155 is thought to contact Nup93 and Nup53/35 within the inner ring of the NPC scaffold (Hawryluk-Gara et al., 2005; Hawryluk-Gara et al., 2008; Sachdev et al., 2012). Therefore, we assume that mitotic post-translational modifications transiently suppress interactions between these proteins. We also purified the Nup98•Gle2 and the Nup62•Nup58•Nup54 complex using anti-Nup98 nanobody TP377 and anti-Nup54 nanobody Nb5, respectively. Here, we included a RanQ69L•GTP wash to release nuclear transport receptor•cargo complexes, which otherwise would remain bound to the FG domains of Nup98 or the Nup62 complex (Figure 3.13 b).

The anti-Nup93 nanobody TP179 purified the expected mixture of the two paralogous Nup93•Nup188 and Nup93•Nup205 complexes (Theerthagiri et al., 2010), which are also part of the structurally least understood NPC inner ring. In this case, we analyzed the natively eluted material straightaway by negative stain electron microscopy (Figure 3.14 a). Class averaging revealed characteristically curved  $\alpha$ -solenoid fold-like particles, which are known to exhibit conformational flexibility (Figure 3.14 b). The obtained structures were very reminiscent of the hook- and eye-shaped structures reported earlier for the Nup188 and Nup205 orthologues from *S. cerevisiae* (Amlacher et al., 2011) and *M. thermophila* (Andersen et al., 2013). This suggests not only that the overall shape of the Nup93 complexes is conserved from fungi to vertebrates, but also that our single step purification strategy for large protein complexes yields material of sufficient quality for a direct structural analysis.

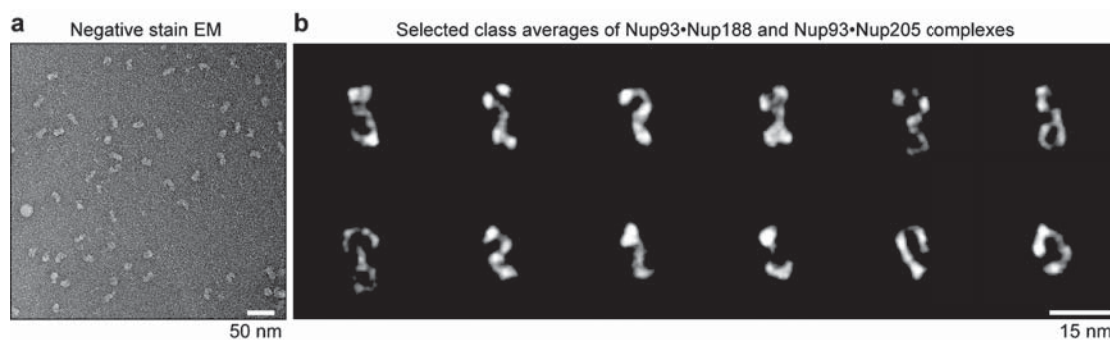


**Figure 3.14. Structural analysis of natively purified Nup93 complexes.**

(a) Anti-Nup93 nanobody TP179-purified Nup93•Nup188 and Nup93•Nup205 complexes were subjected to the GraFix procedure (Kastner et al., 2008) and negative staining for analysis by electron microscopy. (b) Gallery of 12 selected class averages of Nup93•Nup188 and Nup93•Nup205 particles. Negative stain and class average analysis was carried out by Jan Erik Schliep (MPI for Biophysical Chemistry, Göttingen).



### 3.2.3 Site-specific fluorescent labeling of nanobodies

In traditional indirect immunofluorescence, epitopes are initially decorated with a primary antibody and detected with a fluorophore-labeled secondary one, each around 12-15 nm in size (Harris et al., 1998). The effective displacement between label and epitope can reach up to 24-30 nm and thus significantly deteriorate the achievable precision and accuracy of protein localization by super-resolution fluorescence microscopy (Hell, 2009; Huang et al., 2009). Nanobodies (diameter: 4 nm) are an ideal solution to this problem (Ries et al., 2012; Szymborska et al., 2013). This, however, requires a direct nanobody labeling.

Only a few studies so far described the fluorescent labeling of nanobodies (Ries et al., 2012; Fridy et al., 2014; Mikhaylova et al., 2015; Braun et al., 2016) and many used the two anti-GFP and anti-RFP nanobodies (Ries et al., 2012; Kaplan and Ewers, 2015; Platonova et al., 2015a; Platonova et al., 2015b) that are commercially available from Chromotek (Germany). In all these studies, nanobodies were labeled at lysines by N-Hydroxysuccinimide (NHS) ester fluorophores, which is random and rarely quantitative.

In order to use anti-Nup nanobodies for imaging of their targets within intact NPCs, we initially modified them with NHS ester fluorophores. We found, however, that such NHS-labeled nanobodies performed remarkably poorly, in particular when far-red fluorophores were used. As documented by the specific examples below, none of the NHS-labeled nanobodies had sufficient probe quality to allow acquisition of STORM images. Platonova et al. noticed that tagging the widely used anti-GFP nanobody Enhancer (Kirchhofer et al., 2010; Chromotek, Germany) with a C-terminal GKGSKGSKSK peptide 'markedly improved the efficiency of chemical labeling of the protein at lysine residues' (Platonova et al., 2015b). The addition of this oligolysine stretch to divert from labeling framework lysines is, however, only a workaround to the basic problem. We therefore explored alternative and more reliable nanobody-labeling strategies.

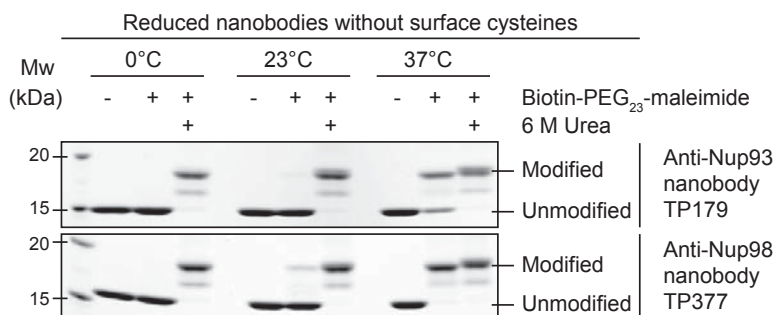


**Figure 3.15. The internal cysteines of reduced nanobodies are inaccessible to maleimide modification at low temperature.**

The indicated nanobodies, expressed in the reductive cytoplasm of *E. coli* BLR, were incubated at the indicated temperatures in the presence or absence of a two-fold molar excess of biotin-PEG<sub>23</sub>-maleimide (1.45 kDa) in 50 mM Tris/HCl pH 7.5, 300 mM NaCl. The addition of 6 M urea served as a positive control for maleimide modification of the internal cysteines upon chemical unfolding. The samples were then analyzed by SDS-PAGE and Coomassie-staining.

One possibility was to label nanobodies at engineered cysteines with maleimides. Massa and colleagues reported the production of a nanobody with a C-terminal cysteine in the periplasm and its conjugation to maleimide radiolabels (Massa et al., 2014). They observed a strong dimerization and a severe reduction in final yield, likely due to folding problems caused by the formation of ‘scrambled’ disulfide bonds. The same negative effect of unpaired cysteines on scFv fragment yield upon periplasmic expression was observed before and attributed to random disulfide bond formation with other periplasmic proteins (Schmiedl et al., 2000). Expression of nanobodies with engineered cysteines in the reductive *E. coli* cytoplasm should not lead to such problems.

This, however, posed the risk of modifying also the scaffold cysteines of the Ig-fold, which inevitably would cause an irreversible unfolding of the nanobodies. To address this issue, we incubated reduced nanobodies with biotin-PEG<sub>23</sub>-maleimide (Figure 3.15). After unfolding by urea, the scaffold cysteines became modified at either 37°C, 23°C, or 0°C. In native buffer, however, modification was quantitative only at 37°C, pointing to a transient exposure of the otherwise buried scaffold cysteines ('thermal breathing'). Importantly, they remained fully protected at 0°C, predicting that maleimide-labeling on ice would be fully selective for engineered surface cysteines.

In order to better guide cysteine placement in the nanobody framework, we solved the crystal structure of the anti-Nup98 nanobody TP377 in complex with the globular Nup98 NPC anchor domain (residues 716-866) at 1.9 Å resolution (Figure 3.16; Table 3.1; PDB: 5E0Q).

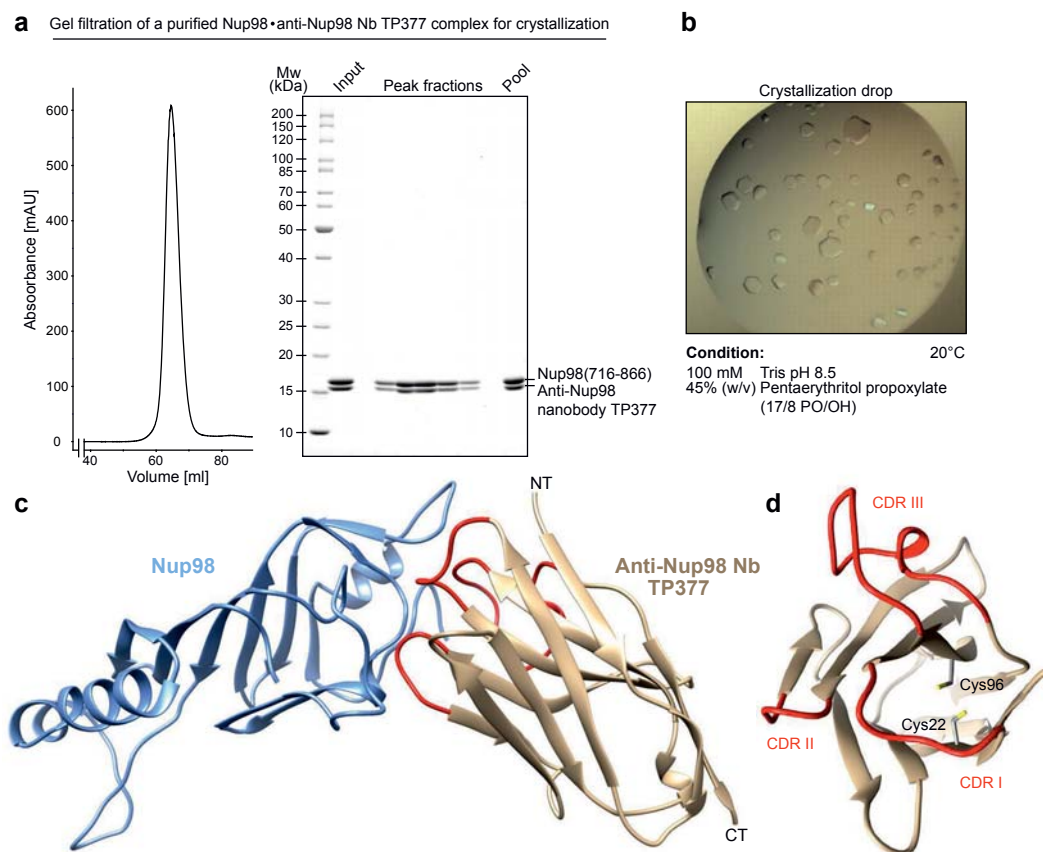


**Figure 3.16. Crystallization of a Nup98•anti-Nup98 nanobody TP377 complex.**

(a) Superdex 75 16/60 gel filtration of the purified Nup98<sup>716-866</sup>•anti-Nup98 nanobody TP377 complex. The complex runs as a single symmetric peak in gel filtration (left) and is highly pure as analyzed by SDS-PAGE and Coomassie-staining. (b) The complex crystallized in two forms yielding rod-shaped (space group  $P4_1$ ) and hexagonal crystals (space group  $P3_221$ ), both diffracted to 1.9 Å. (c) Crystal structure of the Nup98<sup>716-866</sup> (blue) in complex with the anti-Nup98 nanobody TP377 (beige). The three antigen-binding loops (CDR I-III) of TP377 are colored red. (NT = N-terminus, CT = C-terminus) (d) Reduced cysteines in the hydrophobic core of TP377. The anti-Nup98 nanobody TP377 is shown in beige with its CDRs colored in red. The top view illustrates the positions of the internal reduced framework cysteines Cys22 and Cys96.

**Table 3.1 Crystallographic data collection and refinement statistics of the Nup98•anti-Nup98 nanobody TP377 complex<sup>a</sup> PDB 5E0Q**

Data collection		Refinement	
Space group	$P4_1$	Resolution (Å)	47.00-1.90
Cell dimensions		No. Reflections	
a, b, c (Å)	66.59, 66.59, 87.90	Measured	823105
$\alpha, \beta, \gamma$ (°)	90.00, 90.00, 90.00	Unique	30218
Resolution (Å)	47.00-1.90 (1.95-1.90) <sup>b</sup>	$R_{work} / R_{free}$	0.167 / 0.196
		No. atoms	
$R_{sym}$ or $R_{merge}$	0.128 (>1) <sup>b</sup>	Protein	2176
		Water	145
$I / \sigma I$	27.7 (2.6) <sup>b</sup>	Wilson B-factor (Å <sup>2</sup> )	27.4
Completeness (%)	99.5 (98.7) <sup>b</sup>	R.m.s. deviations	
		Bond lengths (Å)	0.010
		Bond angles (°)	1.08
		Ramachandran statistics (%)	
Redundancy	27.4 (27.4) <sup>b</sup>	Favored	98.0
		Allowed	2.0
		Outliers	-

<sup>a</sup>One crystal was used for data collection. <sup>b</sup>Values in parentheses are for highest resolution shell



TP377 contacts its target with all three CDRs and does not block the absolute Nup98 C-terminus (Figure 3.16 c), which anchors Nup98 via Nup96 or Nup88 to the NPC scaffold (Hodel et al., 2002; Griffis et al., 2003; Stuwe et al., 2012). The internal disulfide bond-forming cysteines Cys22 and Cys96 of TP377 are reduced in the crystal structure (Figure 3.16 d).

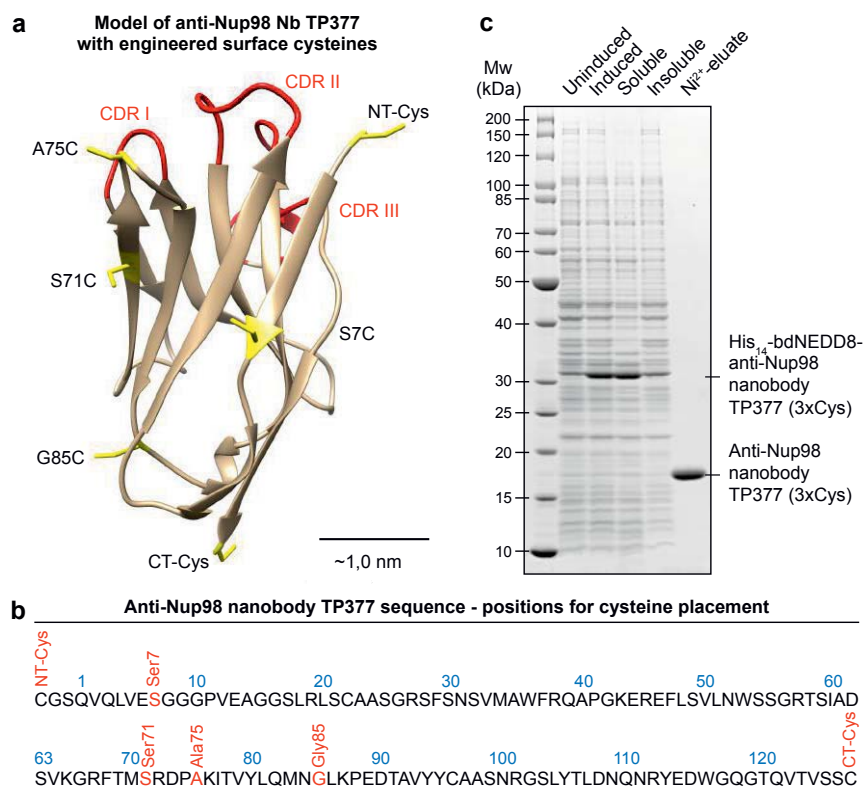


**Figure 3.17. Engineering nanobodies with surface cysteines.**

(a) Tested positions of engineered cysteines (yellow) illustrated for nanobody TP377. CDRs are shown in red. (b) Amino acid sequence of anti-Nup98 nanobody TP377 illustrating the positions chosen for mutation to cysteine (red). (c) SDS-PAGE and Coomassie-staining showing the expression and purification of TP377 with three engineered cysteines (NT-Cys, Ser7Cys, CT-Cys) in the *E. coli* cytoplasm. Single-step purification was performed using Ni<sup>2+</sup>-chelate affinity chromatography and cleavage using the bdNEDP1 protease. NT = N-terminus; CT = C-terminus.

We next mutated solvent-exposed small residues (Gly, Ser and Ala) at six alternative positions of the nanobody scaffold to cysteines (Figure 3.17 a-b). We found that not only all individual mutants, but also nanobodies with up to three ectopic surface cysteines were well-expressed and highly soluble in *E. coli* (Figure 3.17 c). Moreover, cysteines on all six positions on our model anti-Nup98 nanobody TP377 could be quantitatively labeled with maleimide fluorescent dyes (Figure 3.18 a). Based on the crystal structure, we estimate that fluorophores attached via an N-terminal cysteine or A75C to anti-Nup98 nanobody TP377 can be as close as ~2 nm to the target Nup98. Even nanobodies carrying three fluorophores were readily obtained. For this, cysteines



can be introduced at the N-terminus, Ser7 and Ala75 (other amino acids can occur at these positions in different nanobodies) of a given nanobody sequence to achieve the smallest possible label displacement. For easy cloning, three cysteines can also be introduced with primers in a single PCR reaction (positions: N-terminus and Ser7 in the forward primer and at the C-terminus with the reverse primer). Importantly, competitive binding assays indicated that the introduction of ectopic cysteines and their modification did not impair binding to the Nup98 target (Figure 3.18 b).

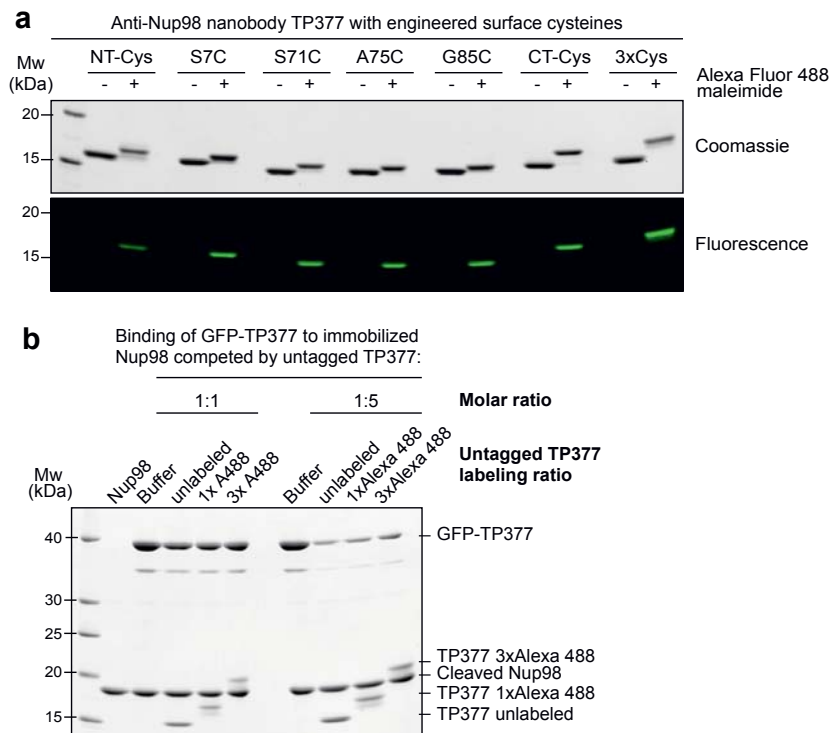


**Figure 3.18. Site-specific fluorescent labeling of nanobodies.**

(a) Quantitative labeling of TP377 with cysteines at the indicated positions with Alexa Fluor 488 maleimide. Labeling introduces a size shift in SDS-PAGE. Detection was either by Coomassie-staining or by in-gel fluorescence. (3xCys = NT-Cys + S7C + S71C)

(b) Relative affinity of TP377 with different labeling ratio to Nup98<sup>716-866</sup>. GFP-tagged TP377 was incubated with biotinylated His<sub>14</sub>-Avi-bdSUMO-tagged Nup98<sup>716-866</sup> immobilized on Streptavidin agarose. For competition, unlabeled, 1x or 3x Alexa Fluor 488 maleimide-labeled TP377 was added in equimolar amount or fivefold molar excess relative to GFP-TP377. Bound nanobodies were eluted by bdSEN1 cleavage and analyzed by SDS-PAGE followed by Coomassie-staining.



### 3.2.4 Imaging with site-specifically labeled nanobodies

In order to test nanobodies in imaging, we grew *Xenopus laevis* XL177 cells on coverslips, digitonin-permeabilized their plasma membranes, incubated them with low nanomolar concentrations (1-10 nM) of labeled nanobody, and fixed them after several washing steps. In this workflow, even nanobodies with fixation-sensitive epitopes could bind their target.

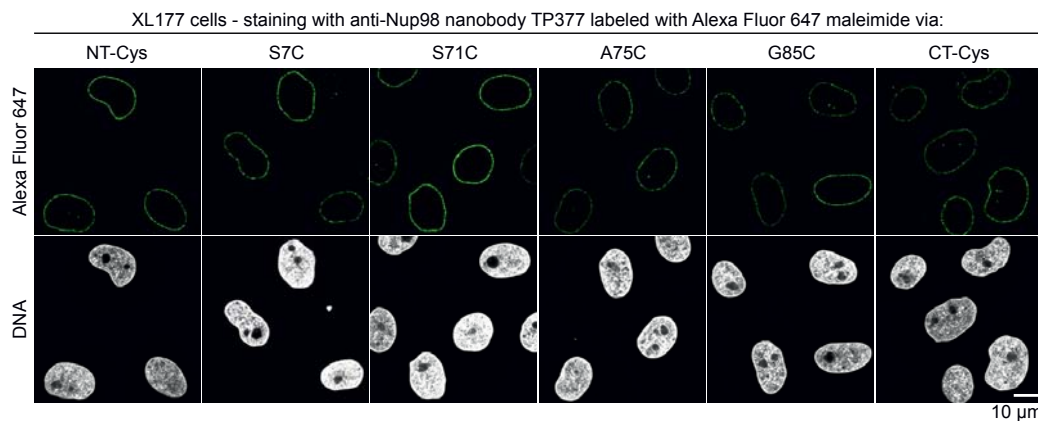


**Figure 3.19. Immunofluorescence with site-specifically labeled anti-Nup98 nanobody TP377.**

Digitonin-permeabilized *Xenopus* XL177 cells were incubated with 10 nM TP377 carrying a single Alexa Fluor 647 molecule at the indicated position. Cells were then washed, fixed and stained with DAPI (DNA). A characteristic nuclear rim stain indicates labeling of NPCs. Note that labeling of TP377 very close to its antigen-binding loops did not perturb binding.

We first tested anti-Nup98 nanobody TP377 carrying a single Alexa Fluor 647 maleimide at the six alternative positions (Figure 3.19). In confocal laser scanning microscopy, all variants produced a very bright punctuate nuclear rim staining of XL177 cells, characteristic for NPCs, against a very low background.

Combining minimal label displacement with ease of cloning, we routinely labeled our nanobodies via an N-terminal cysteine. This way, all chosen NPC targets (Nup98, Nup93, Nup85 and Nup155) could be visualized with specific nanobodies carrying a single N-terminal Alexa Fluor 647 maleimide (Figure 3.20). Despite the presence of only one dye molecule per nanobody, we again obtained very bright nuclear rim stains with very low background. Staining of Nup155 with anti-Nup155 nanobody TP559 required a prior permeabilization with Triton X-100, probably because it is located in close proximity to the pore membrane and buried there by other NPC scaffold components (Mitchell et al., 2010; Eisenhardt et al., 2014; von Appen et al., 2015).

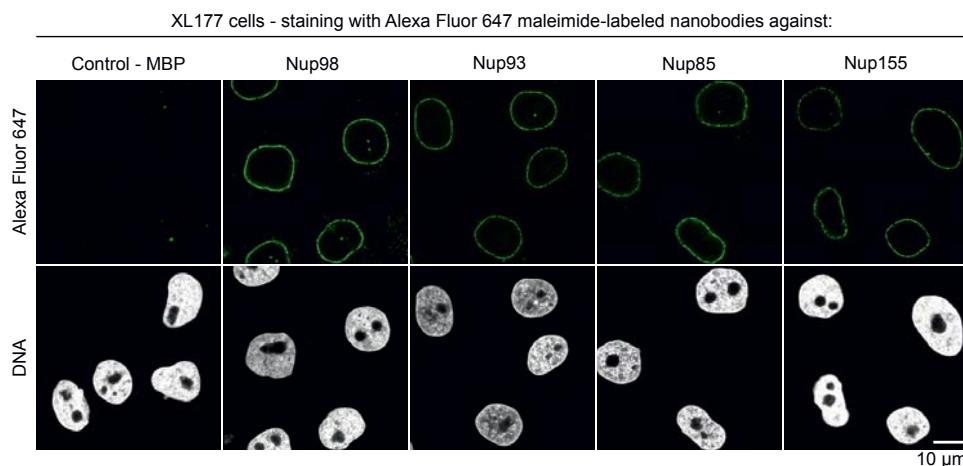


**Figure 3.20. Immunofluorescence with site-specifically labeled anti-Nup nanobodies.**

*Xenopus* XL177 cells were digitonin-permeabilized and stained with anti-Nup nanobodies carrying a single N-terminal Alexa Fluor 647 maleimide dye before fixation and DAPI staining. A characteristic nuclear rim stain indicates labeling of NPCs. A nanobody raised against *E. coli* Maltose-binding protein (MBP) served as a negative control. The following nanobodies were used: anti-MBP = TP250, anti-Nup98 = TP377, anti-Nup93 = TP179, anti-Nup85 = TP510 and anti-Nup155 = TP559.

For a direct comparison of the NHS chemistry for nanobody-labeling at lysines with maleimide-labeling at engineered surface cysteines, we chose Alexa Fluor 647 as a fluorophore and the widely used anti-GFP nanobody ‘Enhancer’ (Kirchhofer et al., 2010) as an example (Figure 3.21 a). When a HeLa Nup153-GFP cell line was stained, we observed a brilliant NPC signal for the Alexa Fluor 647 maleimide-labeled ‘Enhancer’, which perfectly coincided with the (weaker) GFP signal, and an extremely low background (Figure 3.21 b). In contrast, when this nanobody was labeled at lysines with Alexa Fluor 647 NHS ester, it produced strong nucleoplasmic and cytoplasmic background staining, which essentially obscured the specific signal. The degree of labeling was the same for both variants.

When the Alexa Fluor 647 NHS-labeled ‘Enhancer’ was applied to XL177 cells (which lack a GFP-target), we again observed very strong background (Figure 3.21 c). In contrast, its Alexa Fluor 647 maleimide-labeled counterpart behaved like a perfect negative control. High background-staining was also observed with the Alexa Fluor 647 NHS-labeled anti-Nup98 nanobody TP377. The anti-Nup93 nanobody TP179 contains a lysine in CDR II and even lost antigen-binding after NHS modification. The Alexa Fluor 647 maleimide-labeled anti-Nup98 and anti-Nup93 nanobodies, however, behaved as perfect imaging reagents and gave crisp NPC signals against very low backgrounds. This comparison indicated that modification of (multiple) framework lysines likely creates hydrophobic patches that favor unspecific binding and



aggregation. This is certainly sequence context-dependent and milder when reducing the labeling density. However, we did not observe any such complications when labeling nanobodies via engineered cysteines.

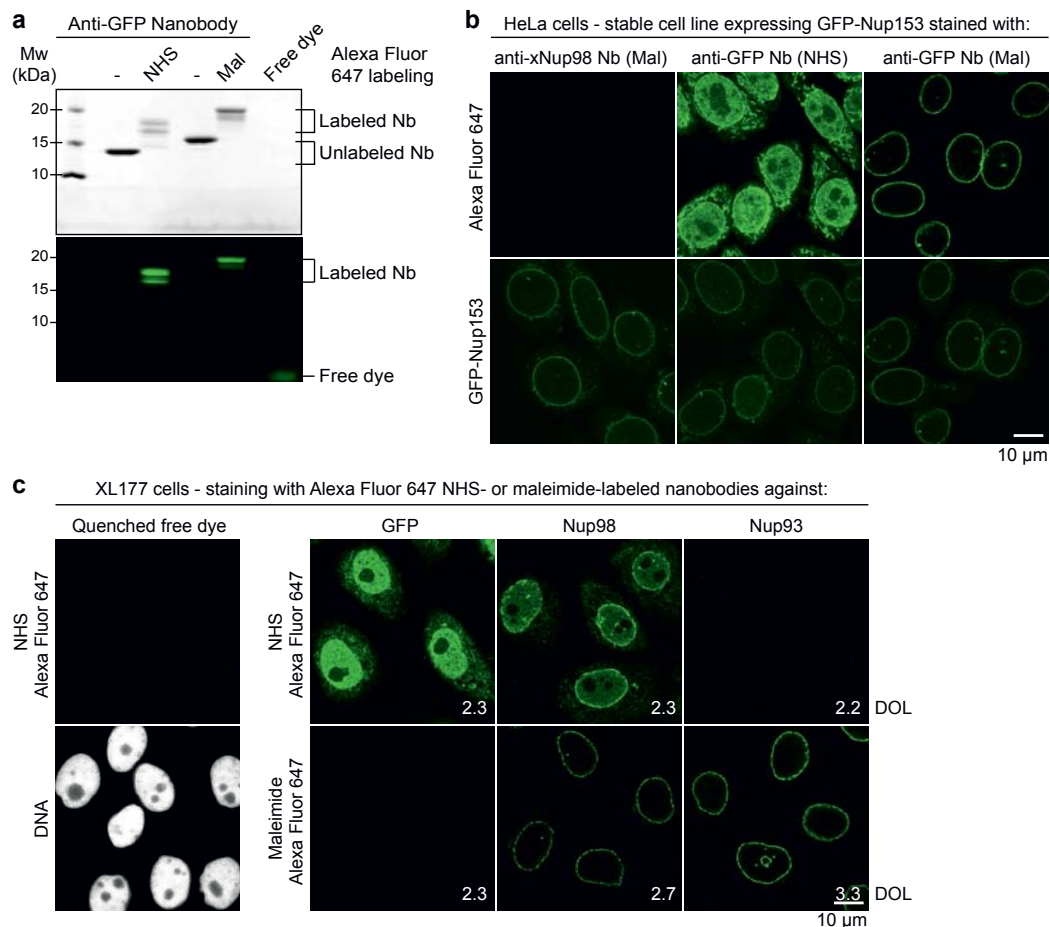


**Figure 3.21. Comparison of Alexa Fluor 647 NHS- and maleimide-labeled nanobodies.**

(a) Labeling of the anti-GFP nanobody Enhancer with Alexa Fluor 647 NHS ester at lysines or at three engineered cysteines using Alexa Fluor 647 maleimide. Labeling introduces a size shift in SDS-PAGE. Detection was either by Coomassie-staining or by in-gel fluorescence. An equal amount of unconjugated (free) Alexa Fluor 647 NHS ester fluorophore was also loaded and can be detected at the very bottom of the gel. Note that both labeled anti-GFP nanobody preparations lack unconjugated fluorophore.

(b) Staining of HeLa cells stably expressing GFP-tagged Nup153 with 10 nM of anti-GFP nanobody labeled via NHS ester or maleimide Alexa Fluor 647. The nanobody TP377, raised against *Xenopus* (x)Nup98, does not cross-react with human Nup98 and served as a negative control. Note that the NHS-labeled GFP nanobody produced strong background-staining, while its maleimide-labeled version yielded bright nuclear rim stains.

(c) Staining of XL177 cells with nanobodies labeled with Alexa Fluor 647 either at their framework lysine residues (NHS ester dye) or via engineered cysteines (maleimide dye). As a control the cells were also incubated with 10 nM quenched unconjugated (free) Alexa Fluor 647 NHS ester dye. Note that the widely used anti-GFP nanobody Enhancer produces significant background staining when labeled via lysines but not when using engineered cysteines and a maleimide dye. All nanobodies were used at a concentration of 10 nM and all images were obtained under identical settings. DOL = degree of labeling.

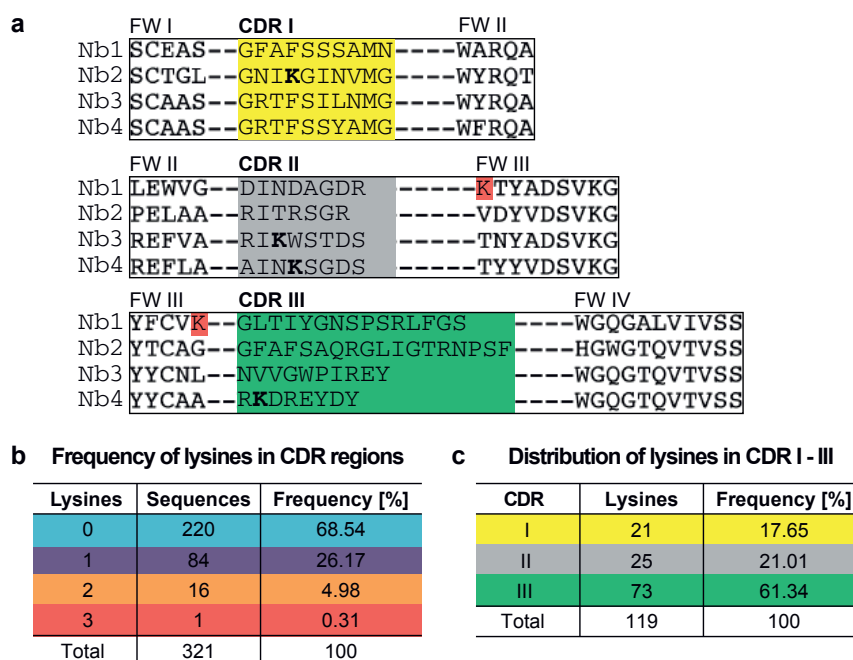


**Figure 3.22. Frequency and distribution of lysines in alpaca nanobody CDR regions.**

The depicted data is based on a protein sequence alignment of 321 random nanobodies that were collected during library quality control. The sequences are derived from three animals.

(a) CDR I-III definition. A reference alignment of the CDR I, CDR II and CDR III regions and the surrounding framework I-IV (FW) regions of four nanobodies is shown. Antigen-binding by nanobodies can also involve framework residues. This is, however, hard to predict and therefore even lysines that are very close to CDRs (shaded in red) were not counted. The statistics in (b) and (c) is thus likely an underestimation. Nb1 contains no CDR Lys, Nb2 has one CDR I Lys, Nb3 has one CDR II Lys and Nb4 has one Lys in CDR II and III.

(b) Number and frequency of lysines found in CDR I-III of 321 nanobody protein sequences. Note that 31.46 % of all nanobodies contained at least one lysine in their CDRs.

(c) Distribution of the identified 119 lysines over the three different CDRs. Note that the majority of lysines was found in CDR III, which often makes the greatest contribution to antigen-binding in nanobodies (Desmyter et al., 2001; Muyldermans, 2013).

Importantly, the anti-GFP nanobody ‘Enhancer’ and the anti-Nup98 nanobody TP377 do not contain lysine residues in their CDRs, in contrast to the anti-Nup93 nanobody TP179 that lost binding upon NHS modification. In order to get a deeper understanding of lysine frequency in CDR loops, we analyzed 321 unselected nanobody protein sequences (Figure 3.22). Strikingly, nearly every third nanobody (31.46%) contained at least one lysine residue in its CDR regions. More than half of all identified lysines (61.34%) were found in CDR III that is known to be the major antigen-contacting loop of nanobodies (Desmyter et al., 2001; Muyldermans, 2013). But even if lysines within CDR regions are not directly involved in binding, their modification with bulky fluorophores is still likely to interfere with antigen recognition. This statistical analysis emphasizes the fact that NHS modification of nanobodies, not only for the purpose of fluorescent labeling but for any kind of derivatization, is not a suitable strategy.



### 3.2.5 Super-resolution imaging with site-specifically labeled nanobodies

Due to a diameter well below the diffraction limit, NPCs have been studied by super-resolution microscopy using either indirect immunofluorescence (Löschberger et al., 2012; Göttfert et al., 2013) or the anti-GFP nanobody (Szymborska et al., 2013). Site-specific fluorescent labeling of nanobodies via cysteines now reliably yields ‘renewable’ high-quality imaging reagents that can bring fluorophores very close to their target. We therefore tested the performance of our anti-Nup nanobodies in super-resolution imaging of XL177 cell NPCs (Figure 3.23, Figure 3.24).

We started with a technique called stochastic optical reconstruction microscopy (STORM; Rust et al., 2006). Interestingly, singly Alexa Fluor 647 maleimide-labeled anti-Nup nanobodies were sufficient to produce enough localizations to reconstruct very detailed views of individual NPCs, where multiple copies of the imaged target proteins (Nup98, Nup93 and Nup155) appear arranged around the central NPC channel (Figure 3.23 c). A whole nucleus stained with the model anti-Nup98 nanobody TP377 is shown in Figure 3.23 a and magnified views of the nuclear envelope stained with anti-Nup93 and anti-Nup155 nanobody are shown in Figure 3.23 b. Even after applying higher concentrations (~100-300 nM) of nanobody to saturate the binding sites, we achieved very low background binding, indicating well-behaved imaging reagents.

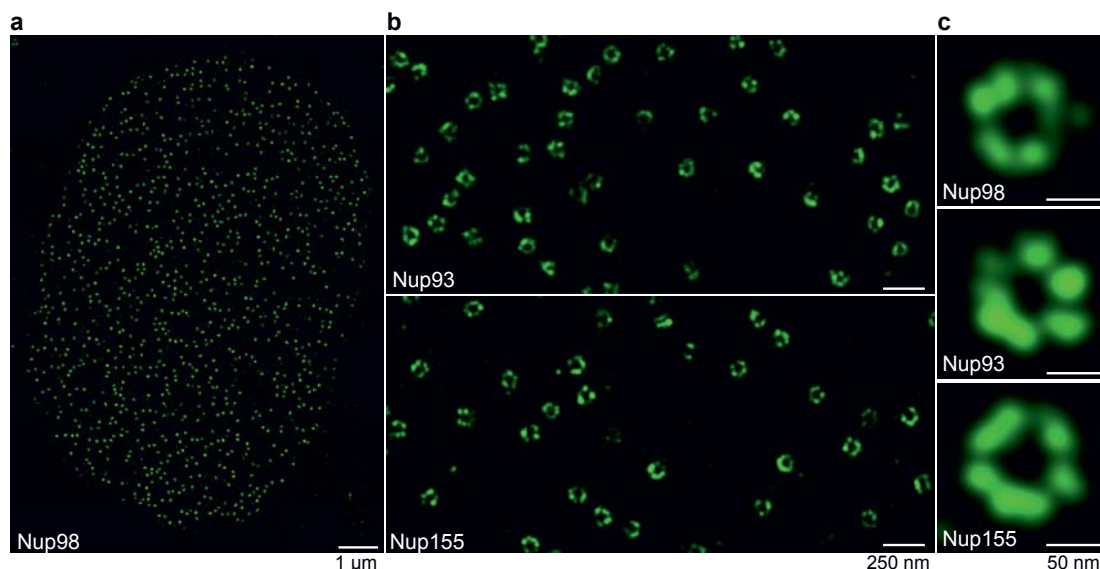


**Figure 3.23. STORM imaging of nuclear pore complexes stained with site-specifically labeled anti-Nup nanobodies.**

(a) STORM image of an entire XL177 cell nucleus stained with anti-Nup98 nanobody TP377 carrying a single N-terminal Alexa Fluor 647 maleimide. (b) Close-up view of XL177 cell nuclear envelope regions stained with anti-Nup93 nanobody TP179 (upper panel) or anti-Nup155 nanobody TP559 (lower panel) containing multiple nuclear pore complexes. (c) STORM images of individual NPCs stained with indicated anti-Nup nanobodies. All images were taken and reconstructed by Mark Bates (MPI for Biophysical Chemistry, Göttingen).



Stimulated emission-depletion (STED) is another prominent technique to break the diffraction resolution limit. The laser intensities usually used to acquire STED images are quite high and lead to rapid photobleaching. This is, however, not so problematic for indirect immunofluorescence since a high fluorophore density (6-10) per epitope can easily be achieved due to the binding of multiple secondary antibodies to one primary antibody. For nanobodies the maximum number of fluorophores probably lies around 3-4. Fabian Göttfert (MPI for Biophysical Chemistry, Göttingen) built a STED microscope that can scan very small areas and thereby reduces photobleaching in the (non-observed) environment. As a result, more specific signal can be collected before the dye bleaches. The setup is optimized for a far-red fluorophore with high photostability called KK114 (Kolmakov et al., 2010). KK114 maleimide (synthesized by Vladimir Belov; MPI for Biophysical Chemistry, Göttingen) was used to label different anti-Nup nanobodies. We stained XL177 cells with such nanobodies and obtained small STED images of individual NPCs that we selected based on a confocal image template (Figure 3.24). All three chosen nanobodies targeting Nup98, Nup93 or Nup155 yielded complete NPC ring stains. For Nup93 and Nup155 individual clusters that reflect the overall eightfold symmetry of the NPC can be distinguished. Nup98 seemed to form more narrow rings.

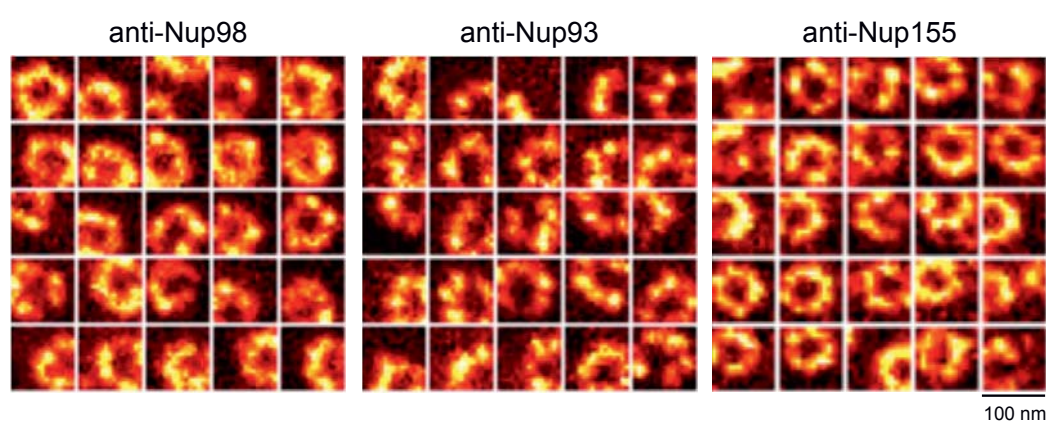


**Figure 3.24. STED imaging of XL177 cell NPCs with KK114-labeled anti-Nup nanobodies.**

Digitonin-permeabilized XL177 cells were stained either with anti-Nup98 nanobody TP377, anti-Nup93 nanobody TP179 or anti-Nup155 nanobody TP559. These nanobodies were labeled with KK114 (also called Abberior Star Red) to a DOL of ~1.0.

For all super-resolution microscopy images, we did not attempt an in-depth statistical analysis of the mean epitope distance from the NPC mid-axis (e.g. like in Szyborska et al., 2013). This is due to the fact that from 2D images it is very hard to tell the x-z/y-z



tilt of NPCs in the (naturally curved) nuclear envelope that would strongly bias an analysis. Even if one could sort this out e.g. by fitting to a circle and then average only the more or less circular NPCs, another problem remains. The imaged proteins are present in multiple copies per asymmetric unit with likely different x-y orientation that would then also be averaged.

### 3.2.6 Rapid epitope mapping via crosslinking mass spectrometry

Site-specifically labeled nanobodies enabled us to visualize their targeted epitope with high precision. Mapping the corresponding ‘visible’ epitopes would therefore reveal surface areas of the target that are accessible in the cellular environment. The complementary ‘invisible’ epitopes on the other hand, would hint to regions that are buried in interaction interfaces.

Epitope-mapping strategies based on binding assays to fragmented or mutated antigens, co-crystallization or NMR observation of chemical shift perturbations are, however, not suited for high-throughput analysis or hardly applicable to conformational epitopes on protein complexes. We therefore considered crosslinking nanobodies to their target followed by sequencing of the crosslinked target peptide via mass spectrometry as a rapid epitope mapping strategy. Here, a crucial aspect is that a shorter crosslinker will provide a better spatial resolution, provided that crosslinkable groups are in reach. As cysteines are by far the best crosslinkable groups, and because we had already placed cysteines at the nanobody surface in close proximity to bound targets, we assessed their suitability for epitope-mapping.

As a proof of principle, we crosslinked two anti-Nup93 nanobodies, with or without an N-terminal cysteine, to Nup93 using either an  $\text{NH}_2$ -to- $\text{NH}_2$  (Bis-NHS; BS3; 11.4Å) or a SH-to- $\text{NH}_2$  (Mal-NHS; BMPS; 5.9Å) crosslinker (Figure 3.25 a). For both anti-Nup93 nanobodies (TP179 and TP324), exclusive amine-crosslinking was very inefficient and produced only few nanobody•Nup93 adducts that run at higher molecular weight in SDS-PAGE. However, combining the N-terminal cysteine on the nanobody with the (far shorter) heterobifunctional crosslinker, produced very prominent nanobody•Nup93 crosslinks. Their position was then clearly identifiable by LC-MS/MS (Figure 3.25 b-c). For a better visualization of the positions of the identified nanobody crosslinks we generated a structural model of Nup93<sup>168-820</sup> using I-TASSER (Zhang, 2008), based on



structures of its yeast ortholog (Jeudy and Schwartz, 2007; Schrader et al., 2008) (Figure 3.25 c).

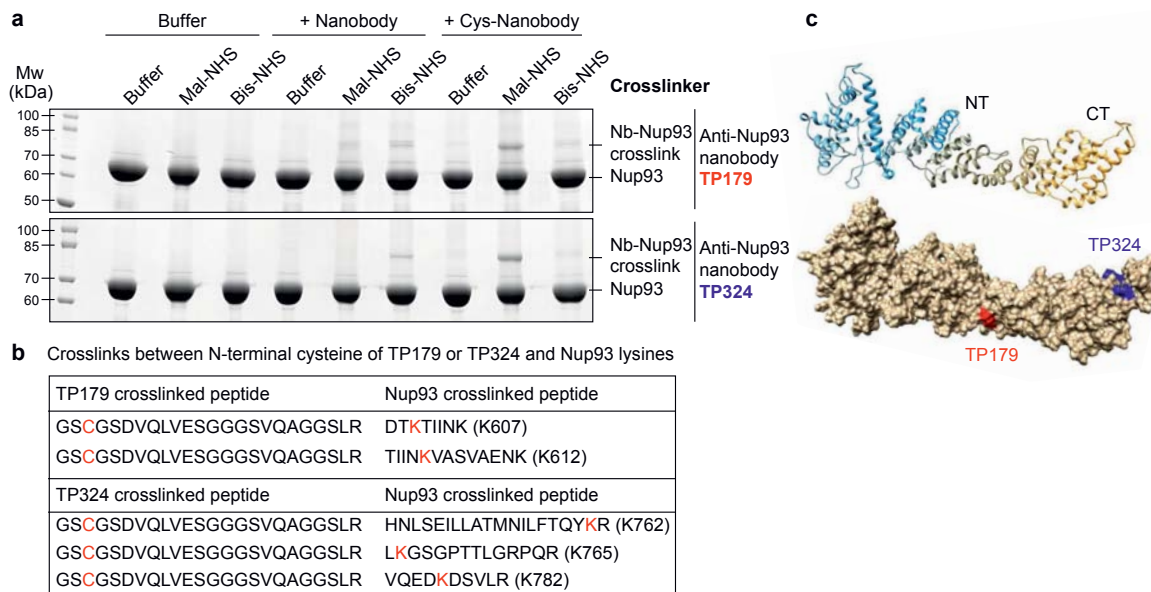


**Figure 3.25. Rapid epitope mapping via crosslinking mass spectrometry.**

(a) Crosslinking of two different anti-Nup93 nanobodies (TP179 and TP324) to Nup93 using amine-to-amine ("Bis-NHS"; BS3; 11.4 Å linker length) or thiol-to-amine ("Mal-NHS"; BMPS; 5.9 Å linker length) crosslinking reagents. The combination of the very short Mal-NHS crosslinker with an engineered cysteine close to the antigen-binding loops provided for both nanobodies by far the highest yield of crosslinked nanobody•Nup93 adduct.

(b) List of identified crosslinked peptides involving Nup93 lysines and Cys-TP179 or Cys-TP324. The crosslinked amino acids are highlighted in red.

(c) Crosslinked lysines of Nup93 to the N-terminal cysteine on anti-Nup93 nanobodies TP179 (red) or TP324 (blue) are depicted on a structural model of Nup93<sup>168-820</sup> generated by I-TASSER (Zhang, 2008). Based on the orthologous yeast crystal structures (Jeudy and Schwartz, 2007; Schrader et al., 2008), Nup93 is predicted to form a similar J-shaped structure (color gradient: NT = N-terminus in blue to CT = C-terminus in orange). Whereas TP179 binds to the central portion, TP324 binds to the C-terminus of Nup93.

We used the anti-Nup93 nanobody TP179 in STORM imaging of Nup93 within the NPC and could now map its accessible epitope. TP179 binds to the middle region of the J-shaped structure of Nup93 surrounding residues K607 and K612, while TP324 has a C-terminal epitope surrounding lysines K762, K765 and K782 of Nup93. The C-terminal region of Nup93 was previously shown to be essential for NPC assembly (Sachdev et al., 2012). Accordingly, anti-Nup93 nanobody TP324 that targets the C-terminus of Nup93 does not stain intact NPCs (see Figure 3.28), but rather represents a good candidate to selectively disrupt NPC assembly.



### 3.3 Anti-Nup nanobody toolbox applied to the study of the NPC

#### 3.3.1 Generation & characterization of the anti-Nup nanobody toolbox

We made use of the optimized nanobody discovery workflow to generate nanobodies against the major constituents of the *Xenopus* nuclear pore complex (Figure 3.26 a). For this, we initially tested many *Xenopus* nucleoporins and nucleoporin fragments for expression in *E. coli* in order to identify well-behaved antigens for immunization. While Nup155 and Nup85 could be expressed as full-length proteins, we had to truncate the Nup93 N-terminus to obtain a well-expressed C-terminal fragment Nup93<sup>168-820</sup>, similar to the construct used to crystallize its yeast ortholog Nic96 (Jeudy and Schwartz, 2007; Schrader et al., 2008). A  $\Delta$ FG domain Nup98<sup>486-866</sup> fragment and a short N-terminal RanBP2<sup>1-144</sup> fragment, based on the existing crystal structures (Kassube et al., 2012), were furthermore immunized. The boundaries of the Nup62<sup>342-547</sup>·Nup58<sup>267-490</sup>·Nup54<sup>146-535</sup> complex were determined before in the lab (Chug et al., 2015). The Nup214 NPC targeting region was mapped before (Bernad et al., 2006). We used this information to reconstitute also a trimeric Nup214<sup>598-1086</sup>·Nup88<sup>2-729</sup>·Nup62<sup>342-547</sup> complex.

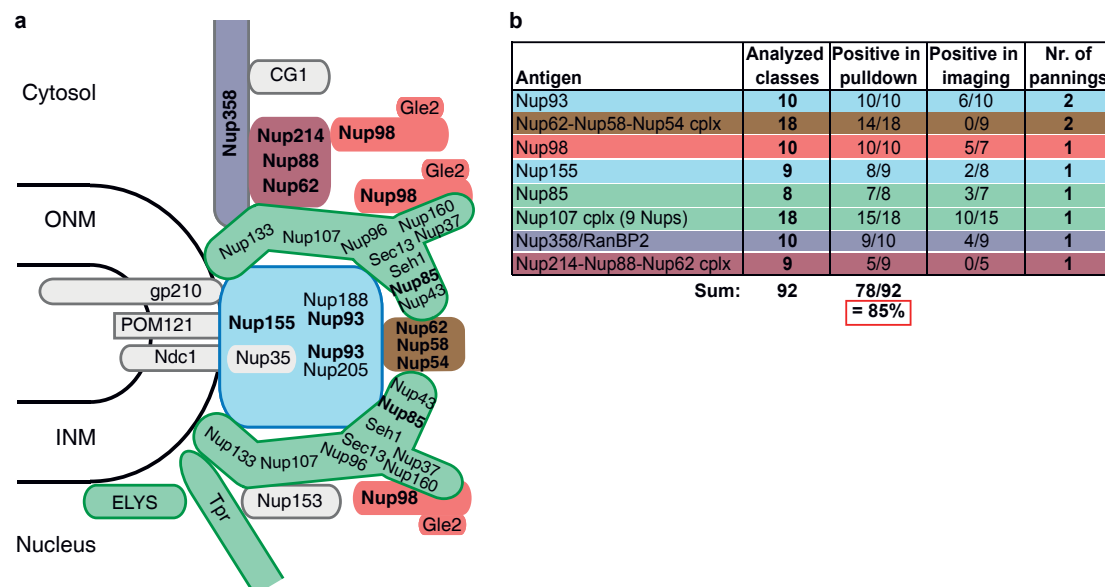


**Figure 3.26. Summary of the anti-Nup nanobody toolbox.**

(a) Schematic representation of the subcomplex organization and relative localization of Nups within an asymmetric unit of the eightfold rotational symmetric vertebrate NPC. Nups against which nanobodies were raised are highlighted in bold. ONM/INM = outer and inner nuclear membrane.

(b) Characterization of anti-Nup nanobodies. The table summarizes the number of nanobodies (different CDR III classes) characterized per antigen. All nanobodies were characterized for specificity in a *Xenopus* egg extract pulldown (positive in pulldown). Negative binders did not recognize their endogenous target. All specific nanobodies were then also tested in immunofluorescence on XL177 cells. The number of nanobodies yielding visible nuclear rim stainings is listed.



Nanobodies against all these antigens were readily obtained. In total, we characterized 92 different nanobodies. All of them were well-expressed in the *E. coli* cytoplasm and the majority of nanobodies (85 %) turned out to be positive and specific (Figure 3.26 b), arguing for a highly effective workflow.

Based on the strategies described in chapter 3.2, we equipped these nanobodies with protease-cleavable affinity tags for native protein complex isolation and with cysteines to fluorescently label them for imaging. In the beginning, we made separate constructs for each nanobody for these two applications. However, this eventually multiplied the amount of work needed to characterize them. A more effective solution was to include all necessary elements into a 'characterization vector' from the start (referred to in chapter 3.1.6; Figure 3.27).



**Figure 3.27. Open reading frame of the nanobody characterization vector pTP621.**

Nanobodies were expressed in the *E. coli* cytoplasm from a pQE80-derived plasmid carrying a kanamycin resistance cassette, a lacI open reading frame (ORF) and a ColE1 origin of replication. Expression of the nanobody-fusion ORF is driven from a Tac promoter. The resulting nanobodies have an N-terminal IF2 N-terminus-Avi peptide-(GlySer)<sub>13</sub> spacer-SUMOStar(\*)-Cys tag, a C-terminal (GlySer)<sub>7</sub> spacer-His<sub>10</sub>-tag and a molecular weight of ~50 kDa.

Enriched sub-libraries were cloned directly into this vector (or derivatives with modified tags) and sequenced. Nanobodies chosen for characterization were then directly expressed as IF2<sup>2-158</sup>-Avi-(GS)<sub>13</sub>-SUMOStar-Cys-Nb-(GS)<sub>7</sub>-His<sub>10</sub> fusion constructs and purified via Ni<sup>2+</sup>-chelate affinity chromatography. Imidazole elution yielded fully tagged nanobodies (~50 kDa), which in their biotinylated form were used for native protein complex isolation as described in chapter 3.2.2. The other half of the lysate was also bound to a Ni<sup>2+</sup>-chelate column, but then treated on-column with SUMOStar protease to cleave off the N-terminal tag. Then Cys-tagged smaller nanobodies (~15 kDa) were eluted with imidazole and labeled with maleimide fluorescent dyes for imaging. Since the N-terminal tag and the protease were easily washed away after on-column cleavage, the finally eluted nanobodies (with C-terminal His<sub>10</sub>-tag) did not contain any protease contamination. Therefore they could be used in binding assays with other nanobodies still carrying the N-terminal tag. This was used to determine if binding of one nanobody to its target is compatible with binding of another nanobody (not shown).



A typical characterization outcome is summarized for ten different anti-Nup93 nanobodies in Figure 3.28. All characterized classes were positive and showed excellent specificity, except for a low-abundant cross-reaction of TP179 (Figure 3.28 a). The best anti-Nup93 nanobodies also showed visible co-purification of endogenous Nup62•Nup58•Nup54 complexes. Six of them could also stain Nup93 within intact NPCs, pointing to accessible epitopes (Figure 3.28 b).

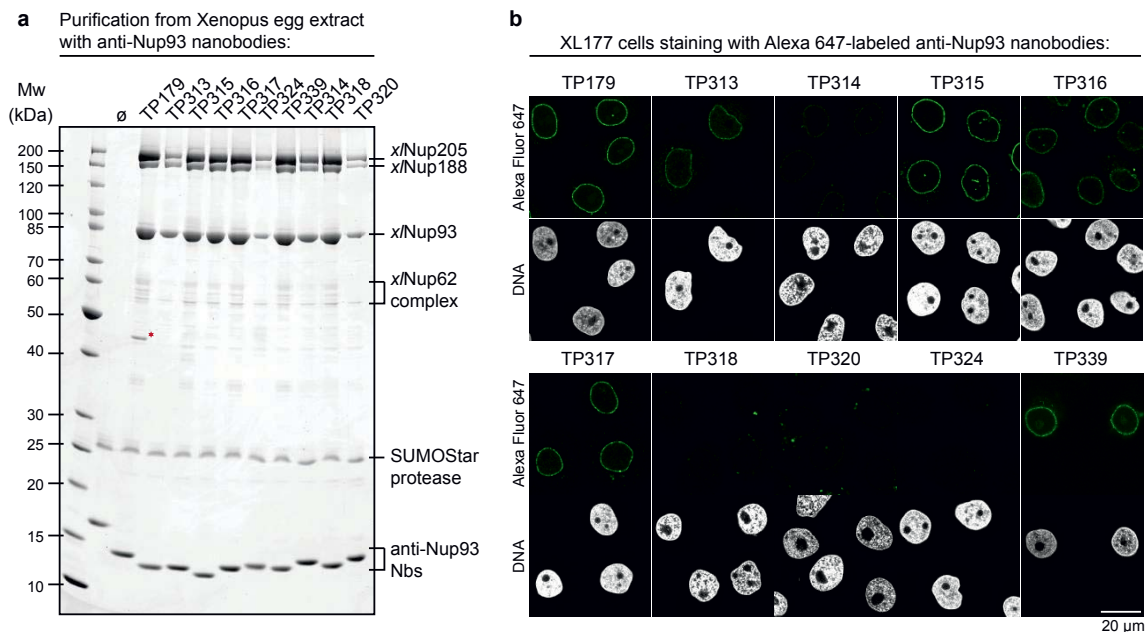


**Figure 3.28. Characterization of 10 different anti-Nup93 nanobodies.**

(a) All ten nanobodies against Nup93 recognize the endogenous Nup93•Nup188 and Nup93•Nup205 complexes. The amount of complexes in the elution fraction likely reflects the overall affinity of the used nanobodies, although hindrance of binding due to modifications cannot be excluded. The band labeled with a red asterisk represents a specific cross-reaction (Pachytene checkpoint protein 2 homolog) of TP179. The overall specificity of all ten nanobodies is nevertheless excellent.

(b) Six out of ten anti-Nup93 nanobodies have accessible epitopes on Nup93 within XL177 cell NPCs. Digitonin-permeabilized XL177 cells were incubated with Alexa Fluor 647-labeled nanobodies as described in chapter 3.2.4. All images were scanned with different laser intensity.

We further obtained nanobodies against one of the largest Nups, namely RanBP2. Nine out of ten nanobodies allowed native purification of large amounts of RanBP2•RanGAP1-SUMO complex from *Xenopus* egg extract (Figure 3.29 a). Multiple classes also brightly stained RanBP2 of XL177 cell NPCs (Figure 3.29 c). The panning against the Nup214•Nup88•Nup62 complex yielded a few positive nanobodies that could purify only small amounts of endogenous complex (Figure 3.29 b). None of these stained XL177 cell NPCs in an immunofluorescence workflow. Likewise, none of the very good anti-Nup62•Nup58•Nup54 complex nanobodies we obtained was able to yield a significant nuclear rim staining. Their epitopes are thus buried within intact NPCs.

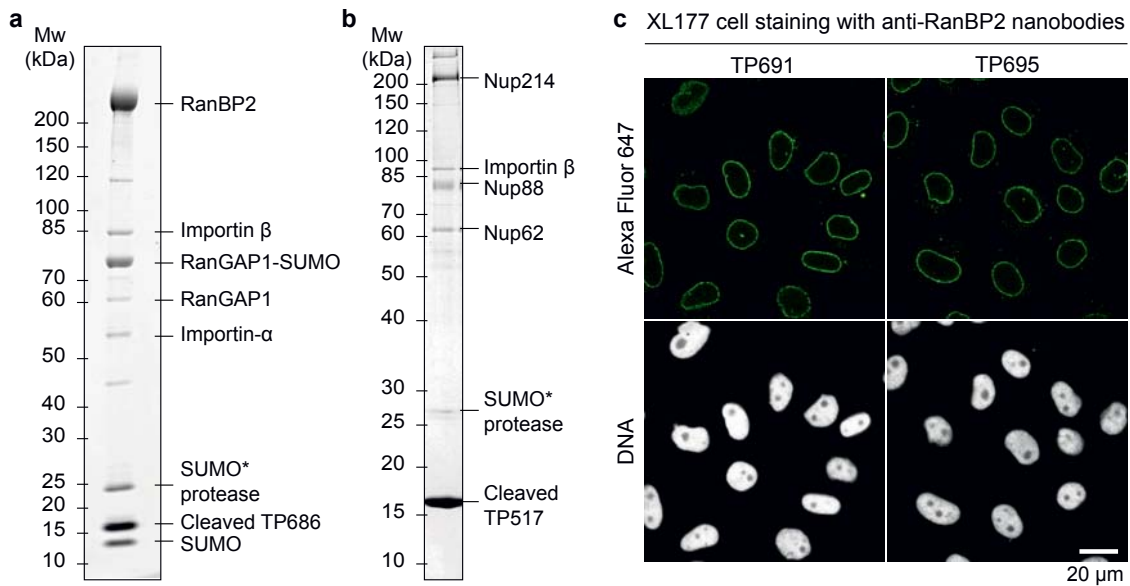


**Figure 3.29. Characterization of anti-RanBP2 and anti-Nup214•Nup88•Nup62 complex nanobodies.**

(a) Native isolation of RanBP2 and its interaction partners from *Xenopus* egg extract with TP686, carrying a biotinylated IF2<sup>2-158</sup>-Avi-(GS)<sub>13</sub>-SUMOStar-Cys-Nb-(GS)<sub>7</sub>-His<sub>10</sub>-tag, immobilized on magnetic Streptavidin beads. (b) Native isolation of Nup214•Nup88•Nup62 complex with biotinylated TP517. (c) XL177 cell staining with Alexa Fluor 647 maleimide-labeled anti-RanBP2 nanobodies TP691 and TP695.

### 3.3.2 Selection of nanobodies against natively isolated xlNup107 complex

Native isolation of endogenous protein complexes not only permitted their direct structural analysis, but also provided us with enough material for a renewed immunization. We initially identified Nup85 as a well-expressed and soluble antigen of the ~750 kDa nonameric Nup107 complex. All other members of this complex, however, were either highly insoluble or degraded after expression in *E. coli*, even after co- or triple expression of several neighboring subunits. The only way to obtain nanobodies against these subunits was to immunize the natively isolated endogenous complex. The anti-Nup85 nanobody TP512 was used to isolate ~75 μg of this complex from *Xenopus* egg extract per immunization (described in chapter 3.2.2; Figure 3.30). After four immunizations, the resulting library was searched for binders against the endogenous Nup107 complex that had been freshly immobilized on magnetic Streptavidin beads out of egg extract with the same nanobody TP512. The panning was very efficient and we obtained a very high enrichment against almost negligible background (see qPCR quantification Figure 3.7). Sequencing revealed a high diversity of nanobody classes and single sequences (Figure 3.8). 15 of 18 characterized nanobodies were able to natively isolate the Nup107 complex from egg extract (11 of



them shown in Figure 3.30 b). Many of these nanobodies also had accessible epitopes and yielded bright NPC stainings (Figure 3.30 c).

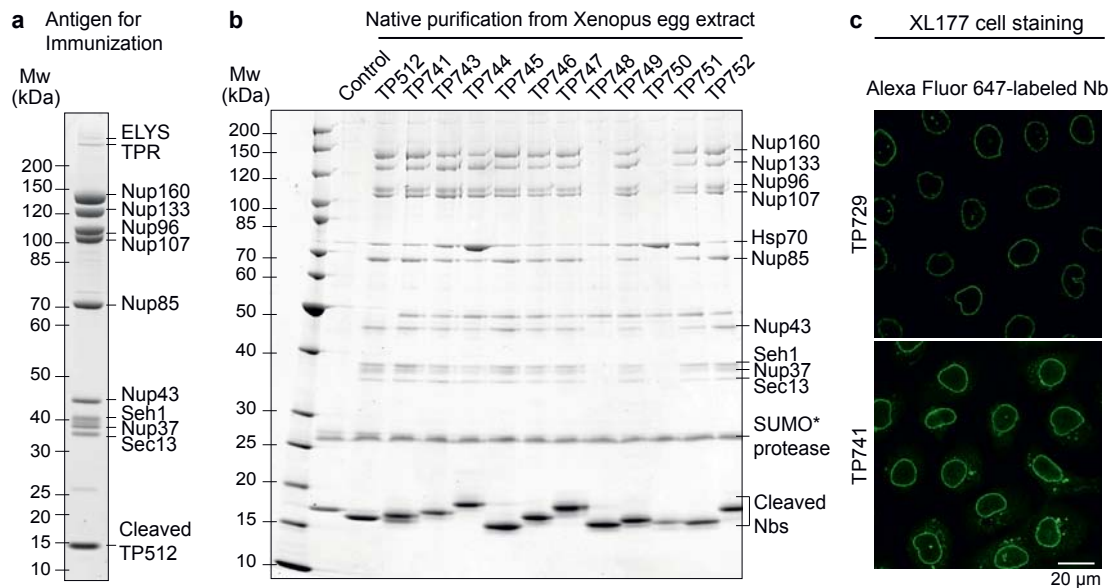


**Figure 3.30. Selection of nanobodies against natively isolated endogenous Nup107 complex.**

(a) Native isolation of the Nup107 complex from *Xenopus* egg extract for immunization with anti-Nup85 nanobody TP512.

(b) Native isolation of the Nup107 complex with nanobodies selected against the endogenous complex immobilized on Streptavidin agarose. An anti-MBP nanobody served as negative control and the anti-Nup85 nanobody TP512 as positive control. Note that the smaller pore size of the agarose did not allow for a similarly high enrichment of the large Nup107 complex as could be obtained with magnetic beads. (c) Digitonin-permeabilized XL177 cells were stained Alexa Fluor 647 maleimide-labeled anti-Nup107 complex nanobodies TP729 and TP741.

In future experiments, we will identify which subunits these nanobodies bind exactly. Crosslinking mass spectrometry-based epitope mapping (described in chapter 3.2.6) is definitely the most promising way to tackle this question.

### 3.3.3 NPC assembly investigation with the anti-Nup nanobody toolbox

The possibility to reconstitute entire functional nuclei with NPCs in the test tube (Figure 3.31) has been crucial to study NPC assembly and function. The process resembles the natural post-mitotic re-assembly of the nuclear envelope around chromatin. Importantly, the cytosol used for nuclear assembly can be depleted of individual nucleoporins to probe their contribution to NPC assembly and function (Finlay and Forbes, 1990; Walther et al., 2003; Hülsmann et al., 2012). Likewise, recombinant full-length, truncated or mutant Nups can be added back to map critical domains. The resulting reconstituted nuclei contain engineered NPCs and can be functionally analyzed with transport assays or structurally for the presence of other Nups.

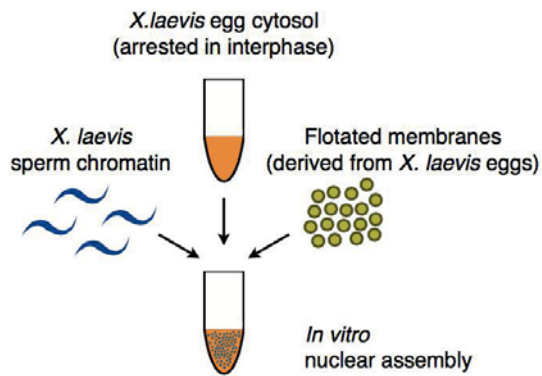


**Figure 3.31. Scheme illustrating the *in vitro* nuclear assembly assay.**

*Xenopus laevis* eggs are activated with an ionophore in the presence of calcium, which triggers them to leave their metaphase II arrest and reach an interphase-like state. Cytosol prepared from activated eggs is then mixed with sperm chromatin and membranes in the test tube and incubated at 18-20°C for 2 h. Nuclei with intact nuclear envelope and NPCs form that can be functionally analyzed e.g. by transport assays. The scheme was adapted from the thesis of Dr. Bastian Hülsmann with permission.

Antibodies were crucial tools to deplete Nups or to stain for their presence within engineered NPCs. Polyclonal antibodies or derived Fab-fragments were even added to the nuclear assembly assay to inhibit the incorporation of their target protein into NPCs (Antonin et al., 2005).

We wanted to test our anti-Nup nanobodies for binders that hit critical epitopes relevant for NPC assembly. For this, we pre-incubated them with cytosol before addition of sperm chromatin and membranes. In principle, nanobodies binding to epitopes not involved in protein-protein interactions should be incorporated along with their bound target. Those that bind assembly-relevant interfaces should reduce the NPC incorporation of their target. As a proof-of-principle, we aimed at reproducing a previously described phenotype. The depletion of a single FG-repeat nucleoporin, Nup98, was shown to lead to the assembly of NPCs with disrupted permeability barrier (Hülsmann et al., 2012). We screened the transport capacities of nuclei reconstituted in the presence of anti-Nup98 nanobodies (Figure 3.32) that were raised against the structured C-terminal domain known to be involved in NPC anchoring (see crystal structure Figure 3.16). Assembly in the presence of buffer or anti-Nup98 nanobody TP372 (as well as TP377; not shown) did not compromise the accumulation of IBB-MBP-GFP in the reconstituted nuclei. A group of Nup98 nanobodies including TP373, however, led to very small nuclei with strongly reduced import.

An obvious explanation for this effect would be that TP373, but not TP372, interferes with Nup98 incorporation into NPCs. We therefore probed nuclei reconstituted in the presence of buffer or TP373 for different nucleoporins. Importantly, such analysis previously required a lengthy indirect immunofluorescence workflow using primary and secondary antibodies. Fluorescently labeled nanobodies targeting the major NPC subcomplexes can, however, easily be co-incorporated into assembling nuclei or simply added after assembly (Figure 3.33).

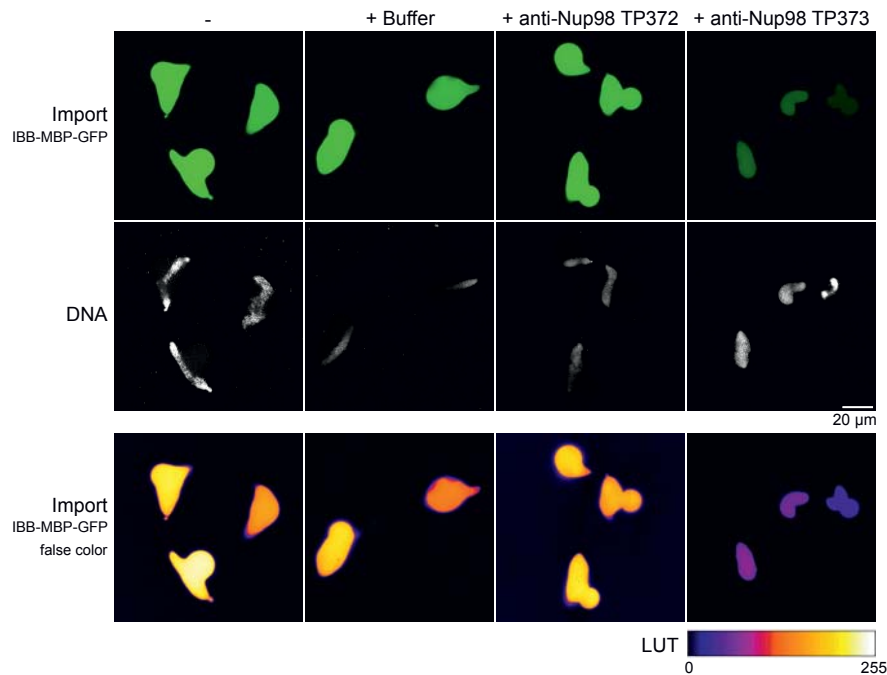


**Figure 3.32. *In vitro* nuclear assembly in the presence of anti-Nup98 nanobodies.**

The cytosolic fraction used for nuclear assembly was pre-incubated for 10 min at 20°C with either S250 buffer, 4 μM untagged anti-Nup98 nanobody TP372 or 4 μM untagged anti-Nup98 nanobody TP373. Then sperm chromatin and membranes were added as described (6.5.5). As a positive control no buffer was added (-). The resulting nuclei were incubated for 1 h at 20°C with 3 μM hsRch1 IBB-MBP-GFP and DAPI and then analyzed unfixed by confocal microscopy. A false-color representation of the nuclear import signal is given with a modified lookup table (LUT).

As expected, nuclei reconstituted in the presence of TP373 showed strongly reduced levels of Nup98, whereas structural NPC scaffold Nups like the Nup107 complex or Nup155 remained unaffected. Surprisingly, however, a much weaker nuclear rim stain was also observed for RanBP2. So far Nup98 was not implied in having a role in NPC anchorage of RanBP2, although reports about it having a structural role in the NPC are emerging (Fischer et al., 2015).

We reasoned that the specific effect of TP373 must be due to an inhibition of Nup98 NPC anchorage via its absolute C-terminus. Nup96 and Nup88 are known binding partners of the Nup98 C-terminus and are required for anchoring Nup98 at the NPC (Hodel et al., 2002; Griffis et al., 2003; Stuwe et al., 2012). We therefore immobilized the Nup96<sup>867-885</sup> N-terminus, which originates from autoproteolytic cleavage of the Nup98-Nup96 precursor protein (Fontoura et al., 1999) in the cell and binds to the Nup98 C-terminus, on silica beads and incubated it either with Nup98 alone or Nup98 in complex with different anti-Nup98 nanobodies (Figure 3.34).

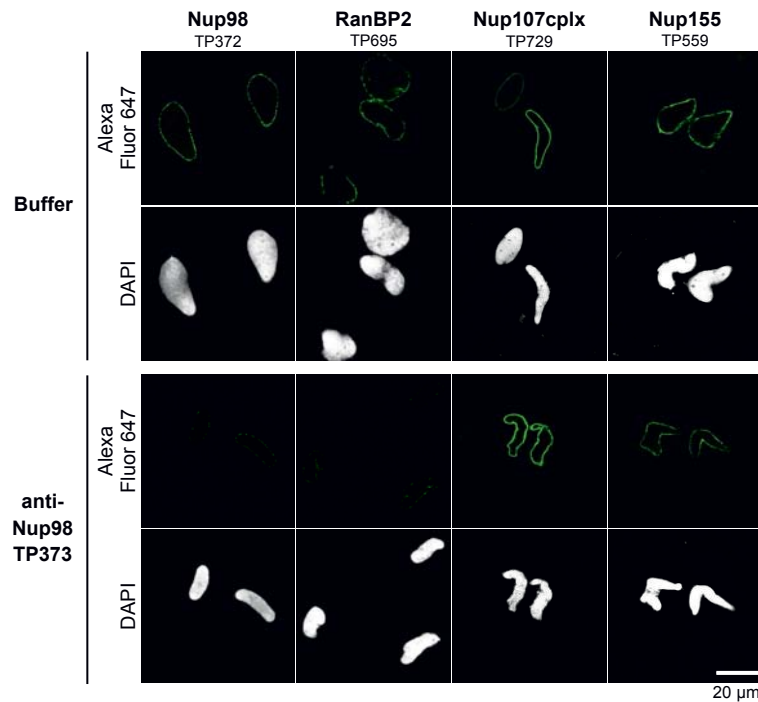


**Figure 3.33. Nup composition of nuclei reconstituted in the presence of anti-Nup98 Nb TP373.**

Nuclei were reconstituted in the presence of S250 buffer or 4  $\mu$ M anti-Nup98 nanobody TP373. For analysis of the Nup composition of the resulting NPCs, 200 nM of the indicated Alexa Fluor 647 maleimide-labeled anti-Nup nanobodies were also added prior to assembly. After assembly, nuclei were stained with DAPI, fixed, centrifuged on aminosilan-coated coverslips and mounted for analysis by confocal microscopy. Note that nuclei reconstituted in the presence of TP373 have strongly reduced levels of Nup98 and RanBP2 at their NPCs.

Strikingly, the anti-Nup98 nanobody TP373 completely inhibited the interaction between Nup98 and Nup96 N-terminus, explaining its negative effect on Nup98 NPC incorporation. Binding of other nanobodies like TP372, however, was largely compatible.

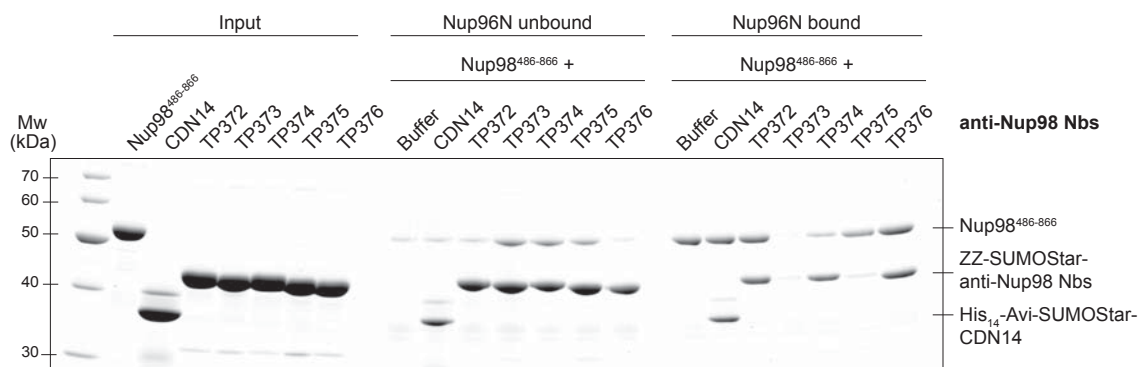


**Figure 3.34. Inhibition of Nup96 binding by anti-Nup98 nanobodies.**

Nup98<sup>486-866</sup> was pre-incubated with buffer or twofold molar excess of different anti-Nup98 nanobodies. The complexes were then bound to silica beads with immobilized Nup96<sup>867-885</sup> N-terminus and after washing eluted with SDS-PAGE sample buffer (bound). Input, unbound and bound fraction were analyzed by SDS-PAGE and Coomassie-staining. Note that TP372 did not interfere with binding of Nup98 to Nup96, while TP373 strongly inhibited this interaction.



### 3.3.4 Analysis of interphase and mitotic nucleoporins

Post-translational modifications of nucleoporins like phosphorylation are thought to regulate NPC disassembly at the onset of mitosis (Laurell et al., 2011; Bui et al., 2013). In order to get a comprehensive overview of mitotic modifications of Nups, we aimed at their purification from a cytostatic factor (CSF)-arrested *Xenopus* egg extract (Tunquist and Maller, 2003; Hannak and Heald, 2006) (Figure 3.35). We validated the quality of these ‘mitotic-like’ extracts by their ability to form microtubule asters in the presence of RanQ69L<sup>5-180</sup>•GTP and bipolar spindles in the presence of sperm chromatin. Importantly, these extracts could be sent into an ‘interphase-like’ state by addition of CaCl<sub>2</sub> and cycloheximide. Such cycled extracts could assemble import-competent nuclei (Figure 3.35 a).

As a proof of principle we purified the Nup93 complexes, the Nup107 complex and Nup155 from undiluted crude CSF extract and one that had been sent to interphase before (Figure 3.35 b). Although the presence of membranes and whole organelles caused a higher background, somewhat elevated in non-cycled CSF-extract, individual Nup bands can be distinguished. Indeed, it seems that some Nups run at apparently higher molecular weight in SDS-PAGE when purified from CSF extract in comparison to ‘interphase-like’ extract. This is likely due to phosphorylation and can be seen e.g. for Nup96, Nup107, TPR and Elys. RanBP2, Nup98 and the Nup62•Nup58•Nup54 complex can also be purified from both types of extract (not shown). We are currently optimizing the workflow for identification of phosphorylation sites and other possible modifications. Especially the mapping of native O-glycosylation sites of Nups will be pursued.

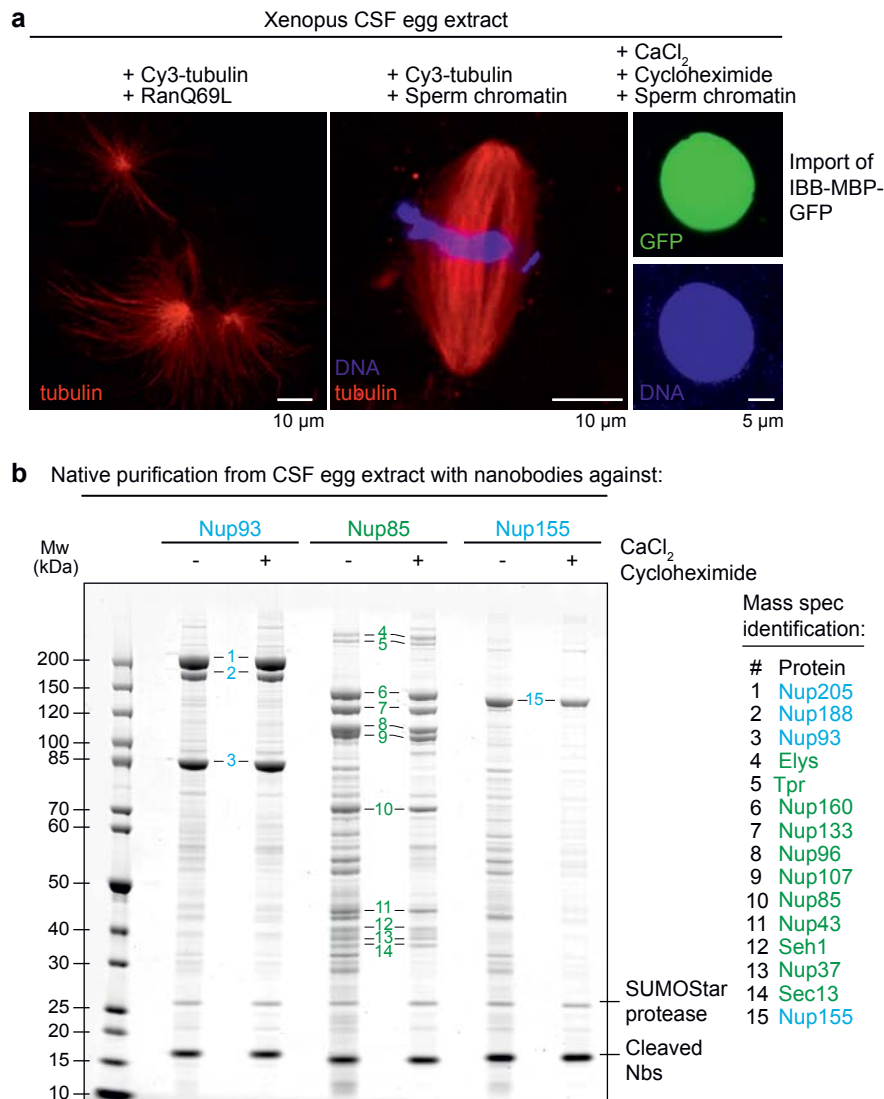


**Figure 3.35. Native isolation of nucleoporin complexes with nanobodies from ‘mitotic’ and ‘interphase-like’ *Xenopus* egg extract.**

(a) Validation of Cytostatic factor (CSF)-arrested extract. The mitotic quality of every extract was validated before use in affinity chromatography. Good mitotic extracts allowed the formation of ‘Ran asters’ in the presence of 20 μM RanQ69L<sup>5-180</sup>•GTP and Cy3-labeled tubulin (kind gift of Dr. Simone Reber). When sperm chromatin and Cy3-labeled tubulin were added, bipolar spindle formation could be observed *in vitro* after ~ 1 h incubation at 20°C. Importantly, CSF extract could be cycled back to an interphase-like state after incubation with 0.6 mM CaCl<sub>2</sub> and 100 μg/ml cycloheximide. This led to the disassembly of pre-formed Ran asters and nuclear envelope formation around added sperm chromatin. The nuclei formed in cycled CSF extracts were fully functional and could accumulate the import cargo IBB-MBP-GFP.

(b) Native isolation of indicated nucleoporins from crude low-speed supernatant CSF and cycled CSF extracts with nanobodies immobilized on magnetic beads. After isolation the beads were washed and bound complexes eluted via SUMOStar protease cleavage.



## 4 Discussion

### 4.1 A rapid phage display-based nanobody discovery workflow

We developed a highly optimized phage display-based nanobody production workflow that features improvements of nearly all involved steps. As a result, we were able to routinely obtain and characterize diverse sets of nanobodies against desired antigens within only 14 working days. The workflow does not require high-throughput capabilities and instead relies on standard techniques, uses common laboratory equipment and can be completed by a single person. A certainly still restricting factor is the availability of animals for immunization. However, more and more companies are now routinely offering alpaca or llama immunization. Furthermore, our workflow could easily be adapted also to synthetic libraries circumventing the need for animal immunization in the first place. All required reagents can be bought from commercial suppliers or actually self-produced in the lab. We only outsourced the 96-well plate sequencing, which is a routine service in most sequencing companies.

Our workflow is more than twice as fast as the current standard protocols for nanobody production (3-4 months Pardon et al., 2014; 4-6 weeks Fridy et al., 2014). Consequently, a higher throughput in nanobody discovery can be achieved, saving hands-on time and money. The recombinant nanobody technology has great potential to replace the generation of conventional antibodies, yielding well-characterized reagents with known sequence that can be shared across the research community. A cheap, fast and efficient workflow for nanobody generation as presented in this study should greatly facilitate the implementation of the nanobody technology in other labs and encourage the community to invest in its expansion. The major improvements over the current phage display-based nanobody production workflows (Vincke et al., 2012; Pardon et al., 2014) will now be discussed individually.

#### 4.1.1 Rapid and accurate library construction via Gibson assembly

The standard restriction enzyme-based approach for library construction leads to an irreversible loss of valuable binders and is also very time-consuming. In order to achieve efficient digestion of phagemid and nanobody library, the restriction reactions were incubated over night. A similar over night incubation step was required for



efficient ligation of the resulting restriction fragments (Vincke et al., 2012). Importantly, the same restriction sites then also have to be used to clone the selected nanobodies after panning into different vectors. However, we experienced that entire classes of successfully selected binders possessed these sites within their sequence after panning, making them very hard to clone. A likely reason would be that these internal restriction sites were missed during library construction or formed through spontaneous mutations during the phage display process. The same problems should affect the generation of single-chain Fv- or Fab-antibody libraries even more severely due to the much larger size of these fragments as compared to nanobodies.

To the best of our knowledge, Gibson assembly has never been employed to construct antibody libraries. As illustrated in chapter 3.1.2, it allowed a very efficient joining of phagemid and nanobody library PCR products, with 98% of all sequenced clones showing a correctly inserted nanobody sequence. Importantly, assembly takes only 30 minutes allowing all steps of library construction to be carried out on a single day. Therefore, application of Gibson assembly in library construction greatly increases speed and fidelity. The introduced Gibson assembly overhangs further render the absolute ends of the nanobody sequence constant. These constant regions then serve as primer-binding sites for the cloning of enriched sub-libraries after panning into the characterization vector and prevent a loss of valuable clones due to amplification bias.

Importantly, all three enzymes (Pfu Polymerase, 5'- T5 exonuclease and Taq DNA ligase) required for the final Gibson assembly mix can be produced in large quantities in *E. coli*. We therefore prepared our own Gibson assembly mix and did not rely on the still expensive commercial product.

#### **4.1.2 A 'minimal phagemid' facilitates construction of large libraries**

A multitude of phagemids with different promoters, signal sequences, tags, multiple cloning sites, antibiotic resistance cassettes and replication origins have been constructed within the last ~25 years of phage display all over the world (Qi et al., 2012). Studies that compared different phagemids for their performance in phage display and evaluated individual elements are rare (Soltes et al., 2007). Most routinely used phagemids are rather large ~4-5 kbp, although it is clearly evident that a smaller



vector would allow the construction of larger libraries due to the dependence of the *E. coli* transformation efficiency on the plasmid size (Hanahan, 1983).

We systematically deleted individual elements of a pHEN4 source phagemid (~4860 bp with a ~380 bp nanobody insert; Arbabi Ghahroudi et al., 1997). Every single deletion was tested for functionality by analysis of phage production and nanobody-pIII fusion protein display level. All functional deletions were combined into the final minimal phagemid pTP826 of only ~3060 bp in size (including a ~380 bp nanobody insert). To the best of our knowledge, this is the smallest pIII-based phagemid ever constructed. This allowed us to obtain a fourfold higher transformation efficiency of *E. coli* and around  $2.5\text{-}4.5 \times 10^8$  transformants per transformation (with 0.5  $\mu\text{g}$  DNA). This tremendously facilitates the construction of large libraries. For example, the generation of a library of  $1 \times 10^{10}$  transformants would require only around 20-40 transformations, instead of several hundreds (Vaughan et al., 1996).

Such library sizes are certainly not required for nanobody immune libraries. Here, the actual library size is limited by the number of different heavy-chain antibody producing B cells that can be found in the blood sample taken after immunization ( $\sim 10^7\text{-}10^8$ ). However, in order to also represent the rare clones in the final library, around 100-fold coverage of this initial diversity is desirable. The situation is completely different when scFv fragment libraries have to be constructed. During total RNA isolation, information about the coupling of variable heavy and variable light chain domains is lost. Very large library sizes are required to statistically restore a greater number of original VH-VL combinations with high affinity. The same holds true for synthetic antibody libraries that are based on either partially or completely randomized CDRs. In fact, many alternative protein scaffolds have been randomized and turned into protein binders after affinity selection (Beste et al., 1999; Binz et al., 2004; Koide et al., 1998; Nord et al., 1997). Often, it is virtually impossible to represent the entire theoretical diversity of such libraries. Still, also here, it holds true that the bigger the library is the higher the chances are of finding a binder with a decent affinity. Gibson assembly and the minimal phagemid could thus certainly be of very great use not only for constructing nanobody immune libraries, but especially for large synthetic antibody or alternative scaffold libraries.



Ampicilin is used as a selection marker in many phagemids, although it does not allow for stable vector propagation (Krebber et al., 1997). In fact, it is metabolically consumed by the encoded beta lactamase enzyme and essentially used up once cells reach a late log phase of growth. Since phage production needs to take place over night at 37°C, the phage producing cells very quickly reach stationary phase and selection pressure is lost. This leads to phagemid loss and is best reflected by the high number of helper phage genome virions (nearly 50% as shown in Figure 3.5 c) produced from the phagemid pHEN4. When a phagemid with a strong packaging signal is missing, nascent virions package the helper phage genome that contains a much weaker packaging signal (Vieira and Messing, 1987). We introduced trimethoprim as a selection marker in this study. It combines multiple beneficial properties: the resistance cassette is very small, the antibiotic is cheap and active even at high cell densities. Therefore only ~4,4 % of all virions produced from the minimal phagemid could package a helper phage genome (Figure 3.5 c). This ensures a robust coupling of all encoded library members to their respective genetic information, which is the basis for a successful phage display selection.

#### 4.1.3 qPCR quantification of phage display

The analysis of panning by titering (see Figure 3.6) is labor intensive, not reproducible and only infective virions can be counted by this method. This limits the number of panning reactions or conditions that can be analyzed in parallel. The final results depend on the number of resistant *E. coli* cells. The handling of multiple samples, however, leads to a significant time delay during which the cells continue to divide thus introducing some bias. For the actual analysis, colonies on multiple plates have to be counted on the next day and only then a conclusion can be formed and protocols adjusted for the next round of panning.

We implemented a straightforward qPCR approach for the rapid analysis of panning that requires very little hands-on time and yields absolute numbers of phages within 1 h. Our phagemid primers are very specific and do not show any mispriming on helper phage genome DNA. The method is very robust and does not require any pre-treatment of the phages before PCR amplification. Indeed, crude culture supernatant could be used to quantify phagemid and helper phage virions (Figure 3.5). Such a simple one-step analysis will facilitate the parallel optimization of panning conditions or allow



a larger number of panning reactions to be handled. For example, different wash protocols or elution conditions could be easily compared.

Most interestingly, phage display can be completely automated (Hornsby et al., 2015) and carried out in 96-well plates. Pipetting robots or magnetic bead processors have been employed for phage display (Konthur et al., 2010; Paduch et al., 2013). This is highly compatible with the qPCR format, so that even the masterplate and the phage dilutions for qPCR could be pipetted by such a machine. In the end, one would only need to transfer the plate to the real-time PCR cycler.

#### **4.1.4 The importance of a characterization strategy**

A successful selection yields a large panel of nanobodies with diverse sequences that needs to be characterized. Characterization can be very time-consuming, especially if not only a mere binding to the antigen is desired, but more specific properties of the final binders are sought after (e.g. crystallization chaperone activity, inhibition of enzymatic activity or protein-protein interaction). Whenever possible, the selection strategy should be adjusted to enrich binders with the desired properties in order to minimize characterization efforts.

Pardon et al. and Vincke et al. employed an ELISA approach to identify antigen-binding nanobodies directed to the periplasm via the secretion signal from the phagemid (Vincke et al., 2012; Pardon et al., 2014). ELISA-positive clones are then sequenced and chosen for periplasmic expression. The small C-terminal His<sub>6</sub>-tag originating from the phagemid allows for a Ni<sup>2+</sup>-chelate affinity purification of nanobodies. This is certainly sufficient if only antigen-nanobody complexes for crystallization have to be formed. Nickel matrices are, however, not suited for affinity purification from eukaryotic extracts to assess nanobody specificity due to the presence of endogenous histidine-rich proteins. Furthermore, for fluorescent labeling, only the natural lysine residues could be modified with NHS ester dyes, leading to all the negative effects that were described in chapter 3.2.2. Thus, in order to extend the scope of characterization, every single nanobody would have to be cloned individually to a new vector.

We implemented a characterization strategy that saved valuable hands-on time and effectively allowed all desired applications to be carried out from a single construct, preventing laborious subcloning. We cloned entire enriched sub-libraries after different



selection rounds into the characterization vector via Gibson assembly and directly transformed an *E. coli* expression strain. Then, individual clones were sequenced, analyzed and interesting candidates directly picked for expression from the master plate. Due to the high frequency of positive binders (~85%), the waste of resources on the sequencing and expression of ‘negative’ nanobodies was negligible.

Our characterization vector (Figure 3.27) makes use of cytoplasmic expression in *E. coli*, enables the novel nanobody engineering strategies described in chapter 3.2 and allows characterization of specificity, fluorescent labeling and epitope orthogonality from a single construct.

#### **4.1.5 Comparison to mass spectrometry-based nanobody production workflow**

Fridy and colleagues described a novel workflow for the identification of antigen-binding nanobodies based on mass spectrometry (Fridy et al., 2014). They purified heavy-chain antibodies from the serum of an immunized animal, bound them to antigen on beads and then cleaved off their constant domains with papain, yielding only the variable domains. The eluted VHH domains are then sequenced by tandem mass spectrometry (MS/MS) and the identified peptides matched to a specifically created deep sequencing library of VHH domains from the same animal. Candidate binders are ordered as gene syntheses, expressed in the periplasm and tested for binding.

It is evident that multiple crucial steps of this workflow like deep sequencing, MS/MS and gene synthesis have to be outsourced to experts. Thus, a coordination of at least three different collaborations is necessary and will likely slow down the overall discovery process. Furthermore, the costs of deep sequencing and gene synthesis are still very high. Considering the reported success rates of ~50 % for GFP, a considerable amount of resources is spent on the gene synthesis and characterization of negative nanobodies. This certainly could be improved by applying more stringent selection conditions. However, in contrast to phage display, no selective enrichment of binders with certain traits is possible. Therefore, low abundant clones might escape detection. Surely, the sensitivity of mass spectrometry will increase in the future to (partially) compensate for this. An important criterion for nanobody identification is to gain a complete coverage of its CDR regions. CDR III loops are, however, often very long and



contain hydrophobic residues. Therefore more in-depth analyses are needed to exclude that CDR composition biases nanobody identification in this approach.

Fridy et al. remarked that their method does not require an intermediary expression system that could introduce bias. However, in the end all nanobodies have to be expressed in *E. coli*, and even with optimized codon usage they can still misfold. Phage display inherently selects for other traits than just affinity. Nanobodies that show a low expression level, poor solubility, non-specificity or misfolding are less competitive than other clones and will be selected against. In fact, many strategies were described to actively select for proper folding and stability (Gu et al., 1995; Kristensen and Winter, 1998; Sieber et al., 1998; Wörn and Plückthun, 2001; Jespers et al., 2004).

## 4.2 Cytoplasmic expression of engineered nanobodies

The disulfide bond-forming cysteines within the hydrophobic core of all antibody variable heavy and light chain domains are highly conserved and important for antibody stability. Disruption of this disulfide bond in scFv fragments by mutation often led to severe folding problems and aggregation (Glockshuber et al., 1992; Ramm et al., 1999; Wörn and Plückthun, 2001). Only in very few individual cases disulfide-free scFv fragments were functional. This was either due to an intrinsically high stability of these scFv fragments (Langedijk et al., 1998; Wörn and Plückthun, 1998) or due to stabilizing compensatory mutations that were found by engineering approaches (Martineau et al., 1998; Proba et al., 1998).

Nanobodies, however, are intrinsically more stable than scFv fragments or isolated variable heavy domains of conventional antibodies (van der Linden et al., 1999; Pérez et al., 2001; Dumoulin et al., 2002). In our hands, the absence of the conserved disulfide bond from nanobodies did not cause any folding problems or aggregation. All 92 nanobodies characterized in this study could be expressed in the reductive *E. coli* cytoplasm and were soluble. The vast majority of them (85%) recognized their respective endogenous target protein, emphasizing their correct folding. The thermostability of two reduced nanobodies was, as expected, decreased in comparison to their oxidized counterparts expressed in the periplasm, but still far above standard incubation temperatures (Figure 3.10).



A systematic analysis of the thermostability of reduced nanobodies could yield important insights. For example, is there a difference in stability between nanobodies derived from different VHH3 family subclasses (Achour et al., 2008)? Are there any hallmark amino acid substitutions that confer high thermostability in the absence of the disulfide bond? Importantly, it needs to be investigated how stable reduced nanobodies are after prolonged incubation at 37°C, which is crucial for therapeutic applications. Furthermore, it would be interesting to see if reduced nanobodies can still reversibly refold as described for oxidized nanobodies (Pérez et al., 2001). Many nanobody applications in research, however, require incubation at 4°C or room temperature. Affinity isolations from eukaryotic extracts are performed at 4°C to avoid protease activity and protein aggregation. Classical immunofluorescence is usually carried out at room temperature. (Co-)crystallization reactions are also incubated at 4°C or room temperature. Therefore, for these major applications of nanobodies in research, reduced nanobodies should be perfectly suited.

Incorporation of a routine selection step for highly thermostable (reduced) nanobodies into the phage display workflow would be very attractive. However, this is complicated by the fact that phages are assembled in the periplasm and thus all displayed nanobodies are oxidized. Heating phage-displayed nanobodies in the presence of reducing agent prior to antigen binding, however, could be an option to find thermostable variants that could resist high temperatures and subsequently refold to their native conformation in the absence of the disulfide bond.

Certainly, efficient disulfide bond formation during cytoplasmic expression could be an elegant way to combine the advantage of increased tagging options with high thermostability. Engineered *E. coli* strains like SHuffle or Origami contain mutations in the major cytoplasmic reduction pathways and thus accumulate oxidized thioredoxins that catalyze disulfide bond formation (Derman et al., 1993; Bessette et al., 1999; Ritz et al., 2001). These strains were successfully used to express strictly disulfide bond-dependent proteins in the cytoplasm. Surprisingly, we found that only a fraction of nanobodies expressed in *E. coli* SHuffle actually had a formed disulfide bond (Figure 3.9). The major fraction was fully reduced. A likely reason is that nanobody folding does not depend on disulfide bond formation and can proceed very rapidly in its absence. If folding is faster than oxidation, no disulfide bond can form.



A second disulfide bond is often found between CDR I and CDR III in camel and llama nanobodies (Vu et al., 1997; Nguyen et al., 2000; Harmsen et al., 2000). In our alpaca nanobodies, a second disulfide bond was found to be very rare (~8,6% of all selected nanobodies) and exclusively formed between FW II and CDR III. Also those nanobodies could be expressed under reducing conditions and were active. Govaert et al. showed that the absence of the interloop disulfide bond from camel nanobodies caused a decrease in antigen affinity (Govaert et al., 2012). This was attributed to a higher entropy penalty upon binding, due to the necessary rearrangement of the long flexible loops in the absence of a stabilizing disulfide bond. A more systematic analysis of (selectively) reduced and oxidized nanobodies with an additional CDR I-CDR III or FW II-CDR III disulfide bond could shed more light on their importance for antigen binding. Interestingly, alpaca nanobodies do not employ a CDR I-CDR III linkage at all as can be inferred from our sequence data and an analysis of alpaca germline VHH sequences (Achour et al., 2008). Due to the higher frequency of a second disulfide bond in camel and dromedary nanobodies as compared to llama and alpaca nanobodies (Muyldermans, 2013; this study), it is conceivable that the latter might be much more suited for expression under reducing conditions and consequently also more amenable to the novel engineering strategies described in this study.

#### 4.2.1 Native protein complex isolation

Functional cytoplasmic expression of nanobodies allowed us to design elaborate tags and fusion modules for novel applications. Nanobodies with protease-cleavable affinity tags containing long interspersed unfolded linkers enabled highly efficient affinity capture followed by specific proteolytic release under physiological conditions (Figure 3.12). In contrast to peptide elution that is not applicable to the vast majority of nanobodies, due to their preference for folded epitopes, the SUMOStar protease strategy should work for every nanobody. Native isolation of protein A-tagged protein complexes using a specific nanobody modified with a dithiothreitol (DTT)-cleavable crosslinker (Fridy et al., 2015) achieved only modest yields. The presence of any thiol-reducing agent (like DTT or glutathion) during binding is incompatible with this method. Our protease strategy, however, reproducibly led to a near quantitative release of the purified material (Figure 3.13 a).



Importantly, nanobodies against a single epitope of a larger protein complex now allow a native single-step purification of the entire complex, and thus a subsequent structural and functional analysis (Figure 3.14). This is especially useful for complexes that are not directly accessible to recombinant production. Furthermore, nanobody-purified endogenous complexes can be used as antigens for another round of immunization, and binders against all complex components can then be selected from the successive nanobody library. This was successfully demonstrated for the *Xenopus* Nup107 complex (Figure 3.30). Certainly, even more complex antigens could be envisaged. An obvious next step would be the immunization of whole nuclear envelopes or annulate lamellae containing densely packed NPCs and associated proteins. Entire vesicles or organelles could be immunized to generate sub-proteome immune libraries that can be searched for binders to all individual components. Mapping epitopes via crosslinking mass spectrometry will become especially important when selecting nanobodies against such complex antigens that cannot be made recombinantly.

For direct structural analysis of natively isolated protein complexes by electron microscopy (EM) the used nanobody could be fused to an additional high affinity tag. After native elution of the bound protein complex the binding partner of this high affinity tag could be an EM marker itself (Flemming et al., 2010) or be fused to a very small gold grain. This would enable a raw mapping of the nanobody target protein location within a larger complex just by spotting the additional mass density.

Functional biochemical assays with natively isolated proteins that are very hard to express recombinantly could also be envisaged. Chaperonins like the TRiC complex could be used for *in vitro* folding assays or mitotic kinases for *in vitro* phosphorylation or mitotic disassembly assays. A pre-requisite would only be the availability of soluble small fragments of these proteins for immunizations.

#### **4.2.2 Reliable fluorescent labeling of nanobodies**

We introduced a method for a reliable & site-specific fluorescent labeling of nanobodies using engineered surface cysteines and maleimide chemistry. We obtained well-behaved imaging reagents that could effectively position fluorescent dyes as close as 1-2 nm to their targets. Maleimide-labeled nanobodies consistently recognized their antigens far better and produced less background than the corresponding NHS-modified



variants. Our sequence analysis revealed that nearly every third nanobody possesses at least one lysine residue in its CDR regions that is likely involved in antigen recognition. We predict that most of such nanobodies will actually be inactivated by NHS modification, as shown for the anti-Nup93 nanobody TP179 (Figure 3.21 d). All other nanobodies that were labeled only via framework lysine residues showed high background staining - pointing to a systematic problem.

What could be the reason for their poor performance in fluorescence microscopy? One possibility could be isoelectric precipitation since NHS modification leads to the formation of an uncharged amide bond between a formerly positively charged  $\epsilon$ -amino group of a lysine residue and the fluorescent dye, thus decreasing the net surface charge. Alternatively, framework lysines residues could be involved in extended hydrogen bond networks on the surface of VHH domains thus contributing to their overall solubility. Inspection of many nanobody crystal structures from the PDB, however, revealed that is not the case. Interestingly, most framework lysines are located on the C-terminal side of the VHH domain. In conventional VH domains, this region is part of the hydrophobic VH-CH1 domain interface. The introduction of hydrophilic mutations at this former interface was shown to dramatically increase the yield of an scFv fragment and this was attributed to a lower aggregation potential (Nieba et al., 1997). Some but not all VHH germline genes have acquired similar mutations (Muyldermans et al., 1994; Vu et al., 1997; Harmsen et al., 2000). Since VHH genes likely evolved from pre-existing VH genes (Achour et al., 2008) it is possible that the former VH-CH1 interface is still a potential aggregation hot spot of nanobodies. Abolishing surface charges in this region could thus create extended hydrophobic patches that cause the observed unspecific binding. This could actually be tested by modification of different nanobodies with small amine-reactive chemicals like succinic anhydride in different molar ratios. Any resulting aggregation could be measured e.g. by dynamic light scattering. Furthermore, it would be interesting to see if a well-performing maleimide-labeled nanobody could be induced to cause similar background staining in fluorescence imaging as its NHS-labeled variant by additional modification of its lysines with succinic anhydride.

Our method for fluorescent nanobody labeling relies on site-specifically placed surface cysteines. For this, we exclusively chose amino acids in the  $\beta$ -sheet of the Ig-fold that is opposite to the sheet that formerly constituted the VH-VL interface. In VHH domains



the VH-VL interface is mutated and often the long CDR III loop folds back onto this side and is stabilized there by hydrophobic contacts. Many nanobodies bind their target exclusively with CDR III in this configuration (Desmyter et al., 2001). We therefore did not introduce cysteines on this side of nanobodies. Some nanobodies, however, use all three CDRs to bind their target. From the multitude of possible nanobody-antigen interfaces, it cannot be excluded that fluorescent dyes attached close to the CDR regions interfere with antigen recognition. In such rare cases positions on the C-terminal side of a nanobody should be tested.

Expression of nanobodies with (multiple) engineered surface cysteines in the reductive cytosol of *E. coli* did not cause any folding problems or significant reduction in yield, as observed for periplasmic expression before (Massa et al., 2014). Importantly, the internal cysteines of reduced nanobodies cannot be modified at low temperatures making our approach an orthogonal labeling strategy. At room temperature only minute amounts of the two nanobodies we tested got modified. The extent of modification seemed to correlate with the nanobody's thermostability, indicating that there was 'thermal breathing' of the nanobody scaffold that led to transient accessibility of the internal cysteines.

Labeling of the engineered surface cysteines was also very quantitative even when just stoichiometric amounts of labeling reagent were added. In contrast, NHS esters react not only with amino groups, but also rapidly hydrolyze in aqueous buffers. This makes it difficult to adjust labeling densities and requires addition in substantial molar excess. Site-specific and quantitative fluorescent labeling of nanobodies is going to be crucial for super-resolution microscopy aiming at detailed structural analyses or determination of absolute protein copy numbers. It also allows predicting the effective label displacement, a fact that will be especially important when applying particle averaging techniques to localization microscopy data (Szyzborska et al., 2013). Because of its well-defined dimension and symmetric structure, the NPC has become a benchmark for many new advancements of super-resolution microscopy (Schermelleh et al., 2008; Szyzborska et al., 2013; Göttfert et al., 2013). The anti-NPC nanobodies described here excelled in super-resolution imaging; they can be renewably produced in high yields and are therefore ideal labeling reagents for such benchmark studies.



### 4.2.3 Mapping conformational epitopes via crosslinking mass spectrometry

While the ability to generate large arrays of recombinant antibodies to diverse antigens is growing steadily (Schofield et al., 2007; Colwill et al., 2011; Marcon et al., 2015), technologies to rapidly characterize their binding sites are lagging behind.

Conventional antibodies and derived fragments often bind linear epitopes that can be mapped with libraries of overlapping synthetic peptides that cover the entire target protein sequence (Stadler et al., 2008). Due to their unique paratope structure, nanobodies prefer conformational epitopes that are notoriously hard to map. In case the targeted antigen is a single protein, its truncation can give raw information about the contacted domain. Domain boundaries are, however, hard to map precisely and truncation often leads to misfolding. Furthermore, nanobodies are often raised against multi-protein complexes and can thus interact with different proteins at the same time (Chug et al., 2015), making a truncation analysis very difficult. Another approach that was for example used to map conformational epitopes of multiple monoclonal antibodies on GPCRs (Paes et al., 2009) is shotgun mutagenesis of the target. This requires the laborious construction of mutant libraries that cover the entire protein sequence. Further it needs to be controlled if these mutations abolish antibody binding or actually cause misfolding of the target in the first place. Certainly, the gold standard of epitope mapping is co-crystallization with the target (Desmyter et al., 2015). This is very time-consuming and challenging especially when working with larger multi-domain proteins or multi-protein complexes. Binding sites can also be mapped by NMR (see e.g. Fridy et al., 2014), but this is still limited to small proteins.

The epitope mapping approach introduced in this study does not rely on laborious antigen manipulation and instead relies on nanobodies with engineered cysteines that can be crosslinked to their target. These cysteines are already introduced during the initial characterization workflow since they are also useful for site-specific fluorescent labeling. The minimal preparations needed for crosslinking experiments thus should aid in achieving a higher throughput in epitope mapping. The technique relies on the availability of NHS-reactive lysine residues on the antigen that are close to the site-specifically placed cysteine on the nanobody. These lysines have to be in reach of the used heterobifunctional crosslinker. It is evident that the shortest working crosslinker gives the highest resolution, however, in some cases no reactive lysines are



in reach and longer crosslinkers might have to be tested. The pH value might also be varied to modulate crosslinking efficiency. The crosslinked lysines residues are not part of the actual nanobody binding site but are rather surrounding it. It is thus best to delineate a likely contacted surface region.

A common problem with the identification of bulky and long crosslinked peptides is their slow elution from gel pieces and their stickiness to the reverse phase columns used for LC-MS/MS. An interesting extension of the presented strategy would be to include a small His<sub>6</sub>-tag in the same tryptic peptide as the cysteine used for crosslinking. The crosslinked peptides could then be enriched on Ni<sup>2+</sup>-beads after in-solution digestion. All unrelated peptides could be washed away and then the crosslinks could be eluted under acidic conditions in a volatile buffer like acetonitrile. Such elution fraction could be directly applied to a mass spectrometer for mass fingerprinting and therefore gel extraction and column purification be avoided. Using magnetic Ni<sup>2+</sup>-beads and a 96-well format this approach could represent a general high throughput epitope mapping strategy applicable to conformational epitopes on complex antigens.

### 4.3 Exploration of the anti-Nup nanobody toolbox

In this study, we generated a large array of nanobodies that can be used to study the structure, function and assembly of the *Xenopus* nuclear pore complex (Figure 3.26). On the example of anti-Nup98 nanobodies, we illustrated how the anti-Nup nanobody toolbox could be screened for binders that inhibit protein-protein interactions critical for the assembly of functional NPCs. Such binders might trap novel NPC assembly intermediates for structural and mechanistic analyses. Anti-Nup98 nanobody TP373 blocked the C-terminal Nup98 NPC anchor domain and thus significantly decreased Nup98 NPC incorporation. A complete inhibition could not be observed, probably because multiple weak interactions contribute to efficient NPC anchorage (Yoshida et al., 2011; Fischer et al., 2015). Therefore, multiple nanobodies against the same or different targets should also be pooled and analyzed for combinatorial effects. NPC assembly defects can easily be identified via transport assays and defective nuclei then analyzed for protein content. For this, fluorescent nanobodies targeting all major Nups can simply be added after NPC assembly or even co-incorporated during NPC assembly. A potential drawback might be that true interface-blocking nanobodies are



likely rare due to the higher conservation and hence lower immunogenicity of such epitopes.

A crucial role of post-translational modifications like phosphorylation in the regulation of NPC disassembly at the onset of mitosis is emerging (Macaulay et al., 1995; Favreau et al., 1996; Glavy et al., 2007; Laurell et al., 2011; Bui et al., 2013). The anti-Nup nanobody toolbox can be used to purify nearly all Nups from an NPC assembly-competent 'interphase'-like extract and also from a 'mitotic' CSF-arrested extract in high yields (Figure 3.35). We aim to identify and compare Nup phosphorylation sites that are cell cycle state-specific to gain a deeper mechanistic understanding of NPC (dis)assembly. Our nanobodies could also be used to purify intact NPCs from *Xenopus* oocytes. This could enable a comparison of the modification pattern of Nups in an assembled and disassembled state.

A very intriguing question is how soluble subcomplexes are triggered to interact and oligomerize at the end of mitosis to form entire NPCs. We are now able to purify these large subcomplexes under native conditions and in high yields. It would be interesting to test whether they can be induced to form ring-like assemblies e.g. if all relevant weak multivalent interaction partners are provided or phosphatases that remove putative inhibitory phosphorylations are added. Can subcomplexes oligomerize in the absence of a membrane template?

The overall structure of the NPC scaffold will likely be solved in the near future by cryo-electron tomography (Bui et al., 2013; Eibauer et al., 2015; von Appen et al., 2015). However, the structure of the permeability barrier that is built up from non-globular FG repeat domains can likely not be studied by this approach. Structural analysis by super-resolution microscopy could provide important complementary information. The nanobodies we produced could be used to precisely map the location of Nups and especially FG repeat Nup anchor points within the NPC. Powerful 3D STORM setups required for such analyses were already developed (Huang et al., 2008) and are currently being optimized to achieve higher z-axis resolution. In combination with FG repeat-specific peptide-binding nanobodies this technique could even clarify the structural organization of the NPC permeability barrier and thus settle a long-standing debate in the field of nucleocytoplasmic transport (Schmidt and Görlich, 2016).



## 5 Materials

### 5.1 Reagents

General laboratory reagents were purchased from the following companies: AppliChem (Germany), Calbiochem (USA), Life Technologies (USA), Merck (Germany), New England Biolabs (USA), Serva (Germany), Promega (USA), Roche (Germany), Roth (Germany) and Sigma-Aldrich (USA).

Specific reagents are listed in the following tables:

**Table 5.1** Reagents used for nanobody discovery & characterization

Reagent	Purpose	Supplier
Squalen	Immunization adjuvant	Sigma-Aldrich, USA
$\alpha$ -tocopherol	Immunization adjuvant	Sigma-Aldrich, USA
Tween-80	Immunization adjuvant	Sigma-Aldrich, USA
Adjuvant peptide (Muramyl dipeptide)	Immunostimulant	Sigma-Aldrich, USA
Poly(I:C)	Immunostimulant	Invivogen, USA
Phenol, crystalline, >99.5%	RNA preparation	Sigma-Aldrich, USA
Guanidine thiocyanate	RNA preparation	Sigma-Aldrich, USA
Sodium N-lauroyl sarcosinate	RNA preparation	Sigma-Aldrich, USA
RNA Storage Solution	RNA preparation	Thermo Scientific, USA
SUPERase <sup>•</sup> In	RNA preparation	Thermo Scientific, USA
Nuclease-free water	RNA preparation	Thermo Scientific, USA
RNase-free Microfuge Tubes	RNA preparation	Thermo Scientific, USA
RNaseZap RNase Decontamination Wipes	RNA preparation	Thermo Scientific, USA
ssRNA ladder	RNA quality control	New England Biolabs, USA
PEG-8000	Phage precipitation	Sigma-Aldrich, USA
anti-pIII monoclonal antibody	Phage Western blot	New England Biolabs, USA
Dynabeads MyOne Streptavidin T1	Phage display & nanobody pulldowns	Thermo Scientific, USA
Biotin-PEG-COOH	Blocking Streptavidin beads	Iris Biotech, Germany
Biotin-dPEG(23)-mal	Cysteine modification	Iris Biotech, Germany
Sypro Orange dye	Thermofluor analysis	Sigma-Aldrich, USA
Urea	Nanobody unfolding	Sigma-Aldrich, USA
Guanidine hydrochloride	Nanobody unfolding	Sigma-Aldrich, USA

**Table 5.2** Reagents used for *Xenopus* egg extract methods

Reagent	Purpose	Supplier
Chorionic gonadotropin	Induction of egg laying	Sigma-Aldrich, USA
L-Cysteine	Dejellering	Roth, Germany
A23187 Ca <sup>2+</sup> ionophore	Egg activation	Sigma-Aldrich, USA



Cytochalasin B	Actin polymerization inhibitor	Calbiochem, USA
Cycloheximide	Translation inhibitor	Sigma-Aldrich, USA
Aprotinin	Protease inhibitor	Calbiochem, USA
Leupeptin	Protease inhibitor	Calbiochem, USA
Elastatinal	Protease inhibitor	Calbiochem, USA
Chymostatin	Protease inhibitor	Calbiochem, USA
Pepstatin A	Protease inhibitor	Calbiochem, USA
E-64	Protease inhibitor	Sigma-Aldrich, USA
Z-VAD-FMK	Caspase inhibitor	Calbiochem, USA
creatine phosphate	Energy mix	Sigma-Aldrich, USA
creatine kinase	Energy mix	Sigma-Aldrich, USA
ATP	Energy mix	Sigma-Aldrich, USA
GTP	Energy mix	Sigma-Aldrich, USA

**Table 5.3** Reagents used for fluorescence microscopy

Reagent	Purpose	Supplier
Fetal bovine serum	Cell culture	Pan-Biotech GmbH, Germany
DMEM high glucose medium + pyruvate + glutamine	Cell culture	Sigma-Aldrich, USA
Penicillin + Streptomycin	Cell culture	Thermo Scientific, USA
Trypsin/EDTA	Cell culture	Thermo Scientific, USA
Paraformaldehyde (PFA)	Immunofluorescence	Riedel-de-Häen, Germany
Triton X-100	Immunofluorescence	AppliChem, Germany
Digitonin, High Purity	Immunofluorescence	Calbiochem USA
Borane dimethylamine complex	Immunofluorescence	Sigma-Aldrich, USA
$\beta$ -mercaptoethanol	Reduction agent	Roth, Germany
DTT	Reduction agent	Enzo Life Sciences, Germany
TCEP	Reduction agent	Thermo Scientific, USA
Alexa Fluor 647 C2 maleimide	Fluorescent labeling	Life Technologies, USA
Alexa Fluor 488 C5 maleimide	Fluorescent labeling	Life Technologies, USA
Alexa Fluor 647 NHS ester	Fluorescent labeling	Life Technologies, USA
Abberior Star Red (KK114)	Fluorescent labeling	Dr. Vladimir Belov
DAPI	DNA staining	
$\beta$ -mercaptoethylamine	STORM switching buffer	Sigma-Aldrich, USA
Glucose oxidase	STORM switching buffer	Sigma-Aldrich, USA
Catalase	STORM switching buffer	Sigma-Aldrich, USA
SlowFade Gold Antifade Mountant	Mounting medium	Thermo Scientific, USA
SlowFade Diamond Antifade Mountant	Mounting medium	Thermo Scientific, USA
Multitest slide (10 well, 8 mm diameter, PTFE coating)	Sample mounting	MP Biomedicals, USA
Microscope cover slides, 24x60 mm	Sample mounting	Thermo Scientific, USA
Microscope cover glasses, round 12 mm diameter, 1.5 mm thick	Sample mounting	Thermo Scientific, USA
Microscope glass slides 76x26x1 mm	Sample mounting	Thermo Scientific, USA



## 5.2 Buffers and solutions

**Table 5.4** DNA/RNA buffers and solutions

<b>Solution</b>	<b>Composition</b>
Orange G sample buffer	10 mM Tris-HCl (pH 8.0), 10 mM EDTA (pH 8.0), 50 % (w/v) glycerin and 25 % (w/v) Orange G
TAE buffer (50x)	242 g Tris base, 57.1 ml acetic acid, and 100 ml 0.5 M EDTA (pH = 8.0) in 1 l H <sub>2</sub> O
Ethidium bromide	20 mg/ml ethidium bromide in water
T4 DNA Ligase buffer (10x)	500 mM Tris (pH 7.5), 100 mM MgCl <sub>2</sub> , 100 mM DTT, 10 mM ATP and 250 µg/ml BSA
Phusion HF buffer (5x)	Thermo Scientific, USA
PfuS Triple Mix (100x)	Self-made mixture containing 100 ng/µl PfuS polymerase, 15 ng/µl pyrophosphatase, and 6 ng/µl dUTPase
dNTPs (10x)	2.5 mM of each desoxynucleotide in ddH <sub>2</sub> O
Gibson Assembly mix (2x)	Self-made mixture containing 5' Exonuclease, DNA polymerase and DNA ligase
SSo Advanced SYBR Green Supermix (2x)	Bio-Rad Laboratories Inc., USA
DNA ladder	GeneRuler 1 kb Plus (Thermo Scientific, USA)
RNA Storage Solution	1 mM sodium citrate, pH 6.4 + 35 U SUPERase-In
Solution D	4 M GuSCN, 25 mM sodium citrate, pH 7.0, 0.5 % (w/v) sarkosyl, 50 mM DTT
Blood dilution buffer	1xPBS, 0,4 % glucose, 25 mM EDTA

**Table 5.5** Protein buffers and solutions

<b>Solution</b>	<b>Composition</b>
SDS sample buffer	3 % SDS, 125 mM Tris/HCl (pH 6.8), 50 mM DTT, 1 M saccharose, bromphenolblue
Protein ladder (SDS-PAGE)	PageRuler Unstained (Thermo Scientific, USA)
Protein ladder (Western Blot)	PageRuler Plus Prestained (Thermo Scientific, USA)
SDS-running buffer (10x)	150 g glycine, 30 g Tris base, and ddH <sub>2</sub> O to 1 l volume
Coomassie staining solution	2 % w/v Coomassie Brilliant Blue G250 in 50 % ethanol
Amido Black staining solution	0.2 % (w/v) Amido Black in 2 % acetic acid
1xPBS	137 mM NaCl, 2.7 mM KCl, 8.1 mM Na <sub>2</sub> HPO <sub>4</sub> , 1.76 mM KH <sub>2</sub> PO <sub>4</sub>
Biotinylation buffer (5x)	250 mM Tris/HCl pH 7.5, 500 mM NaCl, 50 mM ATP, 62.5mM MgCl <sub>2</sub> , 1.25 mM biotin
Protein resuspension buffer	50 mM Tris/HCl pH 7.5, 150-500 mM NaCl, 2-20 mM imidazole, 0-5 mM DTT
Osmo-shock buffer	200 mM Tris/HCl pH 8.0, 500 mM sucrose, 5 mM EDTA pH 8.0
Ni <sup>2+</sup> -elution buffer	50 mM Tris/HCl pH 7.5, 150-500 mM NaCl, 500 mM imidazole, 250 mM sucrose, 0-5 mM DTT
Antigen physiological buffer	20 mM Tris/HCl pH 7.5, 150 mM NaCl, 250 mM sorbitol
AS03 Plus adjuvant	Per dose: 22 mg squalen, 24 mg α-tocopherol, 10 mg Tween-80, 10 µg monophosphoryl lipid A
Phage precipitation buffer	20 % PEG 8000, 2.5 M NaCl
Wash & Block buffer (WBB)	50 mM Tris/HCl pH 7.5, 300 mM NaCl, 0.1 % (w/v) BSA

**Table 5.6** Buffers and solutions for *Xenopus* egg extract methods

Solution	Composition
S250 buffer	20 mM HEPES pH 7.5, 90 mM KAc, 2 mM MgAc, 250 mM sucrose
Marc's Modified Ringers (MMR) buffer (10x)	50 mM HEPES/KOH pH 7.8, 1 M NaCl, 20 mM KCl, 10 mM MgCl <sub>2</sub> , 20 mM CaCl <sub>2</sub> , 1 mM EDTA
Dejelling solution	165 mM L-cysteine pH 7.8 in 0.25x MMR buffer
Protease-inhibitor mix (500x)	5 mg/ml aprotinin, 5 mg/ml leupeptin, 2.5 mg/ml elastatinal, 2.5 mg/ml chymostatin, 0.5 mg/ml pepstatin A
E-mix (20x)	20 mM HEPES/KOH pH 7.5, 200 mM creatine phosphate, 10 mM ATP, 10 mM GTP, 1 mg/ml creatine kinase, 250 mM sucrose
XB buffer	10 mM Hepes/KOH pH 7.7, 100 mM KCl, 0.1 mM CaCl <sub>2</sub> , 1 mM MgCl <sub>2</sub> , 50 mM sucrose
CSF-XB buffer	1x XB buffer + 1 mM MgCl <sub>2</sub> + 5 mM EGTA
Spindle fix solution	1x MMR, 48% (v/v) glycerol, 11% (w/v) formaldehyde

**Table 5.7** Buffers and solutions for fluorescence microscopy

Solution	Composition
<i>Xenopus</i> cell culture medium	25 % (v/v) water, 10 % (w/v) fetal bovine serum, 65 % DMEM high glucose medium + pyruvate + glutamine, 50 U/ml Penicillin + 50 µg/ml Streptomycin
NHS labeling buffer	100 mM sodium bicarbonate pH 7.8, 300 mM NaCl
Maleimide labeling buffer	100 mM potassium phosphate pH 6.4, 150 mM NaCl, 1 mM EDTA, 250 mM sucrose
Transport buffer (TRB)	20 mM HEPES pH 7.5, 5 mM MgAc, 110 mM KAc, 1 mM EGTA, 250 mM sucrose
Digitonin permabilization buffer	25 µg/ml digitonin in TRB
MEA imaging buffer (STORM)	50 mM Tris-HCl pH 8.0, 10 mM NaCl, 10 % glucose (w/v), 10 mM β-mercaptoethylamine pH 8.5, 0.5 mg/ml glucose oxidase, 40 µg/ml

### 5.3 E. coli strains and media

**Table 5.8** Media for *E. coli* growth

Solution	Composition
TB liquid medium	12 g tryptone, 24 g yeast extract, 0.4% (v/v) glycerol, 72mM K <sub>2</sub> HPO <sub>4</sub> , 17mM KH <sub>2</sub> PO <sub>4</sub>
2YT liquid medium	16 g tryptone, 10 g yeast extract, and 5 g NaCl, and H <sub>2</sub> O to 1 l
LB liquid medium	10 g tryptone, 5 g yeast extract, and 10 g NaCl, and H <sub>2</sub> O to 1 l
SOB liquid medium	20 g tryptone, 5 g yeast extract, 10 mM NaCl, 2.5 mM KCl, 10 mM MgCl, 10 mM MgSO <sub>4</sub> , and H <sub>2</sub> O to 1 l
Agar plates	2YT liquid medium + 15 g/l agar

All media were autoclaved before use. LB and 2YT medium were supplemented with 2 % (v/v) glycerol and 20 mM K<sub>2</sub>HPO<sub>4</sub> for bacterial culture. The following antibiotics were used in this study and added at the given concentration to the culture medium (Table 5.9).

**Table 5.9** Antibiotics for *E. coli* culture

Antibiotic	Final concentration	Solvent for 1000x stock solution
Ampicillin (Amp)	100 µg/ml	70 % v/v ethanol in water
Kanamycin (Kan)	25 µg/ml	Water
Spectinomycin (Spec)	100 µg/ml	Water
Trimethoprim (Tmp)	10 µg/ml	70 % v/v ethanol in water

The following *E. coli* strains were used in this study (Table 5.10).

**Table 5.10** *E. coli* strains used in this study

Strain	Purpose	Genotype	Supplier
5-alpha	cloning	<i>fhuA2 Δ(argF-lacZ)U169 phoA glnV44 Φ80 Δ(lacZ)M15 gyrA96 recA1 relA1 endA1 thi-1 hsdR17</i>	New England Biolabs, USA
10-beta	cloning	<i>Δ(ara-leu) 7697 araD139 fhuA ΔlacX74 galK16 galE15 e14-φ80dlacZΔM15 recA1 relA1 endA1 nupG rpsL (Str<sup>R</sup>) rph spoT1 Δ(mrr-hsdRMS-mcrBC)</i>	New England Biolabs, USA
BLR	protein expression	<i>F<sup>-</sup> ompT gal dcm hsdS<sub>B</sub>(r<sub>K</sub><sup>-</sup>m<sub>B</sub><sup>-</sup>) Δ(srl-recA)306::Tn10(Tet<sup>R</sup>)</i>	Novagen, USA
NEB express	protein expression	<i>fhuA2 [lon] ompT gal sulA11 R(mcr-73::miniTn10--Tet<sup>S</sup>)2 [dcm] R(zgb-210::Tn10--Tet<sup>S</sup>) endA1 Δ(mcrC-mrr)114::IS10</i>	New England Biolabs, USA
TG1	phage display	<i>[F<sup>+</sup>] traD36 proAB lacIqZ ΔM15] supE thi-1 Δ(lac-proAB) Δ(mcrB-hsdSM)5(rK - mK -)</i>	Lucigen, USA
SS320	phage display	<i>[F<sup>+</sup>]proAB+lacIqlacZΔM15 Tn10 (tet<sup>r</sup>) hsdR mcrB araD139 Δ(araABC-leu)7679ΔlacX74 galUgalK rpsL thi</i>	Lucigen, USA

## 5.4 Lab equipment

**Table 5.11** Technical lab equipment

Instrument	Manufacturer
Analytical scale	Sartorius, Germany
Arium® Pro UV ultrapure water system	Sartorius, Germany
Agilent 2100 Bioanalyzer	Agilent Technologies, USA
Centrifuges	
Eppendorf 5415R and 5424 tabletop centrifuges	Eppendorf, Germany
Multifuge 3L-R	Heraeus, Germany
Sorval RC6+ centrifuge	Sorvall/Thermo Scientific, USA
Sorval Lynx 6000	Sorvall/Thermo Scientific, USA
Sorval Wx Ultra ultracentrifuge	Sorvall/Thermo Scientific, USA
Discovery M120 SE ultracentrifuge	Sorvall/Thermo Scientific, USA
CFX96 Touch™ Real-Time PCR Detection system	Bio-Rad Laboratories Inc., USA
MicroPulser™ electroporation apparatus	Bio-Rad Laboratories Inc., USA
NanoDrop 2000c	PeqLab, Germany
Thermomixer comfort	Eppendorf, Germany
Epson Perfection V700 Photo scanner	Epson, Japan
Sonifier 450	Branson Ultrasonics, UK
Odyssey infrared imaging system	LI-COR Biosciences, USA
Eppendorf Biophotometer	Eppendorf, Germany
Incubator/ Climo-Shaker ISF1-X	Adolf Kühner AG, Switzerland
TCS SP5 confocal laser scanning	Leica, Germany



microscope	
M165C stereo microscope	Leica, Germany
Cell culture hood Herasafe	Thermo Scientific, USA
CO <sub>2</sub> Incubator C200	Labotect, Germany
Thermocycler	SensoQuest, Germany
DNA gel documentation system	Vilber Lourmat, Switzerland
Äkta Purifier + Äkta Explorer	Pharmacia, Sweden
CM200 FEG transmission electron microscope	Phillips, Netherlands
UltiMate™ 3000 RSLCnano system	Thermo Scientific, USA

## 5.5 Software & Online tools

**Table 5.12** Software used in this study

Software	Developer
Adobe Illustrator + Photoshop CS5.1	Adobe Systems Inc., USA
Microsoft Excel for Mac 2011	Microsoft Corp., USA
MacPyMol 1.7.4.1	Schrödinger LLC, USA
UCSF Chimera 1.10.1	Resource for Biocomputing, Visualization, and Informatics, UCSF, USA
CFX Manager™ 3.1.1517.0823	Bio-Rad Laboratories Inc., USA
Odyssey 3.0.30	LI-COR Biosciences, USA
Oligo 7.58	Molecular Biology Insights Inc., USA
SeqBuilder; Protean; MegAlign; SeqMan; Gene Quest – all version 11.2.1	DNASTAR, USA
Gene Designer 2.0	DNA2.0, USA
Scaffold 4	Proteome Software, USA
Rockmaker	Formulatrix, USA
LASAF	Leica, Germany
Virtual Box	Oracle Corp., USA
UNICORN 5.0	Amersham Biosciences, Sweden
Bookends	Sonny Software, USA
Python 2.7.10	Python Software Foundation
Mac OS X Yosemite Vers.10.10.5	Apple, USA

**Table 5.13** Online tools used in this study

Tool	Website
International Immunogenetics Information System	<a href="http://www.imgt.org">http://www.imgt.org</a>
BLAST	<a href="http://blast.ncbi.nlm.nih.gov/Blast.cgi">http://blast.ncbi.nlm.nih.gov/Blast.cgi</a>
ClustalW	<a href="http://ebi.ac.uk/Tools/msa/clustalw2">http://ebi.ac.uk/Tools/msa/clustalw2</a>
Uniprot	<a href="http://uniprot.org">http://uniprot.org</a>
PsiPred	<a href="http://bioinf.cs.ucl.ac.uk/psipred">http://bioinf.cs.ucl.ac.uk/psipred</a>
I-Tasser	<a href="http://zhanglab.ccmb.med.umich.edu/I-TASSER/">http://zhanglab.ccmb.med.umich.edu/I-TASSER/</a>
Protein Data Bank	<a href="http://rcsb.org/pdb">http://rcsb.org/pdb</a>
OligoAnalyzer 3.1	<a href="http://eu.idtdna.com/calc/analyzer">http://eu.idtdna.com/calc/analyzer</a>



## 6 Methods

### 6.1 Standard methods in molecular biology

#### 6.1.1 Production of electro-competent *E. coli* cells

All homemade electro-competent cells were produced by Gabriele Hawlitschek and Uwe Hoffmann. Pre-cultures of bacterial strains were grown in liquid SOB medium, supplemented with the appropriate antibiotics, at 37°C over night. After dilution with pre-warmed SOB medium the pre-cultures were further incubated at 37°C until an OD<sub>600</sub> of 0.8 was reached. Bacteria were pelleted at 3,500 rpm for 10 min at 4°C (RC6 plus centrifuge, F10 rotor; Sorvall, USA) and the supernatant carefully removed. The cells were then resuspended in 10 ml 1.4 % (w/v) glycerol, centrifuged and washed once more under the same conditions. Finally, the cells were resuspended in 14 % (w/v) glycerol, aliquoted, snap-frozen in liquid nitrogen and stored at -80°C until further use.

#### 6.1.2 Transformation of *E. coli* cells by electroporation

For a standard transformation, 50 ng plasmid DNA were mixed with 40 µl of electro-competent *E. coli* cells in an electroporation cuvette (Biorad, Hercules, CA, USA) on ice. Electroporation was performed using a GenePulser (BioRad, Burlington, USA) according to the manufacturer's instruction. For recovery, 1 ml of 2YT medium containing 0.5 % (w/v) glucose was added and the cells were incubated for 1 h at 37°C while shaking. Subsequently, the cells were plated on agar plates containing the appropriate antibiotic(s) and incubated over night at 37°C for selection of transformants. Agar plates containing successfully transformed *E. coli* cells were used to pick single colonies for the inoculation of cultures for plasmid DNA preparation or for protein expression pre-cultures.

#### 6.1.3 DNA purification from *E. coli* cultures and concentration determination

Plasmid DNA was either prepared in an analytical scale ('Mini-prep') using the NucleoSpin Plasmid Kit (Marcherey Nagel, Germany) or in a preparative scale ('Midi-prep') using the NucleoBond PC100 Kit (Marcherey Nagel, Germany), in each case according to the manufacturer's instructions. DNA concentrations were determined using a NanoDrop 2000C spectrophotometer (PeqLab, Germany).



#### **6.1.4 Agarose gel electrophoresis**

Agarose gel electrophoresis was used for the separation and purification of double-stranded DNA fragments (e.g. after restriction digests or PCR products) as described (Sambrook et al., 1989). Agarose concentration varied between 0.8-1.5% (w/v) in 1xTAE buffer depending on the size of the fragments to be separated. In order to visualize DNA, 3  $\mu$ l of 20 mg/ml ethidium bromide were added to 100 ml of molten agarose gel. DNA samples were treated with at least 1/10 volume Orange G sample buffer prior to loading. Agarose gels were run in 1xTAE buffer using a Consort EV233 power supplier (Sigma-Aldrich, Germany).

#### **6.1.5 DNA purification from agarose gels**

DNA fragments from agarose gels were isolated using the Zymoclean Gel DNA recovery kit (Zymo Research CA, USA) according to the manufacturer's instructions. DNA concentrations were determined as described in 6.1.3.

#### **6.1.6 DNA restriction digest and dephosphorylation**

All restriction endonucleases and restriction buffers were purchased from NEB (New England Biolabs, USA). Typical restriction digests were carried out for 2 h at 37°C using around 5 Units of enzyme per  $\mu$ g DNA in the enzyme's respective restriction buffers. In case the plasmid backbone represented the desired restriction fragment, an additional dephosphorylation step was included. For this, 2  $\mu$ l of 1 Unit/ $\mu$ l FastAP (alkaline phosphatase) (Thermo Scientific, USA) was added directly to the restriction digest and incubated for 30 min at 37°C. The reactions were stopped by addition of Orange G sample buffer and the obtained DNA fragments purified by agarose gel electrophoresis (as described in 6.1.4).

#### **6.1.7 DNA ligation**

DNA ligations were performed using the purified enzyme T4 DNA Ligase (prepared in the lab). For a standard ligation reaction 100 ng of restriction digested and dephosphorylated plasmid DNA fragment were pre-incubated with a two-fold molar excess of insert DNA fragment in a minimal volume. Then, an equal volume of a 2x ligation mix (2x T4 DNA ligase in 2x T4 DNA ligase buffer) was added and the reaction further incubated for 30 min at 37°C for sticky-end ligations or at 16°C over



night for blunt-end ligations. As a negative control, no insert and no T4 DNA Ligase reactions were set up in parallel. Ligation reactions were then heat-inactivated for 10 min at 70°C. 1 µl of a heat-inactivated ligation reaction was then used to transform electro-competent *E. coli* cells by electroporation.

### 6.1.8 Polymerase chain reaction (PCR)

PCR was used to amplify defined DNA fragments from a DNA template. Restriction sites or Gibson assembly overhangs for the subsequent cloning of amplified DNA fragments were introduced to the 5' overhangs of the used primers. For the PCR reactions a 'PfuS Triple Mix' (prepared in the lab) was used, containing PfuS polymerase, pyrophosphatase and dUTPase. A 100 µl PCR reaction typically contained 50 ng template DNA, 1 µl PfuS Tripple Mix, 5 µl (100 % v/v) DMSO, 1 µl (100 µM) each of forward and reverse primer, 5 µl of 10x dNTPs (2.5 mM each), 20 µl of 5x Phusion HF buffer (Thermo Scientific, USA) and the appropriate volume of ddH<sub>2</sub>O to add up to 100 µl. PCR reactions were run using a SensoQuest Lab Cyclor (SensoQuest GmbH, Göttingen, Germany) with the following program: (1) initial denaturation at 98.5°C for 2 min, (2) denaturation at 98.5°C for 30 sec, (3) annealing at 58-62°C for 30 sec, (4) elongation at 72°C for 30 sec per 1 kb of PCR product length and (5) final extension at 72°C for 2 min. Steps (2)-(4) were repeated 25-30 times. The annealing temperature was calculated using the primer design software SeqBuilder (DNASar, USA).

### 6.1.9 Blunt-end mutagenesis PCR

For mutagenesis PCR, oligonucleotides were designed that introduced the desired type of mutation and amplified the whole vector starting from the mutation site. These oligonucleotides were ordered with a 5'-phosphoryl group to allow for a later blunt-end ligation of the PCR product. The PCR reaction was performed as described in 4.1.5. PCR products were purified using the MSB spin PCRapace kit (Stratatec, Germany) and treated with *DpnI* for 2 h at 37°C to digest the non-mutated template DNA. The digestion reaction was gel purified and 250 ng linear PCR product was then ligated overnight at 16°C (as described in 6.1.7). The ligation reaction was then diluted to 8 ng/µl and 1 µl was used to transform 40 µl electro-competent *E. coli* cells.



### 6.1.10 Gibson assembly

Gibson assembly (Gibson et al., 2009; Gibson, 2011) enables a single-step joining of (multiple) double-stranded DNA fragments carrying complementary overhangs of 10-18 nucleotides. The overhangs were introduced to the DNA fragments with oligonucleotides by PCR (see 6.1.8) During oligonucleotide design, Gibson assembly overhangs were carefully optimized with the software Gene Quest and SeqBuilder (DNASStar, USA) to exhibit no secondary structure and to possess a melting temperature of ~ 48 °C. For standard reactions, 30 fmol of each DNA fragment were mixed in a volume of 2.5 µl. Then, 2.5 µl of 2x Gibson Assembly Mix (prepared in the lab) were added, containing (1) an exonuclease that digests the 5'-ends of DNA fragments allowing complementary fragments to anneal, (2) a DNA polymerase, which fills the resulting gaps by re-synthesis of double-stranded DNA-regions from the 3'-ends, and (3) a DNA ligase, which covalently links the complementary fragments. The reactions were incubated at 48 °C for 30 min. For the background control, DNA-fragments were incubated with 2.5 µl water in a parallel reaction. Finally, 0.8 µl of the reaction were directly used for the transformation of electro-competent *E. coli* cells (see 6.1.2).

### 6.1.11 Protein test expression

Clonings that resulted in a change of size of an encoded protein product on a plasmid could be conveniently analyzed by test expression in small scale. For this, individual colonies were picked from an agar plate into 200 µl of 2YT medium containing the appropriate antibiotic and grown for 4-5 h at 37°C with shaking. 100 µl of each culture were then mixed with 100 µl fresh 2YT medium containing the appropriate antibiotic and 0.4 mM IPTG to induce protein expression. As a negative control, a colony from the vector-only ligation agar plate was picked and also induced. After further growth for 2-3 h at 37°C, the bacteria were pelleted at 13,000 rpm for 4 min in a tabletop centrifuge (Eppendorf, Germany). The bacteria pellets were then dissolved in 100-200 µl SDS-PAGE sample buffer and analyzed by SDS-PAGE (see 6.2.9). The remaining non-induced 100 µl culture of positive clones were then used to inoculate a DNA Mini- or Midi-preparation (see 6.1.3).



### 6.1.12 Oligonucleotide synthesis, gene synthesis and DNA sequencing

All oligonucleotides used in this study were designed using the SeqBuilder software (DNASTar, USA), synthesized by Sigma-Aldrich (Germany) and dissolved in ddH<sub>2</sub>O to a final concentration of 100 μM. For standard cloning purposes desalted oligonucleotides were ordered. Oligonucleotides with a 5' phosphoryl group, e.g. for mutagenesis PCR, were ordered as HPLC-purified.

Genes were codon-optimized and flanked by restriction sites or Gibson assembly overhangs using the software Gene Designer 2.0 (DNA2.0, USA) and synthesized by GenScript (USA).

All constructed plasmids were sequenced with appropriate primers at Seqlab (Germany). Sequencing results were analyzed using the SeqMan software (DNASTar, USA).

## 6.2 Protein biochemistry methods

### 6.2.1 Protein expression strains

All recombinant proteins used in this study were expressed in *E. coli* strains. Specifically, the *E. coli* strains BLR (Novagen, USA) or NEB Express (New England Biolabs, USA) were most commonly used. Previously, nanobodies were routinely expressed in *E. coli* by periplasmic secretion (Vincke et al., 2012; Pardon et al., 2014; Fridy et al., 2014). The oxidative milieu of the periplasm enabled the formation of their conserved internal disulfide bond. Other groups (Olichon and Surrey, 2007; Zarschler et al., 2013; Djender et al., 2014) and us soon realized that functional nanobodies could be expressed in much higher yields in the *E. coli* cytoplasm. Initially, we expressed all nanobodies and derived constructs in the cytoplasm of *E. coli* SHuffle Express (New England Biolabs, USA), which is a strain that contains a cytoplasmic disulfide isomerase and harbors mutations that render its cytoplasm (moderately) oxidative (Lobstein et al., 2012). We soon discovered that disulfide bond formation is largely dispensable for nanobody function and switched to expression in *E. coli* strains with a normal reductive cytoplasm.



### 6.2.2 Recombinant protein expression

In general, the plasmid encoding the protein of interest was used to transform the desired electro-competent *E. coli* strain by electroporation, as described in 6.1.2. For pre-cultures, 50-100 ml 2YT medium, supplemented with the appropriate antibiotic(s), was inoculated with a single transformed colony in a 5 L flask and incubated over night at 28°C. On the next day, pre-cultures were diluted by addition of a ~ fivefold volume of fresh medium and incubated for 1 h at the desired expression temperature. Then protein expression was induced with 0.1-0.2 mM IPTG at an OD<sub>600</sub> of 1.0-2.0. The induced bacterial cultures were incubated at 18-25°C for 3 h-8 h while shaking at 95 rpm. Before cell harvest, 1 mM PMSF and 10 mM EDTA were added as protease inhibitors and then bacteria were pelleted for 10 min at 7,000 rpm and 4°C (RC6 plus centrifuge, F9 rotor; Sorvall, USA). The bacterial pellet was resuspended in native resuspension buffer of protein-specific composition (50 mM Tris/HCl pH 7.5, 150-500 mM NaCl, 2-20 mM imidazole, 0-5 mM DTT) to an OD<sub>600</sub> of 20-50/ml. Resuspended bacteria were frozen in liquid nitrogen and stored at -80°C until further use.

### 6.2.3 Recombinant protein purification

For cell lysis, the resuspended bacterial pellet was thawed and the cell suspension was sonicated (Sonifier 450, Branson, UK) in an ice-water bath for 4 x 1 min with maximum output and 45 % duty cycle. The lysed cell suspension was cleared by ultracentrifugation at 38,000 rpm and 4°C for 1.5 h (WX Ultracentrifuge, T647.5 rotor, Sorvall). After addition of 250 mM sucrose, the supernatant was frozen in liquid nitrogen and stored at -80°C or directly used for protein purification by affinity chromatography.

All proteins expressed in this study carried N-terminal or C-terminal poly-histidine-tags of varying lengths (His<sub>6</sub>-, His<sub>10</sub>- or His<sub>14</sub>-tags) and could therefore be isolated from *E. coli* lysates using Ni<sup>2+</sup>-chelate affinity chromatography. Purifications were carried out using commercial liquid-chromatography columns (Luer lock, Sigma, USA; 1.0x1.0 or 1.5x1.0 cm) and several distinct Ni<sup>2+</sup>-EDTA-amid silica matrices prepared by Dirk Görlich. For small proteins, a 20 % or a 24 % substituted 500 Å Ni<sup>2+</sup>-EDTA-amid silica matrix was preferably used. Large proteins or protein complexes were purified with



matrices containing larger pores i.e. a 6 % substituted 1000 Å Ni<sup>2+</sup>-EDTA-amid silica. The degree of Ni<sup>2+</sup>-substitution also determined the amount of imidazole that could be added to a lysate in order to compete non-specific background binding of *E. coli* proteins. In general, 15-20 mM imidazole were added when a purification with a 20 % or 24 % substituted matrix was desired, whereas only 2-5 mM imidazole were added when a 6 % substituted matrix was going to be used.

The cleared lysate after ultracentrifugation was applied to Ni<sup>2+</sup>-EDTA-amid silica pre-equilibrated in resuspension buffer of protein-specific composition. The optimal amount of matrix depended on the protein expression level and its solubility. It was determined beforehand in small-scale pre-experiments using Mobi-Cols (MoBiTech, Germany) and ranged from 1.5-5.0 ml per lysate. Lysate and matrix were incubated for 1 h at 4°C in a glass bottle on a tube roller. The suspension was then transferred to a liquid-chromatography column, the flow-through was collected and the matrix was washed with three column volumes of resuspension buffer. Subsequently, His-tagged proteins were eluted in 0.5-1.0 ml fractions using Ni<sup>2+</sup>-elution buffer (50 mM Tris/HCl pH 7.5, 150-500 mM NaCl, 500 mM imidazole, 250 mM sucrose, 0-5 mM DTT). Individual fractions were checked for protein content with Amido Black Quick Staining and peak fractions were pooled. Protein concentration was determined by dividing the absorption at 280 nm with a protein-specific extinction coefficient ( $\epsilon_{280}$ ), predicted by the software Protean (DNASar, USA). Purified protein aliquots were then frozen in liquid nitrogen and stored at -80°C until further use.

Samples for analysis of expression and purification by SDS PAGE were taken of uninduced cells, induced cells after expression, cells after sonication, supernatant and pellet after ultracentrifugation, Ni<sup>2+</sup>-flow-through and of the final pooled Ni<sup>2+</sup>-eluate. SDS PAGE gels were normalized by loading 35 mOD of the above-mentioned fractions and 1-2 µg of the purified protein per lane and stained with Coomassie.

#### **6.2.4 Recombinant protein purification with on-column protease cleavage**

Many nucleoporins and nanobodies were produced as fusion proteins with an N-terminal H<sub>14</sub>-bdSUMO or -bdNEDD8 module (Frey and Görlich, 2014). These modules can be cleaved at their very C-terminus by the highly specific and efficient proteases bdSENP1 and bdNEDP1, respectively. These tags were therefore used when



an untagged protein with a specific or even authentic N-terminus was desired. Such tagged proteins were bound to a Ni<sup>2+</sup>-chelate matrix and washed with three column volumes of resuspension buffer, followed by one wash with the same buffer lacking imidazole. Then the same resuspension buffer (without imidazole) was supplemented with either 50 nM bdSENP1 or 500 nM bdNEDP1 and a volume corresponding to the double matrix bed volume was applied to the column. Very quickly the wash buffer in the matrix bed volume was exchanged with protease-containing buffer with the help of a syringe. Cleavage was allowed to take place for 1 h at 4°C. Next, all protease-eluted untagged protein was collected in 0.5-1.0 ml steps by applying resuspension buffer (without imidazole) containing 250 mM sucrose. Protein content and concentration were determined as above. Untagged proteins were aliquoted, frozen in liquid nitrogen and stored at -80°C until further use.

### 6.2.5 Co-expression of proteins

In this study co-expression of proteins was used to reconstitute recombinant protein complexes in *E. coli* or to biotinylate proteins during expression. A co-expression requires plasmids with different origins of replications and selection markers (antibiotic resistances). In specific cases, we used up to three plasmids at a time, harboring either the ColE1, the pSC101 (E93K) or the p15A origin of replication. Further, these plasmids contained either a kanamycin, spectinomycin, ampicillin or trimethoprim resistance cassette.

In order to select for stoichiometric protein complexes, orthogonal tags were used that allowed successive binding of distinct subunits to different affinity matrices and their respective orthogonal cleavage from these matrices with specific proteases (Frey and Görlich, 2014). Protein complex subunits carrying a ZZ-tag - the Z-domain is derived from an engineered B domain of protein A (Nilsson et al., 1987) - could be purified using a commercial IgG sepharose (GE Healthcare, USA). Here, elution required proteolytic cleavage of a bdSUMO or bdNEDD8 module fused behind the ZZ-tag.

### 6.2.6 Enzymatic biotinylation of proteins

For *in vivo* biotinylation during expression in *E. coli*, proteins were tagged with an N-terminal biotin acceptor peptide, called Avi-tag (primary sequence: GLNDIFEAQKIEWHE), and co-expressed with untagged *E. coli* Biotin ligase BirA



(Schatz, 1993; Beckett et al., 1999) from a plasmid with a p15A origin of replication and a spectinomycin resistance cassette. Before induction of protein expression ~ 20 µg biotin/ml medium were added.

Alternatively, the purified enzyme BirA was added after binding the His<sub>14</sub>-Avi-tagged protein to a Ni<sup>2+</sup>-chelate affinity resin for on-column biotinylation in biotinylation buffer (50 mM Tris/HCl pH 7.5, 100 mM NaCl, 10 mM ATP, 12.5 mM MgCl<sub>2</sub>, 250 µM biotin). For this, 1 µM BirA in 2x bed volume biotinylation buffer was incubated with resin under constant mixing for 2 h at room temperature. The enzyme and excess biotin could then be conveniently washed away and the biotinylated protein eluted with Ni<sup>2+</sup>-elution buffer as described (see 6.2.3).

Proteins were also biotinylated after Ni<sup>2+</sup>-affinity purification with purified BirA in solution. Specifically, Avi-tagged protein was mixed with BirA in a 1:100 molar ratio in biotinylation buffer and incubated for 2 h at room temperature. The reaction was then passed over a PD-10 desalting column (GE Healthcare, USA) to remove excess biotin.

On-column and in-solution biotinylation was especially necessary when co-expression of BirA was not an option e.g. because protein complexes, that were to be biotinylated, were already expressed from three different plasmids.

### 6.2.7 Periplasmic expression of nanobodies

Nanobodies were secreted to the *E. coli* periplasm by fusing them to an N-terminal posttranslational secretion signal derived from *Erwinia carotovora* pectate lyase (pelB) (Lei et al., 1987) and a C-terminal His<sub>6</sub> or His<sub>10</sub>-tag. Expression was carried out as described above (see 6.2.2), but usually cultures were incubated at 18°C for at least 14 h. After cell harvest, the bacterial pellet was resuspended in 10 ml Osmo-shock buffer (200 mM Tris/HCl pH 8.0, 500 mM Sucrose, 5 mM EDTA pH 8.0) (Skerra and Plückthun, 1988) and incubated rotating for 60 min at 4°C. Then, 40 ml ice-cold water were added, the suspension quickly mixed and further incubated for 30 min at 4°C. This osmolytic step frees the periplasmic content, while leaving the plasma membrane intact. After a short centrifugation for 10 min at 7,000 rpm and 4°C (RC6 plus centrifuge, F9 rotor; Sorvall, USA), the supernatant was neutralized with Tris/HCl and supplemented with 150 mM NaCl and 2-5 mM imidazole. It was then centrifuged for 30 min at 30,000 rpm and 4°C (WX Ultracentrifuge, T647.5 rotor; Sorvall, USA). The



periplasmic lysate was either frozen in liquid nitrogen for storage at  $-80^{\circ}\text{C}$  or directly applied to a  $\text{Ni}^{2+}$ -chelate affinity column for protein purification (see 6.2.3).

High-level protein secretion quite often caused the periplasmic content of *E. coli* cells to leak into the surrounding medium. This was checked by filtering the medium after bacterial cell harvest and performing a small-scale  $\text{Ni}^{2+}$ -chelate affinity purification. In some cases, there was more protein in the medium than in the periplasmic fraction after osmolysis.

### 6.2.8 Size exclusion chromatography

In this study, small-scale gel filtration was used to exchange the buffer of protein solutions, mainly to remove imidazole of  $\text{Ni}^{2+}$ -eluates for biological assays or excess biotin after in-solution biotinylation. For this purpose, illustra Nap5 or PD-10 desalting columns (GE Healthcare, USA) were used according to the manufacturers instructions. For analytical experiments, Superdex 200 10/30 (separates proteins in the range of 10-600 kDa) or Superdex 75 10/30 (separates proteins in the range of 3-70 kDa) columns (Pharmacia, Sweden) coupled to an ÄKTA Purifier or ÄKTA Explorer system (Pharmacia, Sweden) were used and gel filtration was performed according to the manufacturer's instructions. Before loading, proteins were concentrated using Amicon Ultra Centrifugal Filters (EMD Millipore, USA) and subjected to ultracentrifugation for 30 min at 38,000 rpm and  $4^{\circ}\text{C}$  (Discovery M120 SE ultracentrifuge, Sorvall, S45-A rotor) to remove protein aggregates. The gel filtration column was equilibrated with a filtered and degased buffer that was identical to the protein buffer. Peak fractions were collected and analyzed by SDS-PAGE and subsequent Coomassie staining. For large-scale gel filtrations, e.g. for crystallization, a Superdex 75 16/60 column was used.

### 6.2.9 SDS polyacrylamide gel electrophoresis (SDS-PAGE)

Sodium dodecyl sulfate polyacrylamide gel electrophoresis (SDS-PAGE) was used to separate proteins according to their molecular weight (Laemmli, 1970). Specifically, 8-12 % SDS polyacrylamide gradient gels were used that were routinely prepared by Gabriele Hawlitschek. All protein samples were diluted with 5x SDS sample buffer and heated at  $95^{\circ}\text{C}$  for 8 min prior to loading. Gels were run at a voltage of 400 V and a current of 50 mA for  $\sim 1.08$  h and then stained by heating them in a Coomassie staining solution for  $\sim 5$  min in a microwave. The staining solution was replaced with distilled



water and the gel was heated again and then incubated under rocking to slightly remove the background staining.

## 6.3 Nanobody library construction

### 6.3.1 Alpaca immunizations

Female alpacas, held at the Max Planck Institute for Biophysical Chemistry (Göttingen, Germany), were immunized with 0.5-1.0 mg protein or protein complex at 3-4 week intervals for 3-4 times. All antigens had been expressed recombinantly in *E. coli*, affinity-purified and the buffer had been exchanged to a physiological buffer (20 mM Tris/HCl pH 7.5, 150 mM NaCl, 250 mM Sorbitol). Antigens were mixed with a mild AS03-like adjuvant (oil-in-water emulsion) and an adjuvant peptide (N-Acetylmuramyl-L-alanyl-D-isoglutamine hydrate; Sigma-Aldrich, USA) before immunization. An animal was immunized with up to five different antigens at the same time. Care was taken to not exceed a maximum volume of 2 ml antigen-adjuvant suspension per animal. Antigens were injected subcutaneously at shaven and locally anesthetized skin areas surrounding the shoulder blades by Dr. Ulrike Teichmann. The injection sites were carefully monitored and no unusual swellings or bump formations as a result of immunization were observed.

### 6.3.2 Lymphocyte isolation and total RNA preparation

Four days after the final boost, 100 ml of blood were collected from the jugular vein of an immunized animal using a vacuum bottle that was pre-filled with 100 ml blood dilution buffer (1xPBS, 0.4 % glucose, 25 mM EDTA) before use to prevent blood coagulation. Peripheral blood lymphocytes (PBLs) were isolated by density gradient centrifugation using Leucosep tubes (Greiner Bio-One) according to the manufacturer's instructions. After centrifugation, PBLs formed a distinct white cell layer on top of the density gradient medium. After washing the PBLs two times in blood dilution buffer, total RNA was prepared according to Chomczynski and Sacchi (2006). It was critical to prepare Solution D (4 M GuSCN, 25 mM sodium citrate, pH 7.0, 0.5 % (w/v) Sarkosyl, 50 mM DTT) freshly each time and to use new aliquots of isopropanol and 75 % ethanol. In general, great care was taken to avoid RNase contamination. One half of each total RNA preparation was stored in 75 % ethanol at -80°C until further use. The other half was dissolved in 100 µl RNA Storage solution (1 mM sodium citrate, pH 6.4)



containing ~35 units of SUPERase-In RNase Inhibitor (Thermo Scientific, USA). RNA concentrations were determined using a NanoDrop 2000C spectrophotometer (PiqLab, Germany). RNA quality was verified by running 2 µg on a 1 % agarose gel with a ssRNA ladder (New England Biolabs, USA) and by capillary gel electrophoresis using the Bioanalyzer RNA 6000 Nano kit (Agilent Technologies, USA).

### 6.3.3 PCR amplification of nanobody encoding genes

All oligonucleotides used for library construction (Table 6.1) were ordered as HPLC-purified, dissolved in RNase/DNase-free water after delivery and aliquoted immediately into single-use portions. All other PCR reagents were also aliquoted to reduce the risk of their contamination.

**Table 6.1** Oligonucleotides for nanobody library construction

<b>primer</b>	<b>purpose</b>	<b>sequence</b>
CALL002	RT-PCR	GGTACGTGCTGTTGAACTGTTCC
AlpVh-L	PCR I	GGTGGTCCTGGCTGC
AlpVHHR1	PCR I	GATCACTAGTGGGGTCTTCGCTGTGGTGCG
AlpVHHR2	PCR I	GATCACTAGTTTGTGGTTTTGGTGTCTTGGG
PT718	PCR II - VHH	<b>CAGGTGCAATTGGTAGAGTCTGGGGGAG</b>
PT719	PCR II - VHH	<b>CAGGTGCAATTGGTAGARTCTGGGGGAG</b>
PT720	PCR II - VHH	<b>CAGGTGCAATTGGTAGAGTCBGGGGGAG</b>
PT721	PCR II - VHH	<b>GACGTTGATGAGACTGTGACCTGGGTCC</b>
PT722	PCR II - VHH	<b>GACGTTGATGAGACTGTGACCHGGGTCC</b>
PT723	PCR II - VHH	<b>GACGTTGATGAGACTGTGACCHGGGYCC</b>
PT1044	PCR II - vector	<b>ACAGTCTCATCAACGTCAAGTAGTAGTAGT</b> AGATCTGGTAG
PT1045	PCR II - vector	<b>CTACCACCAATTGCACCTGAGATCCTGCC</b>

A = adenosine; G = guanosine; C = cytosine; T = thymine; R = A/G; B = G/T/C; H = A/T/C; Y = C/T

For library generation, cDNA was generated from 30 µg of total RNA using the SuperScript III First-Strand Synthesis System (Life Technologies, USA) with an IgG CH2 domain-specific primer, pCALL002 (Conrath et al., 2001). Then, VHH domain encoding genes were amplified by nested PCR. For the first step, 24 PCRs with 5 µl cDNA each as template were performed. The primers AlpVh-L, AlpVHHR1 and AlpVHHR2 (Maass et al., 2007), which anneal in the leader sequence and the VHH-specific hinge regions, yielded ~ 400 bp fuzzy PCR products that were gel-purified (as described in 6.1.5) and pooled. The first PCR product served as a template for amplification with a second set of primers that anneal within the nanobody framework and introduce Gibson assembly overhangs. The three forward primers PT718-720 and



the three reverse primers PT721-723 were individually combined and 9 PCR reactions with 50 ng PCR product I were carried out. All 9 PCR II products were purified using the MSB spin PCRapace kit (Stratatec, Germany) and then mixed in equimolar amounts (VHH insert mix).

#### 6.3.4 Library assembly and transformation

The minimal phagemid pTP826 was digested with AgeI-HF, dephosphorylated and gel-purified. Then, 50 ng of linearized and dephosphorylated phagemid were used as template for PCR amplification with PT1044 and PT1045, yielding a 2725 bp product that was gel-purified. For final library construction, 10  $\mu\text{g}$  (5.6 pmoles) of phagemid PCR product and 5.6 pmoles of VHH insert mix were combined in a total volume of 235  $\mu\text{l}$  and 235  $\mu\text{l}$  of 2x Gibson assembly mix (prepared in the lab) were added. Gibson assembly was allowed to take place for 30 min at 48°C. Then, the reaction was purified using the MSB spin PCRapace kit (Stratatec, Germany) and eluted in 20  $\mu\text{l}$  ddH<sub>2</sub>O (~500 ng/ $\mu\text{l}$  DNA concentration). The assembled library was then used to transform highly electro-competent *E. coli* SS320 cells (Lucigen, USA). We routinely performed 10 transformations using 500 ng of assembled library per vial of *E. coli* SS320 cells (~50  $\mu\text{l}$ ). Transformation efficiencies were around  $5\text{-}9 \times 10^8$  cfu/ $\mu\text{g}$  DNA, allowing the construction of libraries with  $2\text{-}5 \times 10^9$  individual transformants (defined as library size). Transformed cells were grown in Lucigen recovery medium for 1 h at 37°C and then used to inoculate 1 L pre-warmed Terrific Broth medium containing trimethoprim and 2 % (w/v) glucose. After over night growth (~16 h) at 28°C, *E. coli* cells were harvested by centrifugation for 10 min at 4,000 rpm (RC6 plus centrifuge, F9 rotor; Sorvall, USA). The pellet was resuspended in 20 ml TB-trimethoprim-2 % (w/v) glucose and then 15 % (v/v) glycerol was added. The glycerol stock was aliquoted, frozen in liquid nitrogen and stored at -80°C until further use. The OD<sub>600</sub> was determined and used to calculate the number of cells per ml of library glycerol stock, assuming that an OD<sub>600</sub> = 1 corresponds to  $\sim 8.8 \times 10^8$  cells/ml (Vincke et al., 2012). This number is used to calculate the volume of glycerol stock that contains 25-50-fold more cells than the actual library size. This volume is later used as a starting inoculum to generate the nanobody-displaying phage library for phage display.



## 6.4 Phage Display

### 6.4.1 Production of phagemid virions from library glycerol stocks

For phage display, bacteriophages that present all nanobodies encoded in the original library are required. This phage library is produced directly from the nanobody-phagemid library glycerol stock.

The volume of the start inoculum was calculated as described in 6.3.4 and used to inoculate 1.5-2.0 L of 2YT medium containing trimethoprim and 2 % (w/v) glucose. Ideally the start OD<sub>600</sub> should be between 0.05-0.10 to allow for sufficient amplification of the library. The culture was grown at 37°C for 3-4 h with shaking, until an OD<sub>600</sub> of 0.6-1.0 was reached. After keeping the culture without shaking for 5 min at 37°C, to enable reformation of broken F-pili, it was infected with helper phage M13KO7 (New England Biolabs, USA). For this, 20-fold more infective helper phages than the total number of *E. coli* cells in the culture were added, again assuming that an OD<sub>600</sub> = 1 corresponds to ~ 8.8x10<sup>8</sup> cells/ml. Infection was allowed to take place for 30 min at 37°C without shaking. In order to separate excess helper phage, the cells were pelleted by centrifugation for 10 min at 5,000 rpm (RC6 plus centrifuge, F9 rotor; Sorvall, USA) and resuspended in 1.5-2.0 L 2YT medium containing trimethoprim and kanamycin (but no additional glucose!). Cells carrying a phagemid and a helper phage genome with kanamycin resistance cassette are thus selected for. Infected cells were then incubated at 37°C with shaking over night for phage production.

### 6.4.2 Phage purification

For the purification of phages from culture supernatant, bacterial cells were pelleted by centrifugation at 7,000 rpm for 10 min at 4 °C (RC6 plus centrifuge, F9 rotor; Sorvall, USA). Phages in the resulting supernatant were precipitated on ice for 30 min by addition of 1/5 volume of pre-chilled phage precipitation buffer (20 % PEG 8000, 2.5 M NaCl). After centrifugation at 4,000 rpm for 15 min at 4 °C (RC6 plus centrifuge, F9 rotor; Sorvall, USA), the phage pellet was resuspended in 25 ml 50 mM Tris/HCl pH 7.5, 300 mM NaCl. Then, aggregates and bacterial contaminations were removed by centrifugation at 15,000 g for 10 min at 4°C (RC6 plus centrifuge, SS-34 rotor; Sorvall, USA). Phages in the supernatant were again precipitated on ice for 30 min by the addition of 5 ml phage precipitation buffer and pelleted by centrifugation



at 2200 g for 15 min at 4 °C (RC6 plus centrifuge, F13 rotor; Sorvall, USA). The phage pellet was slowly resuspended after addition of 5 ml 50 mM Tris/HCl pH 7.5, 300 mM NaCl by head-over-tail rotation at 4°C for 1 h. Concentrated phage solutions were pipetted carefully to avoid shearing forces that could compromise phage infectivity. The resuspended phage stock solution was centrifuged at 13,000 rpm for 10 min at 4 °C in a tabletop centrifuge to remove aggregates. Then, the concentration of the phage solution was determined spectrophotometrically (see 6.4.3.2) and phages were stored after the addition of 0.1 % w/v BSA at 4 °C until further use. Typically, a total number of  $10^{14}$ - $10^{15}$  phages per 1 L of culture were obtained.

### 6.4.3 Quantification of phage particles

Phage concentrations were either determined by titring, spectrophotometry or real-time/qPCR. In contrast to spectrophotometry and qPCR that measure all phage particles, with titring only infective virions can be quantified.

#### 6.4.3.1 Quantification via titring

For phage titer determination, a tenfold dilution series of the phage stock solution in 2YT medium was prepared. Then, 10 µl of each dilution was mixed with 90 µl of exponentially growing *E. coli* SS320 cells ( $OD_{600} = 0.6$ - $0.9$ ). After infection for 30 min at 37 °C, 50 µl of the appropriate dilutions were plated on selective agar plates and incubated over night at 37 °C. On the next day, the number of resistant colonies was counted and divided by the corresponding dilution factor to yield the phage titer (in colony forming units (cfu)/ml).

#### 6.4.3.2 Quantification via spectrophotometry

Spectrophotometry was routinely used for a quick quantification of concentrated phage solutions. The absorbance of the phage solution was measured at 269 nm and 320 nm. The absorbance of filamentous phage solutions is highest at 269 nm, while the low absorbance of the phage particles at 320 nm can roughly be used to correct for phage-induced light scattering and contaminating non-phage particles. George P. Smith derived the following equation for an estimation of the phage concentration (Formula 1) based on work by Day and Wiseman (Day and Wiseman, 1978):



$$c \left[ \frac{\text{phage}}{\text{ml}} \right] = \frac{(A_{269 \text{ nm}} - A_{320 \text{ nm}}) \cdot 6 \cdot 10^{16}}{\text{phagemid size [bp]}} \quad (1)$$

### 6.4.3.3 Quantification via qPCR

Low concentrated phage solutions (e.g. phage eluates after affinity enrichment) were generally quantified using real-time/qPCR. For this, a PCR in the presence of a DNA-binding fluorescent dye is performed and the fluorescence signal after each cycle measured and plotted. The number of PCR cycles that were necessary to reach a threshold fluorescence signal is determined (C<sub>q</sub>-value). The C<sub>q</sub>-value depends on the number of initial template molecules and can be used for absolute quantification provided a standard curve was obtained (Pfaffl, 2004).

For the generation of the standard curve, ssDNA was isolated from virions enclosing a phagemid vector using the QIAprep Spin M13 kit (Qiagen, Germany) according to the manufacturer's instructions. After the spectrophotometric determination of the ssDNA mass concentration, the molar concentration was determined based on the molecular mass that was calculated by the DNA Molecular Weight Calculator from the Sequence Manipulation Suite (Stothard, 2000). Then, a logarithmic dilution series was prepared comprising 9 different concentrations ranging from 10<sup>10</sup>-10<sup>2</sup> molecules per microliter.

Each PCR amplification was performed in triplicates in 20 µl total volume, containing 10 µl 2x Sso Advanced SYBR Green supermix (Bio-Rad, USA), 8.8 µl ddH<sub>2</sub>O, 1.0 µl template DNA, and 0.1 µl of each primer. For the quantification of phagemid-containing virions, primers PMB042 and PMB043 (see Table 6.2) were used, which specifically amplify a 182 bp fragment from the pIII C-terminus coding region.

Helper phage genomes were quantified using primers PMB048 and PMB049 (Table 6.2) that anneal in the p15A origin of replication producing a 92 bp fragment. After an initial denaturation and polymerase activation step (98 °C, 2 min), amplification was carried out in 40 cycles, comprising one denaturation step (95 °C, 15 s) and one annealing plus extension step (60 °C, 30 s).

**Table 6.2** Oligonucleotides for qPCR quantification of phages

primer	template	sequence
PMB042	phagemid	GATGAAAATGCACTTCAGTCGGAT
PMB043	phagemid	GGCTATTATCTCCGTCCCA
PMB048	M13KO7	TTACGCGCAGACCAAAACGAT
PMB049	M13KO7	ACCAAAATCCCTTAACGTGAGT

In every qPCR run, one single standard curve point was quantified (in triplicate) to re-adjust a previously measured calibration curve to variations in the y-intercept (Pfaffl, 2004). The qPCR workflow was mainly established in the lab by Marc Böhning during the course of his Master thesis work under my supervision.

#### 6.4.4 Selection of antigen-specific nanobodies

After purification and determination of the concentration of the phage library it was screened for phages displaying antigen-specific nanobodies in a process called panning. In general two types of panning can be distinguished that differ in the mode of antigen presentation to the phage library. In on-column panning, the biotinylated antigen was first immobilized on magnetic Streptavidin beads and then mixed with the phage library. Due to the close proximity of antigen molecules on the beads, phages displaying two copies of nanobodies (e.g. with weaker affinities or of lower abundance) are more easily selected for due to avidity effects. This was only performed in the first round of panning to ensure that no binder is lost. In the subsequent rounds, the selection pressure was increased to select for high affinity binders. Here, biotinylated antigen and the phage library were incubated in solution, followed by a very short capture (~ 5 min) of antigen-bound phages with magnetic Streptavidin beads. This reduces the time where avidity effects play a role and shifts the selection to monovalent phages displaying high-affinity binders.

#### 6.4.5 Phage panning protocol

Antigens used for phage display selections were recombinantly produced in *E. coli* with an N-terminal His<sub>14</sub>-Avi-(GlySer)<sub>9</sub>-bdSUMO/bdNEDD8/scSUMOStar-(GlySer)<sub>9</sub>-tag. While the interspersed long unfolded Gly-Ser spacers minimize steric hindrance effects, the bdSUMO/bdNEDD8 or scSUMOStar module serves as a cleavage site that allows the selective elution of antigen-bound phages.



For the first round of panning, ~ 100 pmoles of fully biotinylated antigen was immobilized on 1-3 mg magnetic Dynabeads MyOne Streptavidin T1 (Life Technologies, USA) in wash & block buffer (WBB; 50 mM Tris/HCl pH 7.5, 300 mM NaCl, 0.1 % BSA). The same amount of beads treated with WBB without antigen was used as a negative control in parallel. The capacity of the beads for a specific antigen was determined in a small-scale pre-experiment. Then, the beads were incubated with  $10^{13}$  phages from the initial phage library in a final volume of 1 ml WBB for 1 h at 4°C. Unbound phages were discarded. The beads were then washed 6 times shortly with 1 ml of WBB. Tubes were changed after the first three washes and after the last wash for elution. Then, beads were resuspended in 200 µl WBB containing 100 nM bdSENP1 or 1 µM bdNEDP1 or 1 µM scSUMOStar protease and incubated for 30 min at 4°C. In this step, antigen-bound phages were selectively released from the beads by proteolytic cleavage of the antigen tag with the corresponding protease. One microliter of each eluate was diluted 100-fold in WBB and used directly for quantification via qPCR (see 6.4.3.3).

The eluted antigen-binding phages were then used for re-infection of *E. coli* to amplify them for the next round of selection. For this, the eluate was added to 25 ml of exponentially growing *E. coli* SS320 cells (2YT medium;  $OD_{600} = 0,8-1,0$ ;  $>10^{10}$  cells) for 30 min. at 37°C without shaking. After that, 200 µl of infected *E. coli* cells were used to inoculate a DNA Midi-preparation (250 ml 2YT medium containing trimethoprim and 2 % (w/v) glucose). The remaining cells were diluted with 75 ml pre-warmed 2YT medium containing trimethoprim and 2 % (w/v) glucose and incubated for 30 min at 37°C. Then, the cells were super-infected by the addition of  $2 \times 10^{12}$  cfu of M13KO7 helper phage (self-made and titered) for further 30 min at 37°C. The culture was then centrifuged for 7 min at 4,000 rpm at room temperature (RC6 plus centrifuge, F9 rotor; Sorvall, USA) to remove excess helper phage. The pellet was resuspended in 500 ml of 2YT medium containing trimethoprim and kanamycin (but no glucose) and grown over night at 37°C for phage production. These phages were then purified and used for the next round of selection.

Typically three rounds of panning with increasing selection pressure were performed. For this, the antigen concentration was lowered in every round (e.g. 1. round: 100 nM; 2. round: 25 nM; 3. round: 1-5 nM) and the number of washing steps was increased



(e.g. 1. round: 6 short washes; 2. Round: 7 short washes + 1x 15 min wash; 3. round: 9 short washes + 1x 30 min wash). After three washing steps the beads were transferred to fresh tubes. In later panning rounds the stringency of washing was increased e.g. by adding 0.05 % Tween-20 to WBB or by increasing its salt concentration.

#### 6.4.6 Cloning of enriched nanobody libraries

The phagemid DNA Midi-preparations after each round of panning served as a template for PCR amplification of the enriched nanobody coding sequences. Specifically, 50 ng of each phagemid library were used in PCR reactions with the primers PT830 and PT831 (see Table 6.3). These primers anneal at the absolute 5' and 3' ends of the nanobody coding sequence that were rendered constant during the second PCR step of library construction. This should prevent any amplification bias that could otherwise lead to a loss of valuable sequences. Furthermore, these primers introduce overhangs that allow cloning of the enriched libraries via Gibson assembly into a vector for cytoplasmic expression in *E. coli*. Specifically, the vector pTP621 (IF2N-Avi-(GlySer)<sub>9</sub>-scSUMOStar-(GlySer)<sub>9</sub>-Cys-MCS-His<sub>10</sub>) was used. The resulting nanobody fusion proteins can be adapted for different applications (affinity chromatography, fluorescent labeling, binding assays). For Gibson assembly, the vector was linearized with Acc65I and dephosphorylated and served as template for PCR with the primers PT867 and PT868 (for pTP621) or PT1022 and PT1023 (for pTP779).

**Table 6.3** Oligonucleotides used for cloning enriched nanobody libraries

primer	template	sequence
PT830	VHH library	GGCTCTTGTGGATCCCAGGTGCAATTGGTAG
PT831	VHH library	ACCAGAGCCAGAGGAAGACGTTGATGAGAC
PT867	pTP621	CCTCTGGCTCTGGTTCTGGTGGTAGTGGTAGATC
PT868	pTP621	GGATCCACAAGAGCCACCAATCTGTTC
PT1022	pTP779	CCTCTGGCTCTGGTTCTGGGGGTAGTGGTAG
PT1023	pTP779	GGATCCACAAGAGCCACCGCTAG

#### 6.4.7 Sequencing of enriched nanobody libraries and data analysis

On the next day, 96 individual colonies were picked and used to inoculate 300 µl each of 2YT medium containing kanamycin in a 96 deep well block and incubated for ~ 6 h at 37°C (BioShake iQ; Q.Instruments, Germany) under constant shaking. 120 µl of each well were then transferred to a 96-well PCR plate provided by Seqlab (Göttingen,



Germany) for sequencing with the primer QE-rev (GTTCTGAGGTCATTACTGG). The nanobody coding regions were then automatically extracted from the sequencing data and in-silico translated by a Python algorithm programmed by Dr. Koray Kirli. Nanobody protein sequences were aligned with the software MegAlign (DNASStar, USA) and grouped according to similarity in the CDR III region. Within each class, the nanobody sequence that was closest to the consensus sequence of the class was chosen for further characterization. Individual sequences with unique CDR III regions were also further characterized. In total, typically ~ 10 nanobodies per panning were chosen for expression and further characterization.

#### **6.4.8 Increasing nanobody diversity**

In a few cases, the initial panning yielded only a limited set of nanobody classes or the majority of all classes targeted a specific immuno-dominant epitope of an antigen. Consequently, binders to other regions on the antigen were lost during selection. An easy solution was to use the dominant nanobody classes to mask their epitopes on the antigen during a subsequent second panning. Thus, they were pre-incubated in high molar excess (100x-1000x) with the biotinylated antigen before phages were added. This shifted the selection to nanobodies targeting different epitopes. Another strategy was to biotinylate a member of the dominant nanobody class and use it for the immobilization of non-biotinylated antigen. Consequently, only phages displaying nanobodies with compatible epitopes were selected. Alternatively, a truncated antigen lacking the immuno-dominant epitope was used to select a more diverse set of binders.

#### **6.4.9 Finding binders to specific antigen domains**

The panning strategy can be adapted to enrich binders to distinct regions of an antigen. The following strategies were applied to find nanobodies against the C-terminal coiled-coil domains of the Nup62•Nup58•Nup54 complex. In the first round of panning, the phage library was pre-depleted with biotinylated Nup62 complex lacking the C-terminal domains (Nup62 $\Delta$ C). The unbound phages were then incubated with the full-length complex. In the next round, the enriched phage library was pre-incubated with non-biotinylated Nup62 $\Delta$ C complex (~10 $\mu$ M) before addition of biotinylated full-length complex (50 nM), yielding a 200x molar excess of competitor. By lowering the antigen



concentration in the third round to 10 nM a 1000x molar excess of competitor was achieved and the selection shifted to binders to the C-terminus of the complex.

## 6.5 *Xenopus* egg extract methods

### 6.5.1 Preparation of interphase *Xenopus* egg extract

Female *Xenopus laevis* frogs were primed for ovulation 3-14 days before egg extract preparation by subcutaneous injection of 50 U human chorionic gonadotropin (hCG). One day before, 500 U hCG were injected and the frogs placed into separate boxes containing 1x Marc's Modified Ringers (MMR) buffer. On the next day, eggs laid by different frogs were manually inspected and batches with bad quality (containing many apoptotic or activated eggs) were discarded. Batches with sufficient quality were pooled after thorough manual removal of individual bad quality eggs. The eggs were washed with 1xMMR buffer to remove debris and then treated with dejelling solution (165 mM L-cysteine pH 7.8 in 0.25x MMR buffer) for 5 min under gentle swirling to remove their jelly coat. In order to send the eggs to an interphase-like state, they were incubated with ~ 80 µg of a calcium ionophore (A23187) for 7 min. The eggs were washed multiple times with 1x MMR buffer for 20 min to remove the ionophore, packed into thin-walled centrifuge tubes (13x51 mm; SETON Scientific, USA) and centrifuged for 30 s at 800 rpm and 90 s at 2,000 rpm in an A-4-38 rotor (Eppendorf centrifuge 5702). Excess buffer was removed and the eggs crushed by centrifugation for 20 min at 11,000 rpm at 4°C (RC6 plus centrifuge, HB-6 rotor; Sorvall, USA). The resulting low-speed supernatant (LSS) extract was obtained by puncturing the side of the tube with a needle. The following chemicals were added to the LSS extract: 40 µg/ml Cycloheximide, 5 µg/ml Cytochalasin B, 10 µM caspase inhibitor Z-VAD-FMK, 1x self-made protease inhibitor mix (see Table 5.6). Finally, LSS extract was frozen in 0.5 ml aliquots in liquid nitrogen and stored at -80°C until further use.

### 6.5.2 Preparation of CSF-arrested *Xenopus* egg extract

For the preparation of 'mitotic' CSF-arrested egg extracts (protocol based on Hannak and Heald, 2006), only high quality egg batches were used and kept separate during the whole preparation procedure. Activated or damaged eggs were constantly sorted out. The protocol initially follows the same steps as outline in 6.5.1, but lacks the ionophore incubation step and relies on buffers that contain the Calcium chelator EGTA to avoid



egg activation. After dejellying, the eggs were washed three times with XB buffer. Then, three washes with CSF-XB buffer were performed. The eggs were packed and crushed as described above (see 6.5.1), CSF-egg extract retrieved and used immediately for all downstream applications.

### 6.5.3 Ran-Aster and bipolar spindle assembly

Freshly prepared CSF-extracts were quality-controlled for mitotic activity. The first test relies on the formation of Aster-like microtubule structures in the presence of high concentrations of RanGTP. For this, 50  $\mu$ l CSF extract were supplemented with 20  $\mu$ M RanQ69L<sup>5-180</sup>•GTP and ~2-5  $\mu$ g of Cy3-labeled tubulin (a kind gift of Dr. Simone Reber, Humboldt University Berlin) and incubated for 30 min at 20°C. One microliter of the reaction was then pipetted on a glass slide and fixed by the addition of 5  $\mu$ l spindle fix solution (1x MMR, 48% (v/v) glycerol, 11% (w/v) formaldehyde) before coverslip addition. Samples were analyzed by confocal microscopy (SP5; Leica, Germany). Good mitotic extracts could be sent to an interphase-like state by addition of 0.6 mM CaCl<sub>2</sub> and 100  $\mu$ g/ml cycloheximide for 30 min at 20°C. Consequently, formed Ran-Asters were disassembled.

A second assay tests the formation of bipolar spindles on added *Xenopus laevis* sperm chromatin. For this, 50  $\mu$ l CSF extract were supplemented with ~ 250 sperm nuclei per  $\mu$ l and 2-5  $\mu$ g of Cy3-labeled tubulin and incubated for 1 h at 20°C. Samples for analysis by confocal microscopy were taken as above by adding spindle fix solution containing 2  $\mu$ g/ml DAPI.

### 6.5.4 Protein complex isolation from interphase *Xenopus* egg extracts

Interphase LSS extract was thawed, diluted fourfold in S250 buffer (20 mM HEPES pH 7.5, 90 mM KAc, 2 mM MgAc, 250 mM sucrose), supplemented with 5 mM ATP and 5  $\mu$ g/ml Cytochalasin B and then centrifuged in thin-walled tubes (13 x 51 mm; SETON Scientific, USA) for 1 h at 235,000 g (Discovery M120 SE ultracentrifuge, S52ST rotor; Sorvall, USA). The lipid- and membrane-free high-speed supernatant (HSS) extract was retrieved by puncturing the side of the tube with a needle and served as starting material for affinity purifications.



Biotinylated and SUMOStar-tagged nanobodies were immobilized on magnetic Dynabeads MyOne Streptavidin T1 (Life Technologies, USA) in S250 buffer for 30 min at 4°C. Remaining biotin-binding sites on Streptavidin were subsequently blocked by incubation with 50 µM Biotin-PEG-COOH (Iris Biotech, Germany) in S250 buffer for 10 min. The blocked beads were then added to *Xenopus* egg extract (= HSS) for 1 h at 4°C. Using a magnetic rack, the beads were separated from extract and washed twice in S250 buffer, followed by two washes in 50 mM Tris/HCl pH 7.5, 300 mM NaCl, 0.05% Tween-20. Nanobody•target protein complexes were then eluted by adding 0.5 µM SUMOStar protease (Liu et al., 2008) in 50 mM Tris/HCl pH 7.5, 300 mM NaCl for 45 min at 4°C. For FG-repeat nucleoporin purifications a 10 min wash step at 4°C with 1 µM RanQ69L<sup>S-180</sup>•GTP in 50 mM Tris/HCl pH 7.5, 300 mM NaCl was included to remove bound nuclear transport receptor•cargo complexes.

### 6.5.5 *In vitro* nuclear assembly

Interphase high-speed supernatant (HSS) cytosol, membranes and sperm chromatin were prepared essentially as described (Hülsmann et al., 2012 and references therein). 9 µl HSS cytosol supplemented with 1x E-mix (1 mM HEPES/KOH pH 7.5, 10 mM creatine phosphate, 0.5 mM ATP, 0.5 mM GTP, 50 µg/ml creatine kinase, 12.5 mM sucrose) were pre-incubated with 1 µl S250 buffer (buffer control) or 1 µl 50 µM nanobody in S250 buffer for 10 min at 20°C. Then 0.5 µl sperm chromatin (~3x10<sup>4</sup> sperm heads/µl) were added and allowed to decondense for further 10 min. After addition of 1.0 µl membranes, nuclear assembly proceeded for 2 h at 20°C.

The formation of nuclei with NPCs harboring an intact permeability barrier was then tested by adding 5 µl of import mix (9 µM hsRch1 IBB-MBP-GFP, 7 µg/ml DAPI). After 1 h incubation at 20°C, 1 µl of each reaction was pipetted on a multiwell glass slide and sealed with a large coverslip. Samples were imaged in an unfixed state using a SP5 confocal microscope (Leica, Germany). The transport properties of nuclei were analyzed by scanning through the nuclear midplane.

The presence or absence of individual Nups in reconstituted nuclei was assessed with specific fluorescently labeled anti-Nup nanobodies. Labeled nanobodies were incorporated during NPC assembly by adding ~ 200 nM of them to HSS cytosol before sperm chromatin addition. Alternatively, fully assembled nuclei were incubated with



~200 nM labeled nanobody and 2 µg/ml DAPI for 30 min at 20°C. For both options, stained nuclei were then fixed by addition of 300 µl 2.4 % paraformaldehyde, 1xPBS, 250 mM sucrose for 15 min at room temperature. The fixed reaction was then carefully layered onto 2 ml 30 % (w/v) sucrose, 1xPBS in a 24-well plate and nuclei centrifuged onto aminosilan-coated coverslips for 10 min at 3,000 rpm at 20°C (Heraeus Multifuge; Thermo Scientific, USA). The coverslips were then washed two times with 1xPBS, desalted in ddH<sub>2</sub>O and mounted with SlowFade Gold (Life Technologies, USA) on glass slides. Samples were analyzed by confocal microscopy.

## 6.6 Fluorescence microscopy methods

### 6.6.1 Cell culture

*Xenopus laevis* XL177 epithelial cells (Ellison et al., 1985; Miller and Daniel, 1977) were grown on coverslips at 27°C with 5 % CO<sub>2</sub> in *Xenopus* cell culture medium. Alternatively, *Xenopus laevis* A6 cells (#ATCC CCL-102™) were used.

### 6.6.2 Fluorescent labeling of nanobodies with NHS ester dyes

For Alexa Fluor 647 NHS-labeling, 10 nmoles of nanobody (concentration 75-150 µM) were incubated with an 8-fold molar excess of dye (20 mM stock in DMF) in 100 mM sodium bicarbonate pH 7.8, 300 mM NaCl for 1 h at 23°C. Subsequently, the reaction was quenched and free dye was separated by buffer exchange to 50 mM Tris/HCl pH 7.5, 300 mM NaCl, 250 mM sucrose on a PD10 desalting column (GE Healthcare, USA).

### 6.6.3 Site-specific fluorescent labeling of nanobodies with maleimide dyes

Purified nanobodies with engineered cysteines were freshly reduced by addition of 15 mM TCEP for 10 min on ice. Using PD-10 desalting columns, the buffer was exchanged to Maleimide-labeling buffer (100 mM potassium phosphate pH 6.4, 150 mM NaCl, 1 mM EDTA, 250 mM sucrose) that had been vacuum degased and purged with argon. For a standard labeling reaction, 10 nmoles of nanobody (concentration 75-150 µM) were rapidly mixed with 12 nmoles of Alexa Fluor 647 C2 Maleimide (from a 20 mM stock in DMF), neutralized to pH 7.5 with K<sub>2</sub>HPO<sub>4</sub> and incubated for 1.5 h on ice. Free dye was separated from labeled nanobody by buffer



exchange to Maleimide labeling buffer on PD10 desalting columns. Quantitative labeling was quality controlled by calculating the degree of labeling (DOL), which defines the molar ratio of dye to protein, as well as by SDS-PAGE and Coomassie-staining.

#### 6.6.4 Immunofluorescence

Two different assays were used to stain *Xenopus* cell NPCs with nanobodies. The first assay utilized selective Digitonin-permeabilization of the plasma membrane before nanobody addition. Here, the nuclear envelope remains intact, proteins are unfixed and the resulting dynamics likely benefits access to sterically occluded regions. The second assay relied on direct fixation of the cells, followed by Triton X-100 permeabilization of plasma membrane and nuclear envelope before nanobody addition. Epitopes on the nuclear side or in membrane proximity thus become accessible to nanobody binding. Nanobodies with fixation-sensitive epitopes, however, might show drastically reduced staining. Therefore, most nanobodies were assessed in both assays to gain information about epitope accessibility.

For the Digitonin-based assay, XL177 cells were pre-fixed for 30 sec with 2.4 % (w/v) paraformaldehyde in Transport buffer (TRB) (20 mM HEPES pH 7.5, 5 mM MgAc, 110 mM KAc, 1 mM EGTA, 250 mM Sucrose) to prevent detachment of cells from the coverslips and briefly washed twice with TRB. The cells were then permeabilized for 8 min on ice with pre-chilled TRB containing 25 µg/ml Digitonin. Following two washes with TRB + 1 % (w/v) Bovine Serum Albumin (BSA) for 5 min each, the cells were incubated with 1-10 nM fluorescent nanobody and 2 µg/ml DAPI for 15 min on ice. Subsequently, the cells were washed three times for 5 min with TRB + 1 % (w/v) BSA at room temperature and then fixed for 10 min with 3 % (w/v) paraformaldehyde in TRB. After two short washes in 1xPBS and desalting in ddH<sub>2</sub>O, the coverslips were mounted in SlowFade Gold or Diamond Antifade Mountant and analyzed by confocal laser-scanning microscopy on a Leica SP5 microscope.

For the direct fixation and Triton X-100 permeabilization assay, XL177 cells were fixed for 10 min at room temperature with 3 % (w/v) paraformaldehyde in 1xPBS. After two short washes with 1xPBS, remaining paraformaldehyde was quenched by addition of 20 mM Borane dimethylamine complex BH<sub>3</sub>(CH<sub>3</sub>)<sub>2</sub>NH<sub>2</sub> in 1xPBS for 5 min. The cells



were washed two times with 1xPBS and then permeabilized with 0.3 % Triton X-100 in 1x PBS for 3 min. After three short washes with 1xPBS, 1 % (w/v) BSA in 1xPBS was added for 30 min to block non-specific background binding sites. Then, 10-100 nM of fluorescent nanobody were added in 1 % (w/v) BSA, 1xPBS for 45 min. After three 15 min washes with 1xPBS, coverslips were desalted and mounted on glass slides for confocal microscopy.

### 6.6.5 Super-resolution imaging

In order to obtain the highest labeling efficiency, XL177 cells were stained with Alexa Fluor 647 maleimide-conjugated nanobodies initially after a short pre-fixation and digitonin permeabilization of the plasma membrane. The cells were subsequently fixed, the nuclear envelope was permeabilized with Triton X-100 and labeled nanobodies were added again. The optimal concentration of each nanobody for both steps was titrated before, using confocal microscopy. All STORM imaging experiments were carried out in MEA imaging buffer as previously described (Dempsey et al., 2011). The buffer consisted of 50 mM Tris-HCl pH 8.0, 10 mM NaCl, 10 % Glucose (w/v), 10 mM  $\beta$ -mercaptoethylamine pH 8.5 and 1 % of an enzymatic oxygen scavenger system stock solution, added to the buffer immediately prior to use. The oxygen scavenger stock solution was prepared by mixing glucose oxidase (10 mg) with catalase (50  $\mu$ l, 20 mg/ml) in 200  $\mu$ l final volume of 1x PBS. The mixture was then centrifuged in a tabletop centrifuge at 13,000 rpm for 1 min.

STORM imaging was performed by Mark Bates with his self-built STORM microscope, based on an inverted fluorescence microscope stand (Olympus, Japan) as previously described (Dempsey et al., 2011). The microscope was fitted with a 100x oil-immersion objective lens (UPLANSAPO, NA1.4; Olympus, Japan), which enabled efficient detection of single fluorophores. The objective lens was mounted on a piezo-positioner (Piezo Jena, Germany), which enabled fine focus adjustment. A custom-built focus-lock system was used to maintain a stable focus during data acquisition. For STORM imaging, photo-switchable Alexa Fluor 647 was excited at 642 nm, and in some measurements the sample was also exposed to 405 nm light to increase the activation rate of switching. A fiber laser (2RU-VFL-P-1000-642; MPB Communications, Canada) was used to generate 642 nm light. The laser illumination was configured such that the illumination angle could be varied between an epi-



illumination geometry and a total internal reflection (TIRF) illumination mode. Typically, the sample was illuminated with oblique illumination (not TIRF) for reduced background signal. Fluorescence emission of Alexa Fluor 647 was detected using an EMCCD camera (Ixon DU860; Andor Technology, United Kingdom). STORM data analysis was carried out using custom analysis software, as previously described (Bates et al., 2007).

## 6.7 Structural biology methods

### 6.7.1 Crystallization of protein complexes

The *Xenopus* Nup98<sup>716-866</sup> NPC anchor domain and the anti-Nup98 nanobody TP377 were expressed with an N-terminal His<sub>14</sub>-bdSUMO-tag and purified using Ni<sup>2+</sup>-chelate affinity chromatography. Crystallization required an exchange of the surface-exposed cysteine 821 of Nup98 to serine. Highly pure untagged protein was cleaved off the column using 50 nM bdSENP1 protease (Frey and Görlich, 2014) in 20 mM Tris, 20 mM NaCl. The complex was formed by incubating equimolar amounts of Nup98<sup>716-866</sup> and TP377 over night at 4°C and then subjected to anion exchange chromatography using a HiTrap Q HP 5 ml column (GE Healthcare). The eluted complex was then further purified using gel filtration on a Hi-Load Superdex 75 16/60 column equilibrated in 20 mM Tris/HCl pH 7.5, 50 mM NaCl. The complex was crystallized by the vapor diffusion method in sitting drops. 60 nl of a reservoir solution containing 45 % (w/v) Pentaerythritol propoxylate (17/8 PO/OH; Jena Bioscience, Germany) and 100 mM Tris pH 8.5 was mixed with 60 nl of the prepared protein complex solution concentrated to 25 mg/ml. Crystals grew within 1 day at 20°C and were flash-frozen in liquid nitrogen without additional cryo-protection.

### 6.7.2 X-ray structure determination

Diffraction data were collected at 100 K with a wavelength of 0.9787 Å on the beamline PXII at the Swiss Light Source (SLS) (Paul Scherrer Institute, Switzerland). Crystals belonged to the space group P4<sub>1</sub> and diffracted to 1.9 Å (see Table 1). For structure determination, molecular replacement was performed in PHASER with a published nanobody structure (PDB entry 4KRN; Schmitz et al., 2013) as a search model. The resulting electron density map was used for automated model building in Phenix (Adams et al., 2010).



### 6.7.3 Negative stain electron microscopy

Directly after elution, nanobody-purified Nup93•Nup188 and Nup93•Nup205 complexes were subjected to the GraFix protocol (Kastner et al., 2008) for complex stabilization. Briefly, ~200 pmoles of nanobody-purified complexes (~140 µl) were loaded onto a 4.2 ml 5 % – 20 % (w/v) sucrose-gradient supplemented with 0.1 % (v/v) glutaraldehyde in the 20 % fraction. The gradient was run in a TH-660 ultra-centrifuge rotor (34,000 rpm, 16 h, 4°C; Thermo Scientific, USA) and then fractionated into 200 µl fractions. The chemically stabilized molecules from the peak fraction were adsorbed to a thin carbon film by surface flotation for 1 min and negatively stained in uranyl formate solution. Images were acquired at room temperature at a magnification of 117,333× on a 4k x 4k CCD camera (TVIPS GmbH, Germany) using two-fold pixel binning (2.5 Å/pixel) in a Philips CM200 FEG electron microscope (Philips/FEI) operated at 160 kV acceleration voltage. 8,139 particles were selected from the images (Busche, 2013) and subjected to contrast transfer function correction (Sander et al., 2003). Subsequently, an initial alignment-by-classification (Dube et al., 1993) step followed by iterative multi-reference alignment and multivariate statistical analysis were performed using IMAGIC (van Heel et al., 1996), resulting in 2D class averages. Electron microscopy work was carried out by Jan Erik Schliep.

### 6.7.4 Crosslinking mass spectrometry

Anti-Nup93 nanobodies TP179 or TP324 and Nup93 (~20 µM each) were incubated on ice for 30 min in Maleimide labeling buffer to allow complex formation. After adding 40 µM of crosslinking agent, the pH was increased to 7.5 and the reaction was continued for 1 h on ice. The following crosslinkers were used "Mal-NHS" = BMPS (3-[Maleimido]propionic acid NHS ester, CAS #55750-62-4; Iris Biotech, Germany) and "Bis-NHS" = BS3 (Suberic acid bis[sulfo NHS ester], CAS #82436-77-9; Life Technologies, USA). One-eighth of the reaction was loaded on a SDS-PAGE gel. The band corresponding to crosslinked products was excised and subjected to in-gel trypsin digestion as described (Schmidt and Urlaub, 2009). The peptide fragments were extracted in a solvent system containing 5 % acetonitrile (ACN), 0.1 % formic acid (FA) to a final volume of 20-30 µl and submitted to liquid chromatography-tandem mass spectrometry (LC-MS/MS) analysis.



For LC-MS/MS analysis, 6  $\mu\text{l}$  of the sample solution was injected into a nano-liquid chromatography system (UltiMate™ 3000 RSLCnano system; Thermo Scientific, USA) including a 3 cm  $\times$  150  $\mu\text{m}$  inner diameter C18 trapping column in-line with a 30 cm  $\times$  75  $\mu\text{m}$  inner diameter C18 analytical column (both in-house packed with 1.9  $\mu\text{m}$  C18 material; Dr. Maisch GmbH, Germany). Peptides were desalted on the trapping column for 3 min at a flow rate of 10  $\mu\text{l}/\text{min}$  in 95 % of mobile phase A (0.1 % FA in  $\text{H}_2\text{O}$ , v/v) and 5 % of mobile phase B (80 % ACN and 0.05 % FA in  $\text{H}_2\text{O}$ , v/v), eluted from the trapping column, and separated on the analytical column using a 43 min linear gradient of 15-46 % mobile phase B at a flow rate of 300 nL/min. Separated peptides were analyzed on-line with an Orbitrap Fusion mass spectrometer (Thermo Scientific, USA). The 20 most intense precursor ions with charge states 3-8 in the survey scan (380-1580 m/z scan range) were isolated in the quadrupole mass filter (isolation window 1.6 m/z) and fragmented in the higher energy collisional dissociation (HCD) cell with 30 % normalized collision energy. A dynamic exclusion of 20 s was used. Both the survey scan (MS1) and the product ion scan (MS2) were performed in the Orbitrap at 120,000 and 30,000 resolution, respectively. Spray voltage was set at 2.3 kV and 60 % of S-lens RF level was used. Automatic gain control (AGC) targets were set at  $5 \times 10^5$  and  $5 \times 10^4$  for MS1 and MS2, respectively. All mass spectrometry work was carried out by Chung-Tien Lee.

### 6.7.5 Database search for crosslinked peptides

The raw data of LC-MS/MS analysis were converted to mascot generic format (mgf) files by Proteome Discoverer 2.0.0.802 software (Thermo Scientific, USA). The mgf files were searched against a FASTA database containing the sequences of the nanobody and Nup93 by pLink 1.22 software (Yang et al., 2012) using a target-decoy strategy. Database search parameters included mass accuracies of MS1 <10 ppm and MS2 <20 ppm, carbamidomethylation on cysteine and oxidation on methionine as variable modifications. The number of residues of each peptide on a crosslink pair was set between 4 and 100. A maximum of two trypsin missed-cleavage sites were allowed. The results were obtained with 1 % false discovery rate. The identified crosslinks were filtered with a threshold of at least two spectral counts and a pLink score <  $10e-4$ .



## 7 List of abbreviations

aa	Amino acid
Ac	Acetate
Amp	Ampicillin
ATP	Adenosine 5'-triphosphate
Avi	Biotin acceptor peptide
bd	Brachypodium distachyon
BSA	Bovine serum albumin
bp	Base pairs
CH	Constant heavy chain domain
CL	Constant light chain domain
C-terminus (CT)	Carboxy-terminus
CDR	Complementarity-determining region
Cfu	Colony-forming units
ColE9	Colicin E9
COOH	Carboxyl group
Cq	Cycle threshold value (qPCR)
CSF	Cytostatic factor
DAPI	4',6-Diamidin-2-phenylindol
DFHR	Dihydrofolate reductase
DMEM	Dulbecco's Modified Eagle Medium
DMF	Dimethylformamide
DMSO	Dimethylsulfoxide
DNA	Desoxyribonucleic acid
DOL	Degree of labeling
DTT	Dithiothreitol
E. coli	Escherichia coli
EDTA	Ethylenediaminetetraacetic acid
ELISA	Enzyme-linked immunosorbent assay
ELYS	Embryonic large molecule derived from yolk sac (= Nup)
EM	Electron microscopy
Fab	Antigen-binding fragment of an Ig molecule
Fc	Crystallizable fragment of an Ig molecule
FG	Phenylalanine-glycine dipeptide
FW	Framework
GA	Gibson assembly
GFP	Green fluorescent protein
Gly-Ser (GS)	Glycine-serine spacer/linker
GTP	Guanosine 5'-triphosphate
hCG	human chorionic gonadotropin
HEPES	4-(2-hydroxyethyl)-1-piperazineethanesulfonic acid
HSS	High speed supernatant
IBB	Importin $\beta$ -binding domain of Importin $\alpha$
IF2	<i>E. coli</i> translation initiation factor 2
Ig	Immunoglobuline
IM9	Immunity protein 9
Imp	Importin
IPTG	Isopropyl- $\beta$ -D-thiogalactopyranosid
kDa	Kilodalton
LC	Liquid chromatography
LSS	Low speed supernatant
LUT	Lookup table
mAB	Monoclonal antibody
Mal	Maleimide
MBP	Maltose binding protein
MDa	Megadalton
mRNA	Messenger RNA



---

MS/MS	Tandem mass spectrometry
NEDD8	Neural precursor cell expressed, developmentally down-regulated 8
NEDP1	NEDD8-specific protease
NPC	Nuclear pore complex
Nb	Nanobody
NH <sub>2</sub>	Amino group
NHS	N-Hydroxysuccinimide
N-terminus (NT)	Amino-terminus
NTR	Nuclear transport receptor
Nup	Nucleoporin
OD <sub>600</sub>	Optical density measured at a wavelength of 600 nm
Ori	Origin of replication
pIII	Bacteriophage minor coat protein III
PBS	Phosphate-buffered saline
PBL	Peripheral blood lymphocytes
PCR	Polymerase chain reaction
PDB	Protein data bank
peIB	pectate lyase B secretion signal
PFA	Paraformaldehyde
PMSF	Phenylmethanesulfonylfluoride
Protein III	Bacteriophage minor coat protein III
qPCR	Quantitative PCR
Ran	Ras-related nuclear protein
RanGAP	Ran GTPase-activating protein
Ran-GTP	GTP-bound Ran
RanBP2	Ran-binding protein 2
RIN	RNA integrity number
RNA	Ribonucleic acid
rRNA	Ribosomal RNA
rpm	Revolutions per minute
RT	Room temperature
RT-PCR	Reverse transcription PCR
scFv	Single-chain variable fragment
ss	Periplasmic secretion signal ( <i>E. coli</i> )
ssDNA	Single-stranded desoxynucleic acid
ssRNA	Single-stranded ribonucleic acid
SDS-PAGE	Sodium dodecyl sulfate polyacrylamide gel electrophoresis
SENP1	Sentrin-specific protease 1 / SUMO protease
SH	Thiol group
STED	Stimulated emission depletion
STORM	Stochastic optical reconstruction microscopy
SUMO	Small ubiquitin-related modifier
TB	Terrific broth medium
TCEP	Tris(2-carboxyethyl)phosphin
Tmp	Trimethoprim
TPR	Translocated promoter region protein (= Nup)
Tris	Tris(hydroxymethyl)aminomethane
tRNA	Transfer RNA
VH	Variable heavy chain domain of conventional antibodies
VHH	Variable heavy chain domain of camelid heavy chain antibodies
VL	Variable light chain domain
v/v	Volume/volume
w/v	Weight/volume
xl	<i>Xenopus laevis</i>
YT	Yeast extract tryptone medium
ZZ	IgG-binding domain of <i>Staphylococcus</i> protein A (in tandem)



## 8 Contribution by others

Science is a team effort and also this study relied on the help of many excellent collaborators. First of all, I would like to point out the work of Marc Böhning, who I supervised during his Master thesis in this lab. Marc established the qPCR workflow for phage quantification. Furthermore, he created an initial version of the minimal phagemid and performed all the necessary quality controls. Jens Krull was of permanent help throughout my Ph.D. He helped with alpaca immunizations and total RNA preparation. He also carried out the nanobody selections against RanBP2 and the Nup107 complex under my supervision. Furthermore, Jens supplied me with LSS egg extract.

The electron microscopy work was carried out by Jan Erik Schliep (MPI for Biophysical Chemistry; Department for Structural Dynamics) and involved negative staining, image acquisition and image analysis.

Sergei Trakhanov collected diffraction data of Nup98•anti-Nup98 Nb TP377 complex crystals. He also solved the structure of the complex by molecular replacement.

The super-resolution microscopy part in this thesis is based on two collaborations with the Department of NanoBiophotonics (MPI for Biophysical Chemistry). In all cases I provided the stained cells. Image acquisition and analysis was carried out by my collaborators. STORM images were taken by Mark Bates and STED images by Fabian Göttfert.

For crosslinking mass spectrometry, I provided the crosslinked sample on a gel that was handed over to Chung-Tien Lee (MPI for Biophysical Chemistry; Bioanalytics Group) for in-gel digestion and LC-MS/MS analysis.

Bastian Hülsmann prepared cytosol, membranes and sperm chromatin for nuclear assembly assays and also helped in the preparation of CSF egg extracts.

Bernard Freytag established the use of trimethoprim in the lab.

Koray Kirli wrote an amazing python script for the quick analysis of 96-well sequencing data.



## 9 Acknowledgments

I am very grateful to my supervisor Dirk Görlich for providing me with the unique opportunity to establish an alpaca farm and nanobody production pipeline. It was an incredible experience that I would not have wanted to miss. You taught me what it means to do science and how to do it properly. I very much enjoyed our discussions and troubleshooting sessions and your passion for science that you constantly share with others.

I would like to thank Peter Rehling and Reinhard Lührmann for their input during our thesis committee meetings as well as for reading this thesis.

This work would have been impossible without the constant alpaca care by the animal facility. I would like to especially thank Rolf Rümenapf and Ulrike Teichmann for alpaca immunization and blood withdrawal. Furthermore, I am in great debt of Jens Krull, an extremely skilled technician, who helped me a lot with total RNA isolation, library construction and phage display. Gabriele Hawlitschek did most of my (thousands of) DNA Mini and Midi preparations and also supplied the lab with SDS-PAGE gels, media and buffers (together with Uwe Hoffmann). This was simply luxury! Renate Rees and Jürgen Schünemann helped with protein production.



**Figure 9.1. Alpacas at the MPI for Biophysical Chemistry in August 2013.**

Of course our alpacas deserve to be acknowledged! From left to right: Olga, Rita, Erna, Ramona, Doris and her daughter Klara. Picture by Irene Böttcher-Gajewski, Media service MPIbpc.



I very much enjoyed working in the Görlich lab and would like to thank all members (past and present) for making the many hours spent here worthwhile: Broder Schmidt for the occasional evening beer; Jennifer Seefeldt for an endless supply of chocolate and cookies; Metin Aksu + Kevser Gencalp + Samir Karaca and Bastian Hülsmann for entertaining lunch and coffee breaks; Koray Kirli for motivation, inspiration and good mood; Steffen Frey for constructive criticism! I learned a lot from all of you, especially during our common lab and literature seminars.

My friends and family constantly supported me during this time. I am very grateful to have you. The biggest ‘thank you’, however, can only go to Nataliia Naumenko simply for being there with me in good and bad times. Thank you for your incredible warm-heartedness, joy and love. What would I do without you?

## 10 References

- Achour, I. et al. (2008) Tetrameric and homodimeric camelid IgGs originate from the same IgH locus. *J Immunol*, **181**, 2001-2009.
- Adam, E.J. & Adam, S.A. (1994) Identification of cytosolic factors required for nuclear location sequence-mediated binding to the nuclear envelope. *J Cell Biol*, **125**, 547-555.
- Adams, P.D. et al. (2010) PHENIX: a comprehensive Python-based system for macromolecular structure solution. *Acta Crystallogr D Biol Crystallogr*, **66**, 213-221.
- Alber, F. et al. (2007) The molecular architecture of the nuclear pore complex. *Nature*, **450**, 695-701.
- Amlacher, S. et al. (2011) Insight into structure and assembly of the nuclear pore complex by utilizing the genome of a eukaryotic thermophile. *Cell*, **146**, 277-289.
- Andersen, K.R. et al. (2013) Scaffold nucleoporins Nup188 and Nup192 share structural and functional properties with nuclear transport receptors. *Elife*, **2**, e00745.
- Antonin, W., Franz, C., Haselmann, U., Antony, C. & Mattaj, I.W. (2005) The integral membrane nucleoporin pom121 functionally links nuclear pore complex assembly and nuclear envelope formation. *Mol Cell*, **17**, 83-92.
- Arbabi Ghahroudi, M., Desmyter, A., Wyns, L., Hamers, R. & Muyldermans, S. (1997) Selection and identification of single domain antibody fragments from camel heavy-chain antibodies. *FEBS Lett*, **414**, 521-526.
- Asano, S., Higashitani, A. & Horiuchi, K. (1999) Filamentous phage replication initiator protein gpII forms a covalent complex with the 5' end of the nick it introduced. *Nucleic Acids Res*, **27**, 1882-1889.
- Bailer, S.M. et al. (1998) Nup116p and nup100p are interchangeable through a conserved motif which constitutes a docking site for the mRNA transport factor gle2p. *EMBO J*, **17**, 1107-1119.
- Baneyx, F. & Mujacic, M. (2004) Recombinant protein folding and misfolding in *Escherichia coli*. *Nat Biotechnol*, **22**, 1399-1408.
- Barbas, C.F., Kang, A.S., Lerner, R.A. & Benkovic, S.J. (1991) Assembly of combinatorial antibody libraries on phage surfaces: the gene III site. *Proc Natl Acad Sci U S A*, **88**, 7978-7982.
- Bastos, R., Lin, A., Enarson, M. & Burke, B. (1996) Targeting and function in mRNA export of nuclear pore complex protein Nup153. *J Cell Biol*, **134**, 1141-1156.
- Bastos, R., Ribas de Pouplana, L., Enarson, M., Bodoor, K. & Burke, B. (1997) Nup84, a novel nucleoporin that is associated with CAN/Nup214 on the cytoplasmic face of the nuclear pore complex. *J Cell Biol*, **137**, 989-1000.
- Bates, M., Huang, B., Dempsey, G.T. & Zhuang, X. (2007) Multicolor super-resolution imaging with photo-switchable fluorescent probes. *Science*, **317**, 1749-1753.
- Bauer, M. & Smith, G.P. (1988) Filamentous phage morphogenetic signal sequence and orientation of DNA in the virion and gene-V protein complex. *Virology*, **167**, 166-175.
- Beckett, D., Kovaleva, E. & Schatz, P.J. (1999) A minimal peptide substrate in biotin holoenzyme synthetase-catalyzed biotinylation. *Protein Sci*, **8**, 921-929.
- Belgareh, N. et al. (1998) Functional characterization of a Nup159p-containing nuclear pore subcomplex. *Mol Biol Cell*, **9**, 3475-3492.
- Bernad, R., Engelsma, D., Sanderson, H., Pickersgill, H. & Fornerod, M. (2006) Nup214-Nup88 nucleoporin subcomplex is required for CRM1-mediated 60 S preribosomal nuclear export. *J Biol Chem*, **281**, 19378-19386.
- Bessette, P.H., Aslund, F., Beckwith, J. & Georgiou, G. (1999) Efficient folding of proteins with multiple disulfide bonds in the *Escherichia coli* cytoplasm. *Proc Natl Acad Sci U S A*, **96**, 13703-13708.
- Beste, G., Schmidt, F.S., Stibora, T. & Skerra, A. (1999) Small antibody-like proteins with prescribed ligand specificities derived from the lipocalin fold. *Proc Natl Acad Sci U S A*, **96**, 1898-1903.
- Better, M., Chang, C.P., Robinson, R.R. & Horwitz, A.H. (1988) *Escherichia coli* secretion of an active chimeric antibody fragment. *Science*, **240**, 1041-1043.
- Binz, H.K. et al. (2004) High-affinity binders selected from designed ankyrin repeat protein libraries. *Nat Biotechnol*, **22**, 575-582.
- Bischoff, F.R. & Görlich, D. (1997) RanBP1 is crucial for the release of RanGTP from importin beta-related nuclear transport factors. *FEBS Lett*, **419**, 249-254.
- Bischoff, F.R. & Ponstingl, H. (1991) Catalysis of guanine nucleotide exchange on Ran by the mitotic regulator RCC1. *Nature*, **354**, 80-82.
- Boder, E.T., Midelfort, K.S. & Wittrup, K.D. (2000) Directed evolution of antibody fragments with monovalent femtomolar antigen-binding affinity. *Proc Natl Acad Sci U S A*, **97**, 10701-10705.
- Boss, M.A., Kenten, J.H., Wood, C.R. & Emtage, J.S. (1984) Assembly of functional antibodies from immunoglobulin heavy and light chains synthesised in *E. coli*. *Nucleic Acids Res*, **12**, 3791-3806.

- Bradbury, A. & Plückthun, A. (2015a) Reproducibility: Standardize antibodies used in research. *Nature*, **518**, 27-29.
- Bradbury, A.R. & Plückthun, A. (2015b) Getting to reproducible antibodies: the rationale for sequenced recombinant characterized reagents. *Protein Eng Des Sel*, **28**, 303-305.
- Bradbury, A.R., Sidhu, S., Dübel, S. & McCafferty, J. (2011) Beyond natural antibodies: the power of in vitro display technologies. *Nat Biotechnol*, **29**, 245-254.
- Braun, M.B. et al. (2016) Peptides in headlock - a novel high-affinity and versatile peptide-binding nanobody for proteomics and microscopy. *Sci Rep*, **6**, 19211.
- Breitling, F., Dübel, S., Seehaus, T., Klewinghaus, I. & Little, M. (1991) A surface expression vector for antibody screening. *Gene*, **104**, 147-153.
- Brohawn, S.G., Lekska, N.C., Spear, E.D., Rajashankar, K.R. & Schwartz, T.U. (2008) Structural evidence for common ancestry of the nuclear pore complex and vesicle coats. *Science*, **322**, 1369-1373.
- Brohawn, S.G., Partridge, J.R., Whittle, J.R. & Schwartz, T.U. (2009) The nuclear pore complex has entered the atomic age. *Structure*, **17**, 1156-1168.
- Bui, K.H. et al. (2013) Integrated structural analysis of the human nuclear pore complex scaffold. *Cell*, **155**, 1233-1243.
- Busche, B. (2013) *New Algorithms for Automated Processing of Electronmicroscopic Images*. Shaker Verlag, Göttingen.
- Cabilly, S. et al. (1984) Generation of antibody activity from immunoglobulin polypeptide chains produced in *Escherichia coli*. *Proc Natl Acad Sci U S A*, **81**, 3273-3277.
- Callan, H.G. & Tomlin, S.G. (1950) Experimental studies on amphibian oocyte nuclei. I. Investigation of the structure of the nuclear membrane by means of the electron microscope. *Proc R Soc Lond B Biol Sci*, **137**, 367-378.
- Chi, N.C., Adam, E.J. & Adam, S.A. (1995) Sequence and characterization of cytoplasmic nuclear protein import factor p97. *J Cell Biol*, **130**, 265-274.
- Chomczynski, P. & Sacchi, N. (2006) The single-step method of RNA isolation by acid guanidinium thiocyanate-phenol-chloroform extraction: twenty-something years on. *Nat Protoc*, **1**, 581-585.
- Chug, H., Trakhanov, S., Hülsmann, B.B., Pleiner, T. & Görlich, D. (2015) Crystal structure of the metazoan Nup62•Nup58•Nup54 nucleoporin complex. *Science*, **350**, 106-110.
- Clackson, T., Hoogenboom, H.R., Griffiths, A.D. & Winter, G. (1991) Making antibody fragments using phage display libraries. *Nature*, **352**, 624-628.
- Click, E.M. & Webster, R.E. (1997) Filamentous phage infection: required interactions with the TolA protein. *J Bacteriol*, **179**, 6464-6471.
- Click, E.M. & Webster, R.E. (1998) The TolQRA proteins are required for membrane insertion of the major capsid protein of the filamentous phage f1 during infection. *J Bacteriol*, **180**, 1723-1728.
- Colwill, K., Renewable, Protein Binder Working Group & Gräslund, S. (2011) A roadmap to generate renewable protein binders to the human proteome. *Nat Methods*, **8**, 551-558.
- Conrath, K.E. et al. (2001) Beta-lactamase inhibitors derived from single-domain antibody fragments elicited in the camelidae. *Antimicrob Agents Chemother*, **45**, 2807-2812.
- Cordes, V.C., Reidenbach, S., Rackwitz, H.R. & Franke, W.W. (1997) Identification of protein p270/Tpr as a constitutive component of the nuclear pore complex-attached intranuclear filaments. *J Cell Biol*, **136**, 515-529.
- Cronshaw, J.M., Krutchinsky, A.N., Zhang, W., Chait, B.T. & Matunis, M.J. (2002) Proteomic analysis of the mammalian nuclear pore complex. *J Cell Biol*, **158**, 915-927.
- Cwirla, S.E., Peters, E.A., Barrett, R.W. & Dower, W.J. (1990) Peptides on phage: a vast library of peptides for identifying ligands. *Proc Natl Acad Sci U S A*, **87**, 6378-6382.
- Davies, J. & Riechmann, L. (1994) 'Camelising' human antibody fragments: NMR studies on VH domains. *FEBS Lett*, **339**, 285-290.
- Day, L.A. & Wiseman, R.L. (1978) A Comparison of DNA Packaging in the Virions of fd, Xf, and Pf1. In *The Single-Stranded DNA Phages*, (Eds, Denhardt, D.T., Dressler, D. & Ray, D.S.) Cold Spring Harbor Laboratory, Cold Spring Harbor, NY, USA, pp. 605-625.
- De Genst, E. et al. (2006) Molecular basis for the preferential cleft recognition by dromedary heavy-chain antibodies. *Proc Natl Acad Sci U S A*, **103**, 4586-4591.
- De Genst, E.J. et al. (2010) Structure and properties of a complex of  $\alpha$ -synuclein and a single-domain camelid antibody. *J Mol Biol*, **402**, 326-343.
- de Marco, A. (2009) Strategies for successful recombinant expression of disulfide bond-dependent proteins in *Escherichia coli*. *Microb Cell Fact*, **8**, 26.
- Dempsey, G.T., Vaughan, J.C., Chen, K.H., Bates, M. & Zhuang, X. (2011) Evaluation of fluorophores for optimal performance in localization-based super-resolution imaging. *Nat Methods*, **8**, 1027-1036.

- Deng, L.W., Malik, P. & Perham, R.N. (1999) Interaction of the globular domains of pIII protein of filamentous bacteriophage fd with the F-pilus of *Escherichia coli*. *Virology*, **253**, 271-277.
- Derman, A.I., Prinz, W.A., Belin, D. & Beckwith, J. (1993) Mutations that allow disulfide bond formation in the cytoplasm of *Escherichia coli*. *Science*, **262**, 1744-1747.
- Desmyter, A., Decanniere, K., Muyldermans, S. & Wyns, L. (2001) Antigen specificity and high affinity binding provided by one single loop of a camel single-domain antibody. *J Biol Chem*, **276**, 26285-26290.
- Desmyter, A., Spinelli, S., Roussel, A. & Cambillau, C. (2015) Camelid nanobodies: killing two birds with one stone. *Curr Opin Struct Biol*, **32C**, 1-8.
- Desmyter, A. et al. (1996) Crystal structure of a camel single-domain VH antibody fragment in complex with lysozyme. *Nat Struct Biol*, **3**, 803-811.
- Devlin, J.J., Panganiban, L.C. & Devlin, P.E. (1990) Random peptide libraries: a source of specific protein binding molecules. *Science*, **249**, 404-406.
- Dias-Neto, E. et al. (2009) Next-generation phage display: integrating and comparing available molecular tools to enable cost-effective high-throughput analysis. *PLoS One*, **4**, e8338.
- Dingwall, C., Sharnick, S.V. & Laskey, R.A. (1982) A polypeptide domain that specifies migration of nucleoplasmin into the nucleus. *Cell*, **30**, 449-458.
- Djender, S. et al. (2014) Bacterial cytoplasm as an effective cell compartment for producing functional VHH-based affinity reagents and Camelidae IgG-like recombinant antibodies. *Microb Cell Fact*, **13**, 140.
- Dotto, G.P., Enea, V. & Zinder, N.D. (1981) Functional analysis of bacteriophage f1 intergenic region. *Virology*, **114**, 463-473.
- Doucet, C.M., Talamas, J.A. & Hetzer, M.W. (2010) Cell cycle-dependent differences in nuclear pore complex assembly in metazoa. *Cell*, **141**, 1030-1041.
- Dube, P., Tavares, P., Lurz, R. & van Heel, M. (1993) The portal protein of bacteriophage SPP1: a DNA pump with 13-fold symmetry. *EMBO J*, **12**, 1303-1309.
- Dumoulin, M. et al. (2002) Single-domain antibody fragments with high conformational stability. *Protein Sci*, **11**, 500-515.
- Eibauer, M. et al. (2015) Structure and gating of the nuclear pore complex. *Nat Commun*, **6**, 7532.
- Eisenhardt, N., Redolfi, J. & Antonin, W. (2014) Interaction of Nup53 with Ndc1 and Nup155 is required for nuclear pore complex assembly. *J Cell Sci*, **127**, 908-921.
- Ellison, T.R., Mathisen, P.M. & Miller, L. (1985) Developmental changes in keratin patterns during epidermal maturation. *Dev Biol*, **112**, 329-337.
- Endemann, H. & Model, P. (1995) Location of filamentous phage minor coat proteins in phage and in infected cells. *J Mol Biol*, **250**, 496-506.
- Eriksson, C., Rustum, C. & Hallberg, E. (2004) Dynamic properties of nuclear pore complex proteins in gp210 deficient cells. *FEBS Lett*, **572**, 261-265.
- Favreau, C., Worman, H.J., Wozniak, R.W., Frappier, T. & Courvalin, J.C. (1996) Cell cycle-dependent phosphorylation of nucleoporins and nuclear pore membrane protein Gp210. *Biochemistry*, **35**, 8035-8044.
- Feilmeier, B.J., Iseminger, G., Schroeder, D., Webber, H. & Phillips, G.J. (2000) Green fluorescent protein functions as a reporter for protein localization in *Escherichia coli*. *J Bacteriol*, **182**, 4068-4076.
- Feldherr, C.M. (1962) The nuclear annuli as pathways for nucleocytoplasmic exchanges. *J Cell Biol*, **14**, 65-72.
- Finlay, D.R. & Forbes, D.J. (1990) Reconstitution of biochemically altered nuclear pores: transport can be eliminated and restored. *Cell*, **60**, 17-29.
- Fischer, J., Teimer, R., Amlacher, S., Kunze, R. & Hurt, E. (2015) Linker Nups connect the nuclear pore complex inner ring with the outer ring and transport channel. *Nat Struct Mol Biol*, **22**, 774-781.
- Flajnik, M.F., Deschacht, N. & Muyldermans, S. (2011) A case of convergence: why did a simple alternative to canonical antibodies arise in sharks and camels? *PLoS Biol*, **9**, e1001120.
- Flemming, D. et al. (2012) Analysis of the yeast nucleoporin Nup188 reveals a conserved S-like structure with similarity to karyopherins. *J Struct Biol*, **177**, 99-105.
- Flemming, D., Thierbach, K., Stelter, P., Böttcher, B. & Hurt, E. (2010) Precise mapping of subunits in multiprotein complexes by a versatile electron microscopy label. *Nat Struct Mol Biol*, **17**, 775-778.
- Fontoura, B.M., Blobel, G. & Matunis, M.J. (1999) A conserved biogenesis pathway for nucleoporins: proteolytic processing of a 186-kilodalton precursor generates Nup98 and the novel nucleoporin, Nup96. *J Cell Biol*, **144**, 1097-1112.
- Fornerod, M., Ohno, M., Yoshida, M. & Mattaj, I.W. (1997a) CRM1 is an export receptor for leucine-rich nuclear export signals. *Cell*, **90**, 1051-1060.

- Fornerod, M. et al. (1997b) The human homologue of yeast CRM1 is in a dynamic subcomplex with CAN/Nup214 and a novel nuclear pore component Nup88. *EMBO J*, **16**, 807-816.
- Franz, C. et al. (2005) Nup155 regulates nuclear envelope and nuclear pore complex formation in nematodes and vertebrates. *EMBO J*, **24**, 3519-3531.
- Frey, S. & Görlich, D. (2014a) A new set of highly efficient, tag-cleaving proteases for purifying recombinant proteins. *J Chromatogr A*, **1337**, 95-105.
- Frey, S. & Görlich, D. (2014b) Purification of protein complexes of defined subunit stoichiometry using a set of orthogonal, tag-cleaving proteases. *J Chromatogr A*, **1337**, 106-115.
- Frey, S. & Görlich, D. (2007) A saturated FG-repeat hydrogel can reproduce the permeability properties of nuclear pore complexes. *Cell*, **130**, 512-523.
- Frey, S., Richter, R.P. & Görlich, D. (2006) FG-rich repeats of nuclear pore proteins form a three-dimensional meshwork with hydrogel-like properties. *Science*, **314**, 815-817.
- Fridy, P.C. et al. (2014) A robust pipeline for rapid production of versatile nanobody repertoires. *Nat Methods*, **11**, 1253-1260.
- Fridy, P.C., Thompson, M.K., Ketaren, N.E. & Rout, M.P. (2015) Engineered high-affinity nanobodies recognizing staphylococcal Protein A and suitable for native isolation of protein complexes. *Anal Biochem*, **477**, 92-94.
- Fulford, W. & Model, P. (1988) Bacteriophage f1 DNA replication genes. II. The roles of gene V protein and gene II protein in complementary strand synthesis. *J Mol Biol*, **203**, 39-48.
- Gaik, M. et al. (2015) Structural basis for assembly and function of the Nup82 complex in the nuclear pore scaffold. *J Cell Biol*, **208**, 283-297.
- Gall, J.G. (1954) Observations on the nuclear membrane with the electron microscope. *Exp Cell Res*, **7**, 197-200.
- Gall, J.G. (1967) Octagonal nuclear pores. *J Cell Biol*, **32**, 391-399.
- Gibson, D.G. (2011) Enzymatic assembly of overlapping DNA fragments. *Methods Enzymol*, **498**, 349-361.
- Gibson, D.G. et al. (2009) Enzymatic assembly of DNA molecules up to several hundred kilobases. *Nat Methods*, **6**, 343-345.
- Glavy, J.S. et al. (2007) Cell-cycle-dependent phosphorylation of the nuclear pore Nup107-160 subcomplex. *Proc Natl Acad Sci U S A*, **104**, 3811-3816.
- Glockshuber, R., Schmidt, T. & Plückthun, A. (1992) The disulfide bonds in antibody variable domains: effects on stability, folding in vitro, and functional expression in Escherichia coli. *Biochemistry*, **31**, 1270-1279.
- Görlich, D. et al. (1996a) Importin provides a link between nuclear protein import and U snRNA export. *Cell*, **87**, 21-32.
- Görlich, D. & Kutay, U. (1999) Transport between the cell nucleus and the cytoplasm. *Annu Rev Cell Dev Biol*, **15**, 607-660.
- Görlich, D., Panté, N., Kutay, U., Aebi, U. & Bischoff, F.R. (1996b) Identification of different roles for RanGDP and RanGTP in nuclear protein import. *EMBO J*, **15**, 5584-5594.
- Görlich, D., Prehn, S., Laskey, R.A. & Hartmann, E. (1994) Isolation of a protein that is essential for the first step of nuclear protein import. *Cell*, **79**, 767-778.
- Görlich, D., Vogel, F., Mills, A.D., Hartmann, E. & Laskey, R.A. (1995) Distinct functions for the two importin subunits in nuclear protein import. *Nature*, **377**, 246-248.
- Göttfert, F. et al. (2013) Coaligned dual-channel STED nanoscopy and molecular diffusion analysis at 20 nm resolution. *Biophys J*, **105**(1), L01-L03.
- Govaert, J. et al. (2012) Dual beneficial effect of interloop disulfide bond for single domain antibody fragments. *J Biol Chem*, **287**, 1970-1979.
- Grandi, P. et al. (1997) Nup93, a vertebrate homologue of yeast Nic96p, forms a complex with a novel 205-kDa protein and is required for correct nuclear pore assembly. *Mol Biol Cell*, **8**, 2017-2038.
- Greber, U.F., Senior, A. & Gerace, L. (1990) A major glycoprotein of the nuclear pore complex is a membrane-spanning polypeptide with a large luminal domain and a small cytoplasmic tail. *EMBO J*, **9**, 1495-1502.
- Greenberg, A.S. et al. (1995) A new antigen receptor gene family that undergoes rearrangement and extensive somatic diversification in sharks. *Nature*, **374**, 168-173.
- Griffis, E.R., Xu, S. & Powers, M.A. (2003) Nup98 localizes to both nuclear and cytoplasmic sides of the nuclear pore and binds to two distinct nucleoporin subcomplexes. *Mol Biol Cell*, **14**, 600-610.
- Gu, H. et al. (1995) A phage display system for studying the sequence determinants of protein folding. *Protein Sci*, **4**, 1108-1117.
- Guo, Y.C. et al. (2006) Phage display mediated immuno-PCR. *Nucleic Acids Res*, **34**, e62.

- Güttler, T. et al. (2010) NES consensus redefined by structures of PKI-type and Rev-type nuclear export signals bound to CRM1. *Nat Struct Mol Biol*, **17**, 1367-1376.
- Hamers-Casterman, C. et al. (1993) Naturally occurring antibodies devoid of light chains. *Nature*, **363**, 446-448.
- Hanahan, D. (1983) Studies on transformation of *Escherichia coli* with plasmids. *J Mol Biol*, **166**, 557-580.
- Hannak, E. & Heald, R. (2006) Investigating mitotic spindle assembly and function in vitro using *Xenopus laevis* egg extracts. *Nat Protoc*, **1**, 2305-2314.
- Harel, A. et al. (2003) Removal of a single pore subcomplex results in vertebrate nuclei devoid of nuclear pores. *Mol Cell*, **11**, 853-864.
- Harmsen, M.M. et al. (2000) Llama heavy-chain V regions consist of at least four distinct subfamilies revealing novel sequence features. *Mol Immunol*, **37**, 579-590.
- Harris, L.J., Larson, S.B., Hasel, K.W. & McPherson, A. (1997) Refined structure of an intact IgG2a monoclonal antibody. *Biochemistry*, **36**, 1581-1597.
- Harris, L.J., Skaletsky, E. & McPherson, A. (1998) Crystallographic structure of an intact IgG1 monoclonal antibody. *J Mol Biol*, **275**, 861-872.
- Hase, M.E. & Cordes, V.C. (2003) Direct interaction with nup153 mediates binding of Tpr to the periphery of the nuclear pore complex. *Mol Biol Cell*, **14**, 1923-1940.
- Hase, M.E., Kuznetsov, N.V. & Cordes, V.C. (2001) Amino acid substitutions of coiled-coil protein Tpr abrogate anchorage to the nuclear pore complex but not parallel, in-register homodimerization. *Mol Biol Cell*, **12**, 2433-2452.
- Hawkins, R.E., Russell, S.J. & Winter, G. (1992) Selection of phage antibodies by binding affinity. Mimicking affinity maturation. *J Mol Biol*, **226**, 889-896.
- Hawryluk-Gara, L.A., Platani, M., Santarella, R., Wozniak, R.W. & Mattaj, I.W. (2008) Nup53 is required for nuclear envelope and nuclear pore complex assembly. *Mol Biol Cell*, **19**, 1753-1762.
- Hawryluk-Gara, L.A., Shibuya, E.K. & Wozniak, R.W. (2005) Vertebrate Nup53 interacts with the nuclear lamina and is required for the assembly of a Nup93-containing complex. *Mol Biol Cell*, **16**, 2382-2394.
- Hell, S.W. (2009) Microscopy and its focal switch. *Nat Methods*, **6**, 24-32.
- Hinshaw, J.E., Carragher, B.O. & Milligan, R.A. (1992) Architecture and design of the nuclear pore complex. *Cell*, **69**, 1133-1141.
- Hodel, A.E. et al. (2002) The three-dimensional structure of the autoproteolytic, nuclear pore-targeting domain of the human nucleoporin Nup98. *Mol Cell*, **10**, 347-358.
- Hoffman-Berling, H., Duerwald, H. & Beulke, I. (1963) Ein fädiger DNS-Phage (fd) und ein sphärischer RNS-Phage (fr) wirtsspezifisch für männliche Stämme von *E. coli*. *Z Naturforsch B*, **18**, 893-898.
- Hofschneider, P.H. (1963) Untersuchungen über "kleine" *E. coli* K12 Bakteriophagen. *Z Naturforschung*, **18B**, 203-210.
- Holliger, P. & Hudson, P.J. (2005) Engineered antibody fragments and the rise of single domains. *Nat Biotechnol*, **23**, 1126-1136.
- Hoogenboom, H.R. (2005) Selecting and screening recombinant antibody libraries. *Nat Biotechnol*, **23**, 1105-1116.
- Hoogenboom, H.R. et al. (1991) Multi-subunit proteins on the surface of filamentous phage: methodologies for displaying antibody (Fab) heavy and light chains. *Nucleic Acids Res*, **19**, 4133-4137.
- Hornsby, M. et al. (2015) A High Through-put Platform for Recombinant Antibodies to Folded Proteins. *Mol Cell Proteomics*, **14**, 2833-2847.
- Hsia, K.C., Stavropoulos, P., Blobel, G. & Hoelz, A. (2007) Architecture of a coat for the nuclear pore membrane. *Cell*, **131**, 1313-1326.
- Huang, B., Bates, M. & Zhuang, X. (2009) Super-resolution fluorescence microscopy. *Annu Rev Biochem*, **78**, 993-1016.
- Huang, B., Wang, W., Bates, M. & Zhuang, X. (2008) Three-dimensional super-resolution imaging by stochastic optical reconstruction microscopy. *Science*, **319**, 810-813.
- Hülsmann, B.B., Labokha, A.A. & Gorlich, D. (2012) The permeability of reconstituted nuclear pores provides direct evidence for the selective phase model. *Cell*, **150**, 738-751.
- Huston, J.S. et al. (1988) Protein engineering of antibody binding sites: recovery of specific activity in an anti-digoxin single-chain Fv analogue produced in *Escherichia coli*. *Proc Natl Acad Sci U S A*, **85**, 5879-5883.
- Hutten, S., Flotho, A., Melchior, F. & Kehlenbach, R.H. (2008) The Nup358-RanGAP complex is required for efficient importin alpha/beta-dependent nuclear import. *Mol Biol Cell*, **19**, 2300-2310.
- Hutten, S., Wälde, S., Spillner, C., Hauber, J. & Kehlenbach, R.H. (2009) The nuclear pore component Nup358 promotes transportin-dependent nuclear import. *J Cell Sci*, **122**, 1100-1110.

- Imamoto, N. et al. (1995) The nuclear pore-targeting complex binds to nuclear pores after association with a karyophile. *FEBS Lett*, **368**, 415-419.
- Izaurrealde, E., Kutay, U., von Kobbe, C., Mattaj, I.W. & Görlich, D. (1997) The asymmetric distribution of the constituents of the Ran system is essential for transport into and out of the nucleus. *EMBO J*, **16**, 6535-6547.
- Jaye, D.L. et al. (2003) Use of real-time polymerase chain reaction to identify cell- and tissue-type-selective peptides by phage display. *Am J Pathol*, **162**, 1419-1429.
- Jespersen, L., Schon, O., Famm, K. & Winter, G. (2004) Aggregation-resistant domain antibodies selected on phage by heat denaturation. *Nat Biotechnol*, **22**, 1161-1165.
- Judy, S. & Schwartz, T.U. (2007) Crystal structure of nucleoporin Nic96 reveals a novel, intricate helical domain architecture. *J Biol Chem*, **282**, 34904-34912.
- Kalderon, D., Roberts, B.L., Richardson, W.D. & Smith, A.E. (1984) A short amino acid sequence able to specify nuclear location. *Cell*, **39**, 499-509.
- Kampmann, M., Atkinson, C.E., Mattheyses, A.L. & Simon, S.M. (2011) Mapping the orientation of nuclear pore proteins in living cells with polarized fluorescence microscopy. *Nat Struct Mol Biol*, **18**, 643-649.
- Kaplan, C. & Ewers, H. (2015) Optimized sample preparation for single-molecule localization-based superresolution microscopy in yeast. *Nat Protoc*, **10**, 1007-1021.
- Kassube, S.A. et al. (2012) Crystal structure of the N-terminal domain of Nup358/RanBP2. *J Mol Biol*, **423**, 752-765.
- Kastner, B. et al. (2008) GraFix: sample preparation for single-particle electron cryomicroscopy. *Nat Methods*, **5**, 53-55.
- Kazmierczak, B.I., Mielke, D.L., Russel, M. & Model, P. (1994) pIV, a filamentous phage protein that mediates phage export across the bacterial cell envelope, forms a multimer. *J Mol Biol*, **238**, 187-198.
- Kelley, K., Knockenhauer, K.E., Kabachinski, G. & Schwartz, T.U. (2015) Atomic structure of the Y complex of the nuclear pore. *Nat Struct Mol Biol*, **22**, 425-431.
- Kirchhofer, A. et al. (2010) Modulation of protein properties in living cells using nanobodies. *Nat Struct Mol Biol*, **17**, 133-138.
- Kırlı, K. et al. (2015) A deep proteomics perspective on CRM1-mediated nuclear export and nucleocytoplasmic partitioning. *Elife*, **4**.
- Knockenhauer, K.E. & Schwartz, T.U. (2016) The Nuclear Pore Complex as a Flexible and Dynamic Gate. *Cell*, **164**, 1162-1171.
- Koh, J. & Blobel, G. (2015) Allosteric Regulation in Gating the Central Channel of the Nuclear Pore Complex. *Cell*, **161**, 1361-1373.
- Köhler, G. & Milstein, C. (1975) Continuous cultures of fused cells secreting antibody of predefined specificity. *Nature*, **256**, 495-497.
- Koide, A., Bailey, C.W., Huang, X. & Koide, S. (1998) The fibronectin type III domain as a scaffold for novel binding proteins. *J Mol Biol*, **284**, 1141-1151.
- Kolmakov, K. et al. (2010) Red-emitting rhodamine dyes for fluorescence microscopy and nanoscopy. *Chemistry*, **16**, 158-166.
- Konthur, Z., Wilde, J. & Lim, T.S. (2010) Semi-automated magnetic beads-based antibody selection from phage display libraries. In *Antibody Engineering Vol.1*, (Eds, Kontermann, R. & Dübel, S.) Springer-Verlag, Berlin Heidelberg, pp. 267-287.
- Krebber, A. et al. (1997) Reliable cloning of functional antibody variable domains from hybridomas and spleen cell repertoires employing a reengineered phage display system. *J Immunol Methods*, **201**, 35-55.
- Kristensen, P. & Winter, G. (1998) Proteolytic selection for protein folding using filamentous bacteriophages. *Fold Des*, **3**, 321-328.
- Krull, S., Thyberg, J., Björkroth, B., Rackwitz, H.R. & Cordes, V.C. (2004) Nucleoporins as components of the nuclear pore complex core structure and Tpr as the architectural element of the nuclear basket. *Mol Biol Cell*, **15**, 4261-4277.
- Kutay, U., Bischoff, F.R., Kostka, S., Kraft, R. & Görlich, D. (1997) Export of importin alpha from the nucleus is mediated by a specific nuclear transport factor. *Cell*, **90**, 1061-1071.
- Labokha, A.A. et al. (2013) Systematic analysis of barrier-forming FG hydrogels from Xenopus nuclear pore complexes. *EMBO J*, **32**, 204-218.
- Laemmli, U.K. (1970) Cleavage of structural proteins during the assembly of the head of bacteriophage T4. *Nature*, **227**, 680-685.
- Lanford, R.E. & Butel, J.S. (1984) Construction and characterization of an SV40 mutant defective in nuclear transport of T antigen. *Cell* **37**, 801-813.

- Langedijk, A.C. et al. (1998) The nature of antibody heavy chain residue H6 strongly influences the stability of a VH domain lacking the disulfide bridge. *J Mol Biol*, **283**, 95-110.
- Laurell, E. et al. (2011) Phosphorylation of Nup98 by multiple kinases is crucial for NPC disassembly during mitotic entry. *Cell*, **144**, 539-550.
- Lauwereys, M. et al. (1998) Potent enzyme inhibitors derived from dromedary heavy-chain antibodies. *EMBO J*, **17**, 3512-3520.
- Lei, S.P., Lin, H.C., Wang, S.S., Callaway, J. & Wilcox, G. (1987) Characterization of the *Erwinia carotovora* pelB gene and its product pectate lyase. *J Bacteriol*, **169**, 4379-4383.
- Liu, L., Spurrier, J., Butt, T.R. & Strickler, J.E. (2008) Enhanced protein expression in the baculovirus/insect cell system using engineered SUMO fusions. *Protein Expr Purif*, **62**, 21-28.
- Lobstein, J. et al. (2012) SHuffle, a novel *Escherichia coli* protein expression strain capable of correctly folding disulfide bonded proteins in its cytoplasm. *Microb Cell Fact*, **11**, 56.
- Loeb, T. (1960) Isolation of a bacteriophage specific for the F plus and Hfr mating types of *Escherichia coli* K-12. *Science*, **131**, 932-933.
- Löschberger, A. et al. (2012) Super-resolution imaging visualizes the eightfold symmetry of gp210 proteins around the nuclear pore complex and resolves the central channel with nanometer resolution. *J Cell Sci*, **125**, 570-575.
- Lowman, H.B., Bass, S.H., Simpson, N. & Wells, J.A. (1991) Selecting high-affinity binding proteins by monovalent phage display. *Biochemistry*, **30**, 10832-10838.
- Lubkowski, J., Hennecke, F., Plückthun, A. & Wlodawer, A. (1999) Filamentous phage infection: crystal structure of g3p in complex with its coreceptor, the C-terminal domain of TolA. *Structure*, **7**, 711-722.
- Maass, D.R., Sepulveda, J., Pernthaler, A. & Shoemaker, C.B. (2007) Alpaca (*Lama pacos*) as a convenient source of recombinant camelid heavy chain antibodies (VHHs). *J Immunol Methods*, **324**, 13-25.
- Macaulay, C., Meier, E. & Forbes, D.J. (1995) Differential mitotic phosphorylation of proteins of the nuclear pore complex. *J Biol Chem*, **270**, 254-262.
- Mackay, I.M., Arden, K.E. & Nitsche, A. (2002) Real-time PCR in virology. *Nucleic Acids Res*, **30**, 1292-1305.
- Mahajan, R., Delphin, C., Guan, T., Gerace, L. & Melchior, F. (1997) A small ubiquitin-related polypeptide involved in targeting RanGAP1 to nuclear pore complex protein RanBP2. *Cell*, **88**, 97-107.
- Mansfeld, J. et al. (2006) The conserved transmembrane nucleoporin NDC1 is required for nuclear pore complex assembly in vertebrate cells. *Mol Cell*, **22**, 93-103.
- Marcon, E. et al. (2015) Assessment of a method to characterize antibody selectivity and specificity for use in immunoprecipitation. *Nat Methods*,
- Martineau, P., Jones, P. & Winter, G. (1998) Expression of an antibody fragment at high levels in the bacterial cytoplasm. *J Mol Biol*, **280**, 117-127.
- Massa, S. et al. (2014) Site-specific labeling of cysteine-tagged camelid single-domain antibody-fragments for use in molecular imaging. *Bioconjug Chem*, **25**, 979-988.
- McCafferty, J., Griffiths, A.D., Winter, G. & Chiswell, D.J. (1990) Phage antibodies: filamentous phage displaying antibody variable domains. *Nature*, **348**, 552-554.
- Melcák, I., Hoelz, A. & Blobel, G. (2007) Structure of Nup58/45 suggests flexible nuclear pore diameter by intermolecular sliding. *Science*, **315**, 1729-1732.
- Melchior, F., Paschal, B., Evans, J. & Gerace, L. (1993) Inhibition of nuclear protein import by nonhydrolyzable analogues of GTP and identification of the small GTPase Ran/TC4 as an essential transport factor. *J Cell Biol*, **123**, 1649-1659.
- Mellacheruvu, D. et al. (2013) The CRAPome: a contaminant repository for affinity purification-mass spectrometry data. *Nat Methods*, **10**, 730-736.
- Meyer, T.F. & Geider, K. (1979) Bacteriophage fd gene II-protein. II. Specific cleavage and relaxation of supercoiled RF from filamentous phages. *J Biol Chem*, **254**, 12642-12646.
- Meyer, T.F. & Geider, K. (1982) Enzymatic synthesis of bacteriophage fd viral DNA. *Nature*, **296**, 828-832.
- Michel, B. & Zinder, N.D. (1989) Translational repression in bacteriophage f1: characterization of the gene V protein target on the gene II mRNA. *Proc Natl Acad Sci U S A*, **86**, 4002-4006.
- Mikhaylova, M. et al. (2015) Resolving bundled microtubules using anti-tubulin nanobodies. *Nat Commun*, **6**, 7933.
- Miller, B.R., Powers, M., Park, M., Fischer, W. & Forbes, D.J. (2000) Identification of a new vertebrate nucleoporin, Nup188, with the use of a novel organelle trap assay. *Mol Biol Cell*, **11**, 3381-3396.

- Miller, J.H. & Albertini, A.M. (1983) Effects of surrounding sequence on the suppression of nonsense codons. *J Mol Biol*, **164**, 59-71.
- Miller, L. & Daniel, J.C. (1977) Comparison of in vivo and in vitro ribosomal RNA synthesis in nucleolar mutants of *Xenopus laevis*. *In Vitro*, **13**, 557-563.
- Mitchell, J.M., Mansfeld, J., Capitanio, J., Kutay, U. & Wozniak, R.W. (2010) Pom121 links two essential subcomplexes of the nuclear pore complex core to the membrane. *J Cell Biol*, **191**, 505-521.
- Mohr, D., Frey, S., Fischer, T., Güttler, T. & Görlich, D. (2009) Characterisation of the passive permeability barrier of nuclear pore complexes. *EMBO J*, **28**, 2541-2553.
- Moore, M.S. & Blobel, G. (1993) The GTP-binding protein Ran/TC4 is required for protein import into the nucleus. *Nature*, **365**, 661-663.
- Muyldermans, S. (2013) Nanobodies: natural single-domain antibodies. *Annu Rev Biochem*, **82**, 775-797.
- Muyldermans, S., Atarhouch, T., Saldanha, J., Barbosa, J.A. & Hamers, R. (1994) Sequence and structure of VH domain from naturally occurring camel heavy chain immunoglobulins lacking light chains. *Protein Eng*, **7**, 1129-1135.
- Nguyen, V.K., Hamers, R., Wyns, L. & Muyldermans, S. (1999) Loss of splice consensus signal is responsible for the removal of the entire C(H)1 domain of the functional camel IGG2A heavy-chain antibodies. *Mol Immunol*, **36**, 515-524.
- Nguyen, V.K., Hamers, R., Wyns, L. & Muyldermans, S. (2000) Camel heavy-chain antibodies: diverse germline V(H)H and specific mechanisms enlarge the antigen-binding repertoire. *EMBO J*, **19**, 921-930.
- Nguyen, V.K., Muyldermans, S. & Hamers, R. (1998) The specific variable domain of camel heavy-chain antibodies is encoded in the germline. *J Mol Biol*, **275**, 413-418.
- Nguyen, V.K., Su, C., Muyldermans, S. & van der Loo, W. (2002) Heavy-chain antibodies in Camelidae: a case of evolutionary innovation. *Immunogenetics*, **54**, 39-47.
- Nieba, L., Honegger, A., Krebber, C. & Plückthun, A. (1997) Disrupting the hydrophobic patches at the antibody variable/constant domain interface: improved in vivo folding and physical characterization of an engineered scFv fragment. *Protein Eng*, **10**, 435-444.
- Niesen, F.H., Berglund, H. & Vedadi, M. (2007) The use of differential scanning fluorimetry to detect ligand interactions that promote protein stability. *Nat. Protoc.*, **2**, 2212-2221.
- Nilsson, B. et al. (1987) A synthetic IgG-binding domain based on staphylococcal protein A. *Protein Eng*, **1**, 107-113.
- Nord, K. et al. (1997) Binding proteins selected from combinatorial libraries of an alpha-helical bacterial receptor domain. *Nat Biotechnol*, **15**, 772-777.
- Olichon, A. & Surrey, T. (2007) Selection of genetically encoded fluorescent single domain antibodies engineered for efficient expression in *Escherichia coli*. *J Biol Chem*, **282**, 36314-36320.
- Olsson, M., Schéele, S. & Ekblom, P. (2004) Limited expression of nuclear pore membrane glycoprotein 210 in cell lines and tissues suggests cell-type specific nuclear pores in metazoans. *Exp Cell Res*, **292**, 359-370.
- Opalka, N. et al. (2003) Structure of the filamentous phage pIV multimer by cryo-electron microscopy. *J Mol Biol*, **325**, 461-470.
- Ori, A. et al. (2013) Cell type-specific nuclear pores: a case in point for context-dependent stoichiometry of molecular machines. *Mol Syst Biol*, **9**, 648.
- Paduch, M. et al. (2013) Generating conformation-specific synthetic antibodies to trap proteins in selected functional states. *Methods*, **60**, 3-14.
- Paes, C. et al. (2009) Atomic-level mapping of antibody epitopes on a GPCR. *J Am Chem Soc*, **131**, 6952-6954.
- Pardon, E. et al. (2014) A general protocol for the generation of Nanobodies for structural biology. *Nat Protoc*, **9**, 674-693.
- Parmley, S.F. & Smith, G.P. (1988) Antibody-selectable filamentous fd phage vectors: affinity purification of target genes. *Gene*, **73**, 305-318.
- Pérez, J.M. et al. (2001) Thermal unfolding of a llama antibody fragment: a two-state reversible process. *Biochemistry*, **40**, 74-83.
- Pfaffl, M.W. (2004) Quantification strategies in real-time PCR. In *A-Z of quantitative PCR*, (Ed, Bustin, S.) International University Line, La Jolla, CA, USA, pp. 87-112.
- Pichler, A., Gast, A., Seeler, J.S., Dejean, A. & Melchior, F. (2002) The nucleoporin RanBP2 has SUMO1 E3 ligase activity. *Cell*, **108**, 109-120.
- Platonova, E., Winterflood, C.M. & Ewers, H. (2015a) A simple method for GFP- and RFP-based dual color single-molecule localization microscopy. *ACS Chem Biol*, **10**, 1411-1416.
- Platonova, E. et al. (2015b) Single-molecule microscopy of molecules tagged with GFP or mRFP derivatives in mammalian cells using nanobody binders. *Methods*,



- Porter, R.R. (1959) The hydrolysis of rabbit  $\gamma$ -globulin and antibodies with crystalline papain. *Biochem J*, **73**, 119-126.
- Pritchard, C.E., Fornerod, M., Kasper, L.H. & van Deursen, J.M. (1999) RAE1 is a shuttling mRNA export factor that binds to a GLEBS-like NUP98 motif at the nuclear pore complex through multiple domains. *J Cell Biol*, **145**, 237-254.
- Proba, K., Wörn, A., Honegger, A. & Plückthun, A. (1998) Antibody scFv fragments without disulfide bonds made by molecular evolution. *J Mol Biol*, **275**, 245-253.
- Qi, H., Lu, H., Qiu, H.J., Petrenko, V. & Liu, A. (2012) Phagemid vectors for phage display: properties, characteristics and construction. *J Mol Biol*, **417**, 129-143.
- Radu, A., Moore, M.S. & Blobel, G. (1995) The peptide repeat domain of nucleoporin Nup98 functions as a docking site in transport across the nuclear pore complex. *Cell*, **81**, 215-222.
- Rakonjac, J., Feng, J. & Model, P. (1999) Filamentous phage are released from the bacterial membrane by a two-step mechanism involving a short C-terminal fragment of pIII. *J Mol Biol*, **289**, 1253-1265.
- Ramm, K., Gehrig, P. & Plückthun, A. (1999) Removal of the conserved disulfide bridges from the scFv fragment of an antibody: effects on folding kinetics and aggregation. *J Mol Biol*, **290**, 535-546.
- Rast, J.P., Amemiya, C.T., Litman, R.T., Strong, S.J. & Litman, G.W. (1998) Distinct patterns of IgH structure and organization in a divergent lineage of chondrichthyan fishes. *Immunogenetics*, **47**, 234-245.
- Reichelt, R. et al. (1990) Correlation between structure and mass distribution of the nuclear pore complex and of distinct pore complex components. *J Cell Biol*, **110**, 883-894.
- Rexach, M. & Blobel, G. (1995) Protein import into nuclei: association and dissociation reactions involving transport substrate, transport factors, and nucleoporins. *Cell*, **83**, 683-692.
- Ribbeck, K. & Görlich, D. (2001) Kinetic analysis of translocation through nuclear pore complexes. *EMBO J*, **20**, 1320-1330.
- Ribbeck, K., Lipowsky, G., Kent, H.M., Stewart, M. & Görlich, D. (1998) NTF2 mediates nuclear import of Ran. *EMBO J*, **17**, 6587-6598.
- Riechmann, L. & Holliger, P. (1997) The C-terminal domain of TolA is the coreceptor for filamentous phage infection of *E. coli*. *Cell*, **90**, 351-360.
- Ries, J., Kaplan, C., Platonova, E., Eghlidi, H. & Ewers, H. (2012) A simple, versatile method for GFP-based super-resolution microscopy via nanobodies. *Nat Methods*, **9**, 582-584.
- Ritz, D., Lim, J., Reynolds, C.M., Poole, L.B. & Beckwith, J. (2001) Conversion of a peroxiredoxin into a disulfide reductase by a triplet repeat expansion. *Science*, **294**, 158-160.
- Rothbauer, U. et al. (2008) A versatile nanotrapp for biochemical and functional studies with fluorescent fusion proteins. *Mol Cell Proteomics*, **7**, 282-289.
- Rothbauer, U. et al. (2006) Targeting and tracing antigens in live cells with fluorescent nanobodies. *Nat Methods*, **3**, 887-889.
- Rout, M.P. et al. (2000) The yeast nuclear pore complex: composition, architecture, and transport mechanism. *J Cell Biol*, **148**, 635-651.
- Russel, M. & Model, P. (1985) Thioredoxin is required for filamentous phage assembly. *Proc Natl Acad Sci U S A*, **82**, 29-33.
- Russel, M. & Model, P. (1989) Genetic analysis of the filamentous bacteriophage packaging signal and of the proteins that interact with it. *J Virol*, **63**, 3284-3295.
- Rust, M.J., Bates, M. & Zhuang, X. (2006) Sub-diffraction-limit imaging by stochastic optical reconstruction microscopy (STORM). *Nat Methods*, **3**, 793-795.
- Sachdev, R., Sieverding, C., Flötenmeyer, M. & Antonin, W. (2012) The C-terminal domain of Nup93 is essential for assembly of the structural backbone of nuclear pore complexes. *Mol Biol Cell*, **23**, 740-749.
- Sambrook, J., Fritsch, E.F. & Maniatis, T. (1989) *Molecular cloning : a laboratory manual*. Cold Spring Harbor Laboratory Press, Cold Spring Harbor, NY, USA.
- Sander, B., Golas, M.M. & Stark, H. (2003) Automatic CTF correction for single particles based upon multivariate statistical analysis of individual power spectra. *J Struct Biol*, **142**, 392-401.
- Schatz, P.J. (1993) Use of peptide libraries to map the substrate specificity of a peptide-modifying enzyme: a 13 residue consensus peptide specifies biotinylation in *Escherichia coli*. *Biotechnology (N Y)*, **11**, 1138-1143.
- Schermelleh, L. et al. (2008) Subdiffraction multicolor imaging of the nuclear periphery with 3D structured illumination microscopy. *Science*, **320**, 1332-1336.
- Schmidt, C. & Urlaub, H. (2009) iTRAQ-labeling of in-gel digested proteins for relative quantification. *Methods Mol Biol*, **564**, 207-226.

- Schmidt, H.B. & Görlich, D. (2015) Nup98 FG domains from diverse species spontaneously phase-separate into particles with nuclear pore-like permselectivity. *Elife*, **4**.
- Schmidt, H.B. & Görlich, D. (2016) Transport Selectivity of Nuclear Pores, Phase Separation, and Membraneless Organelles. *Trends Biochem Sci*, **41**, 46-61.
- Schmiedl, A., Breitling, F., Winter, C.H., Queitsch, I. & Dübel, S. (2000) Effects of unpaired cysteines on yield, solubility and activity of different recombinant antibody constructs expressed in E. coli. *J Immunol Methods*, **242**, 101-114.
- Schmitz, K.R., Bagchi, A., Roovers, R.C., van Bergen en Henegouwen, P.M. & Ferguson, K.M. (2013) Structural evaluation of EGFR inhibition mechanisms for nanobodies/VHH domains. *Structure*, **21**, 1214-1224.
- Schofield, D.J. et al. (2007) Application of phage display to high throughput antibody generation and characterization. *Genome Biol*, **8**, R254.
- Schrader, N. et al. (2008) Structural basis of the nic96 subcomplex organization in the nuclear pore channel. *Mol Cell*, **29**, 46-55.
- Scott, J.K. & Smith, G.P. (1990) Searching for peptide ligands with an epitope library. *Science*, **249**, 386-390.
- Sharma, A., Solmaz, S.R., Blobel, G. & Melčák, I. (2015) Ordered Regions of Channel Nucleoporins Nup62, Nup54, and Nup58 Form Dynamic Complexes in Solution. *J Biol Chem*, **290**, 18370-18378.
- Sieber, V., Plückthun, A. & Schmid, F.X. (1998) Selecting proteins with improved stability by a phage-based method. *Nat Biotechnol*, **16**, 955-960.
- Siniossoglou, S. et al. (2000) Structure and assembly of the Nup84p complex. *J Cell Biol*, **149**, 41-54.
- Siniossoglou, S. et al. (1996) A novel complex of nucleoporins, which includes Sec13p and a Sec13p homolog, is essential for normal nuclear pores. *Cell*, **84**, 265-275.
- Skerra, A. & Plückthun, A. (1988) Assembly of a functional immunoglobulin Fv fragment in Escherichia coli. *Science*, **240**, 1038-1041.
- Smith, G.P. (1985) Filamentous fusion phage: novel expression vectors that display cloned antigens on the virion surface. *Science*, **228**, 1315-1317.
- Solmaz, S.R., Blobel, G. & Melčák, I. (2013) Ring cycle for dilating and constricting the nuclear pore. *Proc Natl Acad Sci U S A*, **110**, 5858-5863.
- Solmaz, S.R., Chauhan, R., Blobel, G. & Melčák, I. (2011) Molecular architecture of the transport channel of the nuclear pore complex. *Cell*, **147**, 590-602.
- Soltes, G. et al. (2007) On the influence of vector design on antibody phage display. *J Biotechnol*, **127**, 626-637.
- Sørensen, H.P., Sperling-Petersen, H.U. & Mortensen, K.K. (2003) A favorable solubility partner for the recombinant expression of streptavidin. *Protein Expr Purif*, **32**, 252-259.
- Stade, K., Ford, C.S., Guthrie, C. & Weis, K. (1997) Exportin 1 (Crm1p) is an essential nuclear export factor. *Cell*, **90**, 1041-1050.
- Stadler, V. et al. (2008) Combinatorial synthesis of peptide arrays with a laser printer. *Angew Chem Int Ed Engl*, **47**, 7132-7135.
- Stavru, F. et al. (2006a) NDC1: a crucial membrane-integral nucleoporin of metazoan nuclear pore complexes. *J Cell Biol*, **173**, 509-519.
- Stavru, F., Nautrup-Pedersen, G., Cordes, V.C. & Görlich, D. (2006b) Nuclear pore complex assembly and maintenance in POM121- and gp210-deficient cells. *J Cell Biol*, **173**, 477-483.
- Steiner, D., Forrer, P. & Plückthun, A. (2008) Efficient selection of DARPins with sub-nanomolar affinities using SRP phage display. *J Mol Biol*, **382**, 1211-1227.
- Steiner, D., Forrer, P., Stumpp, M.T. & Plückthun, A. (2006) Signal sequences directing cotranslational translocation expand the range of proteins amenable to phage display. *Nat Biotechnol*, **24**, 823-831.
- Stothard, P. (2000) The sequence manipulation suite: JavaScript programs for analyzing and formatting protein and DNA sequences. *Biotechniques*, **28**, 1102, 1104.
- Stuwe, T. et al. (2015a) Architecture of the fungal nuclear pore inner ring complex. *Science*, **350**, 56-64.
- Stuwe, T. et al. (2015b) Nuclear pores. Architecture of the nuclear pore complex coat. *Science*, **347**, 1148-1152.
- Stuwe, T., von Borzyskowski, L.S., Davenport, A.M. & Hoelz, A. (2012) Molecular basis for the anchoring of proto-oncoprotein Nup98 to the cytoplasmic face of the nuclear pore complex. *J Mol Biol*, **419**, 330-346.
- Sukegawa, J. & Blobel, G. (1993) A nuclear pore complex protein that contains zinc finger motifs, binds DNA, and faces the nucleoplasm. *Cell*, **72**, 29-38.
- Szymborska, A. et al. (2013) Nuclear pore scaffold structure analyzed by super-resolution microscopy and particle averaging. *Science*, **341**, 655-658.

- Theerthagiri, G., Eisenhardt, N., Schwarz, H. & Antonin, W. (2010) The nucleoporin Nup188 controls passage of membrane proteins across the nuclear pore complex. *J Cell Biol*, **189**, 1129-1142.
- Tunquist, B.J. & Maller, J.L. (2003) Under arrest: cytotostatic factor (CSF)-mediated metaphase arrest in vertebrate eggs. *Genes Dev*, **17**, 683-710.
- Ulrich, A., Partridge, J.R. & Schwartz, T.U. (2014) The stoichiometry of the nucleoporin 62 subcomplex of the nuclear pore in solution. *Mol Biol Cell*, **25**, 1484-1492.
- van der Linden, R.H. et al. (1999) Comparison of physical chemical properties of llama VHH antibody fragments and mouse monoclonal antibodies. *Biochim Biophys Acta*, **1431**, 37-46.
- van Heel, M., Harauz, G., Orlova, E.V., Schmidt, R. & Schatz, M. (1996) A new generation of the IMAGIC image processing system. *J Struct Biol*, **116**, 17-24.
- Vasu, S. et al. (2001) Novel vertebrate nucleoporins Nup133 and Nup160 play a role in mRNA export. *J Cell Biol*, **155**, 339-354.
- Vaughan, T.J. et al. (1996) Human antibodies with sub-nanomolar affinities isolated from a large non-immunized phage display library. *Nat Biotechnol*, **14**, 309-314.
- Vieira, J. & Messing, J. (1987) Production of single-stranded plasmid DNA. *Methods Enzymol*, **153**, 3-11.
- Vincke, C. et al. (2012) Generation of single domain antibody fragments derived from camelids and generation of manifold constructs. *Methods Mol Biol*, **907**, 145-176.
- Vollmer, B. & Antonin, W. (2014) The diverse roles of the Nup93/Nic96 complex proteins - structural scaffolds of the nuclear pore complex with additional cellular functions. *Biol Chem*, **395**, 515-528.
- Vollmer, B. et al. (2012) Dimerization and direct membrane interaction of Nup53 contribute to nuclear pore complex assembly. *EMBO J*, **31**, 4072-4084.
- von Appen, A. et al. (2015) In situ structural analysis of the human nuclear pore complex. *Nature*, **526**, 140-143.
- Vu, K.B., Ghahroudi, M.A., Wyns, L. & Muyldermans, S. (1997) Comparison of llama VH sequences from conventional and heavy chain antibodies. *Mol Immunol*, **34**, 1121-1131.
- Wahner-Roedler, D.L. & Kyle, R.A. (2005) Heavy chain diseases. *Best Pract Res Clin Haematol*, **18**, 729-746.
- Walther, T.C. et al. (2003) The conserved Nup107-160 complex is critical for nuclear pore complex assembly. *Cell*, **113**, 195-206.
- Walther, T.C. et al. (2001) The nucleoporin Nup153 is required for nuclear pore basket formation, nuclear pore complex anchoring and import of a subset of nuclear proteins. *EMBO J*, **20**, 5703-5714.
- Walther, T.C. et al. (2002) The cytoplasmic filaments of the nuclear pore complex are dispensable for selective nuclear protein import. *J Cell Biol*, **158**, 63-77.
- Ward, E.S., Güssow, D., Griffiths, A.D., Jones, P.T. & Winter, G. (1989) Binding activities of a repertoire of single immunoglobulin variable domains secreted from Escherichia coli. *Nature*, **341**, 544-546.
- Watson, M.L. (1959) Further observations on the nuclear envelope of the animal cell. *J Biophys Biochem Cytol*, **6**, 147-156.
- Wente, S.R. & Blobel, G. (1994) NUP145 encodes a novel yeast glycine-leucine-phenylalanine-glycine (GLFG) nucleoporin required for nuclear envelope structure. *J Cell Biol*, **125**, 955-969.
- Wente, S.R., Rout, M.P. & Blobel, G. (1992) A new family of yeast nuclear pore complex proteins. *J Cell Biol*, **119**, 705-723.
- Winter, G., Griffiths, A.D., Hawkins, R.E. & Hoogenboom, H.R. (1994) Making antibodies by phage display technology. *Annu Rev Immunol*, **12**, 433-455.
- Winter, G. & Milstein, C. (1991) Man-made antibodies. *Nature*, **349**, 293-299.
- Woolven, B.P., Frenken, L.G., van der Logt, P. & Nicholls, P.J. (1999) The structure of the llama heavy chain constant genes reveals a mechanism for heavy-chain antibody formation. *Immunogenetics*, **50**, 98-101.
- Wörn, A. & Plückthun, A. (1998) An intrinsically stable antibody scFv fragment can tolerate the loss of both disulfide bonds and fold correctly. *FEBS Lett*, **427**, 357-361.
- Wörn, A. & Plückthun, A. (2001) Stability engineering of antibody single-chain Fv fragments. *J Mol Biol*, **305**, 989-1010.
- Wu, J., Matunis, M.J., Kraemer, D., Blobel, G. & Coutavas, E. (1995) Nup358, a cytoplasmically exposed nucleoporin with peptide repeats, Ran-GTP binding sites, zinc fingers, a cyclophilin A homologous domain, and a leucine-rich region. *J Biol Chem*, **270**, 14209-14213.
- Wühr, M. et al. (2014) Deep proteomics of the *Xenopus laevis* egg using an mRNA-derived reference database. *Curr Biol*, **24**, 1467-1475.
- Yang, B. et al. (2012) Identification of cross-linked peptides from complex samples. *Nat Methods*, **9**, 904-906.

- 
- Yokoyama, N. et al. (1995) A giant nucleopore protein that binds Ran/TC4. *Nature*, **376**, 184-188.
- Yoshida, K., Seo, H.S., Debler, E.W., Blobel, G. & Hoelz, A. (2011) Structural and functional analysis of an essential nucleoporin heterotrimer on the cytoplasmic face of the nuclear pore complex. *Proc Natl Acad Sci U S A*, **108**, 16571-16576.
- Zahnd, C. et al. (2004) Directed in vitro evolution and crystallographic analysis of a peptide-binding single chain antibody fragment (scFv) with low picomolar affinity. *J Biol Chem*, **279**, 18870-18877.
- Zarschler, K., Witecy, S., Kapplusch, F., Foerster, C. & Stephan, H. (2013) High-yield production of functional soluble single-domain antibodies in the cytoplasm of Escherichia coli. *Microb Cell Fact*, **12**, 97.
- Zhang, Y. (2008) I-TASSER server for protein 3D structure prediction. *BMC Bioinformatics*, **9**, 40.



## 11 Curriculum vitae

<b>Name</b>	Tino Pleiner
<b>Date of birth</b>	25.08.1988
<b>Place of birth</b>	Zeitz, Germany
<b>Nationality</b>	German

### Education

**2012 – 2016**      **Doctoral studies** in the Department of Cellular Logistics under supervision of Prof. Dr. Dirk Görlich at the Max Planck Institute for Biophysical Chemistry, Göttingen, Germany

Göttingen Graduate School for Neurosciences, Biophysics, and Molecular Biosciences (GGNB) graduate school (Molecular Biology program) at the Georg August University Göttingen

**2010 – 2012**      **M. Sc. in Molecular Biology**  
Department of Cellular Logistics, Max Planck Institute for Biophysical Chemistry, Göttingen, Germany

International Max Planck Research School (IMPRS) for Molecular Biology at the Georg August University Göttingen

**2007 – 2010**      **B. Sc. in Biochemistry**  
Institute of Biochemistry, University of Leipzig under supervision of Prof. Dr. Mario Mörl

**2007**              **High school diploma (Abitur)**  
Geschwister-Scholl-Gymnasium Zeitz, Germany

## 12 List of publications

**Pleiner, T.**, Bates, M., Trakhanov, S., Lee, C.T., Schliep, J.E., Chug, H., Böhning, M., Stark, H., Urlaub, H. & Görlich, D. (2015) Nanobodies: site-specific labeling for super-resolution imaging, rapid epitope-mapping and native protein complex isolation. *Elife*, 4:e11349

Chug, H., Trakhanov, S., Hülsmann, B.B., **Pleiner, T.** & Görlich, D. (2015) Crystal structure of the metazoan Nup62•Nup58•Nup54 nucleoporin complex. *Science*, 350, 106-110.

Migliorini, E., Thakar, D., Sadir, R., **Pleiner, T.**, Baleux, F., Lortat-Jacob, H., Coche-Guerente, L. & Richter, R.P. (2014) Well-defined biomimetic surfaces to characterize glycosaminoglycan-mediated interactions on the molecular, supramolecular and cellular levels. *Biomaterials*, 35, 8903-8915.





